Title

Advancing Label Free Detection Techniques Through Surface Based Sensing and Machine Learning

Author

Stuart, Daniel David

Publication Date

2023

UNIVERSITY OF CALIFORNIA

RIVERSIDE

Advancing Label Free Detection Techniques Through Surface Based Sensing and Machine Learning

A Dissertation submitted in partial satisfaction
of the requirements for the degree of

Doctor of Philosophy

in

Chemistry

by

Daniel David Stuart

December 2023

Dissertation Committee:

Dr. Quan Cheng, Chairperson

Dr. Yinsheng Wang

Dr. Haofei Zhang

The Dissertation of Daniel David Stuart is approved:

_____

_____

_____

Committee Chairperson

University of California, Riverside

Acknowledgements

It is with a bittersweet note that I write this as my time at the University of California, Riverside comes to an end, but a new adventure begins. It at times has been a difficult process but looking back it has been nothing short of marvelous. I have had the opportunity to expand my knowledge in ways that I never thought possible and try anything I could think of. None of this would have been possible without the guidance of my mentor Professor Quan "Jason" Cheng whose support has been unwavering.

Jason, a simple thank you is not enough as the opportunity you have provided me has been life changing. Your advice and mentorship have been instrumental in shaping my view of science and the importance it plays in solving the problems of the world. Furthermore, your guidance and assistance were integral in bringing me out of my shell, through encouraging me to write, publish, and present my work. I would like to particularly thank you for providing an environment that fostered and challenged my critical thinking, training me to tackle any challenge that comes my way. It is awe inspiring to think of the many students, including myself, you have kindled a passion for analytical chemistry in and the many more who are yet to come.

I would also like to thank the faculty and staff at UCR who have all been phenomenally supportive. In particular, the members of my committee, Professor Yinsheng Wang and Professor Haofei Zhang for providing meaningful feedback and kind guidance throughout my graduate career. As well as Professor Joseph Genereux who was

not only a phenomenal teacher but has also been eager to chat and provide advice a plethora of times over my time at UCR.

Though of course none of this would have been possible without my fellow Cheng lab students who kept me sane and made the experience an enjoyable one. Lambert, while your training in my first year was pivotal to my success, the times that will be truly cherished are the conversations about games, movies, books, and the world that brought cheer into every day. Santino, I would not be here without your friendship and the daily lunches where I could complain about the world and God knows what else. Malinick, your ability to say the wrong thing at the right time has been constantly a joy, one I hope to continue to enjoy into the future. To Kelvin, whose guidance was critical and whose unorthodox League builds still bring a smile to my face. Cole, it has been a privilege to teach you and learn from you, I would have significantly more pounds on me without our climbing and my takes would be too extreme without your tempering. To Pete, without whom much of my publication would not have been possible, your kindness and ingenuity were enriching to the lab well beyond your time. Bochao, who also made most of my publication possible, working with you has been a pleasure and a privilege. Zhengdong, thank you for your support in my early years as a graduate student and for exposing me to food I may never have tried. Liza, your joy and compassion were infectious, making coming to lab a delight. Fatimah, working with you on projects was delightful and your perseverance and success is a reminder to me each day to never give up. Caleb, your assistance as an undergraduate researcher was crucial to my progress through graduate school and I am proud to have played even a small part in your inevitably bright future. To

Bryce, the experience and insight you imparted to me while working together has been invaluable and without your work one of my chapters would not have been possible. Andy, I count myself lucky to have been able to witness the finality of your thesis work and learn from your years of experience, seeing your success grow every year has been heartening. Xin, seeing your knowledge grow and project come to fruition has been a delight and I wish you success in your pursuit of a PhD. To each and every one of you thank you for the time you have taken to converse with me and help me through my graduate school experience.

To my parents, I would not be here without your dedication to my education and care for my learning, which is greatly appreciated now even if it may not have been when I was younger. Dad, your passion for science and dedication to supporting my curiosity, have provided me with the tools to find solutions to problems instead of admitting defeat. Mom, your compassion for others and commitment to do what is right have stuck with me and driven me to focus on making the world a better place. Thank you both from the bottom of my heart.

Melinda, my person, your support from day one of graduate school has been monumental, I could not have done this alone. Always understanding and listening to me when days were rough and celebrating when they were good. It is a delight to look back and see how much we have both grown over these years and it is with elation that I look forward to our next step. Of course, including Ziggy, our newest addition, though she might kick me in the head while I sleep nobody can be mad at a puppy that cute.

This is dedicated to you, each name written here and each person reading this, your involvement in my graduate work and the pursuit of science, however small is greatly appreciated, as nothing is achieved alone.

Copyright Acknowledgement

The work presented in Chapter 3 was supported by contributions from both Caleb Pike and Dr. Alexander Malinick.

Some of the text and figures of Chapter 4 are adapted from work currently under review at the journal ACS Applied Materials & Interfaces, Manuscript ID: am-2023-129227.R2. This work was completed in collaboration with Alexander Malinick, Alexander Lambert, and Quan Cheng. The corresponding author, Dr. Quan Jason Cheng, directed and supervised the research that formed the basis of that chapter.

The work presented in Chapter 6 was supported by contributions from both Bryce Davis and Caleb Pike.

A portion of Figure 6.9 is adapted from *HardwareX* (**2020),** *8*, e00112 which is published under a Creative Commons Attribution-NonCommercial-No Derivatives License.

ABSTRACT OF THE DISSERTATION

Advancing Label Free Detection Techniques Through Surface Based Sensing and Machine Learning

by

Daniel David Stuart

Doctor of Philosophy, Graduate Program in Chemistry

University of California, Riverside, 2023

Dr. Quan Cheng, Chairperson

High-performing sensors have played a pivotal role in expanding our understanding of biological systems, disease diagnosis, environmental monitoring, and national security. The technical capability they provide has enabled us to obtain in-depth information and insights towards improving human health. One area of sensing that exemplifies this progress is the development of label free sensors which allow direct analysis of molecular interactions. Among these methods surface plasmon resonance (SPR) has emerged as a powerful, real-time detection technique for studies of biological interactions, drug discovery, and other important aspects that lead to new disease diagnosis. Through the implementation of new materials and methods SPR and other label-free sensors have expanded the range of analytes tested. This Dissertation aims to establish improvements in materials and methodologies through technology advancement for solving current sensor limitations. The work focuses on enhancing sensing signal while limiting the impact of

nonspecific interactions on label-free methods, providing expanded molecular identity information, and overcoming challenges encountered when detecting small molecules.

Chapters 2, 3, and 4 demonstrate advancements in unique biomimetic surfaces to enable the exploration of new biological systems as well as block nonspecific interactions. Chapter 2 focuses on a tethered membrane system to promote incorporation of relevant constituents into lipid bilayers without compromising membrane mobility property and drug delivery interactions. Chapter 3 employs a charged membrane to suppress nonspecific interactions and explores the working mechanism. Chapter 4 expands the capabilities of label-free sensing systems through development of curved membrane platforms that mitigate the decay limits through modeling of lipid distribution in vesicles. Chapter 5 exploits the plasmonic properties of SPR chips to enhance signals in matrix assisted laser desorption ionization mass spectrometry (MALDI-MS) , which is further facilitated with development of machine learning models to identify bacterial species. In Chapter 6, the limitation of small molecule analysis with SPR is tackled by taking advantage of pressure effects to provide specific gas sensing.

Each of these Chapters provides novel advancements in sensing capabilities by addressing performance-impairing limitations in label-free sensors. Research goals are achieved both from improvements to SPR systems and incorporation of other methodologies to augment SPR results.

TABLE OF CONTENTS

List of Figures

List of Tables

Chapter 1: Introduction and Background

1.1 Introduction

The goal of this work is to develop and validate new powerful analytical techniques to improve human life by enhancing sensing capabilities. For our species' entire existence, we have been struggling against diseases from within our own bodies (cancer and autoimmune disease) or from outside forces (bacterial and viral infections). It was only within the last century that we have been able to begin identifying and treating disease, but this is just the beginning. The recent COVID-19 pandemic has made it clear how quickly new threats can emerge and has shown how devastating they can be. The emergence and expansion of antibiotic resistant bacteria has also impacted our society by millions of deaths each year. Therefore, monitoring disease is of key importance to ensure they do not get out of hand. This requires new tools, a portion of which will be discussed in the coming chapters.

The focus of this chapter is to illustrate and review the subject areas that form the backbone of the research demonstrated in the following chapters. The primary area of discussion will comprise the importance and technical aspects of surface-based sensing applications. With subcategories dedicated to expanding on surface-based techniques and their function as or in support of sensors. These subcategories will include surface plasmon resonance (SPR), matrix assisted laser desorption ionization (MALDI), fluorescence imaging, quartz crystal microbalance (QCM), and their application in the development of various sensors. Monte Carlo and machine learning methodologies will also be discussed

in regard to their usage in enabling data analysis of the complex data from these surface-based sensors.

1.2 Principle of Sensors

Sensors are fundamental to the operation of our societal safety structures by providing information crucial for identifying emerging dangers in areas such as disease and human health[1-3], environmental monitoring[4, 5], infrastructure inspection[6, 7], and many other aspects of our lives.[8] In short, sensors enable observation and identification of a target compound

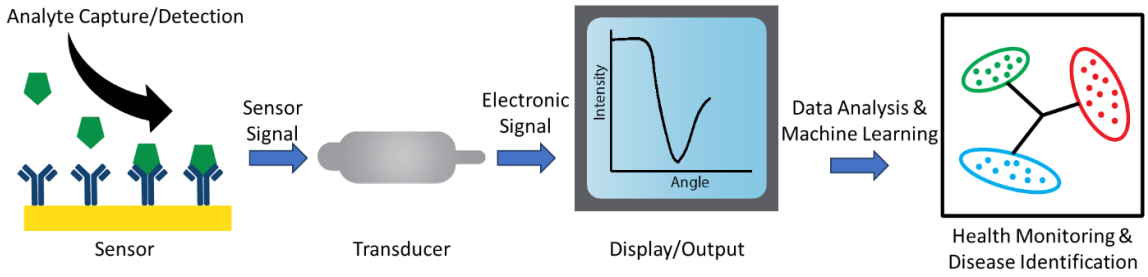

Figure 1.1. Scheme demonstrating the translation of sensor signal to a display through a signal transducer and then application of data processing to employ that data for analyte classification.

or stimuli through a combination of three key components. This starts with selection of the sensor target(s), followed by a mechanism of transduction that indicates target recognition or change, and finally ends with communication of said recognition to the user. The recognition event is identified based on induced electromagnetic field disruptions which depend on the sensor target. These disruptions can be measured through electrical potential (voltage), flow (current), frequency, photon absorption, transmittance, emission, or a combination of these. For example, fluorescence is a combination of photon absorption

and emission that is employed to detect presence of fluorochrome molecules that can be linked to the presence of targets of interest.

Sensors can be used qualitatively for simply recognition, or quantitatively for identification of presence and magnitude of the target. Many of these sensors focus on improving human health through monitoring of biomarkers, biological molecules causing or resulting from a specific disease, these sensors are known as biosensors.[1] While other sensors monitor nonbiological molecules that can impact our health to help ensure safety. These biological molecule targets can range from simple molecules like sugars[9], lipids[10, 11], metabolites[12], nucleic acids[13] and amino acids[14] to complex molecules proteins[15, 16], antibodies[17], and whole viruses[18] or even cells.[19] Examples of commonly used biological sensors are the glucose sensor which relies on a quantitative electrochemical signal produced by reaction between glucose oxidase and glucose[20] or qualitative SARS-COV-2 test kits based on a lateral flow assay generating colored bands through antibody mediated binding to SARS-COV-2 antigens.[21] While nonbiological targets can extend from individual atoms or small molecules to large particle networks. With the most common example of nonbiological sensors being smoke detectors which alert us to small particle build up in the air via a reduction in current flow or reflection of light by these particles.[22]

Sensors can be split into labeled and label-free methodologies. Labeled techniques incorporate non-native secondary components that enable signal generation. Enzyme linked immunosorbent assay (ELISA)[23, 24] is a primary example of this sensor type as it includes a secondary antibody that binds to the initial recognition antibody. This secondary antibody has an enzyme linked to it, commonly horseradish peroxidase (HRP), that

oxidizes small molecule substrates added to the solution resulting in a color change or light production. As one HRP can catalyze many substrates, signal amplification is provided that enables highly sensitive detection to be achieved, however this significantly complicates the sensor and does not directly measure the recognition interaction. Other examples of labeled techniques include fluorescence imaging methods where fluorophore active labels are covalently linked or incorporated into target molecules to enable tracking of binding events via methods such as anisotropy[25, 26] or resonance energy transfer.[27, 28]

Label-free techniques ensure that the recognition interaction is being measured without secondary components. This is particularly important when working with small molecule targets as any included tags have a greater impact on the system based on their size in relation to the target molecule. Commonly utilized label-free techniques are field-effect transistors, quartz crystal microbalance (QCM), and optical techniques like whispering gallery mode and surface plasmon resonance (SPR) sensors. In label-free techniques only the analyte binding interaction is being measured which ensures that signal is consistent with the naturally occurring system as inclusion of tagged molecules can alter these binding interactions. Label-free analysis also enables signal to be obtained quickly in real-time as the interactions in question take place. However, label-free techniques still have challenges to be overcome, notably nonspecific interactions and surface fouling can have profound impacts on sensor performance and reproducibility. Therefore, methodologies to limit or account for these effects are of utmost importance and have been extensively investigated.

1.3 Surface Plasmon Resonance Sensor Theory

One of the primary label free techniques utilized in biological sensor development is surface plasmon resonance, a surface-based sensing tool.[29, 30] In short, the principle behind SPR is that, for plasmonic surfaces, any changes within the nanoscale region above the material have an impact on photon matching conditions thus changing the "SPR angle" which can be tracked to monitor these binding events. While signal is easily analyzed the physical properties behind SPR spectroscopy are significantly more complex due to their reliance on a network of optical relationships. As SPR is a fundamental technique utilized in the studies described in several of the following chapters these optical relationships will be discussed in depth.

1.3.1 Evanescent Field Excitement

When discussing surface plasmon resonance a major component is the excitation of an evanescent field upon plasmonic substrates.[29] This photon absorption and subsequent evanescent field excitation at metal surfaces is predominantly investigated in its total internal reflection (TIR) mode but can also occur in transmission modes from light perpendicular to the surface.[31] This plasmonic coupling also has various uses in enhancing surface sensitivity of other spectroscopic techniques notably; surface enhanced Raman scattering (SERS)[32], metal enhanced fluorescence[33], plasmon enhanced infrared spectroscopy[34] and second harmonic generation[35]. Our methodologies rely on evanescent field excitation in the commonly utilized TIR mode where incident photons, above a critical angle θ_c, passing from one medium n_1 to another of different reactive index n_2 are

completely reflected instead of transmitted or refracted. Our current understanding of TIR stems from the human fascination with light and its phenomena that has driven scientists to strive to understand and utilize its refractive properties for thousands of years. With early explanations of refraction provided by Ptolemy, Ibn Sahl, and Ibn al-Haytham[36] giving way to Willebrord Snellius/Christiaan Huygens[37] and Rene Descartes[38] independently deriving the mathematics describing the TIR effect that enables my work. The critical angle at which the phenomenon of total internal reflection, that has fascinated so many scientists before me, occurs is described by the law of refraction (Snell's Law) as:

$$\theta_c = \arcsin\left(\frac{n_2}{n_1}\right) \tag{1.1}$$

TIR is utilized for many purposes including binoculars, periscopes, telescopes, and fiber

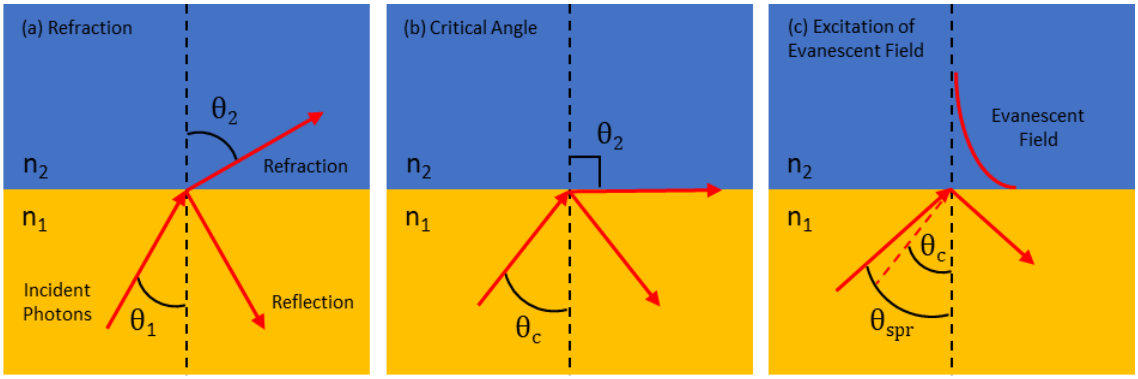

Figure 1.2. Refraction and reflection of light (a), total internal reflection at the critical angle (b), and evanescent field excitation above the critical angle (c).

optic cables to transmit optical information. However, where my work begins to diverge from Descartes and Snell is when a thin noble metal film, commonly gold, is coated on the n_1 material. Where now at angles above θ_c the TIR is no longer complete, as shown in Figure 1.2. Due to some of the incident photons being absorbed by the metal and inducing oscillation of electrons at the surface that generate an evanescent field directly adjacent to

the surface. This evanescent field extends into the second medium, n_2, where it decays exponentially with distance from the metal, this field can be represented as a wave vector parallel to the n_1/n_2 boundary:

$$k_{ev} = \frac{\omega}{c}\sqrt{\varepsilon_p}sin\theta \tag{1.2}$$

Here components ω and c correspond to the angular frequency of incident light and speed of light in a vacuum respectively. The wave vector equation can be modified based on these components' relationship with wavelength, $2\pi c = \lambda\omega$, to instead depend on the wavelength of incident light:

$$k_{ev} = \frac{2\pi}{\lambda}\sqrt{\varepsilon_p}sin\theta \tag{1.3}$$

This can be further simplified when in non-dispersive media as refractive index is equivalent to the square root of the permittivity dielectric constant, ε_p, resulting in a final equation dependent on refractive index:

$$k_{ev} = \frac{2\pi}{\lambda}nsin\theta \tag{1.4}$$

As the critical angle is dependent on n_2, any changes in refractive index within the range of the evanescent field will have an impact on the coupling conditions necessary for optimal photon absorption. When modeling a semi-infinite system this range or penetration depth extends based on the permittivity constant for each medium ε_1 and ε_2 respectively as skin depth, k_i[39]:

$$k_i = \frac{\omega}{c}\sqrt{\frac{-\varepsilon_i^2}{\varepsilon_1+\varepsilon_2}} \tag{1.5}$$

Thus, as shown by Abbas et al., for a commonly utilized gold substrate with 648 nm incident light the penetration depth is 191 nm in water and 351 nm in air[40]. This penetration is fundamental to enabling SPR sensing but its range limits this sensing to thin surface films.

1.3.2 Surface Plasmon Polaritons

As previously mentioned, when metal surfaces are incorporated into TIR setups a portion of incident photons are absorbed instead of reflected resulting in an evanescent field. This field is described as a surface plasmon polariton (SPP), which is an electromagnetic wave that travels along the interface between a metal and a dielectric as shown in Figure 1.3. Where the dielectric can be any other transparent solid material, liquid solution, or gaseous mixture. These polaritons are produced through energy from incident photons or electrons being transferred to the bulk plasma of the metal resulting in electron density oscillations. This relationship can be predicted through Maxwells equations with first description of the theory in 1957 by Ritchie[41] and subsequent experimental verification, by Powell et al., two years later[42]. This work demonstrated how energy transfer from incident photons to the metal layer would result in a distinct decrease in reflected light intensity. When scanning through angles of incidence higher than the critical TIR angle a clear intensity dip can be observed. This plasmonic behavior can be modeled through application of multilayer Fresnel equations[43, 44] with the inclusion of the real (n) and imaginary (k) components of refractive index, for the plasmonic metal used. For a two-

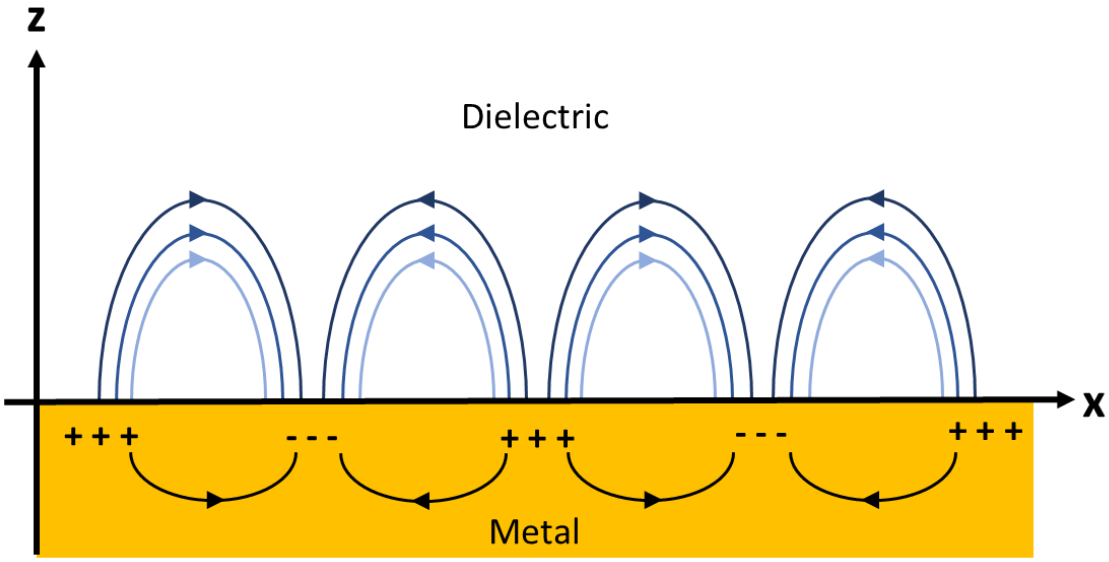

Figure 1.3. Illustration of surface plasmon polariton propagation with axes z and x representing the penetration depth (equation 1.5) and propagation distance (on the order of micrometers) respectively.

layer system the reflectivity dip can be predicted through two of these Fresnel equations, for reflectance of s and p-polarized light respectively:

$$r_s = \frac{n_1 cos\theta_i - n_2 cos\theta_t}{n_1 cos\theta_i + n_2 cos\theta_t} \quad (1.6)$$

$$r_p = \frac{n_2 cos\theta_i - n_1 cos\theta_t}{n_2 cos\theta_i + n_1 cos\theta_t} \quad (1.7)$$

However, for energy transfer to occur photons and SPPs must have equal frequency and momentum therefore a coupling medium is required to overcome dispersion differences. This is commonly achieved through a prism positioned flush to the metal surface in a formation known as the Kretschmann configuration (fig).[45] This system can be expressed through a significantly more complex equation that combines a characteristic matrix from Maxwell's equations of the layered system and the above Fresnel equations.[46] As such, software packages, like WinSpall, are commonly utilized to model expected reflectivity

spectra for these multilayer systems. Within these Fresnel equations n_1 and n_2 correspond to the complex refractive index, n = *n* + *ik*, of the two materials where *n* and *k* are typically derived from the Lorentz-Drude model of electrical conduction. Where, the reflectivity of a thin material ignorant of incident angle is described by:

$$R = \frac{(n-1)^2+k^2}{(n+1)^2+k^2} \tag{1.8}$$

These n and k values rely on the relative permittivity ε_r and the relative permeability μ_r of the material in question. However, as most of the metals employed in plasmonics are non-magnetic their permeability is $\mu_r \approx 1$, resulting in the complex refractive index depending solely on the materials permittivity:

$$n = \sqrt{\frac{\sqrt{\varepsilon_r^2+\varepsilon_i^2}+\varepsilon_r}{2}} \tag{1.9}$$

$$k = \sqrt{\frac{\sqrt{\varepsilon_r^2+\varepsilon_i^2}-\varepsilon_r}{2}} \tag{1.10}$$

When examining permittivity, it is derived from the metal's plasma oscillation ω_p and damping frequency Γ as well as the frequency of incident light ω and can be split into real ε_r and imaginary ε_i parts:

$$\varepsilon_r = 1 - \frac{\omega_p^2}{\omega^2+\Gamma^2} \tag{1.11}$$

$$\varepsilon_i = 1 - \frac{\omega_p^2\Gamma}{\omega(\omega^2+\Gamma^2)} \tag{1.12}$$

Where if electron motion is ignored the plasma oscillation can be described based on the number density of electrons n_e, the charge e and effective mass m^* of an electron, and the vacuum permittivity ε_0:

$$\omega_p = \sqrt{\frac{n_e e^2}{m^* \varepsilon_0}} \tag{1.13}$$

Within this the vacuum permittivity can be defined numerically based on the speed of light in a vacuum c and the approximate value for vacuum permeability μ_0:

$$\varepsilon_0 = \frac{1}{\mu_0 c^2} \approx 8.85419 \text{ x } 10^{-12} \frac{F}{m} \tag{1.14}$$

The number density of a selected metal can be numerically expressed via Avogadro's constant N_A, the density of the metal p_m, its molar mass M, and the number of free electrons Z. As gold, a commonly utilized plasmonic metal, is a monovalent metal its number of free electrons is 1, resulting in a number density of:

$$n_e = \frac{N_A Z p_m}{M} = 5.901 \text{ x } 10^{28} \frac{e^-}{m^3} \tag{1.15}$$

Based on this information and further experimental work, Olmon et al. determine the plasma oscillation (ω_p) of an evaporated gold substrate to be 8.5 ± 0.5 eV.[47]

1.3.3 Surface Plasmon Resonance Spectroscopy

As previously mentioned, when photons incident to a metal surface are appropriately coupled so that their frequency and momentum match that of the SPP, their energy is absorbed leading to a dip in intensity of reflected light. Mathematically this relationship is

represented through comparison of the wave vector of the incident photon with that of the SPP k_{spp} derived from maxwell's equations:

$$k_{spp} = \frac{\omega}{c}\sqrt{\frac{\varepsilon_1\varepsilon_2}{\varepsilon_1+\varepsilon_2}} \tag{1.16}$$

Where ε_1 and ε_2, correspond to the permittivity of the metal and dielectric respectively. Therefore, when refractive index changes occur within the skin depth of our SPP they

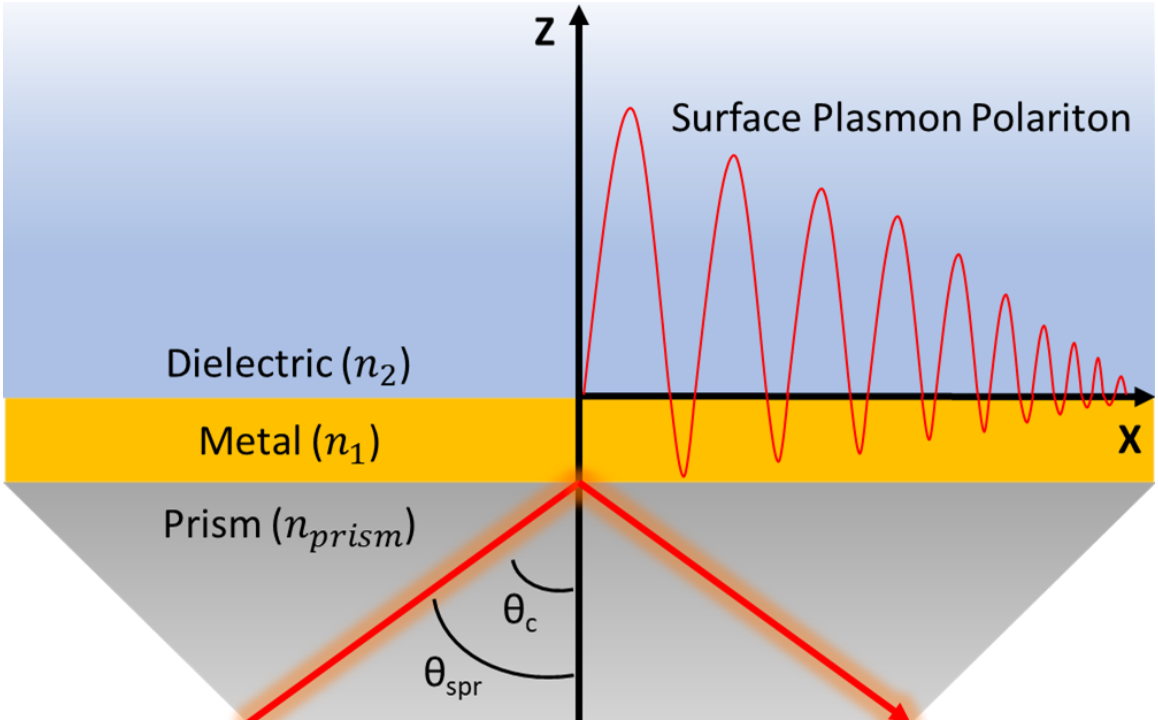

Figure 1.4. Schematic of surface plasmon polariton excitation using a dove prism in the Kretschmann configuration. With polaritons penetrating into the dielectric and propagating along the metal surface.

change its matching condition with our incident photons shifting the angle or wavelength at which optimal absorption occurs. This shift plotted versus time constitutes the basis of SPR spectroscopy, enabling minute refractive index changes to be tracked in real time.

In practice this is predominantly achieved utilizing the Kretschmann configuration (Figure 1.4), which was first conceived in 1968. Here a thin plasmonic film is placed in

contact with a prism, to enable photon coupling, and an analyte of choice. This system makes up the vast majority of commercialized SPR spectroscopy instrumentation and is commonly paired with a laser or LED source. This light source is then introduced through the prism and scanned either angularly using a 650-700 nm light source or across a wavelength range using white light. For angular based systems a range of angles are achieved either through physical rotation or via an array of photodiodes at fixed output angles from the system. SPR spectroscopy can also be achieved through the implementation of waveguide materials in fiber optic SPR[48, 49]. This provides advantages based on the ability to easily introduce the fiber optic cable into the sample of choice. However, consistency is difficult to maintain as any movements of the cable alter the light path and therefore the SPR response.

Further, the SPR evanescent field can couple with other plasmonic materials within its penetration depth. This is particularly distinct with nanostructures where the whole material lies within the evanescent field, in these cases a surface plasmon localized to the nanoparticle is excited and oscillates between edges of the material. This process coined as localized surface plasmon resonance (LSPR)[50] can also be utilized in various other configurations beyond TIR but is outside the scope of this work.

1.4 Sensing with SPR Spectroscopy Systems: Challenges and Solutions

For SPR spectroscopy instrumentation the resulting data of SPR shift versus time is known as a sensorgram and enables the visualization of surface binding events. While the fundamentals of how SPR spectroscopy systems work have been elucidated in the previous

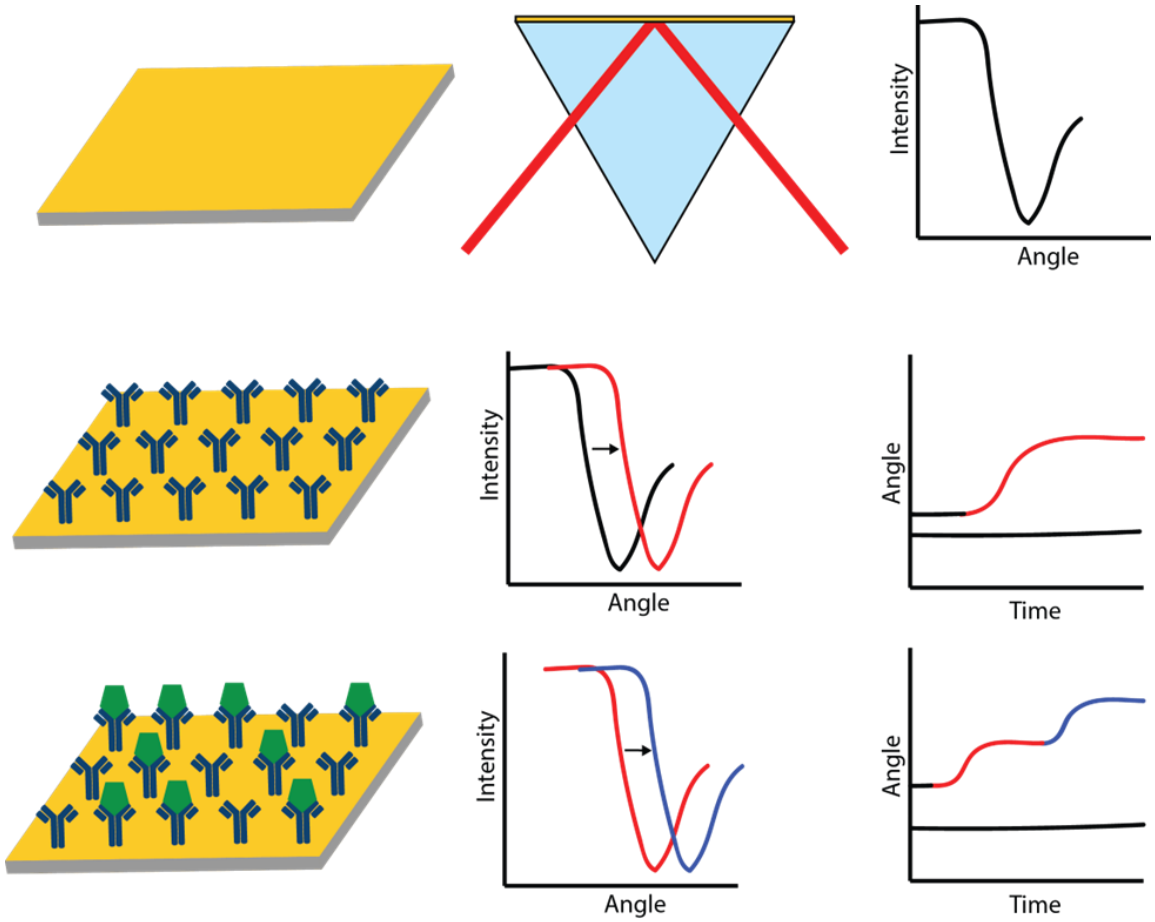

Figure 1.5. Illustration of a surface plasmon resonance sensorgram obtained via tracking the angle of minimum intensity over time which changes upon binding events. Shown here with signal shifts caused by antibody linkage to the sensor surface and then antibody facilitated protein capture.

sections when moving to actual analysis of surface binding events there are challenges that arise. These challenges and avenues to resolve them will be discussed in this section.

1.4.1 SPR Challenges

As anyone who has ever used an analytical technique or instrument will know, there are always limitations and challenges. Knowing what these issues are and accounting for them is an important aspect of pushing analytic capabilities forward. SPR is no stranger to challenges but through careful experiment design and work targeted towards understanding

how to limit their effect on experimental results SPR sensing applications can be improved and expanded.

The first of these challenges for SPR comes from non-specific interactions and surface fouling when working in complex biological media.[51] Here untargeted biological molecules non-specifically adhere to the sensor surface convoluting signal and blocking target molecules from binding. To combat this significant work has been done to formulate and test antifouling surfaces that can limit or block these nonspecific interactions from occurring thus improving SPR signal and consistency. To this end, various small molecules, polymers, DNA, and peptide structures have been developed to block the surface thus forming a barrier to inhibit non-specific interactions with substantial focus on zwitterionic chemical groups as antifouling substrates.[52] Recently lipid membranes have also appeared as a biomimetic system to curb surface fouling events due to their similar role in natural systems. We have contributed substantially to this field and have found lipid systems to be highly effective.[53] However, these lipid systems are not one size fits all and need to be investigated and understood to enable their use in other SPR sensing applications.

Another challenge faced in SPR sensing is that while the molecular identity of target molecules can be inferred based on the inclusion of known binding partners within the sensing scheme it is not directly known. If surface compounds can be classified this solidifies the significance of obtained SPR results. This also links back to non-specific binding challenges where molecular information can help characterize and account for these fouling interactions. Various methodologies have been employed to clarify the

identity of molecules bound to the surface SPR. This has been achieved predominantly through orthogonal surface analysis techniques with mass spectrometry, or more specifically matrix assisted laser desorption ionization mass spectrometry (MALDI-MS), showing the most promise. These uses of mass spectrometry and other instrumentation techniques in conjunction with SPR analysis to expand the molecular information of the sensing surface are discussed by Stuart et al.[54]

SPR is also limited by the exponential decay of surface plasmon polaritons as only refractive index changes within its penetration depth can be sensed. Therefore, sensitivity to binding events occurring beyond ~100 nm from the surface is reduced and is completely lost beyond ~300 nm. This is normally not a problem as proteins and other biological molecules commonly investigated using SPR are significantly smaller than 100 nm and therefore bind within the sensitive area. However, when working with cellular systems or larger biomimetic scaffolds this penetration depth limitation needs to be taken into account. Work with cellular systems has been accomplished using SPR through implementation of appropriate modeling of cellular morphological changes within the SPR sensitive region.[55-57] Other label-free analysis techniques have also been engaged to supplement or supplant SPR spectroscopy when studying these sorts of systems. Notably, quartz crystal microbalance (QCM) has found extensive use studying similar systems to those commonly investigated using SPR but is not limited by penetration depth. QCM will be discussed in more detail in section 1.8 based on this potential to complement SPR.

Finally, as SPR angular shifts are based on refractive index changes signal for small compounds is limited making sensing of these molecules very difficult. Signal

amplification methodologies have been employed, as one avenue, to improve signal of small molecules through secondary binding interactions with other proteins, antibodies, or conjugated nanoparticles.[58] Thus, enabling small biomolecules to still be sensitively detected using SPR. However, one area where these methodologies cannot be employed is in SPR sensing of gaseous molecules as secondary binding molecules or other amplification methodologies are not available for gaseous systems. This makes gas sensing applications with SPR spectroscopy particularly challenging, and these difficulties are further enhanced as refractive index differences between gases are much smaller than those in liquid systems. As such only recently has gas sensing utilized SPR[59] and new approaches are necessary to enhance or deconvolute the signal obtained from gas.

The following sections will provide background on systems, techniques, and concepts that are employed to solve these SPR challenges.

1.4.2 SPR in the Gas Phase

While sensing of gas molecules using SPR methodologies is essentially identical from a mathematical standpoint many differences come to light when looking through an experiment lens. Notably due to the large contrast in refractive index between gas and liquid systems the optimal angle for surface plasmon polariton excitation is significantly shifted. This requires the angle of incident light to be modified accordingly. Also, when compared to the protein systems commonly analyzed using SPR a clear selective binding interaction is not available to ensure that the analyte of interest is responsible for the identified signal. Furthermore, the low refractive index of gas systems limits refractive

index differences between analytes of interest resulting in very limited signal. Therefore, to achieve effective analysis of gaseous systems using SPR setups new surfaces or methodologies are needed that can improve sensitivity or capture target gaseous analytes. To this end various groups have developed sensors from metal oxides[59], nanomaterials[60], and metal organic frameworks[61, 62] to improve signal and impart some form of selectivity.

1.5 Biomimetic Lipid Membranes

Biomimetic systems are of key importance because they enable biological interactions to be investigated without the complexity of *in vivo* studies that often complicate the ability to interrogate an individual protein due to the many nonspecific and off target effects present in a living organism.[63] These biomimetic systems help bridge the gap between *in vitro* and *in vivo* studies by incorporating the most important components of the biological system present within the organism of interest.

To this end, biomimetic lipid bilayers have been utilized extensively to model and study biological systems.[64-66] Especially because the vast majority of drug targets, and many disease pathways, are membrane bound proteins or at minimum need to be able to pass a lipid membrane.[67] Here singular protein or lipid binding systems can be examined and systematically altered to further our understanding of their role in the larger biological setting. Thus, helping scientists understand disease or identify potential drug candidates using *in vitro* methods before costly and complicated *in vivo* studies.[68]

As such, biomimetic lipid membranes have appeared as ideal systems for use within SPR sensing methodologies due to their ability to interrogate these important interactions

and their compatibility with the thin substrates utilized in SPR systems. Where introduced lipid vesicles self-assemble into a bilayer system via a process of vesicle adsorption and subsequent rupture. This vesicle rupture process is based on strain caused by interactions between the vesicle and the underlying support or surrounding vesicles that induce vesicle deformation which can eventually result in liposome rupture[69, 70]. Due to this the underlying substrate is highly impactful on whether spontaneous rupturing occurs. Thus, hydrophilic surfaces are more conducive to vesicle deformation and rupture based on greater van der Waals and electrostatic interactions between hydrophilic substrates, like glass, quartz, or silicon, and lipid headgroups.[70] As such, silica surfaces have been predominantly utilized due to the robust formation of lipid bilayer systems that occurs upon introduction of lipid vesicles. However, gold surfaces, commonly utilized in SPR sensing, do not have such a favorable interaction with lipid vesicles due to their native hydrophobicity leading to limited or incomplete bilayer formation. To alleviate this, and enable formation of biomimetic lipid membranes, various methodologies have been developed to induce vesicle fusion on the unaltered gold substrate[71-75] or change the surface properties[76] to enable vesicle self-assembly. Vesicle fusion on gold surfaces has been achieved through solvent assistance[71, 72], peptide mediation[73], or polymer introduction[74]. While other systems have employed thiol self-assembled monolayers as a scaffold that lipid membranes can form upon, either as single[77] or double[78, 79] lipid layers. Furthermore, addition of thin silica layers, atop the gold, has been demonstrated by our lab to enable lipid self-assembly without impacting SPR sensitivity.[76] We and others have also investigated various chemical tethers to form a barrier between the gold surface and the

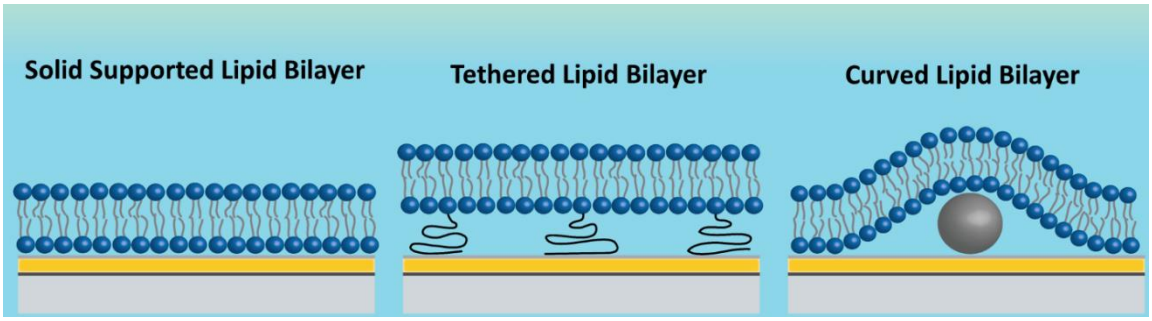

Figure 1.6. Demonstration of how lipid membranes can be formed on sensor surfaces in different ways. Directly formed on flat sensor surfaces, held above the sensor surface via polymer tethers, or formed around nanomaterials to produce membrane curvature.

biomimetic lipid bilayer enabling lipid formation and reducing the effects of the substrate on lipid bilayer properties.[80-83] Underlying protein substrates have likewise been utilized in conjunction with lipid bilayers as a tether and for the antifouling properties of the membrane.[53] Lipid membranes can also be formed around nanostructures on these surfaces arranging into patterns matching those structures, this has been employed to fabricate curved lipid surface for study.[84]

1.5.1 Lipid Bilayers as Antifouling Substrates

As previously mentioned, these biomimetic lipid membranes have emerged as an ideal solution to the aforementioned surface fouling limitation of SPR analyses. This antifouling property has been notably identified for phosphatidylcholine (PC) lipids due to their mimicry of the antifouling properties found for eukaryotic cell surfaces.[85] This property is believed to be due to the strong binding of water molecules by the PC head groups forming a hydration layer that limits the ability of proteins to nonspecifically adsorb.[86] Furthermore, various PC lipids are zwitterionic which match with work on the development of antifouling surfaces finding zwitterionic materials to be particularly

effective at blocking nonspecific interactions.[52, 87] As such, zwitterionic lipid headgroups have been extensively employed in polymer fabrication[88] and successfully utilized to block nonspecific interactions on various sensor surfaces[89-91] with other works employing the whole lipid structure to take advantage of the ease of lipid bilayer formation.[92, 93] Thus

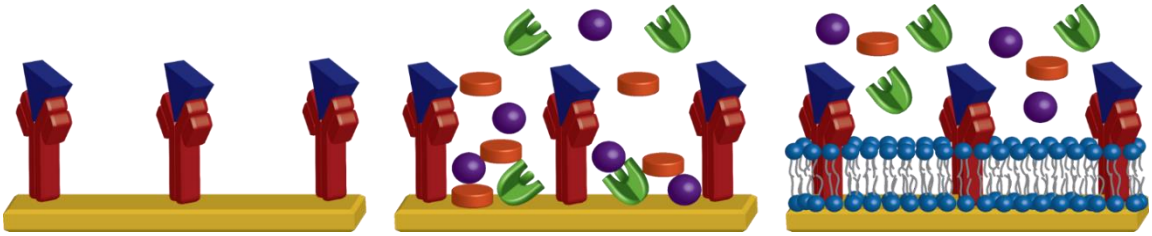

Figure 1.7. Scheme of how nonspecific interactions can impact sensor performance and the application of lipid membranes to block this nonspecific binding.

demonstrating the potential of biomimetic lipid membranes as effective antifouling surfaces. However, these antifouling properties are not exclusive to zwitterionic lipids based on recent results from our group finding a lipid membrane of positively charged ethyl phosphocholine (EPC) to be a highly effective antifouling surface.[53]

Therefore, the mechanisms behind these antifouling effects and information about which lipid groups are responsible for antifouling still lack understanding, opening the door to research focused on explaining and expanding the potential of lipid membranes as robust antifouling substrates.

1.5.2 Drug Delivery and Molecular Diffusion Across Lipid Bilayers

When exploring drug development and delivery the lipid membrane appears as one of the major considerations due to the huge number of drug targets limited by their location within the cell necessitating drugs to pass the cell membrane to be effective.[94, 95] Therefore, lipid membranes are the final barrier to drug effectiveness as without membrane

permeability an infinite amount of drug can be prescribed with no therapeutic effect. When investigating the ability of drug molecules to get to their target there are two main methods of cell entry, passive and active transport. First if the drug molecule is sufficiently small, soluble, and lipophilic then it can passively diffuse across the cell membrane on its own.[96] This passive transport relies on a concentration gradient driving drugs from higher concentration regions (C_h) to low concentration regions (C_l) which can be modeled by Fick's law of diffusion[97, 98]:

$$\frac{dC_l}{dt} = \frac{DKA}{h}(C_h - C_l) \tag{1.17}$$

With the diffusion coefficient of the drug (D), the membrane to fluid partition coefficient of the drug in question (K), surface area of the membrane(A), and thickness of the membrane (h) playing important roles in the rate of drug absorption. These parameters become increasingly convoluted within the immense complexity and variability of biological systems making passive drug transport very difficult to accurately calculate or model.[99, 100] Therefore, experimental approaches are essential to understanding drug permeability.[101] For insoluble compounds[102] and larger drug molecules, which make up the majority of new potential drugs, passive transport is not a feasible option. Consequently, methods to deliver the drug into the cell are necessary notably through cell penetrating chemical structures[103], permeability enhancing molecules[101], or utilization of cellular endocytosis pathways.[104] One delivery complex that has garnered extensive attention are branching polymer dendrimers that form micelles or cavities within their tree-like structures to trap and transport drug molecules.[105, 106] However, the drug delivery

mechanism of dendrimers and how they interact with the cell membrane is not understood and needs to be explored.[107]

1.6 Fluorescence Imaging

When considering the applications of fluorescence imaging one must first consider the fundamental process of fluorescence. In short fluorescence is the emission of light of a certain wavelength after exposure to photons of another wavelength. The subset of molecules where this phenomenon can occur are referred to as fluorophores. These molecules release light based on excitation to a higher energy state through transfer of energy from incident photons that appropriately match the fluorophore. This matching is dependent on the fluorophore chemical structure and surrounding environment. When this molecule returns to the ground state light is emitted of a lower energy due to some energy being lost through internal conversion and vibrational relaxation. This difference between incident and emitted light is known as the Stokes shift[108] which is fundamental to the sensitive detection of fluorescence. Due to this wavelength separation the incident light source can be filtered out allowing for detection of only light emitted by the fluorophore.

This directly ties into the development of imaging systems based on fluorescence which consist of an excitation source, a filter, an optical collection unit, and a fluorophore of choice. Various configurations of microscope have been employed to image fluorescent molecules with epifluorescence microscopes making up the majority of imaging systems.

While confocal and total internal reflection fluorescence microscopes have also

found use due to their unique configurations reducing background and improving resolution.

As I have utilized a confocal microscope in my studies, I will limit my explanation to confocal systems. Confocal microscopy employs a pinhole in line with a dichromatic mirror which enables only fluorescently emitted light within the focal plane to make its way to the detector improving resolution particularly in regard to sample depth. This enables thin slices of a sample to be imaged and when combined with precision stages can create 3D images of a sample. However, as the focal area is smaller this means that smaller numbers of fluorophores are present limiting the amount of fluorescent emission detectable. This generally means that higher numbers of incident photons are required to achieve reliable fluorescent signal which can cause photobleaching which is the chemical alteration of a fluorophore due to excess excitation cycles leading to a permanent loss of ability to fluoresce. While this can seriously hamper fluorescent imaging there are many methodologies to lessen this such as limiting laser power and the number of images taken in a single location of the sample. However, if appropriately controlled this photobleaching effect can actually be quite useful.

1.6.1 Fluorescence Recovery After Photobleaching

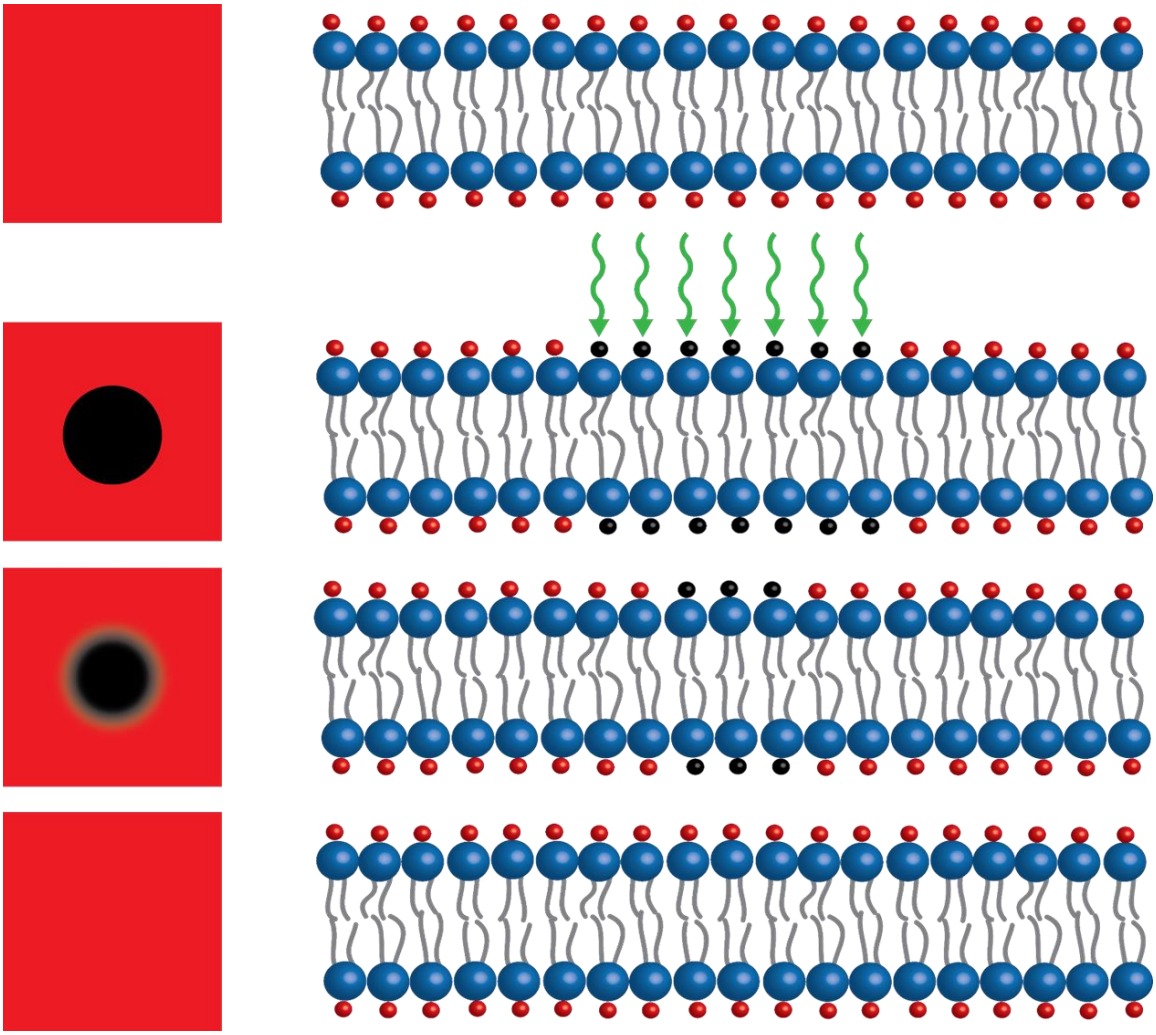

Figure 1.8. Illustration of fluorescence recovery after photobleaching of fluorophore labeled lipids. With a high intensity bleach step followed by recovery over time that is tracked via imaging to track the recovery of fluorescent signal.

One of the ways that fluorescence imaging has been utilized to provide more information about the sample under study is fluorescence recovery after photobleaching (FRAP). Where the photobleaching of fluorophores is used to our advantage enabling the lateral movement of fluorophores in a sample to be monitored. This has been extensively used to measure the mobility of lipids or proteins within a cell or in mimetic systems.[109]

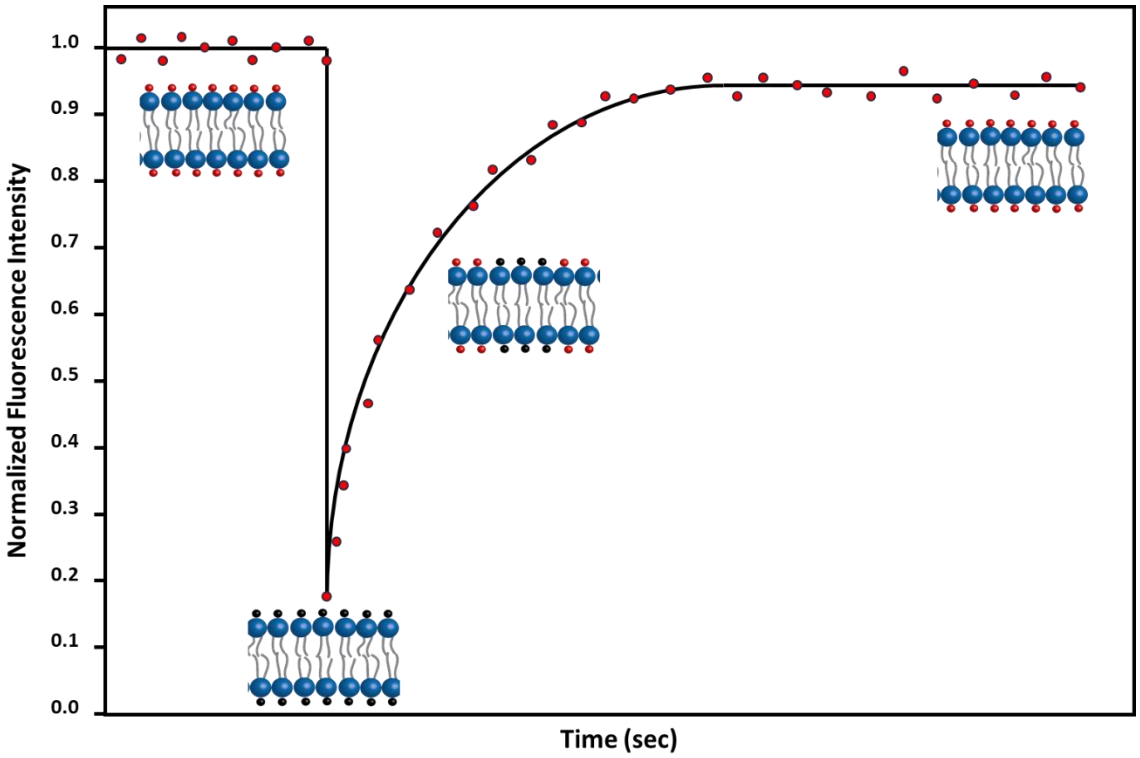

Figure 1.9. Representation of classic FRAP bleach and recovery curve. With pre bleach intensity utilized as a control and then a distinct loss of fluorescence signal immediately after bleaching that quickly recovers and levels off.

FRAP is achieved through first taking several images of the sample followed by a very high energy point irradiation step meant to bleach fluorophores within a small region of the visible area. Then images are taken at consistent time points to monitor the movement of unbleached fluorophore into the bleached region and bleached fluorophore out of the bleached region. All of these images can subsequently be compiled to provide a visualization of the bleached area over time. The intensity of the bleached area within these time resolved images can then be plotted to identify whether any movement of fluorophores occurred. If so a characteristic bleach and recovery curve will be visible. Prior to plotting the intensity values must be normalized against a reference unbleached area:

$$F_c = \frac{F_{bleach}}{F_{ref}} \tag{1.18}$$

$$F_{FR} = \frac{F_c - F_0}{1 - F_0} \tag{1.19}$$

Here F_{bleach} and F_{ref} are the intensities of the bleached and reference areas respectively helping to account for any background bleaching that may occur during the multiple rounds of imaging used to visualize recovery. This corrected fluorescence (F_c) for each time point is then compared against the fluorescence intensity at time zero (F_0) directly after bleaching providing a fluorescence fractional recovery (F_{FR}) for each time point. This information can be further utilized to calculate the diffusion coefficient of the system based on an equation introduced by Axelrod[110]:

$$D = \frac{\omega^2}{4t_{1/2}}\gamma \tag{1.20}$$

Where ω corresponds to the full width at half maximum of the laser determined to be 7.9 μm for our system while γ is correction factor to account for differences in beam geometry and $t_{1/2}$ is the half-time recovery which is obtained from the equation:

$$t_{1/2} = \frac{\ln(2)}{b} \tag{1.21}$$

Where b is obtained from a first order exponential fit of the recovery curve:

$$y = a(1 - e^{-bx}) \tag{1.22}$$

Here a is the mobile fraction of the system providing information on whether there are substantial portions of the bleached fluorophore that were immobile. The diffusion

coefficient is calculated at least N≥3 times on different areas of the sample to ensure statistical significance.

1.7 MALDI-TOF-MS

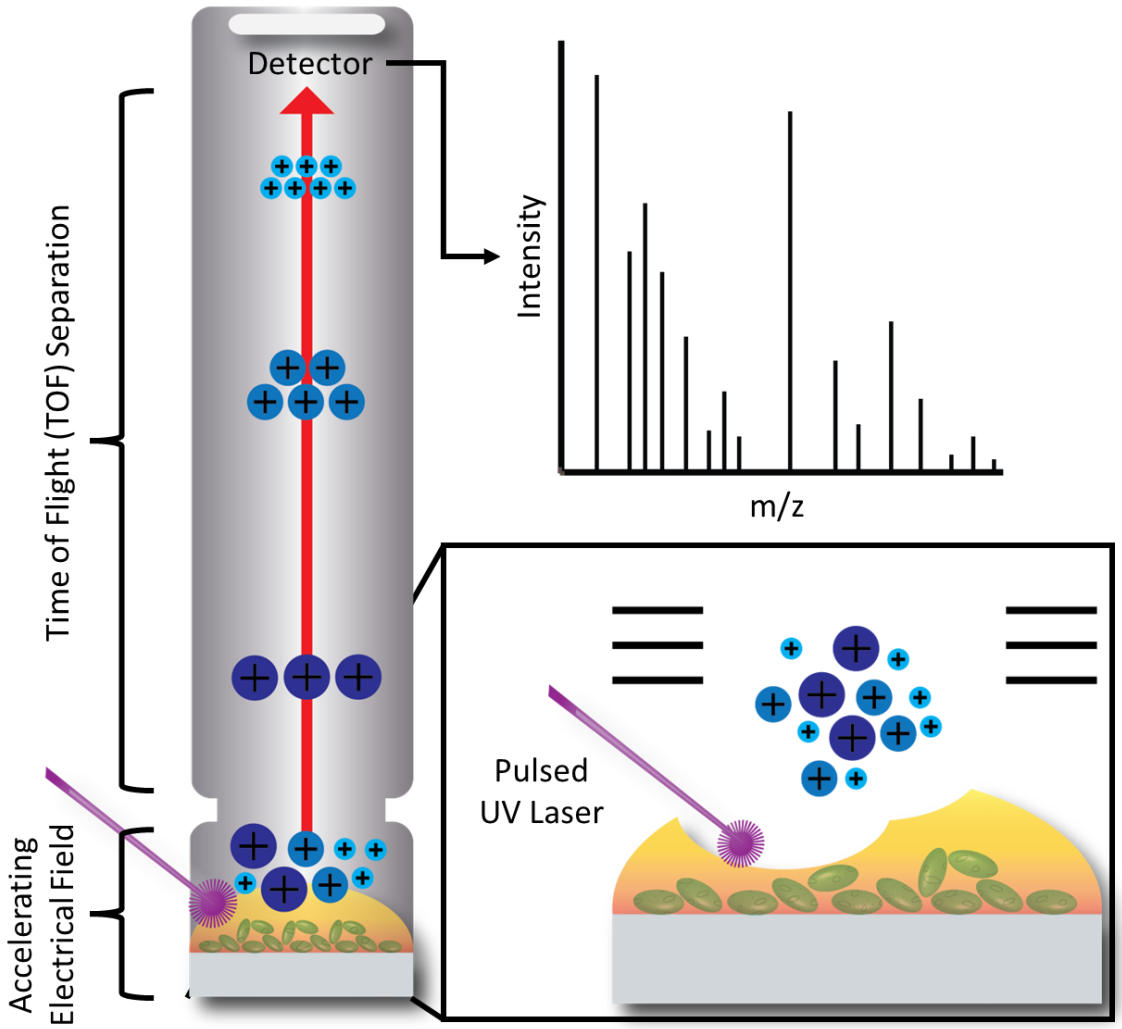

Figure 1.10. Cartoon illustration of sample ionization, ion separation, and detection in a MALDI-TOF-MS instrument. Showing sample coated in matrix being ionized by a pulsed UV laser and then separated over a time-of-flight tube and finally detected to produce a mass spectrum of the sample.

Matrix assisted laser desorption-ionization (MALDI) is a surface-based mass spectrometry technique that relies on UV absorbent matrix molecules that when irradiated

with a UV laser source impart that energy to adjacent sample molecules. This enables samples to be deposited coated with matrix and rapidly ionized to obtain mass spectra within seconds. The matrix effect was first introduced in 1985 by Karas et al. based on observations that UV absorbing amino acid tryptophan improved ionization of alanine.[111] This expanded capabilities of laser desorption-ionization that had been in use since the 1960s.[112] Through study and application of these matrix effects whole protein ionization became possible first demonstrated by Tanaka and others using ultra fine 300 Å cobalt powder to ionize chymotrypsinogen.[113] In the years since this discovery MALDI has been utilized in various medical and bioanalytical applications[114-116] and has found use as an orthogonal analysis technique for SPR due to their shared surface-based methodologies.[54]

In practice MALDI matrices are commonly organic acids with a chromophore moiety that absorbs strongly at the incident laser wavelength. α-Cyano-4-hydroxycinnamic acid (CHCA) and 2,5-Dihydroxybenzoic acid (DHB) are two typically employed matrix molecules. A mixture of DHB and 2-hydroxy-5-methoxybenzoic acid, coined as super-DHB, has also been shown to be highly effective for ionization of whole proteins.[117] In use, this matrix is mixed into an aqueous mixture with acetonitrile and trifluoroacetic acid (TFA) then deposited onto sample spots patterned on a stainless steel MALDI plate. Once dried these matrix spots co-crystallize with analytes in the sample spots and co-ionize/ablate analytes when irradiated with laser light, commonly from 337-nm pulsed nitrogen lasers.[118] The resulting cloud of matrix and analyte is pulled into a mass analyzer most commonly time of flight (TOF) where ions are separated by mass/charge based on the time it takes them to traverse a drift region.[119]

1.7.1 Plasmonic Surface Enhanced MALDI

In addition to the matrix enhancement of laser desorption-ionization various surfaces have also been demonstrated to improve analyte ionization. These substrates have been utilized to wholly circumvent the need for matrix, known as surface assisted laser desorption-ionization (SALDI) or to augment current MALDI applications. Recently we and others have demonstrated enhancement effects from plasmonic metal surfaces which is believed to be based on the plasmonic metal surface enhancing ionization through incident light exciting electrons within the metal producing hot electron bands.[120] As well as plasmonic absorption also converting incident photon energy into thermal heating that aids in the desorption of matrix and analytes. This conversion of incident light to thermal radiation has been demonstrated for plasmonic nanoparticles.[121] In application to MALDI-MS systems this has been demonstrated with Au[11, 120] and Al[122] substrates finding higher enhancement from aluminum metal based on its improved absorption of the 337-nm laser utilized in MALDI instrumentation when compared to gold.

1.7.2 Coupling MALDI-MS with SPR

As SPR and MALDI are both surface based methodologies and the plasmonic materials utilized in SPR sensors provide ionization enhancement when applied to MALDI systems they are prime for orthogonal use. As such, this combination has been used extensively to enable molecular identification of the molecules and proteins captured on SPR sensor surfaces. With the first demonstration of the coupled technique in the 1990's by Krone et. al[123] who demonstrated that SPR chips could simply be transferred to MALDI-MS

instrumentation following an SPR capture experiment. This enables the SPR surface to be characterized using a molecular identification technique which confirms the presence of binding partners as well as other nonspecifically bound molecules.

1.8 Quartz Crystal Microbalance

Quartz crystal microbalance is another technique for measuring binding occurring at a surface that has seen extensive use as a biosensor platform[124] but works through a much

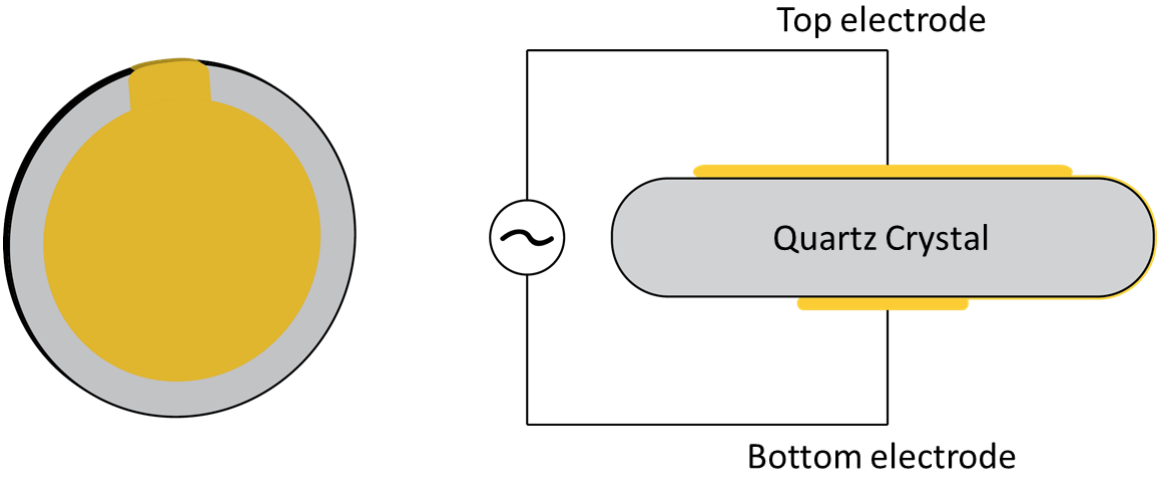

Figure 1.11. Illustration (left) and schematic (right) of a quartz crystal microbalance sensor chip which is oscillated via application of alternating voltage.

different mechanism than SPR. As such, it has proven to be useful in some areas where SPR is limited. QCM measures mass binding to the sensor surface through small variations in a resonating quartz crystal. When mass is added or removed from the surface through binding or growth/decay events then the resonant frequency of the crystal will change accordingly. The quartz chips utilized in QCM systems commonly have frequencies of 5 or 10 MHz which can be measured precisely using commercially available frequency counters. Therefore, very small changes in mass can be detected within the range of 10^{10}–

10^{12} Hz/kg.[125] This relationship between frequency and mass was theoretically demonstrated by Sauerbrey in 1959[126] by the equation:

$$\Delta f = -\frac{2\, f_0^2 \Delta m}{A\sqrt{\rho_q \mu_q}} = -C_f \cdot \Delta m \tag{1.23}$$

Which relies on the frequency of the QCM chip (f_0), 10Mhz in our applications, the effective vibrations area of the chip (A), density of the quartz crystal ($\rho_q = 2.648\ g/cm^3$), shear modulus of the crystal ($\mu_q = 2.947\ x\ 10^{11}\ g/cm \cdot s^2$). Leaving the change in mass (Δm) and resulting frequency shift (Δf) which is inversely related due to the negative within the equation. The other components are often simplified to the Sauerbrey mass sensitivity (C_f). While this equation models QCM systems quite well and explains how QCM can be utilized in a sensing capacity it is a simplified model that ignores a couple key components. Notably the metal electrode, which is an essential aspect of current instrumentation, also it is only satisfied when the additional mass is small, rigid, and uniformly distributed. Regarding the metal electrode, it has been shown to have a substantial impact on sensor mass sensitivity with gold identified to have greater sensitivity compared to silver.[127] Furthermore, when sensing in liquid systems this is not a completely accurate model due to the lack of rigidity, but it has been more accurately described by Kanazawa[128]:

$$\Delta f = -f_0^{\frac{3}{2}} \left(\frac{\rho_L \eta_L}{\pi \rho_q \mu_q}\right)^{1/2} \tag{1.24}$$

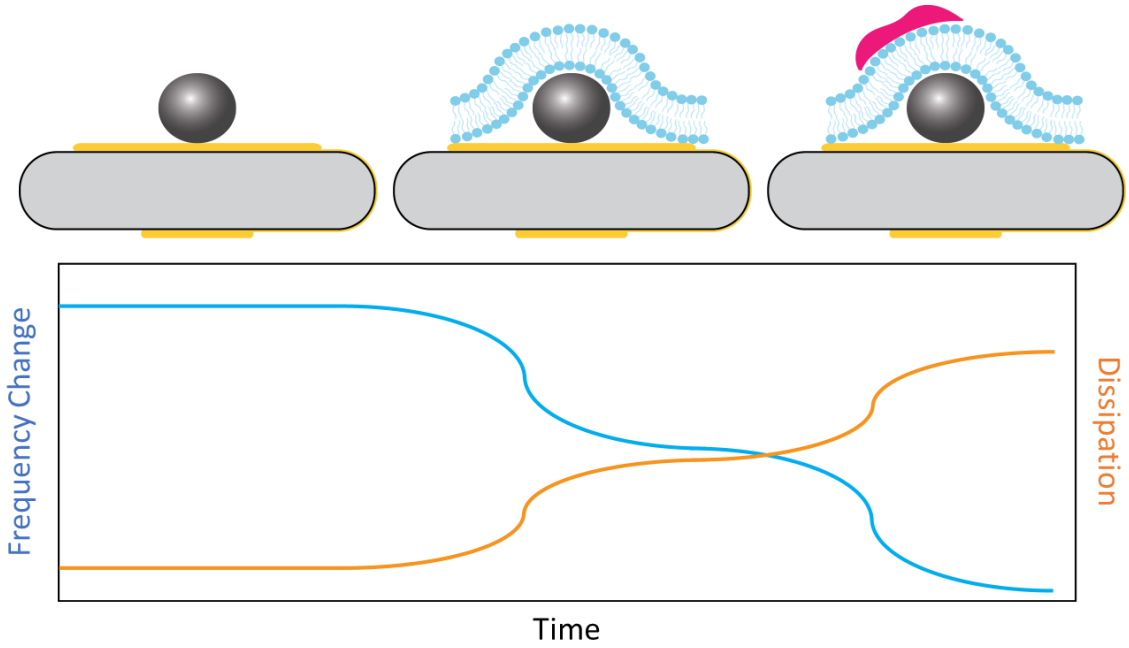

Figure 1.12. Illustration of QCM frequency decrease and dissipation increase upon lipid membrane formation on the sensor surface and then protein binding to the membrane.

This equation includes the variables for the density (ρ_L) and viscosity (η_L) of the liquid. However, the lack of rigidity in a liquid system also propagates the QCM shear wave differently. Notably liquid causes the shear wave to rapidly decay due to dampening an effect that is markedly different from a rigid material adhered to the sensor surface. This dampening can be represented through a calculation of the shear wave's decay length as described by Yang[129]:

$$\delta = \sqrt{\frac{\eta_L}{\pi f_0 \rho_L}} \tag{1.25}$$

Thus, only liquid within the decay length of the shear wave will have an impact on a QCM chips frequency. This begs the question of whether QCM will have similar distance limitations as SPR sensors. However, the mechanism is different and for QCM a penetration depth is specific to liquid systems, rigid structures and molecules can still

impact the QCM frequency at greater depths. This has been confirmed by Martin et al. interestingly finding that surface structures larger than the decay length actually enhance frequency shift associated with a liquid.[130] Therefore, QCM can be utilized to investigate binding events at much farther distances from the sensor surface than is possible with SPR sensors assuming these binding events are linked to a rigid structure protruding from the QCM sensor surface.

1.9 Statistical Modeling and Machine Learning

When developing and testing sensors it immediately becomes clear that many sensors produce an enormous amount of data that is currently ignored or not completely utilized due to the immense time requirement for analysis. Therefore, appropriate methods to contextualize or streamline analysis of this excess data are necessary to enable the next generation of sensors. To this end, various statistical and machine learning algorithms have shown great promise due to their ability to transfer some of the data analysis burden from scientists onto computing power.

1.9.1 Monte Carlo Methods

One subset of these computational algorithms that has proved useful in solving problems within our work has been Monte Carlo methods.[131] This refers to a broad swath of algorithms focused on repeated random sampling which can be utilized to simulate systems through probability distributions. With Ulam first demonstrating the technique to statistically model neutron diffusion[132] and naming it after a well-known casino in Monaco. At its core the method relies on random sampling linked to a specific system therefore any

equations are generally unique to the system being tested. In our uses this takes the form of feeding randomly generated numbers into equations that model vesicle arrangement to identify how vesicle components randomly distribute. The specifics of which will be explained in more detail in chapter 4.

1.9.2 Machine Learning Algorithms

In contrast to using random sampling to simulate our sensor systems, machine learning (ML) algorithms provide the ability to learn about the patterns within the data collected from those sensors. This capability has attracted substantial investigation within the sensor community but still remains in its early stages.[133] To do this many different algorithms have been built to take a subset of collected data coined as training data which it uses to learn and make predictions that can be applied to future or test data.[134] This learning is a subdivision of artificial intelligence based on these algorithms' ability to solve problems without being directly coded to do so. As such, each algorithm is designed to find these patterns in different ways resulting in wildly different results depending on the algorithm in question and the data provided to it.

Within machine learning there are three distinct approaches (reinforcement, unsupervised, and supervised learning) based on what information about the system is provided to the algorithm. Reinforcement learning gives the algorithm a set goal with feedback as it navigates towards a solution. While unsupervised and supervised learning differ from each other based on whether or not example desired outputs are provided as is the case for supervised learning. For supervised learning these outputs can be restricted to

a known set of values or classes (classification) or a range of possible values (regression). Each algorithm and approach has its own advantages and limitations with problems that the algorithm can be more effectively solve. When using machine learning to aid in identification from sensor data, supervised learning with a classification focus is commonly utilized due to there being a known set of possible results from the sensor. This is clear when thinking about a sensor looking to provide a positive or negative response where a supervised classification model can find a data pattern to look for that corresponds to disease positive. Essentially machine learning finds those data patterns that a human could pull out given enough analysis time. Therefore, when looking at something like a simple lateral flow assay where data is in the form of color intensity a human can easily make that distinction as can a machine learning model. But when data becomes more complex, and the number of possible results increases, the time needed for a human to solve the pattern increases exponentially. Here is where machine learning algorithms shine as computational power can be used to cut down pattern recognition time and enable complex data to be easily simplified. However, this can come at odds with scientific thought and goals as the meaning of data and these patterns can quickly be lost within the black box of ML algorithms.[135] This creates a careful balancing act for scientists using machine learning to preserve knowledge of how the model is utilizing their data while maintaining accurate classification, as the combination is far more valuable than the individual parts. As such, the most important work moving forward is focused on building interpretable and explainable ML algorithms.[136]

To this end, we have employed numerous machine learning algorithms available through the caret package[137] in R.[138] This provides us with 238 possible models all of which were tested for their compatibility with our data and ability to accurately classify. Of these only 174 models were compatible with our system and data. This was further narrowed down through systematic testing to identify the algorithms that fit best with our data and goal. The majority of feasible algorithms stem from a small subset of general machine learning model concepts[139], notably neural networks (NN), k-nearest neighbors (KNN), random forest (RF), discriminant analyses and support vector machines (SVM). Each algorithm provides different results and capabilities that when combined can help us understand our system a bit more.

Artificial neural networks[140] take inspiration from our own neural system by building a collection of linked neurons that can transmit information to any of the other neurons that they are connected to. In practice these form in three layers an input, hidden, and output layer. Where input data is linked to multiple neurons within the first hidden layer which further attach to any other hidden layers eventually linking to an output layer which provides a final classification result. Each one of the connections between these artificial neurons is given a weight that is modified based on error from repeated training events, thus producing a pathway from the input to output layer that matches target output results as closely as possible. Essentially the data pattern is encoded into an array of neurons that weigh and combine many data points to accurately classify the data based on classes provided prior to training. This pattern can then be applied to unknown data to classify it based on those predetermined classes. Neural networks have been utilized extensively for

image classification problems[141, 142] but have more recently shown promise in solving chemical sensing questions.[143]

K-nearest neighbors[144] begins from the assumption that data from the same class will be close to each other, hence they will be near neighbors. In practice this takes new data and compares it against its "K" nearest neighbors to see what class they are and classifies this new data based on whichever class the greatest proportion of near neighbors are. This is commonly achieved through calculations of Euclidian distances to identify those nearest neighbors which for one dimensional space is represented by points p and q:

$$d(p,q) = \sqrt{(p-q)^2} \tag{1.26}$$

This can then be easily expanded to higher dimensions with points p and q with coordinates $(p_1, p_2, \cdots p_n)$ and $(q_1, q_2, \cdots q_n)$:

$$d(p,q) = \sqrt{(p_1-q_1)^2 + (p_2-q_2)^2 + \cdots + (p_n-q_n)^2} \tag{1.27}$$

In practice, an unknown example (q) is dropped into space with a set of training samples (x_i) and the distance between it and all the surrounding training samples are calculated for each of the factors (F) within the data with a weighting (w_f) applied to each factor as shown[145]:

$$d(q,x) = \sum_{f \in F} w_f \delta(q_f, x_{if}) \tag{1.28}$$

This provides a set of nearest neighbors that can then be utilized for classification through simple majority voting. However, using this method problems can arise when looking at data sets where one class is more prevalent as prediction will more often fall to that class.

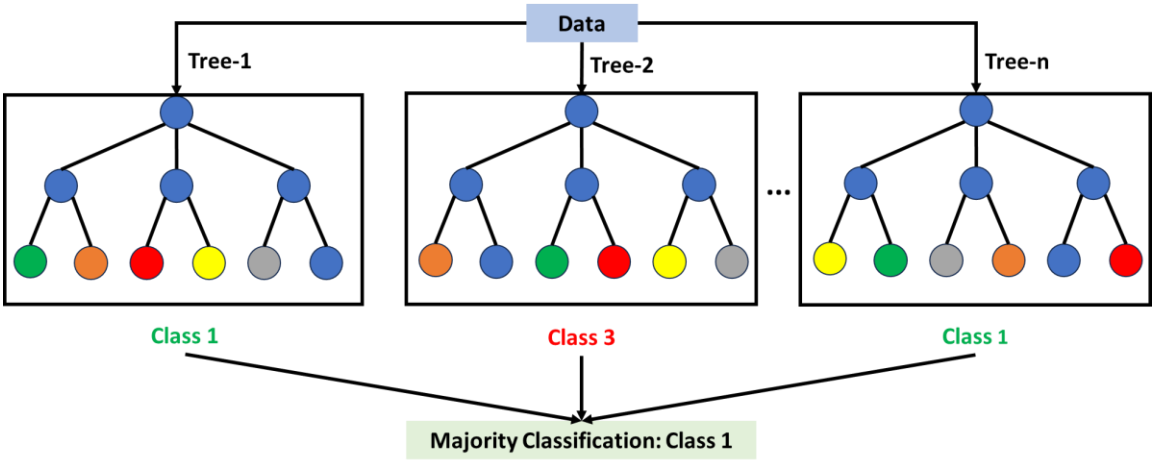

Figure 1.13. Demonstration of random forest classification based on multiple pooled decision trees. Three different trees are built, and the resulting classes are combined to provide a final determination of class from the model.

However, methodologies to alleviate this have been implemented through alternative voting rules that consider differences in number of objects within classes and apply weighting based on distance.[146, 147]

Random forest[148] makes use of multiple decision trees compiling results from each tree to classify based on the most commonly selected class. A decision tree follows the method that a human might use when attempting to find patterns within complex data by deconvoluting it through multiple simple yes or no decisions. Each decision being quite simple built on the presence, absence, or intensity of a portion of the data which feeds into further decisions based on other aspects of the data. However, computing power enables these trees to be built orders of magnitude faster than a human could and allows multiple trees to be assembled in parallel. These many decision trees help account for over fitting that might occur if only a singular tree was employed. However, as these trees are hidden within the algorithm the algorithm functions as a black box classification limiting the interpretability of resulting models. Luckily this can be remedied through the

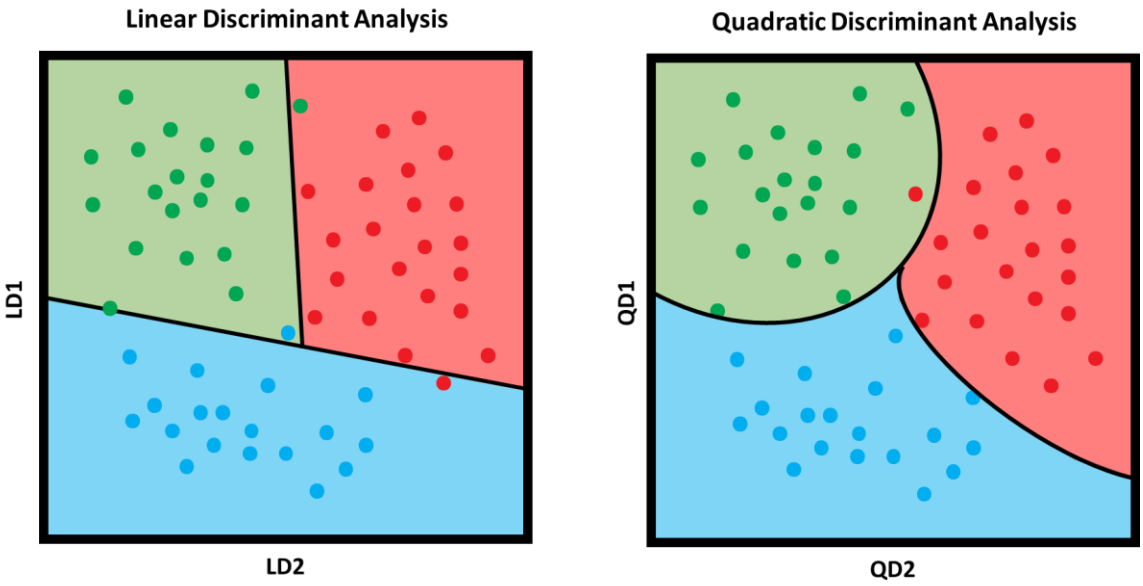

Figure 1.14. Comparison between linear and quadratic methods of discriminant analysis showing differences in classification results.

implementation of out-of-bag error calculations as Breiman demonstrated in his work expanding the capabilities of RF models.[149] This works by leaving out portions of the data during each iteration of model training and then comparing the accuracy of tree voting without that data to the accuracy of trees including that data. Thus, providing information on how the accuracy of the model is affected by loss of certain data features which can be modified into a description of which variables are most important for accurate classification. This is particularly useful when working with datasets containing many different variables as those variables with the most impact can be pulled out indicating what aspects of the input data might be worth exploring more closely.

Discriminant analyses[150], stemming from Fisher's linear discriminant[151], rely on the formation of discriminant functions that provide the best separation of preselected groups. The variance between provided data is compared to build a function(s) that split these

groups as completely as possible. Where discriminant analyses begin to diverge is in the form of these discriminant functions. For example, linear discriminant analysis (LDA) builds linear classification boundaries while quadratic discriminant analysis can build these same sorts of boundaries but using quadratic equations which provides greater flexibility.[152] This is based on differences in assumptions made for LDA and QDA. Both methods assume classes to have a normal gaussian distribution while LDA assume that the covariance matrices are equal while QDA does not. This enables QDA to have nonlinear decision boundaries.

Support vector machines[153] can be considered under the umbrella of linear classifiers but separate classes in a different way than the previously discussed LDA. This difference lies in a focus on finding the largest margin area between two classes. Essentially a hyperplane that provides the greatest distance between the two closest points of the two classes is found which is known as the maximum-margin hyperplane. This not only provides a good boundary for use in classification but also helps limit the probability of overtraining due to a larger margin reducing generalization error. Of course, this works when the training data can be separated via a large margin without errors, however in practice this is often not the case. To remedy this a "soft margin" can be implemented where a new hyperplane is calculated that provides a minimal number of errors enabling remaining non error data points to be optimally separated. This enables datasets with outliers or similar classes to still be separated at the expense of some error, thus providing SVM models with a bit more flexibility than their linear classification predecessors.

Machine learning algorithms are clearly valuable tools to aid in the classification of sensor results especially when dataset size and complexity are large. While many of the models can be highly opaque, appropriate usage and understanding of each algorithm's limitations enables classification to be accompanied by a deeper understanding of the system through interpretable models. By implementing these concepts machine learning has expanded the aims and scope of multiple sensors that will be discussed in this dissertation.

1.10 Aims and Scope of Dissertation

The aim of this dissertation is to aid in the development of new surface-based sensor methodologies and platforms that circumvent current sensor limitations in efforts to improve human health through rapid, sensitive, and accurate sensing technologies. To achieve this, various analytical techniques have been combined to expand the capabilities of current sensing technology through new sensing platforms. These methods were then applied to study relevant interactions from the gas phase to biomimetic surfaces and species differentiation. All aided by robust statistical tools, ML algorithms, and novel modeling techniques to enable a deeper understanding of the system in question and improved sensor identification. The following chapters will demonstrate how these techniques can be utilized in concert to enable sensing, the procedures and methods developed to enable this work will be described in detail and sensor feasibility will be established through in-depth analysis of collected results.

Chapter 2 showcases the design and study of an SPR platform to investigate small molecule membrane transport and dendrimer assisted drug delivery. As well as examine the potential for SPR to detect the diffusion of small molecules across a lipid membrane. Here thiolated small molecules were introduced onto a tethered membrane coated SPR chip and allowed to equilibrate and link to the gold surface if they were able to pass the membrane. Therefore, the membrane can be removed using a surfactant injection leaving only those molecules that were able to pass the membrane adhered. This was further confirmed using on chip MALDI-MS to identify and confirm the presence of these small molecules. These studies were paired with investigations into a potential drug delivery platform in the form of dendrimer micelles that can capture drug molecules and deliver them to cell surfaces. In particular we studied the interaction of these dendrimer molecules with lipid membranes and investigated the effects loading of dendrimers into lipid membranes had on the fluidic properties of the membrane.

Chapter 3 demonstrates and investigates a unique antifouling lipid platform for use in blocking serum nonspecific interactions on SPR sensing substrates. Positively charged lipid EPC was found to completely abrogate interactions from serum when formed over a protein A surface. This system and the membrane antifouling process was further investigated finding that the stable formation of a lipid membrane and maintenance of a hydrophilic layer that is capable of forming a hydration layer are necessary for success of an antifouling lipid layer. To this end, various lipid membranes were formulated on different sensor surfaces and their ability to block non-specific interactions from whole human serum were investigated. With two systems showing effective antifouling

properties notably zwitterionic POPC on a silica substrate and the positively charged EPC lipid formulated over a protein A scaffold. The lipid diffusivity of these membranes was also measured using FRAP, finding that part of the antifouling effectiveness of EPC came from a loss of lipid fluidity. Thus indicating, that charge effects can be overcome under the correct conditions mentioned above, despite some considering zwitterionic charge necessary for blocking of non-specific interactions.

Chapter 4 describes the formulation of a platform for analysis of curvature sensing protein alpha-synuclein. Here quartz crystal microbalance was employed to enable formulation of a curved membrane surface over silica nanoparticles adhered to the sensor surface. Then binding interactions between alpha-syn differently curved surfaces were investigated finding a substantial preference for highly curved surfaces while binding to flat lipid substrates was muted. This demonstrates that alpha-syn's interactions with lipid structures are predominantly dependent on curvature. This was paired with Monte Carlo based study of protein distribution across a lipid surface on both fully spherical and hemispherical surfaces to provide insight into the number and distance between proteins binding to a lipid substrate. Thousands of lipid surfaces were modeled and analyzed to provide normal distribution estimates of lipid and protein distributions across the vesicle or lipid membrane surface in question.

Chapter 5 exhibits the design and implementation of new surfaces for enhanced MALDI-MS ionization of metabolites from Staphylococcus Aureus species which was utilized to accurately classify between methicillin resistant and susceptible strains. For this work two species of S. Aureus differing only in their resistance to antibiotics were cultured

and analyzed to identify their differences in susceptibility to three antibiotics demonstrating one strain to be highly resistant to antibiotics methicillin and oxacillin. Furthermore, these bacteria were studied as whole cells to determine lipid differences and quickly identify the strain in question. This relied on an array chip platform fabricated of aluminum plasmonic metal with a thin silica overlayer that enhances MALDI-MS. That is achieved through improved energy absorption and heating from the metal, confinement of the heat to the surface by the silica layer, and sample confinement within patterned wells on the chip surface. Differentiation of S. Aureus strains was achieved based on spectral differences notably several peaks in the 2400 m/z region which were exclusive to the MRSA strain. This data was further combined with previously collected MALDI-MS data from various bacterial strains to expand the bacterial species/strain within the dataset. This was implemented into a script for MALDI spectra extraction, processing, binning, and peak selection to enable identification of bacteria species.

Chapter 6 focuses on the development of new methodologies and sensors to enable gas phase SPR sensing. Detection of hydrogen gas within a range of 1 to 100% hydrogen in nitrogen and methane was demonstrated. This sensor was further expanded to distinguish between different gases through implementation of an inline pressure sensor enabling differentiation between gases based on differences in gas polarizability. The SPR signal shift for a change in gas pressure could be combined with the amount of pressure change to fit a distinct linear relationship for each gas. Additionally, machine learning algorithms were employed to improve and streamline gas classification especially at lower pressure changes where visual distinction became increasingly difficult. The application of this

novel methodology for gas phase SPR sensing establishes its feasibility for application to gas pipeline monitoring and provides gas differentiability without the need for complex surface chemistry to select for individual gases.

1.10 References:

1. Haleem, A.; Javaid, M.; Singh, R. P.; Suman, R.; Rab, S., Biosensors applications in medical field: A brief review. *Sensors International* **2021,** *2*.

2. Broza, Y. Y.; Zhou, X.; Yuan, M.; Qu, D.; Zheng, Y.; Vishinkin, R.; Khatib, M.; Wu, W.; Haick, H., Disease Detection with Molecular Biomarkers: From Chemistry of Body Fluids to Nature-Inspired Chemical Sensors. *Chem Rev* **2019,** *119* (22), 11761-11817.

3. Arakawa, T.; Dao, D. V.; Mitsubayashi, K., Biosensors and Chemical Sensors for Healthcare Monitoring: A Review. *IEEJ Transactions on Electrical and Electronic Engineering* **2022,** *17* (5), 626-636.

4. Ho, C. K.; Robinson, A.; Miller, D. R.; Davis, M. J., Overview of Sensors and Needs for Environmental Monitoring. *Sensors* **2005,** *5*, 4-37.

5. Chen, J.; Chen, S.; Fu, R.; Li, D.; Jiang, H.; Wang, C.; Peng, Y.; Jia, K.; Hicks, B. J., Remote Sensing Big Data for Water Environment Monitoring: Current Status, Challenges, and Future Prospects. *Earth's Future* **2022,** *10* (2).

6. Soga, K.; Schooling, J., Infrastructure sensing. *Interface Focus* **2016,** *6* (4), 20160023.

7. Sony, S.; Laventure, S.; Sadhu, A., A literature review of next-generation smart sensing technology in structural health monitoring. *Structural Control and Health Monitoring* **2019,** *26* (3).

8. Javaid, M.; Haleem, A.; Rab, S.; Pratap Singh, R.; Suman, R., Sensors for daily life: A review. *Sensors International* **2021,** *2*.

9. Jing, Y.; Chang, S. J.; Chen, C.-J.; Liu, J.-T., Review—Glucose Monitoring Sensors: History, Principle, and Challenges. *Journal of The Electrochemical Society* **2022,** *169* (5).

10. Zullig, T.; Trotzmuller, M.; Kofeler, H. C., Lipidomics from sample preparation to data analysis: a primer. *Anal Bioanal Chem* **2020,** *412* (10), 2191-2209.

11. Li, B.; Stuart, D. D.; Shanta, P. V.; Pike, C. D.; Cheng, Q., Probing Herbicide Toxicity to Algae (Selenastrum capricornutum) by Lipid Profiling with Machine Learning and Microchip/MALDI-TOF Mass Spectrometry. *Chem Res Toxicol* **2022,** *35* (4), 606-615.

12. Wishart, D. S., Metabolomics for Investigating Physiological and Pathophysiological Processes. *Physiol Rev* **2019,** *99* (4), 1819-1875.

13. McWhirter, S. M.; Jefferies, C. A., Nucleic Acid Sensors as Therapeutic Targets for Human Disease. *Immunity* **2020,** *53* (1), 78-97.

14. Hu, X.; Guo, F., Amino Acid Sensing in Metabolic Homeostasis and Health. *Endocr Rev* **2021,** *42* (1), 56-76.

15. Abouhajar, F.; Chaudhuri, R.; Valiulis, S. N.; Stuart, D. D.; Malinick, A. S.; Xue, M.; Cheng, Q., Label-Free Analysis of Binding and Inhibition of SARS-Cov-19 Spike Proteins to ACE2 Receptor with ACE2-Derived Peptides by Surface Plasmon Resonance. *ACS Appl Bio Mater* **2023,** *6* (1), 182-190.

16. Bilitewski, U., Protein-sensing assay formats and devices. *Anal Chim Acta* **2006,** *568* (1-2), 232-47.

17. Malinick, A. S.; Stuart, D. D.; Lambert, A. S.; Cheng, Q., Surface plasmon resonance imaging (SPRi) in combination with machine learning for microarray analysis of multiple sclerosis biomarkers in whole serum. *Biosensors and Bioelectronics: X* **2022,** *10*.

18. Caygill, R. L.; Blair, G. E.; Millner, P. A., A review on viral biosensors to detect human pathogens. *Anal Chim Acta* **2010,** *681* (1-2), 8-15.

19. Suhito, I. R.; Koo, K. M.; Kim, T. H., Recent Advances in Electrochemical Sensors for the Detection of Biomolecules and Whole Cells. *Biomedicines* **2020,** *9* (1).

20. Oliver, N. S.; Toumazou, C.; Cass, A. E.; Johnston, D. G., Glucose sensors: a review of current and emerging technology. *Diabet Med* **2009,** *26* (3), 197-210.

21. Budd, J.; Miller, B. S.; Weckman, N. E.; Cherkaoui, D.; Huang, D.; Decruz, A. T.; Fongwen, N.; Han, G.-R.; Broto, M.; Estcourt, C. S.; Gibbs, J.; Pillay, D.; Sonnenberg, P.; Meurant, R.; Thomas, M. R.; Keegan, N.; Stevens, M. M.; Nastouli, E.; Topol, E. J.; Johnson, A. M.; Shahmanesh, M.; Ozcan, A.; Collins, J. J.; Fernandez Suarez, M.; Rodriguez, B.; Peeling, R. W.; McKendry, R. A., Lateral flow test engineering and lessons learned from COVID-19. *Nature Reviews Bioengineering* **2023,** *1* (1), 13-31.

22. Gaur, A.; Singh, A.; Kumar, A.; Kulkarni, K. S.; Lala, S.; Kapoor, K.; Srivastava, V.; Kumar, A.; Mukhopadhyay, S. C., Fire Sensing Technologies: A Review. *IEEE Sensors Journal* **2019,** *19* (9), 3191-3202.

23. Engvall, E.; Perlmann, P., Enzyme-Linked Immunosorbent Assay (Elisa) Quantitative Assay of Immunoglobulin-G. *Immunochemistry* **1971,** *8* (9), 871-&.

24. Van Weemen, B. K.; Schuurs, A. H., Immunoassay using antigen-enzyme conjugates. *FEBS Lett* **1971,** *15* (3), 232-236.

25. Weber, G., Rotational Brownian Motion and Polarization of the Fluorescence of Solutions. *Advances in Protein Chemistry* **1953,** *8*, 415-459.

26. Hendrickson, O. D.; Taranova, N. A.; Zherdev, A. V.; Dzantiev, B. B.; Eremin, S. A., Fluorescence Polarization-Based Bioassays: New Horizons. *Sensors (Basel)* **2020,** *20* (24).

27. Edelhoch, H.; Brand, L.; Wilchek, M., Fluorescence Studies with Tryptophyl Peptides. *Biochemistry* **1967,** *6* (2), 547-&.

28. Kaur, A.; Kaur, P.; Ahuja, S., Forster resonance energy transfer (FRET) and applications thereof. *Anal Methods* **2020,** *12* (46), 5532-5550.

29. Hinman, S. S.; McKeating, K. S.; Cheng, Q., Surface Plasmon Resonance: Material and Interface Design for Universal Accessibility. *Anal Chem* **2018,** *90* (1), 19-39.

30. Wang, Q.; Ren, Z.-H.; Zhao, W.-M.; Wang, L.; Yan, X.; Zhu, A.-s.; Qiu, F.-m.; Zhang, K.-K., Research advances on surface plasmon resonance biosensors. *Nanoscale* **2022,** *14* (3), 564-591.

31. Singh, P., SPR Biosensors: Historical Perspectives and Current Challenges. *Sensors and Actuators B: Chemical* **2016,** *229*, 110-130.

32. Fleischmann, M.; Hendra, P. J.; Mcquillan, A. J., Raman-Spectra of Pyridine Adsorbed at a Silver Electrode. *Chemical Physics Letters* **1974,** *26* (2), 163-166.

33. Drexhage, K. H., Influence of a dielectric interface on fluorescence decay time. *Journal of Luminescence* **1970,** *1* (2), 693-701.

34. Hartstein, A.; Kirtley, J. R.; Tsang, J. C., Enhancement of the Infrared Absorption from Molecular Monolayers with Thin Metal Overlayers. *Physical Review Letters* **1980,** *45* (3), 201-204.

35. Franken, P. A.; Hill, A. E.; Peters, C. W.; Weinreich, G., Generation of Optical Harmonics. *Physical Review Letters* **1961,** *7* (4), 118-119.

36. al-Haytham, I., Book of Optics. 1021.

37. Huygens, C., *Traité de la Lumière: Où Sont Expliquées les Causes de ce qui Luy Arrive Dans la Reflexion & Dans la Refraction*. Chez Pierre vander Aa: A Leide, 1690.

38. Descartes, R., La dioptrique. In *Discours de la Méthode Pour bien conduire sa raison, et chercher la vérité dans les sciences*, Leiden, 1637.

39. Pitarke, J. M.; Silkin, V. M.; Chulkov, E. V.; Echenique, P. M., Theory of surface plasmons and surface-plasmon polaritons. *Reports on Progress in Physics* **2007,** *70* (1), 1-87.

40. Abbas, A.; Linman, M. J.; Cheng, Q., New trends in instrumental design for surface plasmon resonance-based biosensors. *Biosens Bioelectron* **2011,** *26* (5), 1815-24.

41. Ritchie, R. H., Plasma Losses by Fast Electrons in Thin Films. *Physical Review* **1957,** *106* (5), 874-881.

42. Powell, C. J.; Swan, J. B., Origin of the Characteristic Electron Energy Losses in Aluminum. *Physical Review* **1959,** *115* (4), 869-875.

43. Fresnel, A., *Oeuvres complètes d'Augustin Fresnel*. Imprimerie Impériale: Paris, 1866; Vol. 1.

44. Fresnel, A., Note sur le calcul des teintes que la polarisation développe dans les lames cristallisées. 1821; pp 102–11.

45. Kretschmann, E. a. R., H., Notizen: Radiative Decay of Non Radiative Surface Plasmons Excited by Light. *Zeitschrift für Naturforschung A* **1968,** *23* (12), 2135-2136.

46. Kanso, M.; Cuenot, S.; Louarn, G., Sensitivity of Optical Fiber Sensor Based on Surface Plasmon Resonance: Modeling and Experiments. *Plasmonics* **2008,** *3* (2-3), 49-57.

47. Olmon, R. L.; Slovick, B.; Johnson, T. W.; Shelton, D.; Oh, S.-H.; Boreman, G. D.; Raschke, M. B., Optical dielectric function of gold. *Physical Review B* **2012,** *86* (23), 235147.

48. Villuendas, F.; Pelayo, J., Optical Fiber Device for Chemical Sensing Based on Surface-Plasmon Excitation. *Sensor Actuat a-Phys* **1990,** *23* (1-3), 1142-1145.

49. Chauhan, M.; Kumar Singh, V., Review on recent experimental SPR/LSPR based fiber optic analyte sensors. *Optical Fiber Technology* **2021,** *64*.

50. Kim, D. M.; Park, J. S.; Jung, S. W.; Yeom, J.; Yoo, S. M., Biosensing Applications Using Nanostructure-Based Localized Surface Plasmon Resonance Sensors. *Sensors (Basel)* **2021,** *21* (9).

51. Frutiger, A.; Tanno, A.; Hwu, S.; Tiefenauer, R. F.; Voros, J.; Nakatsuka, N., Nonspecific Binding-Fundamental Concepts and Consequences for Biosensing Applications. *Chem Rev* **2021,** *121* (13), 8095-8160.

52. Laughlin, R. G., Fundamentals of the Zwitterionic Hydrophilic Group. *Langmuir* **1991,** *7* (5), 842-847.

53. McKeating, K. S.; Hinman, S. S.; Rais, N. A.; Zhou, Z.; Cheng, Q., Antifouling Lipid Membranes over Protein A for Orientation-Controlled Immunosensing in Undiluted Serum and Plasma. *ACS Sens* **2019,** *4* (7), 1774-1782.

54. Stuart, D. D.; Ebel, C. P.; Cheng, Q., Biosensing empowered by molecular identification: Advances in surface plasmon resonance techniques coupled with mass spectrometry and Raman spectroscopy. *Sensors and Actuators Reports* **2022,** *4*.

55. Sadeghi, Z.; Shirkani, H., Highly sensitive mid-infrared SPR biosensor for a wide range of biomolecules and biological cells based on graphene-gold grating. *Physica E: Low-dimensional Systems and Nanostructures* **2020,** *119*, 114005.

56. Idil, N.; Bakhshpour, M.; Perçin, I.; Mattiasson, B. Whole Cell Recognition of Staphylococcus aureus Using Biomimetic SPR Sensors *Biosensors* [Online], 2021.

57. Abouhajar, F. B. A. Advanced Surface Plasmon Resonance (SPR) Techniques for Peptide-Based Inhibition Study and Multi-Parametric Cell Analysis. Ph.D., University of California, Riverside, United States -- California, 2022.

58. Ferrari, E. Gold Nanoparticle-Based Plasmonic Biosensors *Biosensors* [Online], 2023.

59. Tabassum, R.; Kant, R., Recent trends in surface plasmon resonance based fiber–optic gas sensors utilizing metal oxides and carbon nanomaterials as functional entities. *Sensors and Actuators B: Chemical* **2020,** *310*.

60. Pawar, D.; Kale, S. N., A review on nanomaterial-modified optical fiber sensors for gases, vapors and ions. *Mikrochim Acta* **2019,** *186* (4), 253.

61. Kreno, L. E.; Hupp, J. T.; Van Duyne, R. P., Metal-Organic Framework Thin Film for Enhanced Localized Surface Plasmon Resonance Gas Sensing. *Analytical Chemistry* **2010,** *82* (19), 8042-8046.

62. Vandezande, W.; Janssen, K. P. F.; Delport, F.; Ameloot, R.; De Vos, D. E.; Lammertyn, J.; Roeffaers, M. B. J., Parts per Million Detection of Alcohol Vapors via Metal Organic Framework Functionalized Surface Plasmon Resonance Sensors. *Anal Chem* **2017,** *89* (8), 4480-4487.

63. Robinson, A. O.; Venero, O. M.; Adamala, K. P., Toward synthetic life: Biomimetic synthetic cell communication. *Curr Opin Chem Biol* **2021,** *64*, 165-173.

64. Sut, T. N.; Yoon, B. K.; Jeon, W.-Y.; Jackman, J. A.; Cho, N.-J., Supported lipid bilayer coatings: Fabrication, bioconjugation, and diagnostic applications. *Applied Materials Today* **2021,** *25*.

65. Sarkis, J.; Vie, V., Biomimetic Models to Investigate Membrane Biophysics Affecting Lipid-Protein Interaction. *Front Bioeng Biotechnol* **2020,** *8*, 270.

66. Andersson, J.; Bilotto, P.; Mears, L. L. E.; Fossati, S.; Ramach, U.; Koper, I.; Valtiner, M.; Knoll, W., Solid-supported lipid bilayers - A versatile tool for the structural and functional characterization of membrane proteins. *Methods* **2020,** *180*, 56-68.

67. Yin, H.; Flynn, A. D., Drugging Membrane Protein Interactions. *Annu Rev Biomed Eng* **2016,** *18*, 51-76.

68. Bilginer, R.; Arslan Yildiz, A., *Biomimetic Lipid Membranes: Fundamentals, Applications, and Commercialization* Springer, Cham: 2019.

69. Richter, R. P.; Berat, R.; Brisson, A. R., Formation of solid-supported lipid bilayers: An integrated view. *Langmuir* **2006,** *22* (8), 3497-3505.

70. Tamm, L. K.; Mcconnell, H. M., Supported Phospholipid-Bilayers. *Biophysical Journal* **1985,** *47* (1), 105-113.

71. Ferhan, A. R.; Yoon, B. K.; Park, S.; Sut, T. N.; Chin, H.; Park, J. H.; Jackman, J. A.; Cho, N. J., Solvent-assisted preparation of supported lipid bilayers. *Nat Protoc* **2019,** *14* (7), 2091-2118.

72. Tabaei, S. R.; Choi, J. H.; Haw Zan, G.; Zhdanov, V. P.; Cho, N. J., Solvent-assisted lipid bilayer formation on silicon dioxide and gold. *Langmuir* **2014,** *30* (34), 10363-73.

73. Zan, G. H.; Jackman, J. A.; Cho, N. J., AH peptide-mediated formation of charged planar lipid bilayers. *J Phys Chem B* **2014,** *118* (13), 3616-21.

74. Lentz, B. R.; Lee, J. K., Poly(ethylene glycol) (PEG)-mediated fusion between pure lipid bilayers: a mechanism in common with viral fusion and secretory vesicle release? *Mol Membr Biol* **1999,** *16* (4), 279-96.

75. Anne L. Plant; Michael Brigham-Burke; Eugene C. Petrella; O'Shannessy, D. J., Phospholipid/Alkanethiol Bilayers for Cell-Surface Receptor Studies by Surface Plasmon Resonance. *Analytical Biochemistry* **1995,** *226*, 342-348.

76. Phillips, K. S.; Wilkop, T.; Wu, J. J.; Al-Kaysi, R. O.; Cheng, Q., Surface plasmon resonance imaging analysis of protein-receptor binding in supported membrane arrays on gold substrates with calcinated silicate films. *J Am Chem Soc* **2006,** *128* (30), 9590-9591.

77. Lingler, S.; Rubinstein, I.; Knoll, W.; Offenhausser, A., Fusion of small unilamellar lipid vesicles to alkanethiol and thiolipid self-assembled monolayers on gold. *Langmuir* **1997,** *13* (26), 7085-7091.

78. Twardowski, M.; Nuzzo, R. G., Molecular recognition at model organic interfaces: Electrochemical discrimination using self-assembled monolayers (SAMs) modified via the fusion of phospholipid vesicles. *Langmuir* **2003,** *19* (23), 9781-9791.

79. Williams, L. M.; Evans, S. D.; Flynn, T. M.; Marsh, A.; Knowles, P. F.; Bushby, R. J.; Boden, N., Kinetics of the unrolling of small unilamellar phospholipid vesicles onto self-assembled monolayers. *Langmuir* **1997,** *13* (4), 751-757.

80. W. Knoll; C.W. Frank; C. Heibel; R. Naumann; A. Offenhausser; J. Ruhe; E.K. Schmidt; W.W. Shen; Sinner, A., Functional tethered lipid bilayers. *Reviews in Molecular Biotechnology* **2000,** *74*, 137-158.

81. Taylor, J. D.; Linman, M. J.; Wilkop, T.; Cheng, Q., Regenerable Tethered Bilayer Lipid Membrane Arrays for Multiplexed Label-Free Analysis of Lipid-Protein Interactions on Poly(dimethylsiloxane) Microchips Using SPR Imaging. *Analytical Chemistry* **2009,** *81* (3), 1146-1153.

82. Taylor, J. D.; Phillips, K. S.; Cheng, Q., Microfluidic fabrication of addressable tethered lipid bilayer arrays and optimization using SPR with silane-derivatized nanoglassy substrates. *Lab Chip* **2007,** *7* (7), 927-30.

83. Penkauskas, T.; Preta, G., Biological applications of tethered bilayer lipid membranes. *Biochimie* **2019,** *157*, 131-141.

84. Paracini, N.; Gutfreund, P.; Welbourn, R.; Gonzalez-Martinez, J. F.; Zhu, K.; Miao, Y.; Yepuri, N.; Darwish, T. A.; Garvey, C.; Waldie, S.; Larsson, J.; Wolff, M.; Cárdenas, M., Structural Characterization of Nanoparticle-Supported Lipid Bilayer Arrays by Grazing Incidence X-ray and Neutron Scattering. *ACS Applied Materials & Interfaces* **2023,** *15* (3), 3772-3780.

85. Chen, S. F.; Zheng, J.; Li, L. Y.; Jiang, S. Y., Strong resistance of phosphorylcholine self-assembled monolayers to protein adsorption: Insights into nonfouling properties of zwitterionic materials. *J Am Chem Soc* **2005,** *127* (41), 14473-14478.

86. Chen, S.; Li, L.; Zhao, C.; Zheng, J., Surface hydration: Principles and applications toward low-fouling/nonfouling biomaterials. *Polymer* **2010,** *51* (23), 5283-5293.

87. Schlenoff, J. B., Zwitteration: coating surfaces with zwitterionic functionality to reduce nonspecific adsorption. *Langmuir* **2014,** *30* (32), 9625-36.

88. Nakaya, T.; Li, Y. J., Phospholipid polymers. *Prog Polym Sci* **1999,** *24* (1), 143-181.

89. Li, H.; Dauphin-Ducharme, P.; Arroyo-Curras, N.; Tran, C. H.; Vieira, P. A.; Li, S.; Shin, C.; Somerson, J.; Kippin, T. E.; Plaxco, K. W., A Biomimetic Phosphatidylcholine-Terminated Monolayer Greatly Improves the In Vivo Performance of Electrochemical Aptamer-Based Sensors. *Angew Chem Int Ed Engl* **2017,** *56* (26), 7492-7495.

90. Goda, T.; Tabata, M.; Sanjoh, M.; Uchimura, M.; Iwasaki, Y.; Miyahara, Y., Thiolated 2-methacryloyloxyethyl phosphorylcholine for an antifouling biosensor platform. *Chem Commun (Camb)* **2013,** *49* (77), 8683-5.

91. Ishihara, K.; Fukumoto, K.; Iwasaki, Y.; Nakabayashi, N., Modification of polysulfone with phospholipid polymer for improvement of the blood compatibility. Part 1. Surface characterization. *Biomaterials* **1999,** *20* (17), 1545-1551.

92. Phillips, K. S.; Han, J. H.; Cheng, Q., Development of a "membrane cloaking" method for amperometric enzyme immunoassay and surface plasmon resonance analysis of proteins in serum samples. *Analytical Chemistry* **2007,** *79* (3), 899-907.

93. Hinman, S. S.; Ruiz, C. J.; Cao, Y.; Ma, M. C.; Tang, J.; Laurini, E.; Posocco, P.; Giorgio, S.; Pricl, S.; Peng, L.; Cheng, Q., Mix and Match: Coassembly of Amphiphilic Dendrimers and Phospholipids Creates Robust, Modular, and Controllable Interfaces. *ACS Appl Mater Interfaces* **2017,** *9* (1), 1029-1035.

94. Imming, P.; Sinning, C.; Meyer, A., Opinion - Drugs, their targets and the nature and number of drug targets. *Nature Reviews Drug Discovery* **2006,** *5* (10), 821-834.

95. Yang, R.; Wei, T.; Goldberg, H.; Wang, W.; Cullion, K.; Kohane, D. S., Getting Drugs Across Biological Barriers. *Adv Mater* **2017,** *29* (37).

96. Vargason, A. M.; Anselmo, A. C.; Mitragotri, S., The evolution of commercial drug delivery technologies. *Nat Biomed Eng* **2021,** *5* (9), 951-967.

97. Fick, A., V. On liquid diffusion. *The London, Edinburgh, and Dublin Philosophical Magazine and Journal of Science* **1855,** *10* (63), 30-39.

98. Breen, S. S. J. a. P. J., *Basic Pharmacokinetics*. Pharmaceutical Press: London, UK, 2009; Vol. 76.

99. Doak, B. C.; Over, B.; Giordanetto, F.; Kihlberg, J., Oral druggable space beyond the rule of 5: insights from drugs and clinical candidates. *Chem Biol* **2014,** *21* (9), 1115-42.

100. Obata, K.; Sugano, K.; Saitoh, R.; Higashida, A.; Nabuchi, Y.; Machida, M.; Aso, Y., Prediction of oral drug absorption in humans by theoretical passive absorption model. *Int J Pharm* **2005,** *293* (1-2), 183-92.

101. Drucker, D. J., Advances in oral peptide therapeutics. *Nat Rev Drug Discov* **2020,** *19* (4), 277-289.

102. Kalepu, S.; Nekkanti, V., Insoluble drug delivery strategies: review of recent advances and business prospects. *Acta Pharm Sin B* **2015,** *5* (5), 442-53.

103. Niu, Z.; Tedesco, E.; Benetti, F.; Mabondzo, A.; Montagner, I. M.; Marigo, I.; Gonzalez-Touceda, D.; Tovar, S.; Dieguez, C.; Santander-Ortega, M. J.; Alonso, M. J., Rational design of polyarginine nanocapsules intended to help peptides overcoming intestinal barriers. *J Control Release* **2017,** *263*, 4-17.

104. Bareford, L. M.; Swaan, P. W., Endocytic mechanisms for targeted drug delivery. *Adv Drug Deliv Rev* **2007,** *59* (8), 748-58.

105. Kesharwani, P.; Jain, K.; Jain, N. K., Dendrimer as nanocarrier for drug delivery. *Prog Polym Sci* **2014,** *39* (2), 268-307.

106. Patel, V.; Rajani, C.; Paul, D.; Borisa, P.; Rajpoot, K.; Youngren-Ortiz, S. R.; Tekade, R. K., Dendrimers as novel drug-delivery system and its applications. In *Drug Delivery Systems*, 2020; pp 333-392.

107. Bandaru, R.; Sanket, A. S.; Rekha, S.; Kamble, O.; Dewangan, R. P.; Kesharwani, P.; Samal, S. K.; Dandela, R., Biological interaction of dendrimers. In *Dendrimer-Based Nanotherapeutics*, 2021; pp 63-74.

108. Stokes, G. G., On the change of refrangibility of light. *Philosophical Transactions of the Royal Society of London* **1852,** *142*, 463–562.

109. Day, C. A.; Kang, M. The Utility of Fluorescence Recovery after Photobleaching (FRAP) to Study the Plasma Membrane *Membranes* [Online], 2023.

110. D. AXELROD, D. E. K., J. SCHLESSINGER, E. ELSON, andw. W. WEBB, MOBILITY MEASUREMENT BY ANALYSIS OF FLUORESCENCE PHOTOBLEACHING RECOVERY KINETICS. *BIOPHYSICAL JOURNAL* **1976,** *16*, 1055-1069.

111. Karas, M.; Bachmann, D.; Hillenkamp, F., Influence of the Wavelength in High-Irradiance Ultraviolet-Laser Desorption Mass-Spectrometry of Organic-Molecules. *Analytical Chemistry* **1985,** *57* (14), 2935-2939.

112. CAPELLEN, R. J. C. a. J. M., A REVIEW OF THE APPLICATIONS TO SOLIDS OF THE LASER ION

SOURCE IN MASS SPECTROMETR. *IntemationaI Journal of Mzss Spectrometry and Ion Physics,* **1980,** *34*, 197-271

113. Koichi Tanaka, H. W., Yutaka Ido, Satoshi Akita, Yoshikazu Yoshida and Tamio Yoshida, Protein and polymer analyses up to m z 100 000 by laser ionization. *Rapid Comm Mass Spectrometry* **1988,** *2* (8), 151-153.

114. Tsuchida, S.; Umemura, H.; Nakayama, T., Current Status of Matrix-Assisted Laser Desorption/Ionization-Time-of-Flight Mass Spectrometry (MALDI-TOF MS) in Clinical Diagnostic Microbiology. *Molecules* **2020,** *25* (20).

115. Berghmans, E.; Boonen, K.; Maes, E.; Mertens, I.; Pauwels, P.; Baggerman, G., Implementation of MALDI Mass Spectrometry Imaging in Cancer Proteomics Research: Applications and Challenges. *J Pers Med* **2020,** *10* (2).

116. Li, D.; Yi, J.; Han, G.; Qiao, L., MALDI-TOF Mass Spectrometry in Clinical Analysis and Research. *ACS Meas Sci Au* **2022,** *2* (5), 385-404.

117. Tsarbopoulos, A.; Karas, M.; Strupat, K.; Pramanlk, B. N.; Nagabhushan, T. L.; Hillenkamp, F., Comparative Mapping of Recombinant Proteins and Glycoproteins by Plasma Desorption and Matrix-Assisted Laser Desorption/Ionization Mass-Spectrometry. *Analytical Chemistry* **1994,** *66* (13), 2062-2070.

118. Murray, K. K., Lasers for matrix-assisted laser desorption ionization. *J Mass Spectrom* **2021,** *56* (6), e4664.

119. Singhal, N.; Kumar, M.; Kanaujia, P. K.; Virdi, J. S., MALDI-TOF mass spectrometry: an emerging technology for microbial identification and diagnosis. *Front Microbiol* **2015,** *6*, 791.

120. Shanta, P. V.; Li, B.; Stuart, D. D.; Cheng, Q., Plasmonic Gold Templates Enhancing Single Cell Lipidomic Analysis of Microorganisms. *Analytical Chemistry* **2020,** *92* (9), 6213-6217.

121. Pallavicini, P.; Chirico, G.; Taglietti, A., Harvesting Light To Produce Heat: Photothermal Nanoparticles for Technological Applications and Biomedical Devices. *Chemistry – A European Journal* **2021,** *27* (62), 15361-15374.

122. Lambert, A. S. Integrating New Methodologies and Materials Towards Advanced Surface Plasmon Resonance-Based Bioanalysis. UC Riverside, ProQuest, 2022.

123. Krone, J. R.; Nelson, R. W.; Dogruel, D.; Williams, P.; Granzow, R., BIA/MS: Interfacing biomolecular interaction analysis with mass spectrometry. *Analytical Biochemistry* **1997,** *244* (1), 124-132.

124. Bonyadi, F.; Kavruk, M.; Ucak, S.; Cetin, B.; Bayramoglu, G.; Dursun, A. D.; Arica, Y.; Ozalp, V. C., Real-Time Biosensing Bacteria and Virus with Quartz Crystal Microbalance: Recent Advances, Opportunities, and Challenges. *Crit Rev Anal Chem* **2023**, 1-12.

125. Huang, X.; Chen, Q.; Pan, W.; Yao, Y., Advances in the Mass Sensitivity Distribution of Quartz Crystal Microbalances: A Review. *Sensors (Basel)* **2022,** *22* (14).

126. SAUERBREY, G., Use of quartz vibration for weighing thin films on a microbalance. *J. Phys.* **1959,** *155*, 206-222.

127. Huang, X.; Chen, Q.; Pan, W.; Hu, J.; Yao, Y., Assessing the Mass Sensitivity for Different Electrode Materials Commonly Used in Quartz Crystal Microbalances (QCMs). *Sensors (Basel)* **2019,** *19* (18).

128. II, K. K. K. a. J. G. G., The Oscillation Frequency of a Quartz Resonantor in Contact with a Liquid. *Analytica Chimica Acta* **1985,** *175*, 99-105.

129. Huang, L. Y. a. X., Response of Quartz Crystal Microbalance Loaded with Single-drop Liquid in Gas Phase. *The Open Electrical & Electronic Engineering Journal* **2014,** *8*, 197-201.

130. Martin, S. J.; Granstaff, V. E.; Frye, G. C., Characterization of a Quartz Crystal Microbalance with Simultaneous Mass and Liquid Loading. *Analytical Chemistry* **1991,** *63* (20), 2272-2281.

131. Metropolis, N.; Ulam, S., The Monte Carlo method. *J Am Stat Assoc* **1949,** *44* (247), 335-41.

132. Richtmyer, D. J. P. S. U. *STATISTICAL METHODS IN NEUTRON DIFFUSION*; Los Alamos National Lab: 1947.

133. Cui, F.; Yue, Y.; Zhang, Y.; Zhang, Z.; Zhou, H. S., Advancing Biosensors with Machine Learning. *ACS Sens* **2020,** *5* (11), 3346-3364.

134. Greener, J. G.; Kandathil, S. M.; Moffat, L.; Jones, D. T., A guide to machine learning for biologists. *Nat Rev Mol Cell Biol* **2022,** *23* (1), 40-55.

135. Linardatos, P.; Papastefanopoulos, V.; Kotsiantis, S., Explainable AI: A Review of Machine Learning Interpretability Methods. *Entropy (Basel)* **2020,** *23* (1).

136. Rudin, C., Stop Explaining Black Box Machine Learning Models for High Stakes Decisions and Use Interpretable Models Instead. *Nat Mach Intell* **2019,** *1* (5), 206-215.

137. Kuhn, M., Building Predictive Models in R Using the caret Package. *Journal of Statistical Software* **2008,** *28* (5), 1-26.

138. Team, R. C. *R: A language and environment for statistical computing.*, R Foundation for Statistical Computing: Vienna, Austria, 2022.

139. Amanpreet Singh, N. T., and Aakanksha Sharma, A Review of Supervised Machine Learning Algorithms. In *2016 3rd International Conference on Computing for Sustainable Global Development*, IEEE: New Delhi, India 2016.

140. HOPFIELD, J. J., Neural networks and physical systems with emergent collective

computational abilities. *Proc. NatL Acad. Sci.* **1982,** *79*, 2554-2558.

141. M. Egmont-Petersen, D. d. R., H. Handels, Image processing with neural networks—a review. *Pattern Recognition* **2002,** *35*, 2279–2301.

142. Chen, L.; Li, S.; Bai, Q.; Yang, J.; Jiang, S.; Miao, Y., Review of Image Classification Algorithms Based on Convolutional Neural Networks. *Remote Sensing* **2021,** *13* (22).

143. Byun, S. J.; Kim, D. G.; Park, K. D.; Choi, Y. J.; Kumar, P.; Ali, I.; Kim, D. G.; Yoo, J. M.; Huh, H. K.; Jung, Y. J.; Kim, S. K.; Pu, Y. G.; Lee, K. Y., A Low-Power Analog Processor-in-Memory-Based Convolutional Neural Network for Biosensor Applications. *Sensors (Basel)* **2022,** *22* (12).

144. Hodges, E. F. a. J. L. *Discriminatory Analysis Nonparametric Discrimination Consistency Properties*; University of California Berkely: USAF School of Aviation Medicine, Randolph Field, Texas, 1951.

145. Cunningham, P.; Delany, S. J., k-Nearest Neighbour Classifiers - A Tutorial. *ACM Computing Surveys* **2021,** *54* (6), 1-25.

146. Massart, D. C. a. D. L., Alternatives k-Nearest Neighbor Rules in Supervised Pattern Recognition. *Anafyfica Chimica Acta* **1982,** *136*, 15-27.

147. Stone, C. J., Consistent Nonparametric Regression. *Ann Stat* **1977,** *5* (4), 595-645.

148. Tin Kam, H., Random decision forests. In *Proceedings of 3rd International Conference on Document Analysis and Recognition*, IEEE: Montreal, QC, Canada 1995; pp 278-282.

149. Breiman, L., Random forests. *Machine Learning* **2001,** *45* (1), 5-32.

150. Huberty, C. J., Discriminant Analysis. *Review of Educational Research* **1975,** *45* (4), 543-598.

151. Fisher, R. A., The Use of Multiple Measurements in Taxonomic Problems. *Annals of Eugenics* **1936,** *7* (2), 179-188.

152. Crowley, B. G. a. M., Linear and Quadratic Discriminant Analysis: Tutorial. *arXiv:1906.02590 [stat.ML]* **2019**.

153. Cortes, C.; Vapnik, V., Support-Vector Networks. *Machine Learning* **1995,** *20* (3), 273-297.

Chapter 2: Formulation of Biomimetic Tethered Lipid Membrane on Gold Substrate Enabling Understanding of Drug Delivery Processes via Surface Plasmon Resonance

2.1 Introduction

Lipid membranes compose a crucial portion of biological systems acting as containment for cellular components and barriers to entry of exogenous materials.[154] As such, deeper understanding of the interactions at these interfaces is key to the development and application of drug molecules which must navigate across the membrane to intracellular targets.[155, 156] Methodologies to mimic this important cellular environment aid in expanding this understanding, allowing individual interactions to be isolated from the complexity of the cellular environment and analyzed.[157] In this regard, biomimetic lipid bilayers have emerged as powerful tools with self-assembly of solid supported lipid bilayers employed in many sensing applications.[158-160] Though one of the major limitations comes from the solid support which can limit lipid mobility, provides a one sided view of the bilayer system, and can result in protein denaturation.[161] One avenue to expand the capabilities of these mimetic surfaces is the inclusion of tethers producing a fluid region between the solid support and the membrane.[162-164] This can enable inclusion of larger membrane components such as proteins without pressing them against the support and facilitate analysis of binding interactions. Furthermore, studies of molecular interactions with the cell membrane can be expanded to examine their membrane diffusion properties. While biomimetic membranes have been demonstrated extensively on silica or mica substrates many sensing methodologies utilize metal surfaces limiting the applicability of these substrates.[165] In particular, surface plasmon resonance (SPR) employs a plasmonic

metal surface, usually gold, which some have employed thiol linked lipids to enable membrane formation on the gold substrate.[166, 167] While we have introduced a thin silica coating atop the gold to provide the chemical properties necessary for vesicle fusion[168] and others have introduced methodologies to induce lipid vesicle fusion on a gold substrate.[169] However, a methodology to easily enable a tethered lipid membrane without sensor linkage could prove to be a useful tool in biomimetic studies.

Here we investigate a tethered lipid bilayer formulation for application on gold sensor chips that applies polyethylene glycol (PEG) linked lipids to induce vesicle fusion without the need for covalent linkers. The PEG tether also forms a barrier between the solid support and the lipid bilayer to mimic the cell membrane more accurately. This limits the effect of the solid support on lipid interactions and fluidity enabling inclusion of greater amounts of material within the bilayer without losing fluidity. We demonstrate this effectiveness through incorporation of amphiphilic dendrimers which consist of long hydrophobic alkyl chain tails and branched polyamidoamine or arginine dendrons into the lipid preparation process.[170] These dendrimers have been shown to form supramolecular structures with lipids but quickly decreased lipid fluidity[171], which was alleviated by the incorporation of the lipid tether based on our fluorescence recovery after photobleaching (FRAP) fluidity measurements. We expanded this to study the binding of dendrimers to the lipid membrane with arginine and amine head groups to understand differences in potential for drug delivery. We further employed this substrate to explore molecular transport across the lipid membrane utilizing surface plasmon resonance (SPR) and matrix assisted laser desorption ionization mass spectrometry (MALDI-MS). Our results showed a marked difference in

dendrimer binding to lipid surfaces based on dendrimer headgroups and also demonstrated that small molecule thiols could pass the lipid membrane and link to the gold substrate which could be visualized by SPR angular shifts and confirmed via MALDI-MS. Thus, establishing a new platform for lipid membrane binding studies and monitoring of membrane transport that could potentially be utilized for drug delivery studies.

2.2 Experimental Methods

Materials and Reagents.

A stainless-steel extruder, 100 nm polycarbonate track etched filters, 1-palmitoyl-2-oleoyl-glycero-3-phosphocholine POPC, and 1,2-dioleoyl-sn-glycero-3-phosphoethanolamine-N-(7-nitro-2-1,3-benzoxadiazol-4-yl) (ammonium salt) NBD-PE, were purchased from Avanti Polar Lipids (Alabaster, Al). Plain BK-7 glass microscope slides and phosphate buffered saline (PBS) concentrate were acquired from Fisher Scientific (Hampton, NH). Polydimethylsiloxane (PDMS) two-part polymer kit was obtained from Ellsworth adhesives (Germantown, WI). Triton X-100, 2-2-[2-(2-Mercaptoethoxy)ethoxy]ethoxyethanol and 11-Mercapto-1-undecanol were obtained from MilliporeSigma (Burlington, MA). Ultrapure water (>18 MΩ cm-1) was acquired from a Barnstead E-Pure water purification system. Branching dendrimer molecules with terminal amines[170] or arginine's[172] were obtained from our collaborators in the Peng group and the dendrimer synthesis is discussed in depth in their work.[173]

Lipid Vesicle Preparation.

Lipid vesicles were prepared via a thin film extrusion method[174, 175] where aliquots of lipid solutions were first mixed to reach a desired mol ratio from stock lipid solutions in 1:9 methanol chloroform. Then these aliquots were dried under nitrogen to form a thin lipid film on the bottom of a glass vial and further dried under vacuum for at least 4 hours. Dried films were then resuspended in 1× PBS (10 mM Na2HPO4, 1.8 mM KH2PO4, 137 mM NaCl, 2.7 mM KCL, pH 7.4) to a final lipid concentration of 1 mg/mL. Mixtures were vortexed to dissolve the lipid film and then sonicated to induce vesicle formation. Finally, vesicles were extruded to produce small unilamellar vesicles of desired size, stored at 4°C and used within 5 days.

Fluorescent Imaging and Recovery after Photobleaching.

Fluorescence and bleaching images were generated on an inverted Leica TCS SP5 II confocal microscope (Leica Microsystems, Buffalo Point, IL, USA) at the University of California, Riverside Microscopy and Imaging Core Facility. To enable fluorescent visualization of lipid membrane systems NBD-PE lipids (2% molar ratio) were incorporated into the vesicle preparation methods. To ensure that formed lipid bilayers remained intact in a hydrated state small wells were cut out of thin PDMS sheets where lipid vesicles could be incubated, rinsed, and then covered with a microscope coverslip for visualization. For fluorescent imaging a 488 nm argon laser was utilized to excite the lipid linked NBD fluorophore. Fluorescent emissions between 500 and 600 nm were then detected using a hybrid detector (HyD). For fluorescent recovery after photobleaching

(FRAP) laser power was set to 100% and used for a one second point bleach. The following fluorescence recovery was visualized via image collection every second for at least 80 seconds using the LAS AF FRAP application wizard (Leica) with laser power lowered to 10-20%. After collection images were processed using ImageJ with the Fiji package[176] and analyzed to calculate mobile fraction, recovery, and lipid mobility. Curves were graphed in origin and fit using a one-phase association equation with no offset (BoxLucas1). From this fit equation mobile fractions (ß) and diffusion coefficients (D) were calculated using previously demonstrated methods.[177]

Fabrication of SPR Chips.

Surface plasmon resonance sensor chips were fabricated following previously published methodologies.[178] In short, glass microscope slides were coated with a thin film of gold using an electron beam physical vapor deposition (EBPVD) system (Temescal, Berkeley, CA) in the University of California, Riverside Center for Nanoscale Science and Engineering Nanofabrication Facility. To achieve this, slides were first cleaned in boiling piranha acid 3:1, H_2SO_4:H_2O_2) for 1 hour. Followed by a rinse with water then ethanol and dried under a nitrogen stream. Then slides were taped to silicon wafers and slotted into the EBPVD where 2 nm of Cr, as an adhesion layer, and 48 nm of gold were deposited. The resulting chips were then utilized for SPR spectroscopy measurements.

SPR Analysis

Fabricated SPR chips were utilized on a NanoSPR5-321 (NanoSPR, Chicago, IL) instrument with a 670 nm GaAs semiconductor laser source for all SPR experiments. The

system includes a triangular prism (n= 1.61), with a silver-plated backing to reflect light back to the detector, and a dual channel 30 µL Teflon flow cell. For SPR experiments n = 1.5167 matching fluid (Cargille, Cedar Grove, NJ) was applied to the glass bottom of a sensor chip and clamped to the prism surface then rinsed (5 mL/h) with 1x PBS as a running buffer prior to lipid formulation and interaction studies.

MALDI-MS Spectra Collection

To transfer SPR chips to MALDI-MS instrumentation the chips were first dried under air and then spotted in multiple locations with 1 µL of 10mg/mL super DHB matrix in a (2:1, v/v) mix of acetonitrile and 1% TFA/water solution. MALDI-MS experiments were then conducted on an AB-Sciex 5800 time-of-flight mass spectrometer equipped with a 337nm nitrogen UV laser. Spectra were acquired in positive mode with a laser power of 5000 a.u. with each spectrum made up of 200 laser shots fired over a selected area.

2.3 Results and Discussion

While tethered lipid membranes have been demonstrated the self-assembly of a wholly

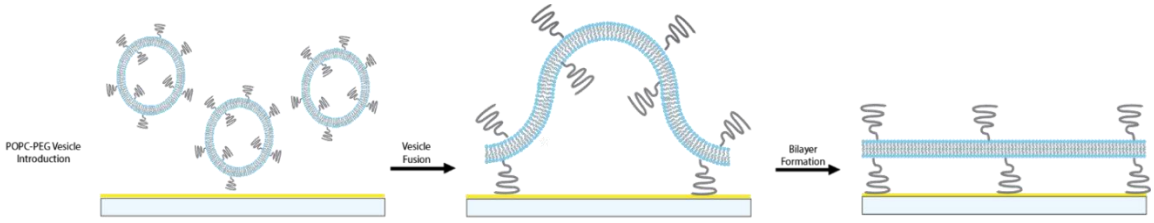

Figure 2.1. Scheme of polyethylene glycol tethered lipid membrane formation on a gold surface.

mobile tethered system on a gold substrate has been elusive as gold is not conducive to lipid self-assembling thus limiting biomimetic membrane use in various sensor configurations. Therefore, we took from literature reports of PEG inducing lipid vesicle

fusion on gold substrates[179] to design a PEG tethered lipid membrane that was not linked to the substrate ensuring that all components could be mobile (Figure 2.1). With this a tethered lipid bilayer could be employed in sensing applications utilizing gold surfaces. This was employed to study dendrimers for their ability to form supramolecular structures with the lipid assembly and investigate the binding interactions between these dendrimer micelles and a lipid substrate. Thus, providing insight into how they may act in drug delivery applications. The formation of a tethered membrane on gold was also employed to monitor the passage of small drug analogs across the membrane. For this small molecule thiols were introduced and would link to the gold surface if they passed the lipid membrane. After which the lipid membrane was removed allowing measurement of just those small molecules that passed the bilayer.

Tethered Membrane Formulation and Characterization

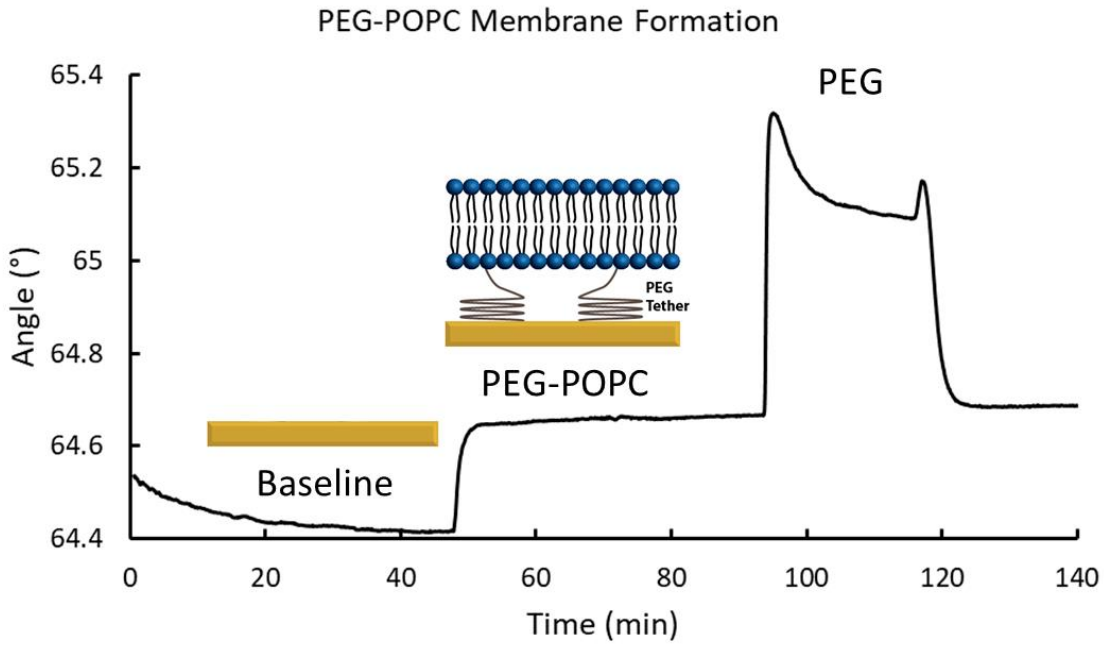

Figure 2.2. SPR sensorgram of PEG-POPC tethered membrane formation on gold sensor surface with included PEG injection that induces vesicle fusion showing no change in membrane signal.

To begin the proposed tethered membrane system was formulated based on the thin film extrusion method[174, 175] detailed above with inclusion of 0.5% molar ratio 5K PEG linked PE lipids to ensure ample cushion between the lipid bilayer and solid support with minimal impact on the membrane composition. These lipid formulations were then tested for their ability to self-assemble on commonly utilized glass substrates and on an SPR gold sensor surface (Figure 2.2). Finding robust membrane formation in both systems though to ensure vesicle fusion and complete lipid coverage a secondary PEG injection step was included on the gold substrates. This PEG injection had little to no impact on the signal for the lipid membrane indicating that the membrane system was self-assembling and did not require vesicle fusion to be induced. Now that lipid membrane formation was confirmed and appeared to be comparable to a traditional solid supported POPC system we utilized FRAP

to measure and compare the lipid fluidity of these two systems. The PEG-POPC tethered membrane demonstrated similar lipid fluidity to that seen with a POPC bilayer as can be seen in Figure 2.3. This was promising as it indicated that despite the incorporation of long

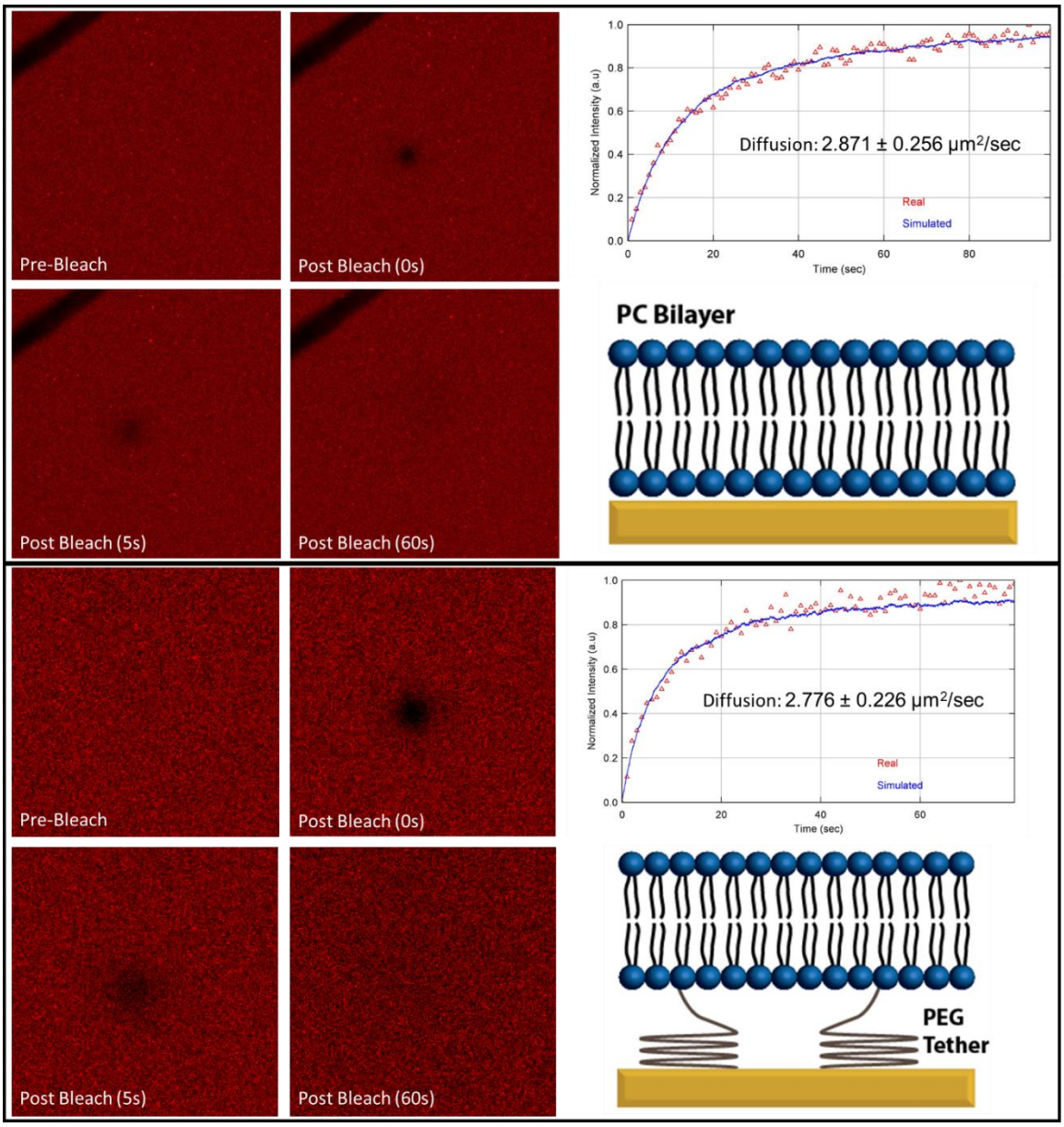

Figure 2.3. Fluorescent images of bleaching and recovery and resulting FRAP curves and diffusion calculations for POPC solid supported membrane (Top) and PEG-POPC tethered membrane (Bottom).

PEG tethers the lipid lateral mobility was minimally impacted. Therefore, lipid fluidity was maintained in the system while providing lift from the sensor surface allowing it to be utilized for analysis of the whole membrane structure not just those lipids facing away from the sensor. These results then made us consider how this tether affected or enabled the incorporation of other materials into the membrane system.

Impact of Dendrimer Loading on Bilayer Fluidity

As the tethered system creates a barrier between the solid support and the lipid membrane, we expected the incorporation of other molecular constituents into this system to have a more muted effect on fluidity. Thus, enabling loading of greater amounts of

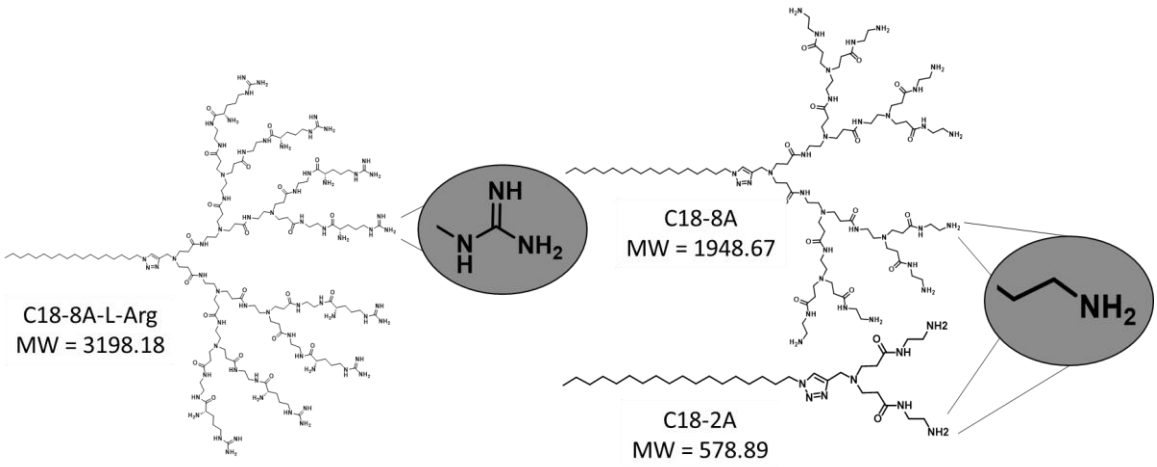

Figure 2.4. Structures of dendrimers utilized in these studies with two terminating in amine groups (right, C18-8A and C18-2A) while the other (left, C18-8A-L-Arg) terminates in an arginine group.

materials while still maintain the important fluidity characteristics of a lipid bilayer. To investigate this, we formulated supramolecular structures composed of various lipids and dendrimer compositions following the lipid vesicle preparation procedures previously described and measured lipid fluidity via FRAP. For these experiments three different

branched dendrimers were investigated, two with branches terminating in amine groups and one with a greater number of branches terminating in arginine's. The structure of these dendrimers can be seen in Figure 2.4. After forming these combined lipid dendrimer

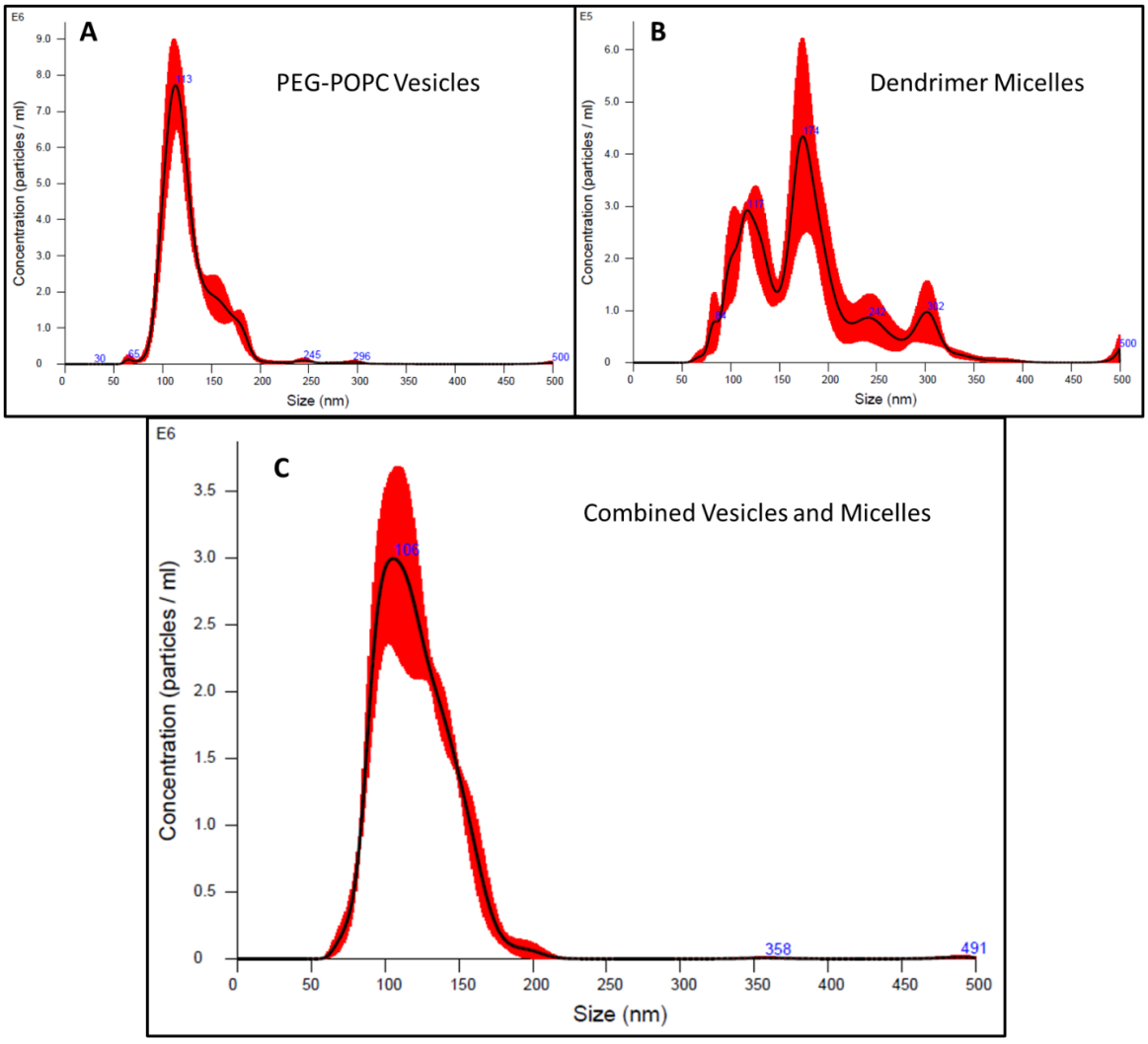

Figure 2.5. Nanoparticle tracking analysis results of three average tracking runs for PEG-POPC vesicles (A), dendrimer micelles (B) and the two combined into a singular structure (C).

structures, we employed nanoparticle tracking analysis to probe whether they were in fact combing into singular structures. These results can be seen in Figure 2.5 and show a distinct peak for the PEG-POPC vesicles and various peaks for the dendrimer micelles which disappear upon combination with the vesicles forming a singular peak indicating an average diameter of 106 nm for the supramolecular structures. This gave us confidence that the lipid and dendrimers were intermingling and forming the expected structures. Then to explore the limits of dendrimer incorporation into the PEG tethered membrane system we first focused on the highly branched Arg-8A dendrimer and

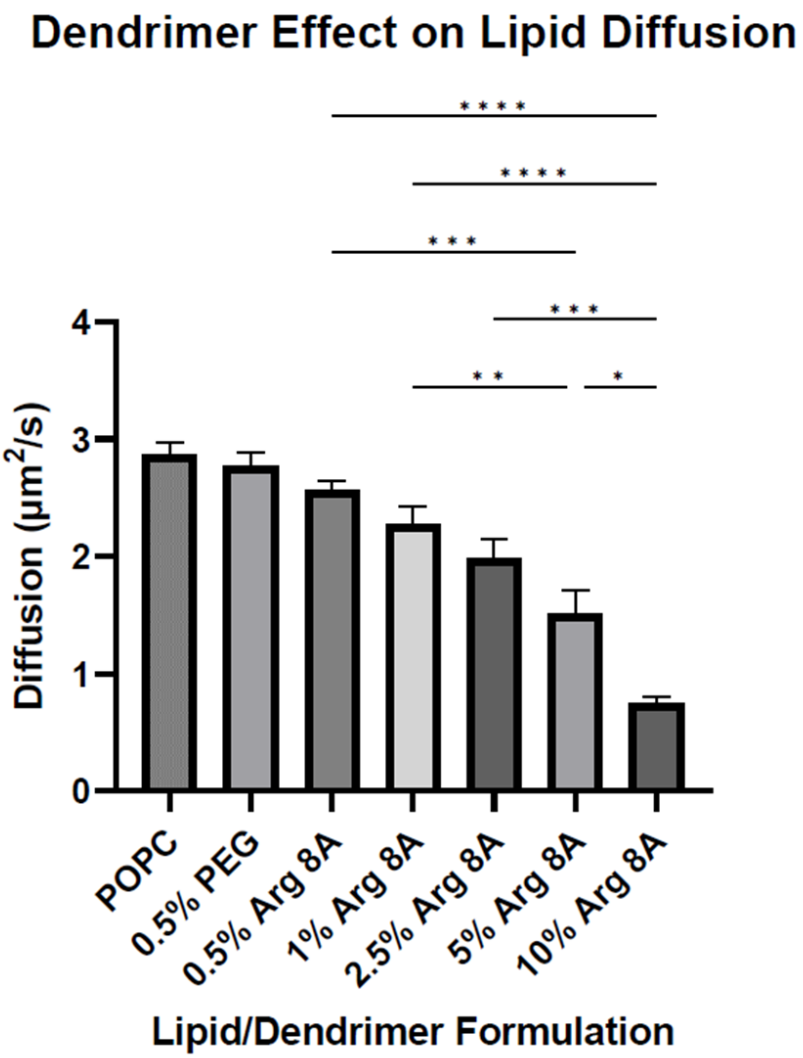

Figure 2.6. Impact of arginine terminated dendrimers on lipid bilayer fluidity. Lipid diffusivity was decreased substantially by introduction of greater amounts of dendrimer, but large proportions of dendrimer were able to be incorporated without completely stopping lipid diffusion as seen for the 10% Arg 8A.

integrated it into vesicle preparation procedures from (0.5 to 10%) as can be seen in Figure 2.6. With results demonstrating a decrease in lipid fluidity with increasing Arg-8A loading

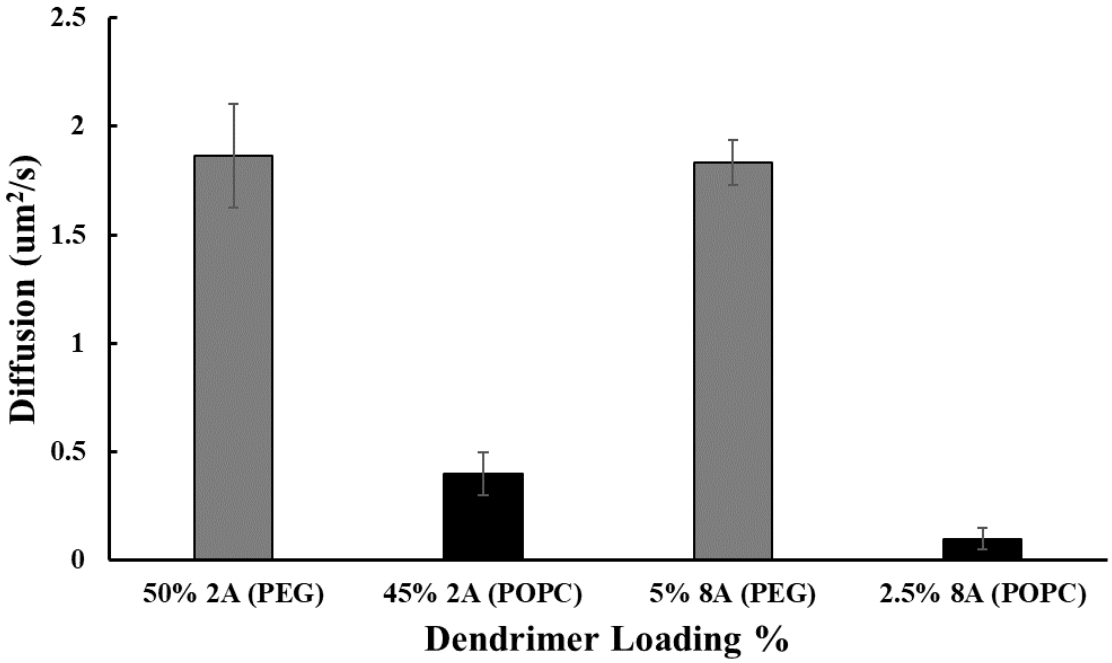

Figure 2.7. Diffusion coefficient obtained from FRAP studies of combined dendrimer and lipid membrane systems. Showing significantly higher diffusion when PEG-POPC tethered lipids (grey) were combined with dendrimers than traditional POPC (black).

though some mobility was still measurable even at 10% dendrimer loading demonstrating that the tether significantly reduced membrane interactions with the underlying support enabling membrane mobility to be maintained even with large amounts of dendrimer loading. As dendrimer lipid formulations with dendrimers 2A and 8A have been previously investigated with solid supported POPC[171] we utilized them to confirm the fluidity improvements provided by the PEG tether. These results can be seen in Figure 2.7 showing a substantial decrease in lipid fluidity with increasing dendrimer size and percentage for a POPC solid supported membrane system with a much lower decrease for the PEG-POPC tethered system. With a POPC membrane lipid mobility is almost completely lost with

loading of 45 and 2.5% of 2A and 8A dendrimer respectively. While, with the PEG tethered membrane the lipid mobility is not even decreased by half with introduction of higher amounts of 50% 2A and 5% 8A dendrimer. This demonstrates the profound impact interactions with the solid support surface have on biomimetic membrane mobility and indicates that this tethered system can remedy these effects and more accurately represent a cellular surface.

Dendrimer Binding to Tethered Lipid Membrane

As these dendrimers have been shown to create supramolecular structures with lipids[171] and have been considered as potential avenues for drug delivery[180] we endeavored to understand the interactions between these dendrimers and our lipid system. As these interactions play an important role in both supramolecular assembly and in drug delivery mechanisms. To achieve this, we utilized SPR spectroscopy techniques to monitor binding events between dendrimer micelles and the PEG tethered lipid bilayer. Previously amine terminated dendrimer micelles had been shown to have no binding to a solid supported POPC membrane[171], but the arginine terminated dendrimers had not been explored. Therefore, we first investigated whether Arg-8A dendrimer micelles would bind to the tethered lipid membrane, finding substantial signal associated with dendrimer binding remained even after a rinse. Notably a twofold greater binding signal was obtained for the arginine terminated dendrimers compared to the amine terminated dendrimers. This matches with models demonstrated by Li et al.[181] showing strong interactions between both lysine and arginine resulting in membrane deformation. Furthermore, they found that arginine pulled in more lipid headgroups than lysine which would match with our SPR

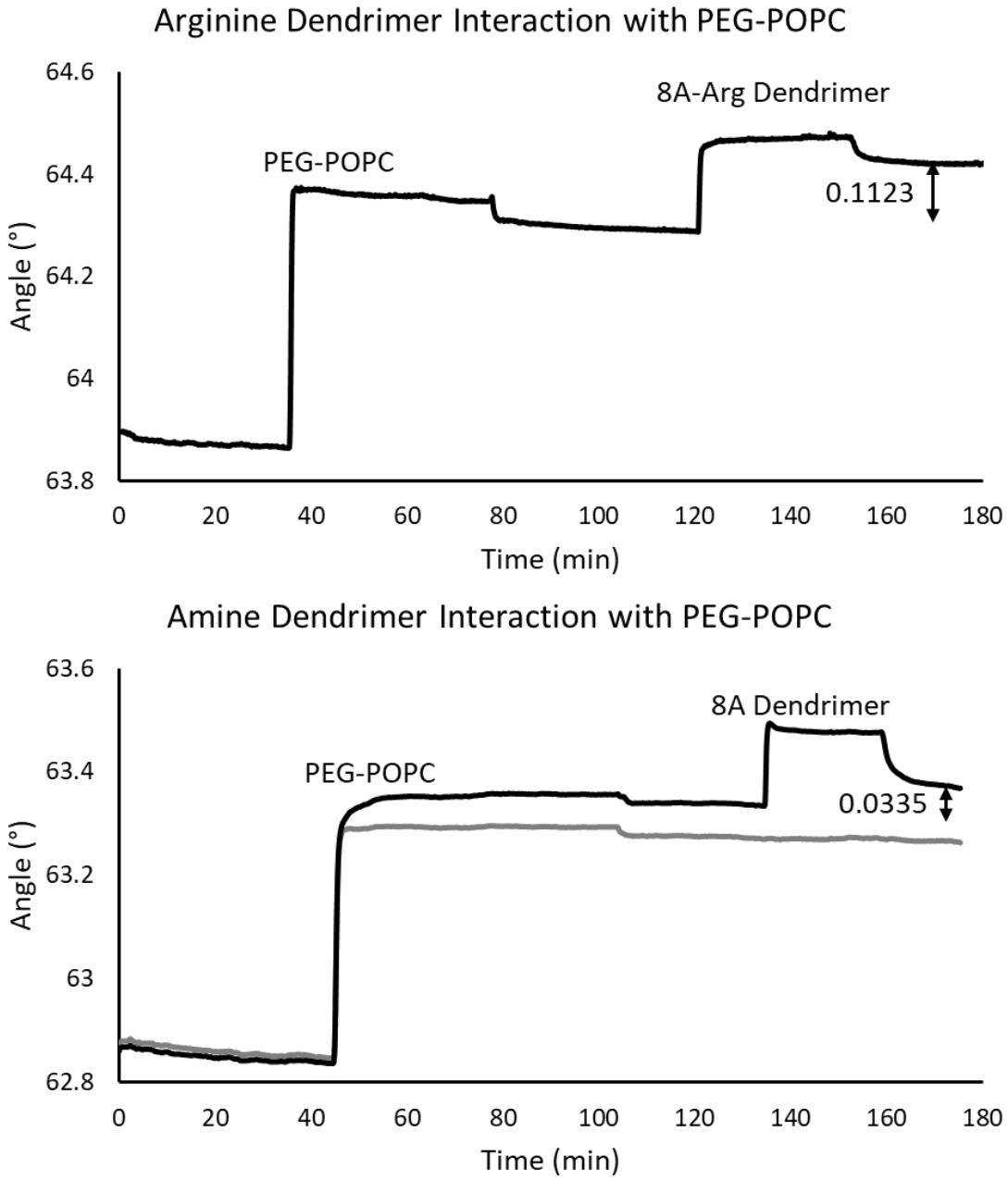

Figure 2.8. Surface plasmon resonance sensorgrams demonstrating differential binding of arginine and amine dendrimers to PEG tethered lipid bilayers. Over two-fold higher binding signal was observed for the arginine dendrimer on the PEG-POPC surface.

binding results. This likely plays a large part in the binding differences occurring between arginine terminated and amine terminated dendrimers and is linked to the membrane

penetration properties of arginine containing peptides that have been demonstrated in literature.[182, 183] We then expanded our work to explore whether the tethered membrane had any impact on binding in regards to the amine terminated dendrimers, finding significantly less binding than seen for the Arg-8A but more than was observed on a solid supported POPC substrate as can be seen in Figure 2.8. This demonstrates that at least for the 8A dendrimer the underlying solid support seems to play a role in limiting these binding interactions from occurring potentially due to the lack of membrane malleability in the vertical direction.

SPR Analysis of Membrane Transport

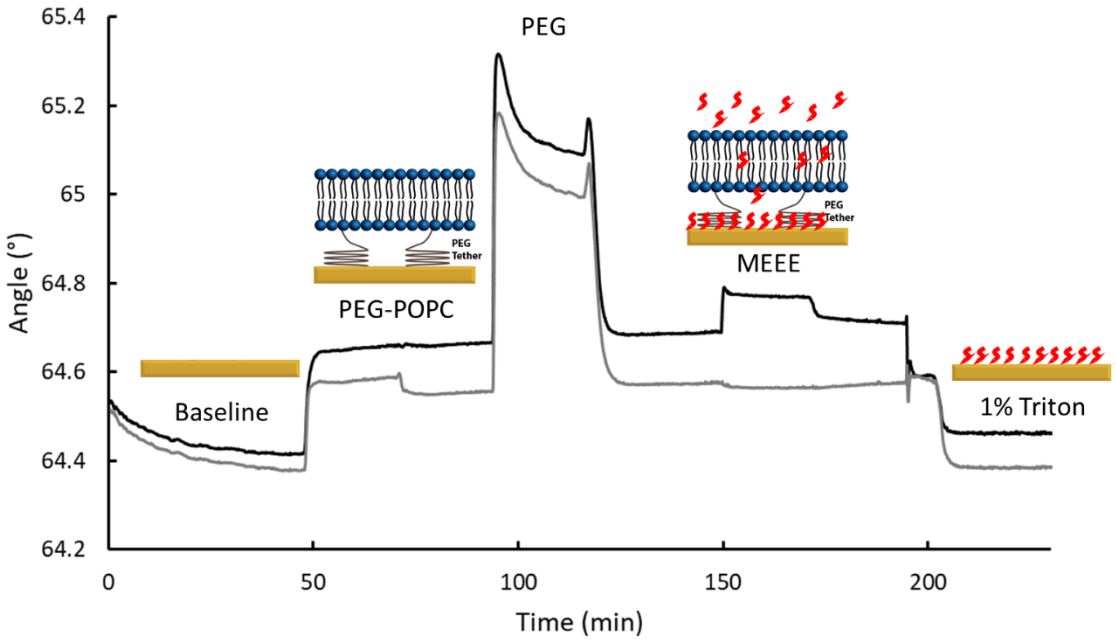

Figure 2.9. SPR sensorgram (black) demonstrating detection of small molecules passing a membrane system with signal remaining from molecules linked to the sensor chip after triton removal of the lipids. Control (grey) without the addition of small molecule thiol shows a return to baseline due to complete removal of lipids.

Now that we had demonstrated a robust tethered bilayer system that mimicked the two-sided nature of a cellular membrane and could be formulated on gold sensor chips, we

employed it to investigate the transport of small drug analogs across a membrane. To achieve this PEG tethered POPC membranes were formulated on SPR chips and monitored as small molecule drug analogs were introduced to the system to visualize their passage across the membrane and covalent linkage to the sensor surface as can be seen in Figure 2.9. Following this a 1% Triton X-100 solution was injected to disrupt and remove the lipid membrane[184] leaving only those small molecules that had been able to traverse the bilayer barrier. For the small molecule 2-[2-[2-(2-Mercaptoethoxy)ethoxy]ethoxy]ethanol (MEEE) these results showed an increase in signal remaining after membrane removal indicating that it was able to cross the lipid bilayer and adhere to the gold substrate. Similar results were obtained for another small molecule thiol 11-Mercapto-1-undecanol. However, with a large molecule or protein this signal was not observed indicating inability to pass the membrane mimic. Demonstrating the feasibility of utilizing this platform to investigate the membrane permeability of various drug molecules. However, further work was needed to concretely determine that the signal identified was from the small molecule of interest.

MALDI-MS Confirmation of Small Molecule Bilayer Crossing

To this end, we employed on chip MALDI-MS after our SPR spectroscopy experiments to confirm the presence of these small molecules and the lack of lipids. For this SPR chips were dried with air after experiment completion and the areas of the chip consistent with the flow cell were covered in sDHB matrix before transfer to a MALDI-MS instrument. Following this, various areas of the chip could be ionized and the molecular constituents within the selected area could be identified. As can be seen in Figure 2.10 MEEE is clearly

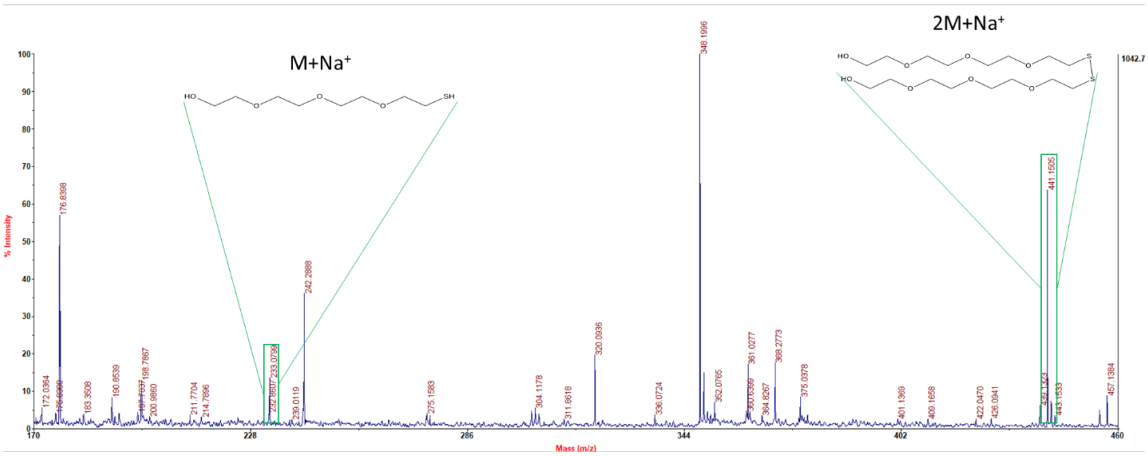

Figure 2.10. MALDI-MS spectra showing sodiated peaks of MEEE thiols from SPR sensor chips after passage across the membrane system. Two peaks associated with the molecule are seen at high abundance corresponding to a single thiol and disulfide form of the molecule present on the surface.

visible in the MALDI-MS spectra indicating that it was capable of passing the lipid membrane. Thus, demonstrating the potential of the SPR tethered membrane platform to investigate these important membrane diffusion properties especially with the addition of MALDI-MS for confirming the molecular identity of molecules remaining on the sensor chip after experimentation.

2.4 Conclusion

We have demonstrated a new wholly mobile tethered lipid membrane that enables self-assembly on gold surfaces which up to now has been difficult. This is achieved through the inclusion of long PEG chains that form a cushion between the lipids and the solid support. This cushion has been shown to significantly improve the membranes resistance to mobility reductions from molecular loading when compared to traditionally utilized solid supported lipid membranes. We further investigated the binding of dendrimer micelles to this membrane surface and identified unique interactions that occur only with this surface.

Finally, this substrate was employed as a platform for monitoring of small molecule drug analog passage across a membrane system with MALDI-MS used to confirm the molecular identity of the passing molecules. This constitutes a preliminary study demonstrating the feasibility of utilizing and unlinked tethered membrane and results indicating its highly promising properties for accurately mimicking the cell surface.

2.5 References

1. van Meer, G.; Voelker, D. R.; Feigenson, G. W., Membrane lipids: where they are and how they behave. *Nat Rev Mol Cell Biol* **2008,** *9* (2), 112-24.

2. Seddon, A. M.; Casey, D.; Law, R. V.; Gee, A.; Templer, R. H.; Ces, O., Drug interactions with lipid membranes. *Chemical Society Reviews* **2009,** *38* (9), 2509-2519.

3. Bunea, A.-I.; Harloff-Helleberg, S.; Taboryski, R.; Nielsen, H. M., Membrane interactions in drug delivery: Model cell membranes and orthogonal techniques. *Advances in Colloid and Interface Science* **2020,** *281*, 102177.

4. Richter, R. P.; Bérat, R.; Brisson, A. R., Formation of Solid-Supported Lipid Bilayers: An Integrated View. *Langmuir* **2006,** *22* (8), 3497-3505.

5. Castellana, E. T.; Cremer, P. S., Solid supported lipid bilayers: From biophysical studies to sensor design. *Surface Science Reports* **2006,** *61* (10), 429-444.

6. Han, W. B.; Kang, D.-H.; Kim, T. S., 3D Artificial Cell Membranes as Versatile Platforms for Biological Applications. *BioChip Journal* **2022,** *16* (3), 215-226.

7. Andersson, J.; Bilotto, P.; Mears, L. L. E.; Fossati, S.; Ramach, U.; Köper, I.; Valtiner, M.; Knoll, W., Solid-supported lipid bilayers – A versatile tool for the structural and functional characterization of membrane proteins. *Methods* **2020,** *180*, 56-68.

8. Knoll, W.; Bender, K.; Förch, R.; Frank, C.; Götz, H.; Heibel, C.; Jenkins, T.; Jonas, U.; Kibrom, A.; Kügler, R.; Naumann, C.; Naumann, R.; Reisinger, A.; Rühe, J.; Schiller, S.; Sinner, E.-K., Polymer-Tethered Bimolecular Lipid Membranes. In *Polymer Membranes/Biomembranes*, Meier, W. P.; Knoll, W., Eds. Springer Berlin Heidelberg: Berlin, Heidelberg, 2010; pp 197-233.

9. Rebaud, S.; Maniti, O.; Girard-Egrot, A. P., Tethered bilayer lipid membranes (tBLMs): Interest and applications for biological membrane investigations. *Biochimie* **2014,** *107*, 135-142.

10. Jackman, J. A.; Knoll, W.; Cho, N.-J. Biotechnology Applications of Tethered Lipid Bilayer Membranes *Materials* [Online], 2012, p. 2637-2657.

11. Andersson, J.; Köper, I. Tethered and Polymer Supported Bilayer Lipid Membranes: Structure and Function *Membranes* [Online], 2016.

12. Keller, C. A.; Glasmästar, K.; Zhdanov, V. P.; Kasemo, B., Formation of Supported Membranes from Vesicles. *Physical Review Letters* **2000,** *84* (23), 5443-5446.

13. Basit, H.; Van der Heyden, A.; Gondran, C.; Nysten, B.; Dumy, P.; Labbé, P., Tethered Bilayer Lipid Membranes on Mixed Self-Assembled Monolayers of a Novel Anchoring Thiol: Impact of the Anchoring Thiol Density on Bilayer Formation. *Langmuir* **2011,** *27* (23), 14317-14328.

14. Knoll, W.; Köper, I.; Naumann, R.; Sinner, E.-K., Tethered bimolecular lipid membranes—A novel model membrane platform. *Electrochimica Acta* **2008,** *53* (23), 6680-6689.

15. Phillips, K. S.; Wilkop, T.; Wu, J.-J.; Al-Kaysi, R. O.; Cheng, Q., Surface Plasmon Resonance Imaging Analysis of Protein-Receptor Binding in Supported Membrane Arrays on Gold Substrates with Calcinated Silicate Films. *J Am Chem Soc* **2006,** *128* (30), 9590-9591.

16. Tabaei, S. R.; Choi, J.-H.; Haw Zan, G.; Zhdanov, V. P.; Cho, N.-J., Solvent-Assisted Lipid Bilayer Formation on Silicon Dioxide and Gold. *Langmuir* **2014,** *30* (34), 10363-10373.

17. Yu, T.; Liu, X.; Bolcato-Bellemin, A.-L.; Wang, Y.; Liu, C.; Erbacher, P.; Qu, F.; Rocchi, P.; Behr, J.-P.; Peng, L., An Amphiphilic Dendrimer for Effective Delivery of Small Interfering RNA and Gene Silencing In Vitro and In Vivo. *Angewandte Chemie International Edition* **2012,** *51* (34), 8478-8484.

18. Hinman, S. S.; Ruiz, C. J.; Cao, Y.; Ma, M. C.; Tang, J.; Laurini, E.; Posocco, P.; Giorgio, S.; Pricl, S.; Peng, L.; Cheng, Q., Mix and Match: Coassembly of Amphiphilic Dendrimers and Phospholipids Creates Robust, Modular, and Controllable Interfaces. *ACS Applied Materials & Interfaces* **2017,** *9* (1), 1029-1035.

19. Liu, X.; Liu, C.; Zhou, J.; Chen, C.; Qu, F.; Rossi, J. J.; Rocchi, P.; Peng, L., Promoting siRNA delivery via enhanced cellular uptake using an arginine-decorated amphiphilic dendrimer. *Nanoscale* **2015,** *7* (9), 3867-3875.

20. Ya-Ting Huang, A.; Kao, C. L.; Selvaraj, A.; Peng, L., Solid-phase dendrimer synthesis: a promising approach to transform dendrimer construction. *Materials Today Chemistry* **2023,** *27*, 101285.

21. Zhang, H., Thin-Film Hydration Followed by Extrusion Method for Liposome Preparation. In *Liposomes: Methods and Protocols*, D'Souza, G. G. M., Ed. Springer New York: New York, NY, 2017; pp 17-22.

22. Xiang, B.; Cao, D.-Y. J. L.-b. d. d. s., Preparation of drug liposomes by thin-film hydration and homogenization. **2021**, 25-35.

23. Schindelin, J.; Arganda-Carreras, I.; Frise, E.; Kaynig, V.; Longair, M.; Pietzsch, T.; Preibisch, S.; Rueden, C.; Saalfeld, S.; Schmid, B.; Tinevez, J.-Y.; White, D. J.; Hartenstein, V.; Eliceiri, K.; Tomancak, P.; Cardona, A., Fiji: an open-source platform for biological-image analysis. *Nature Methods* **2012,** *9* (7), 676-682.

24. Axelrod, D.; Koppel, D. E.; Schlessinger, J.; Elson, E.; Webb, W. W., Mobility measurement by analysis of fluorescence photobleaching recovery kinetics. *Biophys J* **1976,** *16* (9), 1055-69.

25. Abouhajar, F.; Chaudhuri, R.; Valiulis, S. N.; Stuart, D. D.; Malinick, A. S.; Xue, M.; Cheng, Q., Label-Free Analysis of Binding and Inhibition of SARS-Cov-19 Spike Proteins to ACE2 Receptor with ACE2-Derived Peptides by Surface Plasmon Resonance. *ACS Applied Bio Materials* **2023,** *6* (1), 182-190.

26. Lentz, B. R.; Lee, J., Poly(ethylene glycol) (PEG)-mediated fusion between pure lipid bilayers: a mechanism in common with viral fusion and secretory vesicle release? (Review). *Molecular Membrane Biology* **1999,** *16* (4), 279-296.

27. Chauhan, A. S. Dendrimers for Drug Delivery *Molecules* [Online], 2018.

28. Li, L.; Vorobyov, I.; Allen, T. W., The Different Interactions of Lysine and Arginine Side Chains with Lipid Membranes. *The Journal of Physical Chemistry B* **2013,** *117* (40), 11906-11920.

29. Schmidt, N.; Mishra, A.; Lai, G. H.; Wong, G. C. L., Arginine-rich cell-penetrating peptides. *FEBS Letters* **2010,** *584* (9), 1806-1813.

30. Futaki, S.; Nakase, I.; Tadokoro, A.; Takeuchi, T.; Jones, A. T., Arginine-rich peptides and their internalization mechanisms. *Biochemical Society transactions* **2007,** *35* (Pt 4), 784-7.

31. Gooran, N.; Yoon, B. K.; Jackman, J. A. Supported Lipid Bilayer Platform for Characterizing the Membrane-Disruptive Behaviors of Triton X-100 and Potential Detergent Replacements *International Journal of Molecular Sciences* [Online], 2022.

Chapter 3: Charged Biomimetic Lipid Membranes for Highly Effective Antifouling against Clinically Relevant Matrices in Biosensing

3.1 Introduction

Analysis of biomarkers in complex biological media is an important step for tracking human disease states, drug effectiveness, toxicant exposure, and overall patient health. A number of biosensors have been developed for this important application[1, 2], but they mostly face a considerable technical issue, which is to effectively separate signals from biomarkers of interest and the signal caused by nonspecific interactions from the plethora of other biological molecules. Many biological molecules in clinically relevant fluids (blood, saliva, cerebrospinal fluid, and nasopharyngeal swabs) notoriously nonspecifically adhere to sensor surfaces and convolute sensor signals.[3] To curtail this problem, extensive research efforts have been focused on the development of surfaces and methodologies to block, remove or correct for nonspecific interactions.[4-8] These methods generally rely on surface blocking with thiol self-assembled monolayers (SAMs)[9, 10], polymer surfaces[11], DNA structures[12], or peptides[13, 14]. Lipids, another subset of biological molecules, have also recently been found to be a reliable method for blocking nonspecific adsorption as they are a major component of inherently antifouling cell membranes.[4, 15, 16] The ability of lipids to self-assemble into bilayers allow them to be easily presented on sensor surfaces[17] and can be utilized to mimic cell surface environments in addition to the adsorption-blocking capabilities.[18] However, these surfaces are considerably underutilized despite their inherent benefits. New designs towards more effective antifouling and a better understanding of the process behind antifouling effects are clearly needed.

A variety of lipids have been utilized for constructing the sensing interface that improved the performance of biomarker analysis in serum[4] and blood[19,20]. Zwitterionic polymers have been broadly used due to lack of strong charge that is often considered an advantage in antifouling.[21, 22] As such, zwitterionic lipids have been viewed as an ideal starting point for lipid membrane-based antifouling.[19] However, the role charged lipids play in nonspecific interactions appears to be complex. On certain surfaces, zwitterionic lipid bilayer are found to be far less effective.[4] On the other hand, charged lipids have not been fully explored for their potential in antifouling, despite many of which play important roles in cellular membranes.[23-25] Until recently there were no reports using a charged lipid membrane interface for sensing application with biological matrices where reduced background was noticed. However, we recently demonstrated that positively charged ethyl phosphocholine (EPC) lipid membrane showed better antifouling property than zwitterionic lipids in protein detection on a Protein A substrate in undiluted serum.[4] Though the process behind the antifouling properties of EPC and the EPC lipid system was not fully understood.

In this work, we further characterized the positively charged EPC lipid membrane and sought to identify key factors that determined the antifouling behavior in human serum (Figure 3.1). A number of techniques, including SPR, FRAP, and MALDI-TOF-MS, were utilized to provide molecular level understanding of the membrane properties, especially those on a Protein A substrate. Zwitterionic POPC lipid, a standard lipid molecule broadly used for antifouling purposes, will be employed for comparison. POPC appears to demonstrate effective antifouling capabilities on certain surfaces, such as glass and

calcinated Au substrates[15], but functions less effectively on a protein-modified surface. Negatively charged lipids, on the other hand, proved difficult to even form into a membrane system on Protein A and silica surfaces, let alone the surface antifouling effect. The study

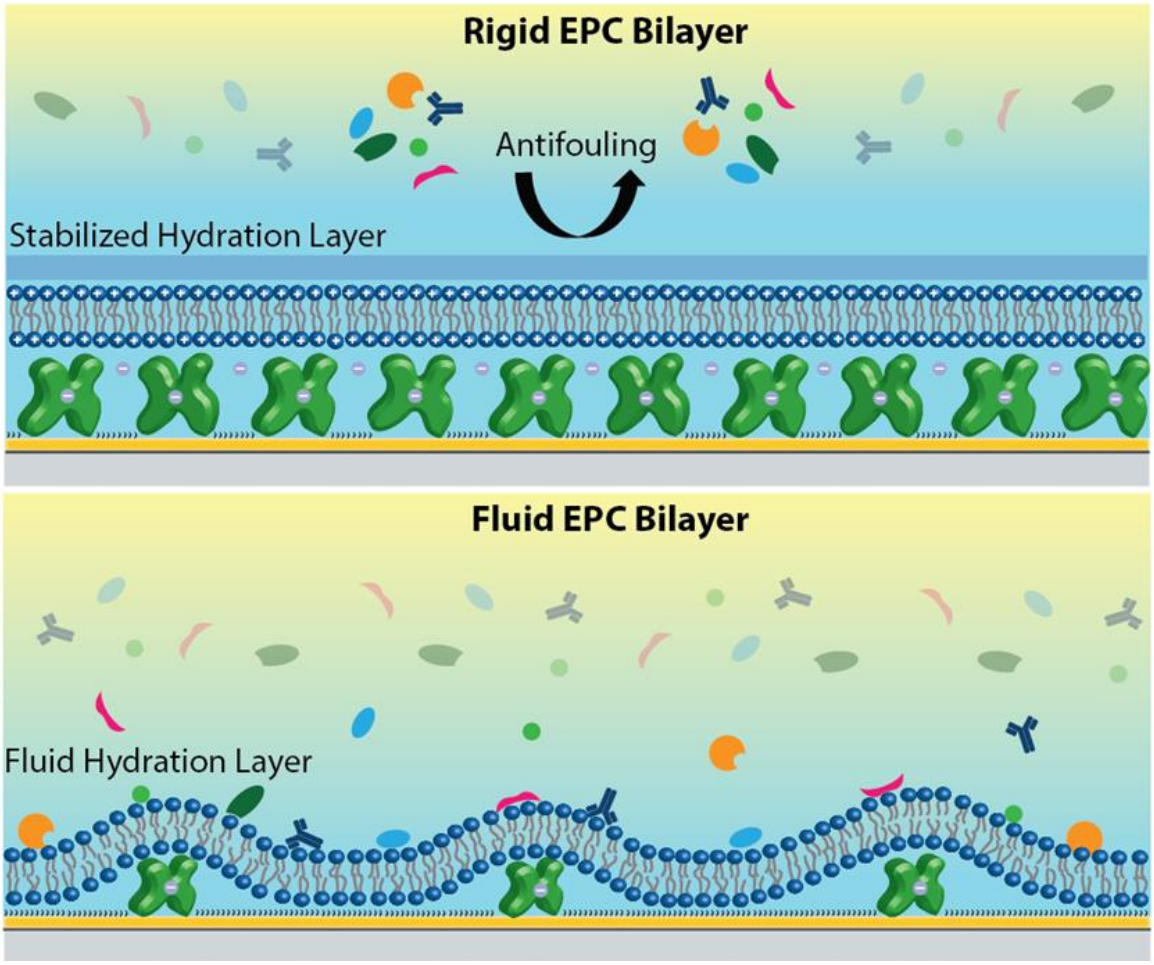

Figure 3.1. Antifouling differences of EPC lipid membranes on protein A scaffolds. With rigid EPC bilayers forming on high concentration protein A surfaces leading to a highly antifouling surface (top). While EPC bilayers formed on low concentration protein A surfaces were less compact, more mobile, and susceptible to non-specific serum interactions (bottom).

into the mechanisms behind the antifouling properties of EPC lipids could provide knowledge and guidance for construction and utilizing of lipid membranes to suppress nonspecific signals in biosensor research.

3.2 Experimental Methods

Materials and Reagents.

Super dihydrobenzoic acid (sDHB), acetonitrile (ACN), and trifluoroacetic acid (TFA) with purity (>99%) were purchased from Sigma Aldrich. Premium Plain BK-7 glass microscope slides and phosphate buffered saline (PBS) concentrate were purchased from Fisher Scientific. Thiolated recombinant protein A was purchased from ProteinMods. Ultrapure water (>18 MΩ cm-1) was acquired from a Barnstead E-Pure water purification system.

Lipid Vesicle Preparation.

Stocks of 1-palmitoyl-2-oleoyl-sn-glycero-3-phosphocholine (POPC; 5 mg mL^{-1}), 1,2-dioleoyl-sn-glycero-3-ethylphosphocholine (EPC; 5 mg mL^{-1}), 1-palmitoyl-2-oleoyl-sn-glycero-3-phospho-(1'-rac-glycerol) (POPG; 5 mg mL^{-1}), and 1,2-dipalmitoyl-sn-glycero-3-phosphoethanolamine-N-(7-nitro-2-1,3-benzoxadiazol-4-yl) (ammonium salt) (NBD-PE; 5 mg mL^{-1}) were obtained from Avanti Polar Lipids, then diluted in chloroform to the designated concentration and stored at −80 °C. For lipid vesicle formation, lipid stock solution was aliquoted into glass vials and dried under nitrogen forming thin lipid films which were further dried overnight in a vacuum desiccator. The dried lipids were resuspended in 1× PBS (10 mM Na_2HPO_4, 1.8 mM KH_2PO_4, 137 mM NaCl, 2.7 mM KCL, pH 7.4) to a final concentration of 1 mg mL^{-1} (above critical micelle concentration), followed by vigorous vortexing and bath sonication for 30 min to induce vesicle formation. The resulting lipid vesicles were then extruded through a polycarbonate filter (Whatman,

100 nm) to produce small unilamellar vesicles of uniform 100nm size. All lipid vesicle suspensions were stored at 4 °C and used within 1 week of preparation to ensure consistent vesicle structure and resulting membrane formation.

Fabrication of Sensor Chips.

Gold SPR chips were fabricated from BK-7 glass slides based on a previously published procedure with modification.[26] In short, glass slides were cleaned with boiling piranha solution (3:1 H_2SO_4 and 30% H_2O_2; **Caution!**) for 2 h and then rinsed with equal amounts water and absolute ethanol before drying under nitrogen. A 2-nm layer of chromium (0.5 Å s^{-1}) followed by a 48 nm layer of gold (1.0 Å s^{-1}) was deposited onto the glass slides using an electron-beam physical vapor deposition system (Temescal, Berkeley, CA) at or below 5×10^{-6} Torr. Silicated chips were fabricated through additional deposition of approximately 1-3 nm of SiO_2 via plasma enhanced chemical vapor deposition using a Unaxis Plasmatherm 790 system (Santa Clara, CA), onto previously described gold chips. All sensor chips were fabricated in a Class 100/1000 cleanroom facility (UCR Center for Nanoscale Science & Engineering). Gold sensor chips were chemically functionalized following previously disclosed methods.[4] In short, 10 μg mL^{-1} thiolated protein A and 1mM 3-mercapto-1-propanol were incubated on gold sensor chips for 2h and 1 h, respectively. Chips were then rinsed with ultrapure water, dried under nitrogen, and stored at 4 °C prior to SPR analysis.

SPR Analysis of Membrane Formation and Antifouling Properties.

SPR analysis was conducted on a NanoSPR6 instrument (NanoSPR, Addison, IL, USA) using 1× PBS as the running buffer with a flow rate of 5 mL h^{-1} (ca. 83 μL min^{-1}). Lipid deposition was carried out by injection of 1 mg mL^{-1} of 100 nm lipid vesicles, which were allowed to self-assemble into bilayers over 30 minutes of stopped flow. Following a 30 min rinse with 1× PBS, undiluted human serum was introduced and allowed to interact with the surface for 30 min with flow set to zero, followed by a final 30 min rinse with PBS.

Fluorescence Recovery after Photobleaching.

Fluorescence microscopy and bleaching images were generated on an inverted Leica TCS SP5 II confocal microscope (Leica Microsystems, Buffalo Point, IL, USA). NBD-PE lipids (2% in molar ratio) were incorporated into vesicle preparation methods to enable fluorescent visualization of lipid membranes. For fluorescent imaging an argon laser at the wavelength of 488nm was utilized to excite NBD lipid. Fluorescent emission between 500 and 600 nm was detected using a hybrid detector (HyD). Images were obtained via 3 line averaging and further 3 image averaging. FRAP images were obtained without image averaging and with laser power increased to 100% for one second bleaching. Photobleaching and monitoring of fluorescence recovery within defined regions of interest were performed using the LAS AF software package (Leica). Images were processed using ImageJ with the Fiji package and analyzed using open-source software simFRAP (available

through http://imagej.nih.gov/ij/plugins/sim-frap/index.html).[27] Mobile fractions (ß) and diffusion coefficients (D) were calculated using previously demonstrated methods.[28, 29]

Matrix Assisted Laser Desorption Ionization. Mass profiles of membrane systems before and after serum interaction were obtained with a reflectron AB-Sciex 5800 MALDI-TOF instrument operating in positive ion mode. An individual spectra is represented by m/z values versus intensity (au) obtained by an average of 200 shots collected from a small area of the chip. To enable spectra acquisition post SPR analysis air was slowly injected into the flow system to dry the chip surface leaving behind surface bound materials before removal of the chip from the SPR instrument and matrix deposition prior to MALDI analysis.

3.3 Results and Discussion:

Formation of Lipid Membranes on Functional Surfaces.

Fused EPC lipid membrane on a Protein A substrate has been identified as a unique platform to enable antibody capture and detection in serum that suppresses nonspecific interactions, improves detection limits and deconvolutes data.[4] The underlying principle of the antifouling function with a positively charged membrane, however, remains unclear. In this work we further characterized the EPC system under various conditions, aiming to elucidate how charged lipid membranes enable improvements, both in antifouling and specific sensing, on Protein A supports. We first tested the effect of varied surface charges on the formation of lipid membranes and compared membrane formation on different surfaces using SPR. The test chips were coated with protein A (10 μg mL^{-1}), followed by

passivation with MPO (1mM). Lipid vesicles of negatively charged POPG, positively charge EPC and zwitterionic POPC were introduced into the flow cell for membrane self-assembly.[4] Only positively charged EPC lipids appeared to self-assemble on the Protein A substrate, while POPG and POPC lipid vesicles did not register any binding or fusion

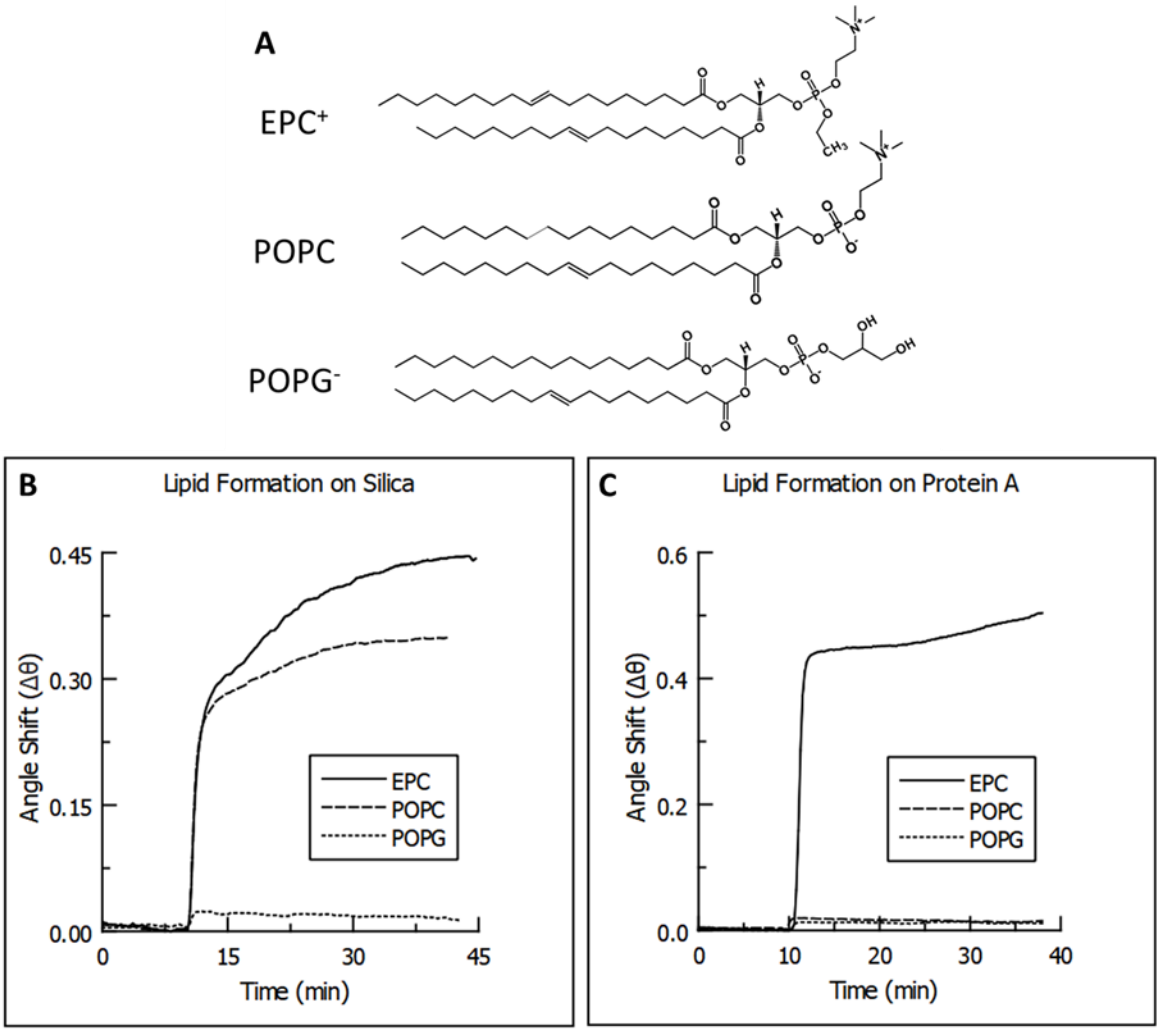

Figure 3.2. (A) Molecular structures of lipids used in this study (EPC, POPC, and POPG). (B) SPR sensorgrams of lipid vesicle adhesion and fusion to form solid supported lipid bilayer systems on silica and protein A of EPC (blue and purple), POPC (grey and orange), and POPG (green and red) respectively.

(Figure 3.2.). The observed response patterns seemed unique, and a possible scenario of electrostatic repulsion or minimal vesicle adhesion without rupture could be proposed as

the cause.[30] It is known that Protein A is negatively charged in the buffer condition used here (pH 7.4) from a theoretical isoelectronic point of 5.4.[31] However, the complete shutoff of POPC lipid vesicles is puzzling. The role of Protein A on membrane formation appears to be more complex than initially believed. We further tested vesicle fusion using silica substrates as they are known to promote self-assembly of lipid membranes.[17] For this comparison work, we utilized calcinated gold chips with SPR that were previously developed in our lab.[32] Figure 3.2B shows that POPC and EPC quickly formed robust membranes, which agrees well with literature reports.[33] There were some differences in signal magnitude for different vesicles, with EPC lipid vesicles producing a greater angular shift ($\Delta\theta = 0.445°$) as compared to POPC vesicles ($\Delta\theta = 0.350°$) (Figure 3.2B). Negatively charged POPG vesicles, however, showed minimal interaction with the calcinated substrates ($\Delta\theta = 0.024°$), likely due to the negative charge of the silica surface in PBS buffer.[34] The observation of positively charged EPC showing favorable interaction with the silica surface provides some explanation about the difference in signal between EPC and POPC lipids. Strong charge interactions constrain EPC lipid vesicles closer to the sensor surface, enabling a better packing of the EPC membrane. Zwitterionic POPC also demonstrates prolific membrane formation on a silica surface, as have been broadly reported.[35-37] The signal was slightly smaller than EPC, indicative of a less tightly packed structure. It is interesting to note that EPC lipids formed on a protein A substrate had a higher angular shift than on the silica surface ($\Delta\theta = 0.576°$), providing further evidence that EPC lipids interact more strongly with the charged Protein A substrates and the impact

of charge density and lipid packaging density play important roles in the interaction and resulting antifouling properties.

Fluorescence microscopy was utilized to characterize the distribution and mobility of EPC and POPC lipid species on the two surfaces. Glass slides and Protein A coated gold chips were prepared in a similar fashion and fitted into a PMDS housing to provide a defined area for vesicle incubation. 2 mol % of NBD-PE was incorporated into the membrane systems to enable fluorescent visualization. To address the concern of fluorescent quenching on gold surfaces, which could limit fluorescent imaging on these chips[38], we first tested if fluorescent signal was impacted on the 50 nm thick gold substrates. We didn't observe any substantial quenching or signal complications, likely thanks to the increased distance of the fluorophores from the gold substrate, separated by the Protein A scaffold. Distance from the gold has been shown to be an important component of gold quenching mechanisms.[38] EPC and POPC distribution on the silica substrate was uniform with no visible, uncovered areas. For comparison, EPC coverage on the Protein A surface was complete while POPC was only sparsely distributed. Mobility measurement by FRAP further separated these lipid surfaces where significant differences were observed. EPC lipids on the Protein A sensor presented a complete lack of lateral mobility while both EPC and POPC demonstrated decent mobility on the silica surface. POPC lipids showed a measured mobility with $D = 2.87 \pm 0.25\ \mu m^2/s$, which is consistent with literature reports,[39] whereas EPC had rather reduced mobility values ($1.89 \pm 0.19\ \mu m^2/s$). These differences fit well into a charge-based model in which increased electrostatic charge plays a larger role in positively charged EPC with negatively charged

silica as compared to zwitterionic POPC lipids thus limiting lipid lateral movement. As POPC vesicles did not fuse onto the Protein A surface, they therefore did not have measurable diffusivity.

Antifouling Properties of Lipid Bilayers.

We then used SPR to quantify the changes upon injection of serum to further characterize the antifouling properties of the lipid membranes. Lipid membranes of POPC, EPC, and POPG were formulated as previously described, and were allowed to interact with serum over a 30-minute period before a final rinse step was performed. Figure 3.3 C and D show the signals as a result of the bulk refractive index change at the interface brought about by the binding of biological molecules in serum. After PBS washing, the bulk signal changed and was replaced in the sensorgram by remaining molecules attributing to the non-specific binding, which was used for quantifying the extent of surface fouling. For membranes where the SPR signal returned to pre-serum levels, the outcome indicated that little to no interaction between the surface and molecules in serum occurred during the incubation and the surface would be thus deemed “effective antifouling”. This property was clearly observed for EPC on a protein A surface and POPC on a silica surface. Other surfaces were observed with substantial remaining signal, which were designated high levels of surface fouling, as seen on the bare chip surfaces and those where lipid membranes did not form.

From SPR surface fouling tests, it is apparent that the Protein A sensor has much more nonspecific interactions than silica substrates. The angular shift remained high after

rinse (0.630 ± 0.042°) while the silica substrate only showed half of the shift (0.383 ± 0.045°). This nearly two-fold higher nonspecific signal demonstrates that nonspecific interactions can severely impair biosensor performance if surface fouling is not effectively addressed. From the results, two substrates with lipid membrane coating stand out: EPC lipids on the Protein A surface and POPC lipids on the silica substrate, with observed angular shifts at -0.095 ± 0.048° and 0.014 ± 0.009°, respectively. The negative values on

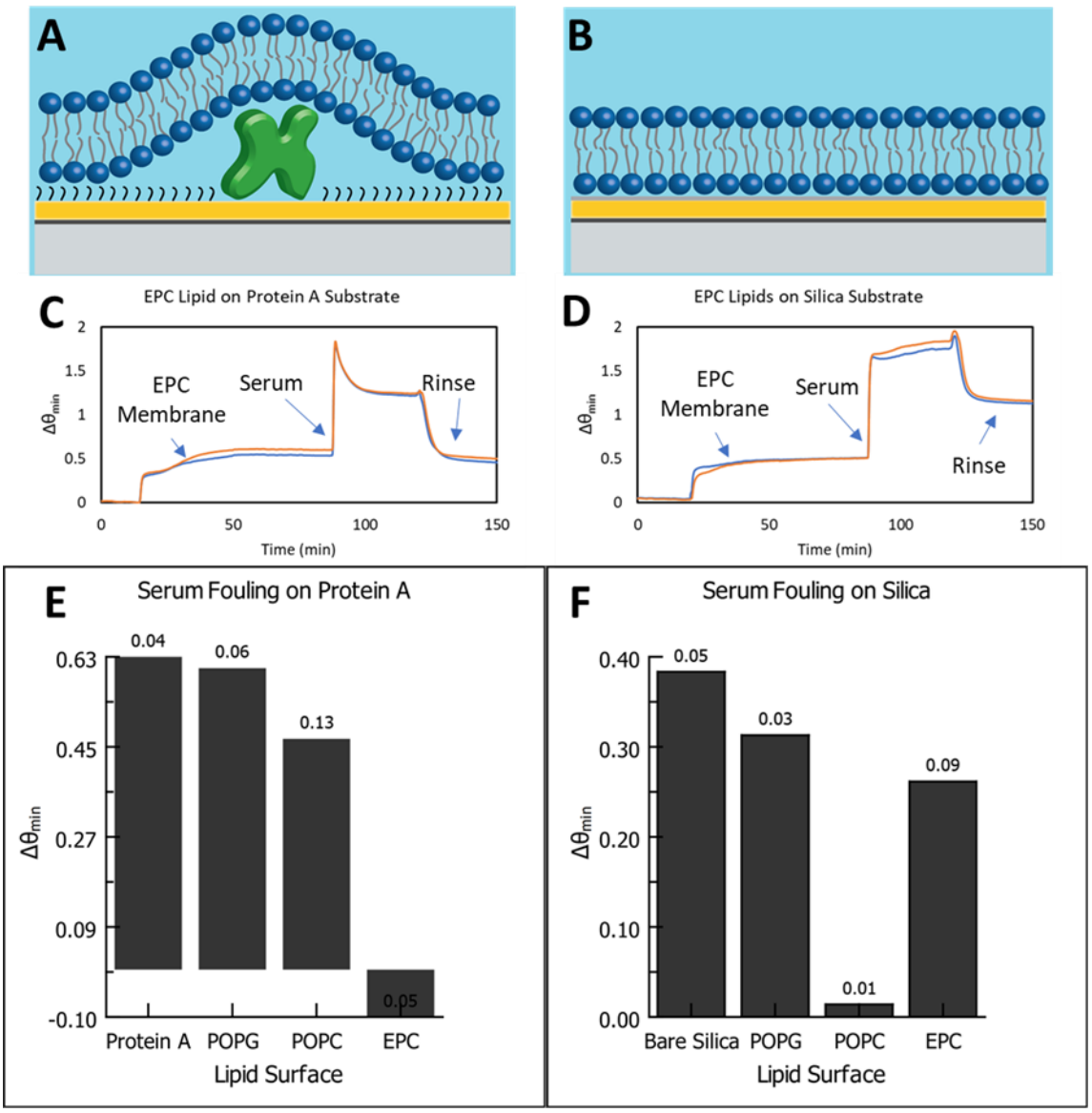

Figure 3.3. Representation of EPC lipid membranes on (A) protein A and (B) silica substrates. (C) SPR sensorgram of serum antifouling effects of EPC on a protein A surface. (D) SPR sensorgram of serum fouling an EPC membrane on a silica substrate. (E) Resulting SPR angular shifts of serum nonspecific interactions on the surfaces of bare silica and a protein A formulation (left most columns). The three other columns represent serum nonspecific binding to lipid membranes (POPG, POPC, and EPC) formed on top of silica (front) or protein A (back).

the Protein A/EPC surface raised questions about whether the lipids were displaced by or exchanged with serum proteins. Therefore, we employed a series of methods including

fluorescent microscopy, FRAP and mass spectrometry to further investigate the surface properties after serum incubation.

It should be mentioned that the POPC and POPG membranes tested in this work showed considerable nonspecific signal, suggesting that a variety of non-specific interactions had occurred between the sensor substrate and biomolecules in serum. Thus, these surfaces would perform poorly for sensor development. However, there is some variation in the extent of fouling among those ineffective surfaces, which may provide some clue on how these surfaces could be improved. POPC lipid vesicles on the Protein A surface, previously mentioned only sparsely adhered to the sensor surface, did provide a lower nonspecific adsorption, with remaining angular shift observed at 0.465 ± 0.130°, which is ~27% less than the noncoated, bare Protein A sensor. The relatively high values match the observed surface condition as only being limitedly covered, suggesting that should mechanisms to induce POPC vesicle fusion on this surface be developed it could prove to be effectively antifouling, as even the small amount of POPC lipids attached were able to reduce the signal from nonspecific interactions. Several approaches such as amphipathic peptide induced fusion[40] and solvent/buffer assisted fusion[41] have been shown to promote lipid coverage. Their effectiveness for POPC on protein A surface remains to be tested. Nevertheless, we showed lipid membranes can be formulated to match surface property of the sensor chips for optimal antifouling results. The highly effective Protein A EPC antifouling system presents the most promising surface in blocking fouling and thus was further investigated to understand what key factors are behind the antifouling properties.

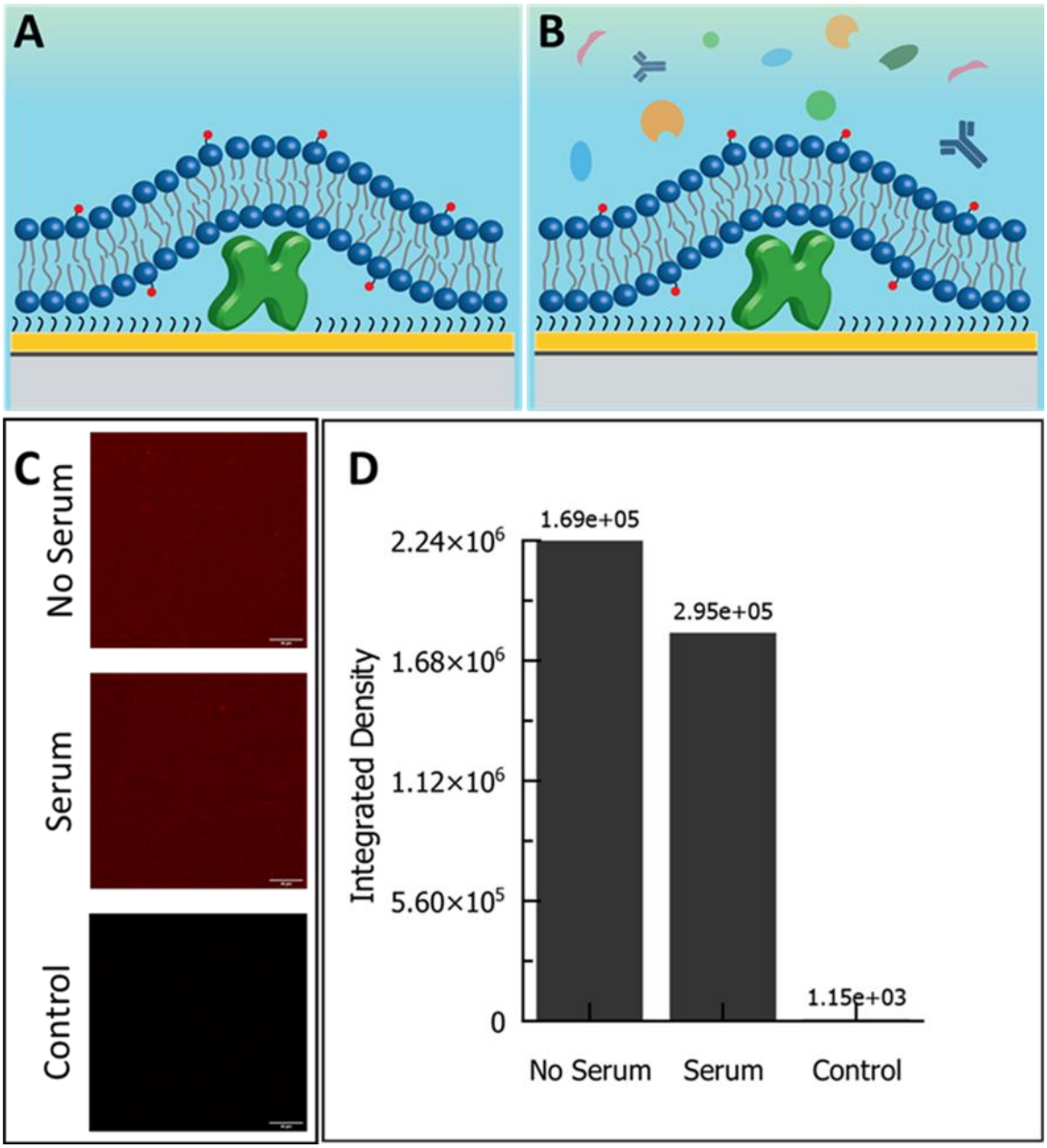

Figure 3.4. Cartoon representation of fluorescently labeled lipid surface on protein A (A) without serum introduction and (B) with serum incubation. Neither showing a significant change in lipid structure. (C) Fluorescent images of EPC lipid surfaces on a protein A scaffold before serum fouling (left), after serum fouling (middle) and without fluorophore labeled lipids (right), as a control. With scale bars set to 40 μm. (D) Integrated density of displayed fluorescent images with error bars calculated based on triplicate results.

Probing Factors behind EPC Antifouling Properties on Protein A Surface.

As previously mentioned, a reduction in signal following serum incubation on the EPC coated Protein A surface was observed. To confirm that EPC lipid membranes remained intact and were not damaged by serum we performed fluorescent microscopic studies to evaluate surface coverage and mobility before and after serum introduction. Protein A/EPC chips with 2% NBD-PE were prepared as with the SPR experiments and were characterized for lipid coverage and bleaching/recovery tracking. Chips without serum incubation were compared to identify differences in coverage and density. Figure

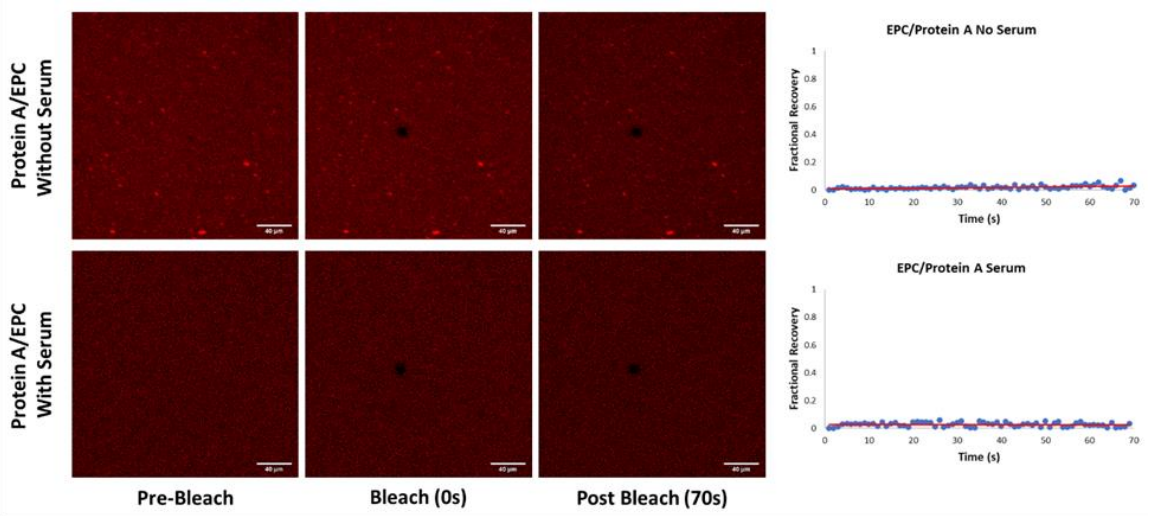

Figure 3.5. FRAP results displaying EPC membranes on protein A surfaces before (top) and after (bottom) serum fouling interactions. Time points showing before the bleach (left column), immediately after bleach (middle column), and 70 seconds after bleaching (right column). Resulting fractional recovery rates are displayed on the far right.

3.4 shows that serum incubation resulted in a small decrease in fluorescent intensity, likely due to the extra washing steps associated with the removal steps. However, the difference was small and complete fluorescent coverage was observed across the whole lipid membrane surface, indicating the membrane remained intact following serum incubation. The result matches well with SPR study that exhibited a small signal reduction following

serum wash off. We speculate the minor signal loss is due to small amounts of lipid debris separating from the surface while the overall membrane structure remains intact. The high stability of the EPC membrane on Protein A in serum is one important factor in abrogating serum fouling. Control study with bare Protein A surface indicated that no fluorescent signal was observed from Protein A or serum, confirming that the lipid membranes were the only source of fluorescent signal. FRAP analysis was performed on both substrates and similar non-recovery behavior was observed (Figure 3.5.). The fractional recovery curve remained flat, suggesting very little lateral diffusion on these surfaces and no change in membrane properties following serum introduction.

MALDI-MS characterization of the sensor chips following SPR analysis was performed to identify molecular constituents on the surface. Sensor chips were removed from the SPR instrument, dried, and spotted with MALDI matrix (sDHB). As can be seen

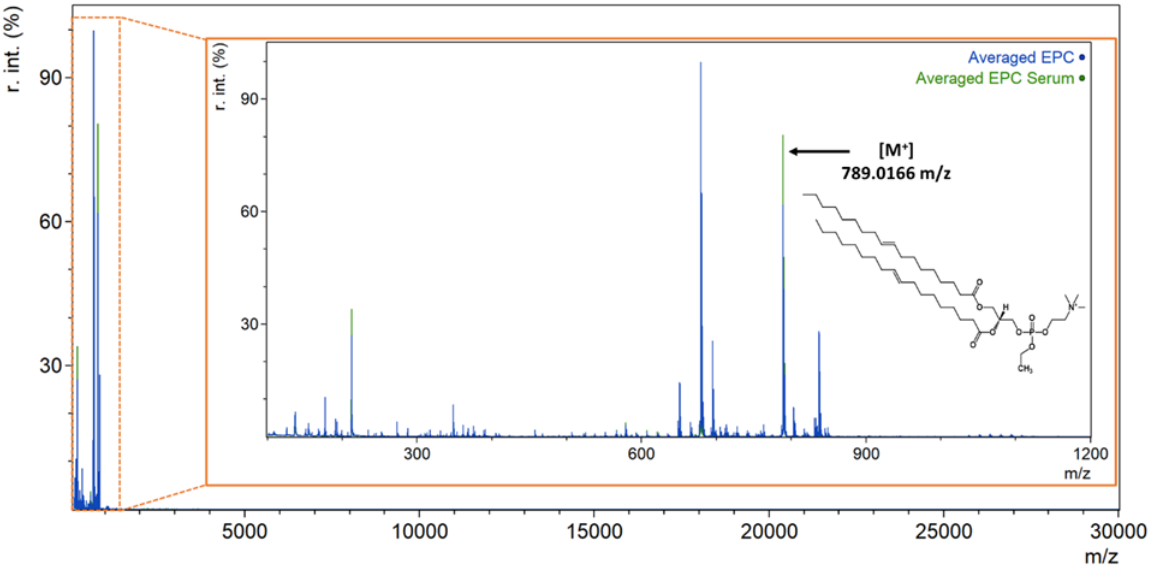

Figure 3.6. (A) Average of 30 MALDI-MS spectra in positive ion mode for an EPC lipid membrane on a protein A surface (blue) and after serum incubation (green) with ions out to 30000 m/z collected. No peaks were identifiable beyond 1200 m/z and EPC lipids were identified at 789.01 m/z as a molecular ion as shown in inset (B).

in Figure 3.6, no peaks for the Protein A chip were detected above noise beyond 3000 m/z; with vast majority appearing below 1200 m/z. Protein A is a 49-kDa protein and a large scan beyond 50,000 m/z was performed to determine if whole Protein A would be ionized. However, no such peaks were observed, likely due to covalent linkage of Protein A to the sensor surface and MALDI's soft ionization meaning fragmentation is rare.[42] Below 1200 m/z range, there was clear signals for EPC lipids, identified at 789.01 m/z appearing in both samples. This matches with MALDI spectra for an EPC standard. As such, it is clear that EPC lipids remained on the sensor surface in large quantity following serum incubation. The overlapped spectra also exhibit no peaks only seen in the serum treated sample, additionally demonstrating that no serum molecules remain nonspecifically interacted with the sensor surface. From the MALDI-MS results, EPC lipid membranes appeared to be very stable on the Protein A surface, exhibiting exceptionally effective function at blocking serum fouling on the surface.

Understanding Potential Antifouling Processes of the EPC Protein A Surface.

With the antifouling effectiveness of EPC lipid membranes on Protein A scaffolds successfully being demonstrated we turned towards understanding how and why this surface was effective. Previous results indicated that strong interaction between the sensor surface and EPC lipids occurs, generating robust SPR signal with diminishing lateral mobility. But how these interactions resulted in such an antifouling surface was elusive. We first tested the effect of Protein A density on lipid membrane formation and property. Sensor chips prepared with varied Protein A concentrations (1 μg mL^{-1}, 100 ng mL^{-1}, and 1 ng mL^{-1}) in the incubation step were fabricated, yielding surfaces with a more disperse

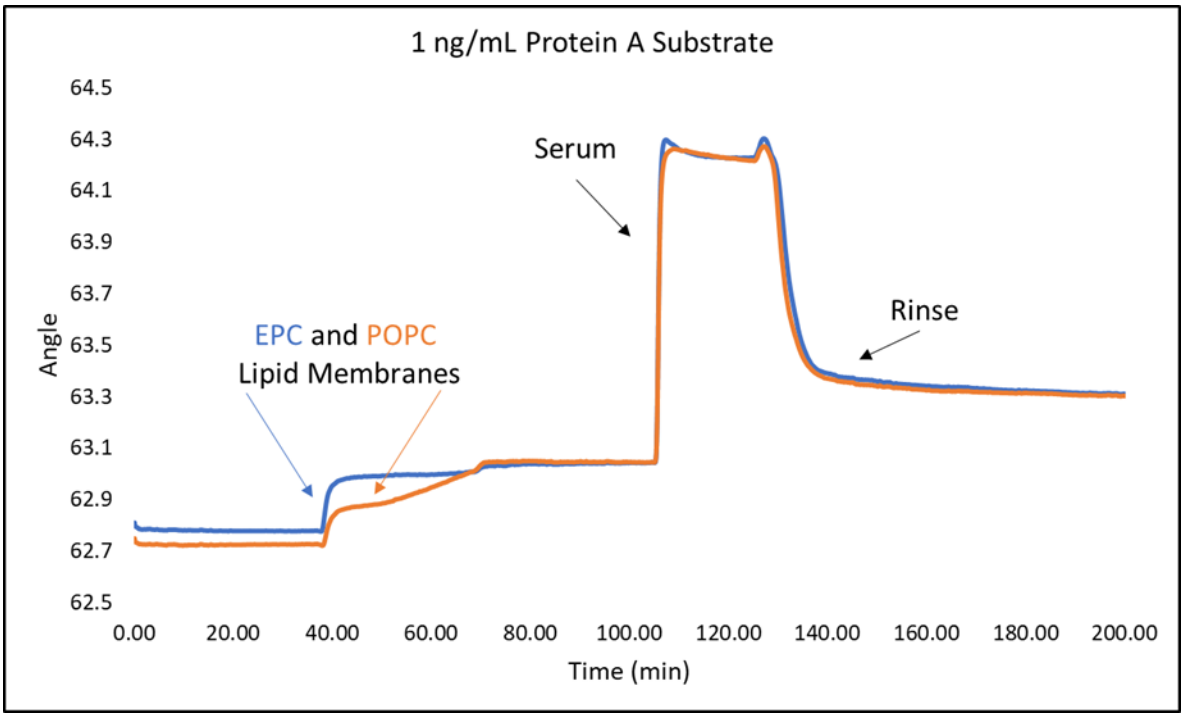

Figure 3.7. Formation and antifouling performance of EPC and POPC lipid membranes on a low concentration (1 ng/mL) protein A substrate. Showing loss of EPC antifouling properties and improved formation of POPC lipid membrane when compared to higher concentration protein A surfaces.

protein distribution. SPR sensorgrams demonstrated significant differences in membrane formation and antifouling properties. Lowering Protein A concentration led to a loss of blocking function towards nonspecific interactions from serum by the EPC lipids on top of it (Figure 3.7). On the other hand, POPC membranes started to steadily form on the sensor surface when concentration of protein A was decreased.

FRAP analysis of EPC membranes formed on these protein A surfaces provided additional information about the mobility changes in the membrane. As Protein A concentration increased, a decrease in lipid fluidity was observed, with a complete loss of fluidity observed at 10 μg mL^{-1} (Figure 3.8). Diffusion coefficient measurement indicates the value decreased by 0.08 $\mu m^2/s$ with concentration increased from 1 to 100 ng mL^{-1},

while a loss of 0.12 $\mu m^2/s$ was determined with the concentration increased from 100 ng mL^{-1} to 1 μg mL^{-1}. Clearly the density of Protein A has a large impact on the formation

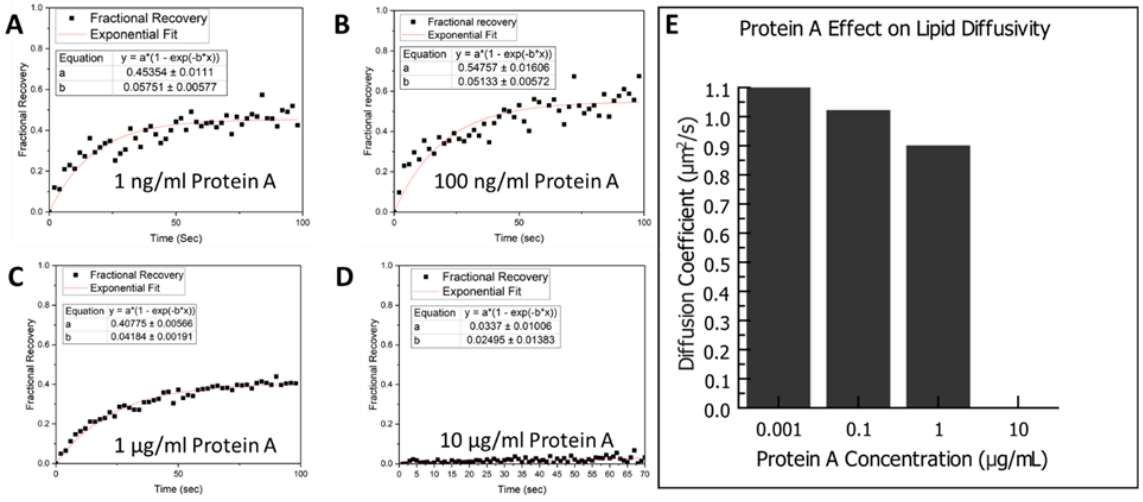

Figure 3.8. Lipid diffusivity changes due to sensor protein A concentration. (A-D) Fractional recovery curves and exponential fits used to calculate lipid diffusivity for EPC lipids formulated on increasing concentrations of protein A sensor chips (1ng/ml, 100 ng/ml, 1 μg/ml, and 10 μg/ml) respectively. (E) Resulting diffusion coefficients obtained from FRAP recovery curve fitting.

and the mobility of EPC lipids. We speculate that the low mobility of the EPC membrane may be a necessary factor for the surface to remain stable in serum and act as an effective antifouling substrate.

While surface charge has been established to play a role in the formation of EPC membrane and the antifouling properties, another factor could be the hydration layer formed above the lipid surface. The highly charged gel phase of EPC lipid has a strong coupling with the interfacial hydration layer, increasing the energy required for proteins to undergo conformational changes that would lead to irreversible nonspecific binding.[43] The scenario is similar to an aluminum oxide surface that proves to be highly antifouling[44] due to the thicker hydration layer, [45] resulting from strong coupling between the positively

charged aluminum oxide and water layer.[46] Furthermore, the EPC terminal phosphocholine group likely plays a large role due to its ability to form multiple hydrogen bonds to water molecules.[47] Recently phosphate groups, despite lacking zwitterionic properties, have been demonstrated to impart antifouling properties due to their strong hydrophilicity.[48] Indicating that zwitterionic charge is not necessary for antifouling and that the hydrophilicity or hydrophobicity of a substrate likely plays a large role in antifouling effectiveness. This explains why EPC antifouling properties are completely lost upon decreasing protein A concentration and the EPC bilayer becomes more fluid and dispersed.

3.4 Conclusion:

We have reported the characterization of membrane formation of differently charged lipids, including POPC, EPC, and POPG on Protein A surface and their respective antifouling properties. POPC and EPC membranes were found to effectively form antifouling substrates against whole human serum. Various formation conditions have been explored and the importance of charge interactions with the underlying surface is found to play a pivotal role in whether antifouling properties are observed. Notably POPC on a silica surface and EPC on a Protein A surface demonstrate highly effective antifouling properties. EPC lipid surfaces were confirmed to remain intact and can block serum molecules from adhering to the surface through robust bilayer formation, electrical repulsion, and formation of a hydration layer. At higher Protein A concentrations EPC lipid membranes are robust therefore antifouling relies on a strong interaction between Protein A and EPC that severely limits lipid mobility. High concentrations of Protein A are required for presenting a high charge density on the surface, leading to a rigid layer with a stable

hydration layer that limits the ability of proteins to irreversibly bind. These results underpin the importance of lipid and surface charges in enabling effective antifouling function as they were only effective with a compatible sensor surface. As such, lipid surfaces show incredible promise in enabling sensing of biological targets in complex media but must be properly incorporated into the sensor development process to account for surface charge and binding effects that play a crucial role in the formation and effectiveness of antifouling lipid surfaces.

3.5 References:

1. Ouyang, M.; Tu, D.; Tong, L.; Sarwar, M.; Bhimaraj, A.; Li, C.; Cote, G. L.; Di Carlo, D., A review of biosensor technologies for blood biomarkers toward monitoring cardiovascular diseases at the point-of-care. Biosens Bioelectron 2021, 171, 112621.

2. Azzouz, A.; Hejji, L.; Kim, K. H.; Kukkar, D.; Souhail, B.; Bhardwaj, N.; Brown, R. J. C.; Zhang, W., Advances in surface plasmon resonance-based biosensor technologies for cancer biomarker detection. Biosens Bioelectron 2022, 197, 113767.

3. Frutiger, A.; Tanno, A.; Hwu, S.; Tiefenauer, R. F.; Voros, J.; Nakatsuka, N., Nonspecific Binding-Fundamental Concepts and Consequences for Biosensing Applications. Chem Rev 2021, 121 (13), 8095-8160.

4. McKeating, K. S.; Hinman, S. S.; Rais, N. A.; Zhou, Z.; Cheng, Q., Antifouling Lipid Membranes over Protein A for Orientation-Controlled Immunosensing in Undiluted Serum and Plasma. ACS Sens 2019, 4 (7), 1774-1782.

5. Malinick, A. S.; Lambert, A. S.; Stuart, D. D.; Li, B.; Puente, E.; Cheng, Q., Detection of Multiple Sclerosis Biomarkers in Serum by Ganglioside Microarrays and Surface Plasmon Resonance Imaging. ACS Sens 2020, 5 (11), 3617-3626.

6. Jiang, C.; Wang, G.; Hein, R.; Liu, N.; Luo, X.; Davis, J. J., Antifouling Strategies for Selective In Vitro and In Vivo Sensing. Chem Rev 2020, 120 (8), 3852-3889.

7. D'Agata, R.; Bellassai, N.; Jungbluth, V.; Spoto, G., Recent Advances in Antifouling Materials for Surface Plasmon Resonance Biosensing in Clinical Diagnostics and Food Safety. Polymers (Basel) 2021, 13 (12).

8. Malinick, A. S.; Stuart, D. D.; Lambert, A. S.; Cheng, Q., Surface plasmon resonance imaging (SPRi) in combination with machine learning for microarray analysis of multiple sclerosis biomarkers in whole serum. Biosensors and Bioelectronics: X 2022, 10.

9. Wang, Y. S.; Yau, S.; Chau, L. K.; Mohamed, A.; Huang, C. J., Functional Biointerfaces Based on Mixed Zwitterionic Self-Assembled Monolayers for Biosensing Applications. Langmuir 2019, 35 (5), 1652-1661.

10. Duanghathaipornsuk, S.; Reaver, N. G. F.; Cameron, B. D.; Kim, D. S., Adsorption Kinetics of Glycated Hemoglobin on Aptamer Microarrays with Antifouling Surface Modification. Langmuir 2021, 37 (15), 4647-4657.

11. Dedisch, S.; Obstals, F.; los Santos Pereira, A.; Bruns, M.; Jakob, F.; Schwaneberg, U.; Rodriguez-Emmenegger, C., Turning a Killing Mechanism into an Adhesion and Antifouling Advantage. Advanced Materials Interfaces 2019, 6 (18).

12. Nie, W.; Wang, Q.; Zou, L.; Zheng, Y.; Liu, X.; Yang, X.; Wang, K., Low-Fouling Surface Plasmon Resonance Sensor for Highly Sensitive Detection of MicroRNA in a Complex Matrix Based on the DNA Tetrahedron. Anal Chem 2018, 90 (21), 12584-12591.

13. Olivier R. Bolduc, J. N. P., †,‡ and Jean-Franc¸ ois Masson, SPR Biosensing in Crude Serum Using Ultralow Fouling Binary Patterned Peptide SAM. Analytical Chemistry 2010, 82, 3699–3706.

14. Mao, Z.; Zhao, J.; Chen, J.; Hu, X.; Koh, K.; Chen, H., A simple and direct SPR platform combining three-in-one multifunctional peptides for ultra-sensitive detection of PD-L1 exosomes. Sensors and Actuators B: Chemical 2021, 346.

15. Sut, T. N.; Yoon, B. K.; Jeon, W.-Y.; Jackman, J. A.; Cho, N.-J., Supported lipid bilayer coatings: Fabrication, bioconjugation, and diagnostic applications. Applied Materials Today 2021, 25.

16. Jiang, X.; Zhu, Q.; Zhu, H.; Zhu, Z.; Miao, X., Antifouling lipid membrane coupled with silver nanoparticles for electrochemical detection of nucleic acids in biological fluids. Anal Chim Acta 2021, 1177, 338751.

17. Jackman, J. A.; Cho, N. J., Supported Lipid Bilayer Formation: Beyond Vesicle Fusion. Langmuir 2020, 36 (6), 1387-1400.

18. Luchini, A.; Vitiello, G., Mimicking the Mammalian Plasma Membrane: An Overview of Lipid Membrane Models for Biophysical Studies. Biomimetics (Basel) 2020, 6 (1).

19. Liu, Y.; Chen, D.; Zhang, W.; Zhang, Y., Mobile DNA tetrahedron on ultra-low adsorption lipid membrane for directional control of cell sensing. Sensors and Actuators B: Chemical 2020, 307.

20. Masson, J. F., Surface Plasmon Resonance Clinical Biosensors for Medical Diagnostics. ACS Sens 2017, 2 (1), 16-30.

21. Baggerman, J.; Smulders, M. M. J.; Zuilhof, H., Romantic Surfaces: A Systematic Overview of Stable, Biospecific, and Antifouling Zwitterionic Surfaces. Langmuir 2019, 35 (5), 1072-1084.

22. Asha, A. B.; Chen, Y.; Narain, R., Bioinspired dopamine and zwitterionic polymers for non-fouling surface engineering. Chem Soc Rev 2021, 50 (20), 11668-11683.

23. Klausen, L. H.; Fuhs, T.; Dong, M., Mapping surface charge density of lipid bilayers by quantitative surface conductivity microscopy. Nat Commun 2016, 7, 12447.

24. Yeung, T.; Grinstein, S., Lipid signaling and the modulation of surface charge during phagocytosis. Immunol Rev 2007, 219, 17-36.

25. Lu, S. M.; Fairn, G. D., Mesoscale organization of domains in the plasma membrane - beyond the lipid raft. Crit Rev Biochem Mol Biol 2018, 53 (2), 192-207.

26. Abbas, A.; Linman, M. J.; Cheng, Q., Patterned resonance plasmonic microarrays for high-performance SPR imaging. Anal Chem 2011, 83 (8), 3147-52.

27. Blumenthal, D.; Goldstien, L.; Edidin, M.; Gheber, L. A., Universal Approach to FRAP Analysis of Arbitrary Bleaching Patterns. Sci Rep 2015, 5, 11655.

28. D. AXELROD, D. E. K., J. SCHLESSINGER, E. ELSON, and W. W. WEBB, MOBILITY MEASUREMENT BY ANALYSIS OF FLUORESCENCE PHOTOBLEACHING RECOVERY KINETICS. BIOPHYSICAL JOURNAL 1976, 16 (9), 1055–1069.

29. Soumpasis, D. M., Theoretical analysis of fluorescence photobleaching recovery experiments. Biophys J 1983, 41 (1), 95-7.

30. Kurniawan, J.; Ventrici de Souza, J. F.; Dang, A. T.; Liu, G. Y.; Kuhl, T. L., Preparation and Characterization of Solid-Supported Lipid Bilayers Formed by Langmuir-Blodgett Deposition: A Tutorial. Langmuir 2018, 34 (51), 15622-15639.

31. Kozlowski, L. P., IPC 2.0: prediction of isoelectric point and pKa dissociation constants. Nucleic Acids Res 2021, 49 (W1), W285-W292.

32. Phillips, K. S.; Wilkop, T.; Wu, J. J.; Al-Kaysi, R. O.; Cheng, Q., Surface plasmon resonance imaging analysis of protein-receptor binding in supported membrane arrays on gold substrates with calcinated silicate films. J Am Chem Soc 2006, 128 (30), 9590-9591.

33. Ferhan, A. R.; Jackman, J. A.; Cho, N. J., Probing Spatial Proximity of Supported Lipid Bilayers to Silica Surfaces by Localized Surface Plasmon Resonance Sensing. Anal Chem 2017, 89 (7), 4301-4308.

34. Anderson, T. H.; Min, Y.; Weirich, K. L.; Zeng, H.; Fygenson, D.; Israelachvili, J. N., Formation of supported bilayers on silica substrates. Langmuir 2009, 25 (12), 6997-7005.

35. Li, H.; Dauphin-Ducharme, P.; Arroyo-Curras, N.; Tran, C. H.; Vieira, P. A.; Li, S.; Shin, C.; Somerson, J.; Kippin, T. E.; Plaxco, K. W., A Biomimetic Phosphatidylcholine-Terminated Monolayer Greatly Improves the In Vivo Performance of Electrochemical Aptamer-Based Sensors. Angew Chem Int Ed Engl 2017, 56 (26), 7492-7495.

36. Cho, N. J.; Frank, C. W.; Kasemo, B.; Hook, F., Quartz crystal microbalance with dissipation monitoring of supported lipid bilayers on various substrates. Nat Protoc 2010, 5 (6), 1096-106.

37. Tamm, L. K.; Mcconnell, H. M., Supported Phospholipid-Bilayers. Biophysical Journal 1985, 47 (1), 105-113.

38. Su, Q.; Jiang, C.; Gou, D.; Long, Y., Surface Plasmon-Assisted Fluorescence Enhancing and Quenching: From Theory to Application. ACS Appl Bio Mater 2021, 4 (6), 4684-4705.

39. Farell, M.; Wetherington, M.; Shankla, M.; Chae, I.; Subramanian, S.; Kim, S. H.; Aksimentiev, A.; Robinson, J.; Kumar, M., Characterization of the Lipid Structure and Fluidity of Lipid Membranes on Epitaxial Graphene and Their Correlation to Graphene Features. Langmuir 2019, 35 (13), 4726-4735.

40. Cho, N. J.; Cho, S. J.; Cheong, K. H.; Glenn, J. S.; Frank, C. W., Employing an amphipathic viral peptide to create a lipid bilayer on Au and TiO2. J Am Chem Soc 2007, 129 (33), 10050-1.

41. Tabaei, S. R.; Choi, J. H.; Haw Zan, G.; Zhdanov, V. P.; Cho, N. J., Solvent-assisted lipid bilayer formation on silicon dioxide and gold. Langmuir 2014, 30 (34), 10363-73.

42. Hosseini, S., Martinez-Chapa, S.O., Principles and Mechanism of MALDI-ToF-MS Analysis. In: Fundamentals of MALDI-ToF-MS Analysis. SpringerBriefs in Applied Sciences and Technology 2017, 1-19.

43. Roach, P.; Farrar, D.; Perry, C. C., Interpretation of protein adsorption: Surface-induced conformational changes. J Am Chem Soc 2005, 127 (22), 8168-8173.

44. Lambert, A. S.; Valiulis, S. N.; Malinick, A. S.; Tanabe, I.; Cheng, Q., Plasmonic Biosensing with Aluminum Thin Films under the Kretschmann Configuration. Anal Chem 2020, 92 (13), 8654-8659.

45. Jackman, J. A.; Tabaei, S. R.; Zhao, Z.; Yorulmaz, S.; Cho, N. J., Self-assembly formation of lipid bilayer coatings on bare aluminum oxide: overcoming the force of interfacial water. ACS Appl Mater Interfaces 2015, 7 (1), 959-68.

46. van Weerd, J.; Karperien, M.; Jonkheijm, P., Supported Lipid Bilayers for the Generation of Dynamic Cell-Material Interfaces. Adv Healthc Mater 2015, 4 (18), 2743-79.

47. Marta Pasenkiewicz-Gierula, Y. T., Hiroo Miyagawa, Kunihiro Kitamura, and Akihiro Kusum, Hydrogen Bonding of Water to Phosphatidylcholine in the Membrane As Studied by a Molecular Dynamics Simulation: Location, Geometry, and Lipid-Lipid Bridging via Hydrogen-Bonded Water. J. Phys. Chem. A 1997, 101, 3677-3691.

48. Qiao, X.; Qian, Z. H.; Sun, W.; Zhu, C. Y.; Li, Y.; Luo, X., Phosphorylation of Oligopeptides: Design of Ultra-Hydrophilic Zwitterionic Peptides for Anti-Fouling Detection of Nucleic Acids in Saliva. Anal Chem 2023.

Chapter 4: Development of Platforms for Label Free Analysis of Curvature Sensing Proteins

4.1 Introduction

In recent decades various proteins have been identified that appear to preferentially bind to curved lipid surfaces. With major roles in various areas of membrane fission[1] including endocytosis[2], cell-cell signaling[3], and membrane reshaping[4, 5] mechanisms. These curvature binding motifs clearly play an important role in our biological function but the specifics of how they selectively bind curved surfaces are still underexplored. One group of these curvature sensing proteins is found from a conserved structure known as the BAR domain that adopts a banana like structure that binds to curved membranes.[6] These BAR domain proteins act not only to sense curved regions but also to generate and propagate curvature[7] followed by acting as a scaffold for binding of partner proteins[8]. Though this is not the only case of curvature sensing that has been identified, intrinsically disordered proteins (IDPs) have also been observed to preferentially bind to curved surfaces. These IDPs have been shown to produce membrane buds and tubules through crowding effects when bound in high enough amounts[5, 9]. One of these IDPs known as alpha-synuclein[10] has also been implicated to play a critical role in Parkinson's disease[11]. So clearly, these curvature sensing proteins are not only necessary for cellular function but can contribute to disease states. Though, a deeper understanding of the binding between these curvature sensing proteins and lipid structures is needed to elucidate the specifics of these unique systems that clearly play a pivotal role in eukaryotic cells.

As such, ways to isolate and study this curvature dependent binding are necessary. However, this curvature has presented a challenge to biomimetic studies that have relied on solid supported lipid membranes for measurements of protein binding dynamics. Therefore, new methodologies to accurately mimic the curved environment that these proteins naturally bind to have been explored utilizing liposomes[12-15] and nanostructures[16-18] to form well defined curved surfaces. However, the majority of these studies rely on fluorophore labeling to investigate this curvature specific binding limiting our ability to see just the binding interaction. As such, surface plasmon resonance (SPR)[19] and quartz crystal microbalance (QCM)[20] emerge as ideal instrumentation to investigate these interactions due to their ability to provide label free analysis of the interactions between proteins and lipid structures which can be expanded to these curved systems if an appropriate platform is developed.

Herein, we demonstrate curved membrane platforms for use in SPR and QCM based analysis of curvature selective protein binding and implement modeling techniques to elucidate the effect of changing constituents on the SPR platform. For SPR based studies a platform consisting of ganglioside containing lipid vesicles linked to cholera toxin on the sensor surface is employed to investigate BIN1 binding to varied vesicle sizes. While another platform utilizes different size silica beads to induce formation of curved lipid membranes for QCM measurements of alpha-syn curvature specific binding. Each platform demonstrates the capability to identify curvature specific binding, finding increased binding to highly curved surfaces. Further, Monte Carlo methods were employed to model the vesicles utilized in the SPR platform and connect differences in binding for

various gangliosides to multivalent interactions with the CT based on expected distribution of gangliosides. These platforms can be easily modified and applied to investigate any curvature sensing protein of interest.

4.2 Experimental Methods

Materials and Reagents.

A stainless-steel extruder, 100 nm polycarbonate track etched filters, 1-palmitoyl-2-oleoyl-glycero-3-phosphocholine POPC, and 1,2-dioleoyl-sn-glycero-3-phosphoethanolamine-N-(7-nitro-2-1,3-benzoxadiazol-4-yl) (ammonium salt) NBD-PE, were purchased from Avanti Polar Lipids (Alabaster, Al). 10 mm filter supports were acquired from Cytiva (Marlborough, MA). Silica nanospheres of sizes 50, 100, and 500 nm were obtained from nanoComposix (San Diego, CA). 10 MHz quartz crystal chips were purchased from openQCM (Pompei, Italy). Plain BK-7 glass microscope slides, phosphate buffered saline (PBS) concentrate, and alpha-synuclein protein were acquired from Fisher Scientific (Hampton, NH). Polydimethylsiloxane (PDMS) two-part polymer kit was obtained from Ellsworth adhesives (Germantown, WI).

Lipid Vesicle Preparation.

Lipid vesicles were prepared following previously published procedures[21]. In short, a stock solution of 5 mg/mL POPC in 1:9 methanol chloroform solution kept at -80 °C was thawed, aliquoted into a glass vial, and dried under nitrogen to form a thin lipid film. This film was further dried in a vacuum desiccator overnight before resuspension in 1× PBS (10 mM Na2HPO4, 1.8 mM KH2PO4, 137 mM NaCl, 2.7 mM KCL, pH 7.4) to a final

concentration of 1 mg/mL. Following resuspension, lipid mixtures were thoroughly vortexed to ensure the lipid film was fully dissolved then were sonicated for 30 minutes at room temperature to induce vesicle formation. Vesicles were then extruded through membranes to produce small unilamellar vesicles of the desired 100 nm size and then stored at 4°C for use within 5 days.

Fluorescent Imaging and Fluorescence Recovery after Photobleaching of Curved Lipid Surfaces.

Fluorescence microscopy images were acquired on an inverted Leica TCS SP5 II. For fluorescent imaging of lipid bilayers NBD-PE fluorophore labeled lipids were incorporated into the lipid vesicle preparation at a 2% molar ratio. NBD excitation was achieved with a 488 nm argon laser at 10-20% laser power and collected using a Leica hybrid detector (HyD), which combines photomultiplier tube and avalanche photodiodes, set to collect 500-600 nm light. To visualize the formation of lipid membranes on curved surfaces, silica nanoparticles were drop cast into small wells cut into thin PDMS sheets on piranha cleaned glass microscope slides and then lipid vesicles were introduced and allowed to equilibrate before being thoroughly rinsed with water. The remaining lipids bound to the silica nanosphere surfaces were Z-stack imaged with a step size of 0.042 micron. Each image was collected using 3-fold line and image averaging. Following data collection images were processed using ImageJ with the Fiji[22] package to combine intensity values from each Z-stack to visualize the fluorescence across the entire sphere volume. FRAP measurements were achieved using the same instrument using identical parameters with modification to 100% laser power for bleaching and no line or image averaging when collecting bleach

recovery images to enable collection of an image every second. From these recovery images the fluorescence intensity of the bleach spot was collected at each time point and normalized against an unbleached control area of the same size to produce a graph of fractional recovery.

Fabrication of SPR Chips.

Gold coated surface plasmon resonance chips were formulated on glass microscope slides in accordance with previously published procedures[23]. For this glass slides were cleaned in boiling piranha acid (3:1, H_2SO_4:H_2O_2) for 1 hour to remove any organic material. Then chips were washed with water followed by ethanol and dried via a nitrogen stream. These chips were then transferred to the University of California, Riverside Center for Nanoscale Science and Engineering Nanofabrication Facility where they were coated in 2 nm chromium and 48 nm of gold using an electron beam physical vapor deposition (EBPVD) system (Temescal, Berkeley, CA). Finally, 1-3nm of silica was deposited on these gold coated chips using a Unaxis 790 (Pfäffikon, Schwyz, Switzerland) plasma enhanced chemical vapor deposition (PECVD) instrument.

SPR Analysis.

These silica coated gold sensor chips were utilized for SPR experiments on a NanoSPR5-321 (NanoSPR, Chicago, IL) instrument that employs a 670 nm GaAs semiconductor laser. The system includes a silver backed triangular prism (n=1.61) that is matched to the glass slides using matching fluid (n = 1.5167) (Cargille, Cedar Grove, NJ). Biological components are injected into the dual channel system through a home-built injection

system consisting of two 6-way HPLC injection valves and a two-channel syringe pump with flow rate set to 5 mL/h.

Fabrication of QCM-D Chips.

To fabricate QCM chips capable of readily forming lipid bilayers a thin layer of silica was deposited onto the 10 MHz QCM chips from openQCM[24] to enable robust lipid bilayer formation upon lipid vesicle introduction. This was achieved using plasms enhanced chemical vapor deposition following previously published procedures for SPR chips[25] with modifications to accommodate the QCM chips. To produce curved surfaces for lipids to adhere to, 100 µL of silica nanospheres (10 mg/mL) were drop cast onto the chip and spin coated for 30 seconds at 4000 rpm. These silica sphere coated chips were then introduced to QCM instrumentation for lipid and protein binding studies.

QCM Analysis.

Sensing of alpha-syn binding to curved lipid surfaces was achieved using an openQCM[24] Q-1 instrument (openQCM, Pompei, Italy) that provides frequency and dissipation monitoring with overtone measurement and temperature control. The fabricated chips were inserted into the QCM, and the sensing chamber was slotted into place with an O-ring seal. Then lipids were injected and allowed to form a lipid bilayer which could be monitored in real time based on frequency and dissipation changes. Finally alpha-synuclein protein was injected into the flow system and allowed to equilibrate to measure differences in binding to differently curved lipid surfaces based on silica bead size.

Monte Carlo Modeling of Lipid Surfaces.

Code for the Monte Carlo modeling of vesicles was scripted in R with library rgl[26] utilized for 3D visualization of vesicles. To calculate the number of lipids in the vesicle of interest we utilized equation 4.1 which takes into account the vesicle radius (r), bilayer thickness (h), and lipid area (a).

$$\frac{4\pi r^2+4\pi(r-h)^2}{a} \tag{4.1}$$

This number was then modified to account for only the outer monolayer of lipids through removal of the $4\pi(r-h)^2$ term of the equation which corresponds to the inner layer of lipids. Then this number is multiplied by the lipid percentage to determine the number of an individual lipid or ganglioside type that was incorporated within a single vesicle. To calculate the distance between gangliosides in these models first the chord (c) between each ganglioside and its nearest neighbor was calculated based on the x, y, and z coordinates of the points through equation 4.2. These chord

$$\sqrt{(x_2-x_1)^2+(y_2-y_1)^2+(z_2-z_1)^2} \tag{4.2}$$

values were then utilized to calculate an arc distance, using equation 4.3, which more appropriately

$$r * \sin^{-1}\frac{2c}{2r} \tag{4.3}$$

matches the distance between points on the curved vesicle surface. Once thousands of arc distances had been calculated and combined, they were output as histograms to visualize

the distribution of distances between gangliosides. The code used for these calculations and plotting can be found in appendix A.1.

4.3 Results and Discussion

While SPR and QCM are both label free techniques the difference in how they measure binding events plays an important role in the potential curved membrane platforms that can be effectively implemented. For example, as SPR relies on an evanescent field that decays exponentially with distance from the surface the analysis of interactions at lipid surfaces beyond a certain distance (~300 nm) from the sensor becomes difficult if not impossible. QCM is similarly limited as when working in liquid the shear wave decays within (~250 nm)[27]. However, this decay does not necessarily begin at the sensor surface. If rigid structures are present this decay begins at the end of the structure. As such, implementation of rigid spherical structures could enable QCM analysis of curvature sensing proteins at distances greater than 250 nm from the surface without substantial signal loss.

Therefore, we developed two different curved membrane substrates to facilitate investigation of curvature binding proteins via label free techniques SPR and QCM. For the SPR sensor we employed a solid supported lipid membrane containing DGS-NTA lipids to secure and present CT on the sensor surface allowing for further capture of lipid vesicles containing various gangliosides which are known to bind with CT. Thus, presenting a malleable curved lipid surface with availability for binding close to the sensor surface limiting the loss of signal from evanescent field decay. The QCM sensor utilized silica beads to formulate a surface of rigid spherical nodes taking advantage of QCMs

difference in signal decay. Lipid membranes could then be formulated atop these spherical structures inducing a curved surface consistent with the size of the bead used.

Formulation and Characterization of Tethered Vesicle Platform

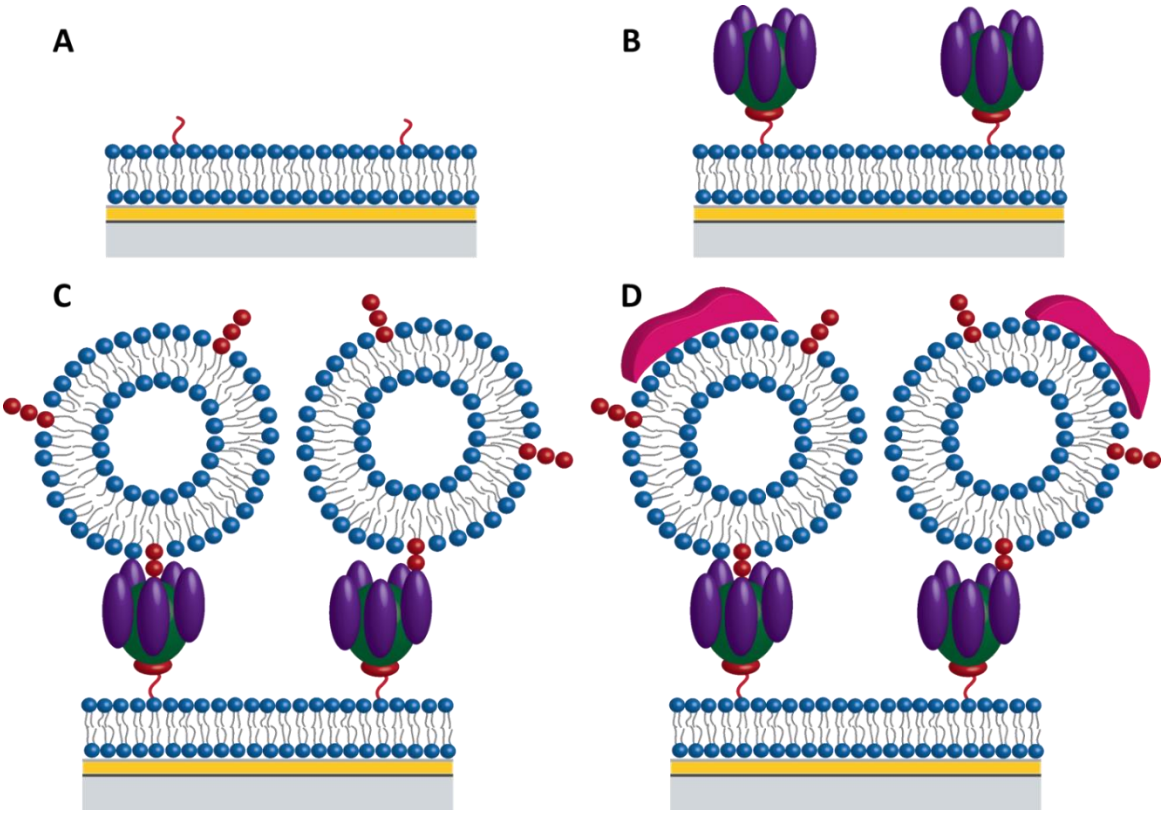

Figure 4.1. Scheme of a tethered vesicle platform for sensing of Bin1 binding to curved surfaces. Built from an underlying lipid bilayer (A) that links to cholera toxin (B). Then capture of lipid vesicles based on CT binding to gangliosides (C) and finally curvature specific binding of Bin1 to the vesicles (D).

To begin a tethered vesicle system was designed and characterized for its functionality within an SPR sensing system, an illustration of this system can be seen in Figure 4.1. The formulation of each step within the sensor scaffold formulation was monitored via SPR finding robust signal associated with initial solid supported lipid bilayer formation, CT linkage, and then vesicle binding as seen in Figure 4.2. This demonstrated that each part of the system was forming on the silica coated SPR sensor surface but as the

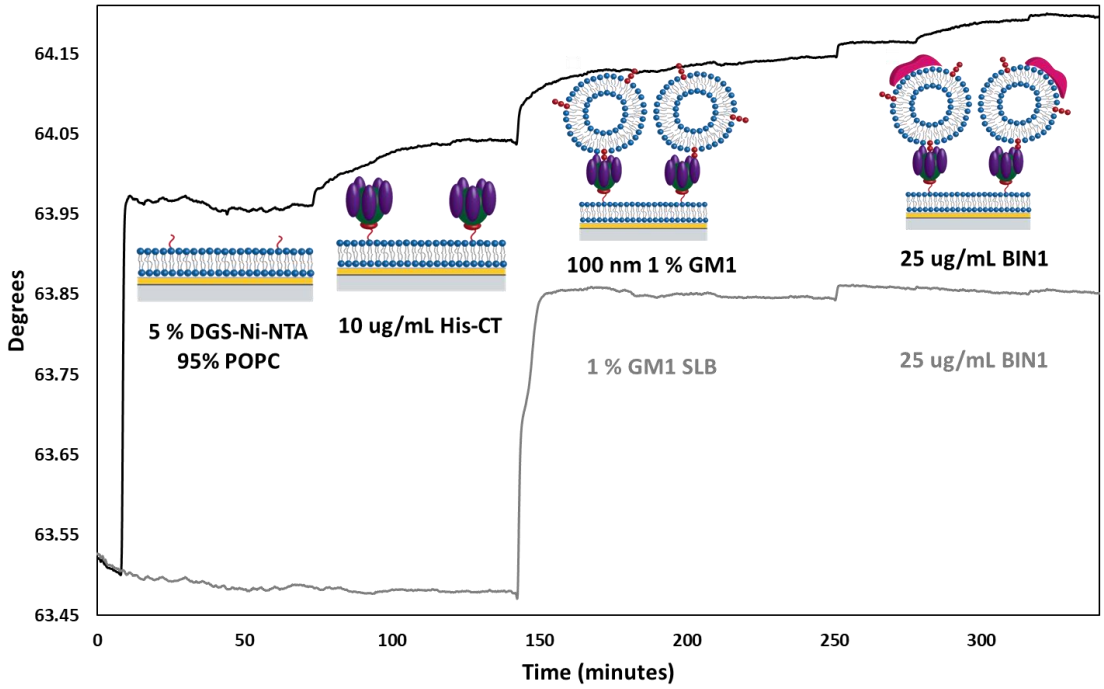

Figure 4.2. SPR sensorgram of tethered vesicle formation steps including solid supported DGS-NTA/POPC fusion, then histidine tagged CT capture, ganglioside containing vesicle binding, and finally curvature specific binding of BIN1.

curved nature of the adhered vesicles is essential to the functionality of the surface further characterization was necessary. We first employed fluorescence recovery after photobleaching to investigate the fluidity of each of the lipid layers as upon bleaching attached lipid vesicles would not be able to recover fluorescence as mobility is confined to the nanometer size of the vesicle itself while a complete bilayer would have lateral diffusivity within the micron sized bleach area and could therefore recover. As shown in Figure 4.3, it can be clearly seen that the solid supported DGS-NTA containing POPC membrane while limited did have fluorescent recovery while when fluorophore labeled lipids were incorporated into the attached vesicles no recovery was observed. Also, the fluorescence intensity of the vesicle step was noticeably lower which indicates that vesicles were separated from each other and not forming into another bilayer system. Following

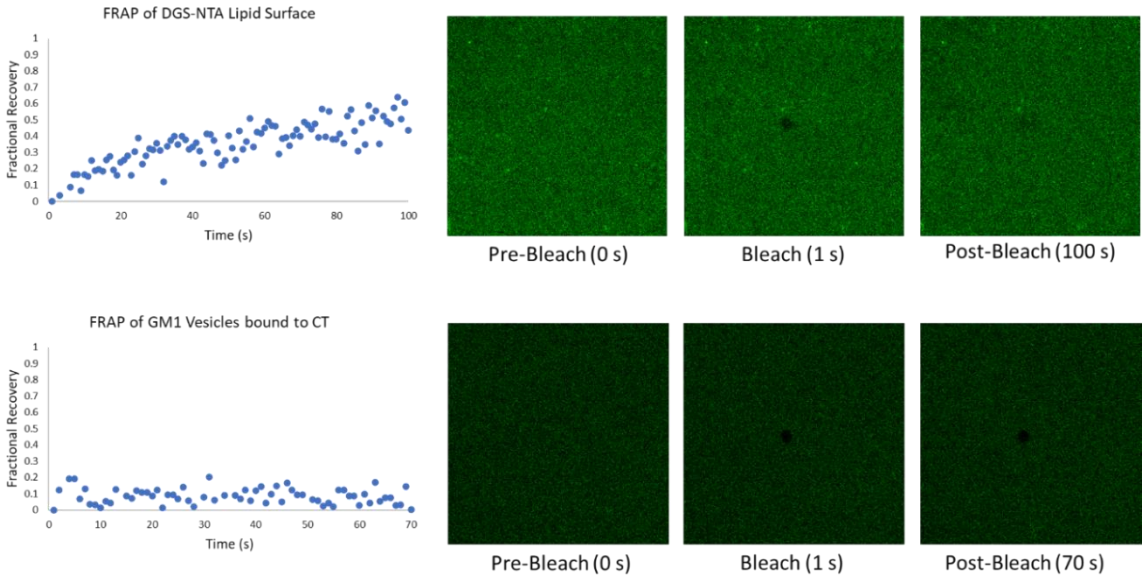

Figure 4.3. FRAP images demonstrating lipid mobility for underlying solid supported DGS-NTA/POPC membrane but no mobility for attached GM1 vesicles.

this preliminary curvature binding studies were completed using Bin1 as a model curvature sensing protein. These results showed a clear preference in binding for highly curved vesicle platforms as seen in the final step of Figure 1. Substantially higher BIN1 binding was observed for the vesicle system when compared to a planar membrane system which demonstrates the curvature sensing of BIN1. Furthermore, higher binding was detected for the 30 nm vesicle platform than the 100 nm system which matches well with literature reports indicating Bin1's preference for highly curved surfaces[28].

Mathematical Modeling of Tethered Vesicle System

During the verification of the CT-ganglioside linked system a substantial increase in vesicle signal was observed for systems containing higher amounts of ganglioside which was more than could have been expected due to improvements in overall affinity. As such, we endeavored to model the distribution of these gangliosides within the tethered vesicles

to identify what was changing with higher concentrations. To achieve this a script was written in R that calculated the expected number of lipids/gangliosides per vesicle based on vesicle diameter utilizing literature reports of lipid area[29] and membrane thickness[30,31]. Then these values were then used to model the vesicles in question using Monte Carlo

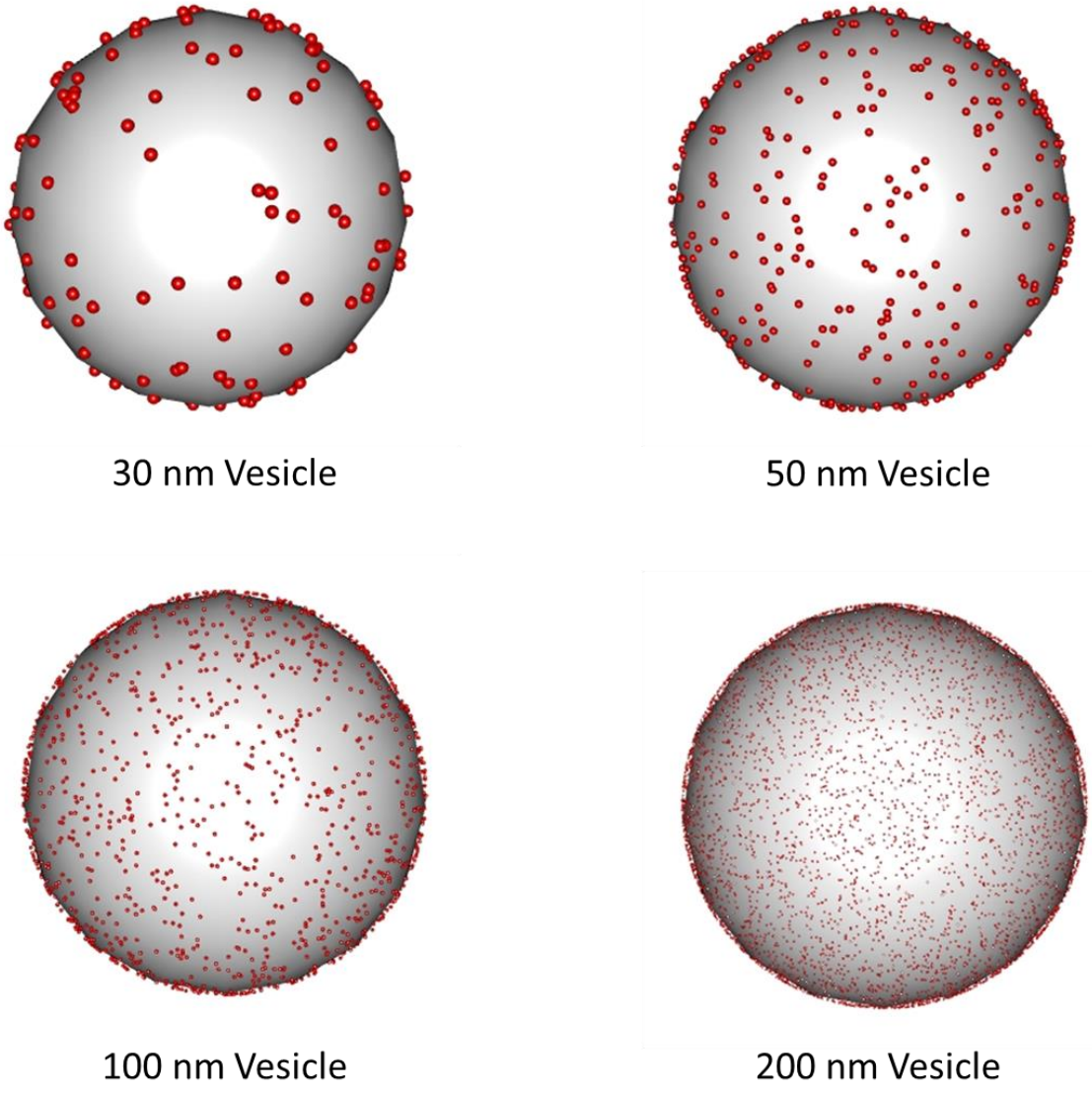

Figure 4.4. 3D models of 5% GM1 vesicles of varying sizes. Red spheres each represent a singular GM1 molecule proportionally sized against the size of the vesicle.

methods. For this a number of random locations for gangliosides were computed to align with the number expected in the outer region of the vesicle. These random locations were

then mapped onto a large white sphere as small colored spheres corrected in size to accurately represent the size of a singular lipid within a vesicle membrane. This immediately enabled us to visualize the substantial differences in number and distribution

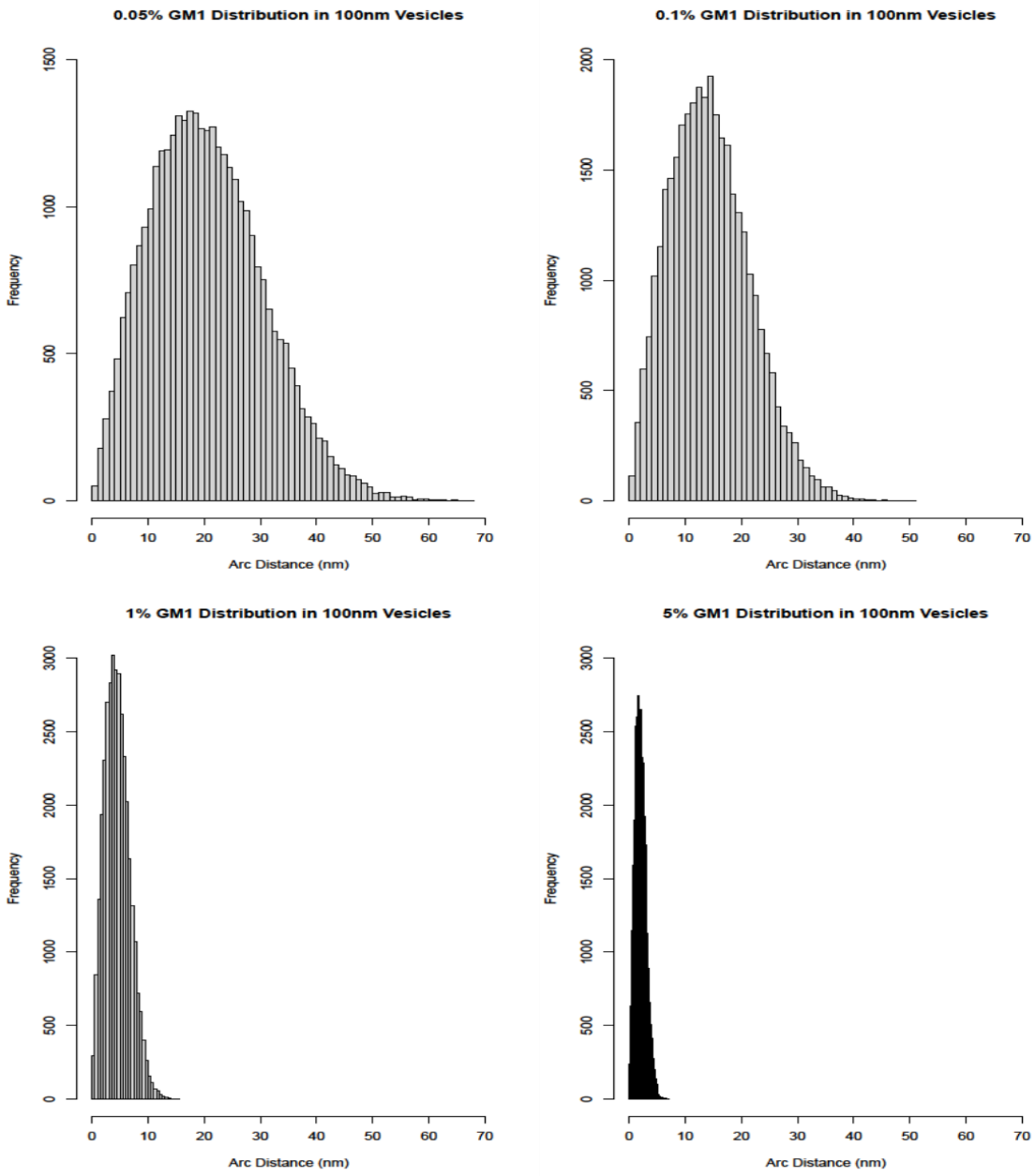

based on vesicle size and ganglioside percentage as can be seen in Figure 4.4. Showing **Figure 4.5.** Distribution of arc length distance between nearest gangliosides obtained from iterative models of 100 nm vesicles with varying ganglioside percentages (0.05, 0.1, 1, and 5% from left to right).

that with the smallest vesicles at the lowest ganglioside percentage only a few gangliosides were present in each vesicle while thousands of gangliosides were present in the larger

vesicles at 5% molar ratio of gangliosides. While this modeling of a singular vesicle provided valuable insight it was far from the whole picture. Therefore, we implemented calculation of the nearest neighbor distance for the gangliosides in these vesicle models and compiled calculations from thousands of simulated vesicles to provide a probability distribution of distance between gangliosides (Figure 4.5). When combined with the multiple ganglioside binding regions of CT this quickly fell into place as vesicles with 5% mol ratio of gangliosides were on average less than 3 nm apart which consequently matches with the distance between binding pockets within CT based on crystal structure measurements[32]. Indicating that at these higher ganglioside percentages multivalent binding was far more likely to occur thus enhancing the binding of gangliosides with lower affinity for CT.

Formation and Characterization of Curved Lipid Surfaces on Silica Beads

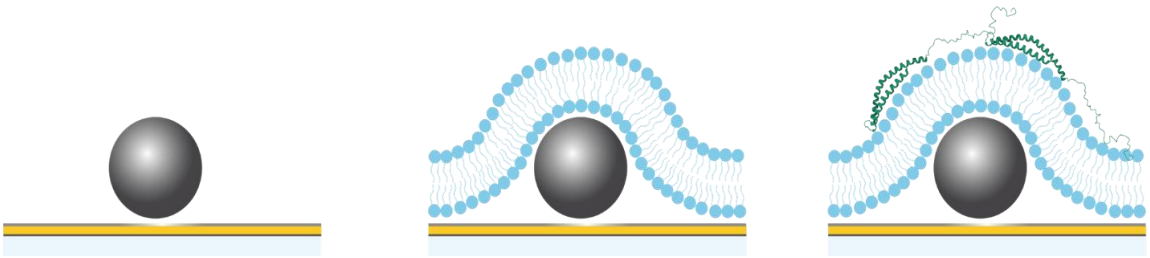

Figure 4.6. Silica bead deposition on QCM chip, lipid membrane formation over silica bead and then alpha-synuclein binding to this curved membrane platform (left to right).

Now focusing on the silica bead curved membrane system (Figure 4.6), we first needed to modify the QCM sensor chips to enable adhesion of silica beads and lipids as the base gold sensor surface is not conducive to either without assitance[33]. To achieve this a thin layer of silica was deposited on purchased QCM chips using PECVD as discussed in the methods section. This silica layer significantly increased surface hydrophilicity as

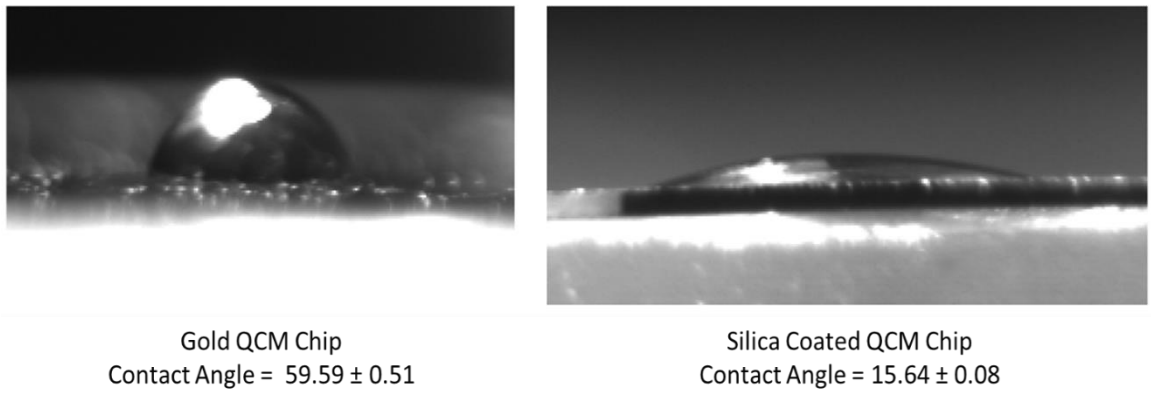

Figure 4.7. Contact angle images and measurements of QCM chip before and after silica coating demonstrating improved hydrophilicity with the addition of silica.

can be seen from contact angle images (Figure 4.7). Now that our sensor surface had an appropriate base the silica bead surface was fabricated through spin coating 100 µL of 10mg/mL silica beads at 4000 rpm for 30 seconds. Then we confirmed that the silica beads adhered to the silica coated QCM chip surface via scanning electron microscopy finding a

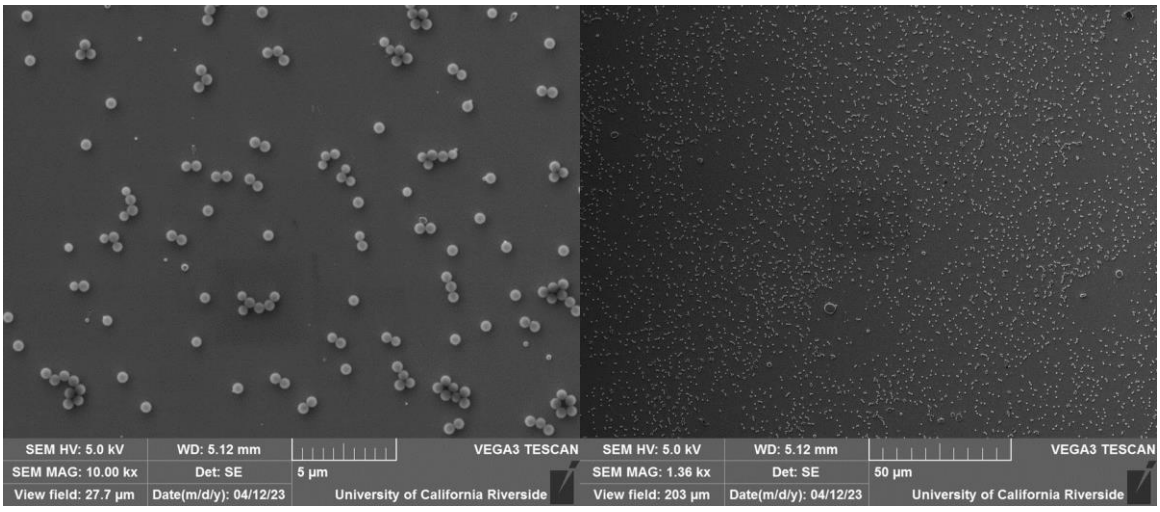

Figure 4.8. SEM images of 500 nm beads distributed on silica coated QCM chip.

large portion of the surface was covered in a single layer of silica beads as can be seen in Figure 4.8. While surface coverage was not complete this system was found to produce a reproducible surface without bead agglomeration which was considered to be more ideal

as any agglomeration could cause us to lose precise control of the lipid curvature. Following this, lipids were introduced to the sensor and lipid membrane formation was observed via QCM frequency shift and dissipation changes with results matching literature reports of vesicle fusion and membrane formation[34]. However, these results were unable to elucidate whether lipids formed around the beads into the curved membrane platform we desired or on top of the beads as a continuous flat membrane. To investigate this, we formulated a similar 500nm silica bead surface on a glass microscope slide and then formulated lipid membranes containing 2% NBD-PE to enable fluorescence microscopy of the lipid membrane. To visualize whether lipids were forming as a flat or curved membrane system we compiled and averaged z-stack images of the fluorescence intensity moving from below to above the silica bead plane. While fluorescence microscopy does not have the resolution to resolve the bead structures themselves when combining the intensity of many Z-stack images areas of higher intensity can be observed which corresponds to the side of a silica bead where a higher number of

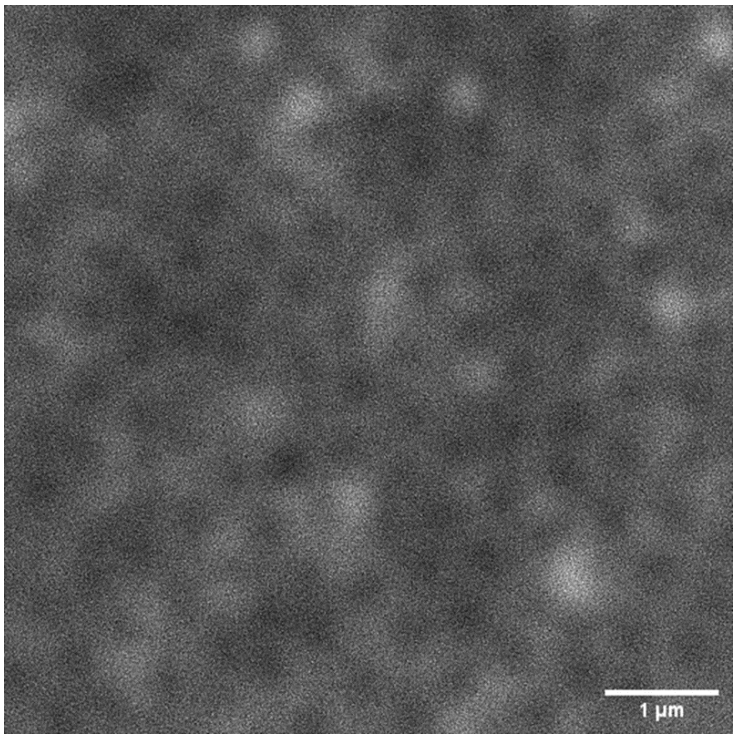

Figure 4.9. Summed intensity of z stack images of fluorescent lipid membrane formulated on 500 nm beads.

fluorescent lipids would be present due to the curved nature of the membrane as is shown in Figure 4.9. Now that we had some indication that our silica bead surface was working as intended, we endeavored to confirm its curvature through investigating differences in binding of a curvature sensing protein to membrane systems with the variable curvature of 50, 100, and 500 nm beads.

Measuring Alpha-Syn Preferential Binding to Curved Lipid Substrates via QCM

To probe the platform's ability to elucidate curvature sensing proteins we employed an IDP alpha-synuclein as a proof of concept. For this curved membrane surfaces of varying

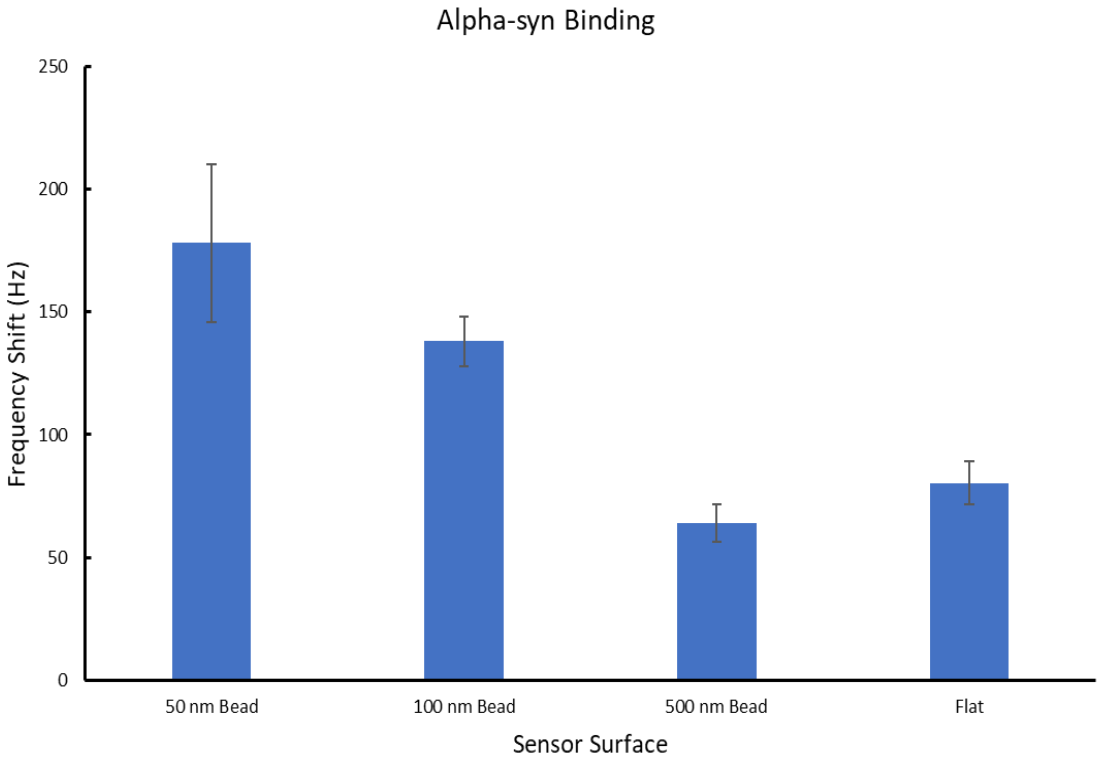

Figure 4.10. Resulting QCM frequency shifts of 50 ug/mL alpha syn binding to POPC membranes formed on different sized silica bead surfaces.

curvature were formulated as previously demonstrated and characterized and then the binding of alpha-syn was measured and compared between these differently curved

substrates. A substantial difference between these curved substrates was immediately apparent with a flat membrane having less signal associated with alpha-syn binding than the curved surfaces, as visible in Figure 4.10. Furthermore, when comparing 50 and 100 nm beads it was found that more binding was observed for the 50 nm bead indicating not just a preference for curved surfaces but highly curved surfaces. This is supported by comparison of alpha-syn binding on a flat membrane surface and a curved surface formulated on 500 nm beads which showed minimal difference between the two indicating that the curvature induced by 500 nm beads is not distinct enough to impart any improvement in alpha-syn binding. Also, these results helped alleviate the concern that the increased surface area from the beads might have an impact on the binding signal as this effect was negligible compared to the curvature effect based on the 500 nm bead results.

4.4 Conclusion

We have demonstrated two curved membrane substrates to enable label free analysis of curvature sensing proteins using SPR and QCM instrumentation. One substrate provides tethered lipid vesicles of variable size and composition enabling detection of differences in curvature preference for curvature sensitive protein Bin1. The surface is also investigated through modeling of expected vesicle size and ganglioside distribution using Monte Carlo methods that can be utilized in modeling any vesicle system. While the QCM substrate exhibits solid supported curved membranes based on a silica bead platform. This platform was utilized to monitor the curvature specific binding of an IDP, alpha-synuclein. These surfaces and techniques together provide a robust method to monitor curvature binding interactions and can be employed to investigate the plethora of curvature binding

proteins that have and are being identified. Furthermore, the properties of these platforms can be easily modified through exchange or addition of lipid species to accurately mimic cellular environments.

4.5 References

1. Snead, W. T.; Stachowiak, J. C., Structure Versus Stochasticity—The Role of Molecular Crowding and Intrinsic Disorder in Membrane Fission. *Journal of Molecular Biology* **2018,** *430* (16), 2293-2308.

2. Kaksonen, M.; Roux, A., Mechanisms of clathrin-mediated endocytosis. *Nature Reviews Molecular Cell Biology* **2018,** *19* (5), 313-326.

3. Diella, F.; Haslam, N.; Chica, C.; Budd, A.; Michael, S.; Brown, N. P.; Trave, G.; Gibson, T. J., Understanding eukaryotic linear motifs and their role in cell signaling and regulation. **2008,** *13* (17), 6580-6603.

4. Beber, A.; Taveneau, C.; Nania, M.; Tsai, F.-C.; Di Cicco, A.; Bassereau, P.; Lévy, D.; Cabral, J. T.; Isambert, H.; Mangenot, S.; Bertin, A., Membrane reshaping by micrometric curvature sensitive septin filaments. *Nature Communications* **2019,** *10* (1), 420.

5. Busch, D. J.; Houser, J. R.; Hayden, C. C.; Sherman, M. B.; Lafer, E. M.; Stachowiak, J. C., Intrinsically disordered proteins drive membrane curvature. *Nature Communications* **2015,** *6* (1), 7875.

6. Peter, B. J.; Kent, H. M.; Mills, I. G.; Vallis, Y.; Butler, P. J. G.; Evans, P. R.; McMahon, H. T., BAR Domains as Sensors of Membrane Curvature: The Amphiphysin BAR Structure. *Science* **2004,** *303* (5657), 495-499.

7. Stanishneva-Konovalova, T. B.; Derkacheva, N. I.; Polevova, S. V.; Sokolova, O. S., The Role of BAR Domain Proteins in the Regulation of Membrane Dynamics. *Acta naturae* **2016,** *8* (4), 60-69.

8. Ferguson, S. M.; Brasnjo, G.; Hayashi, M.; Wölfel, M.; Collesi, C.; Giovedi, S.; Raimondi, A.; Gong, L.-W.; Ariel, P.; Paradise, S.; O'Toole, E.; Flavell, R.; Cremona, O.; Miesenböck, G.; Ryan, T. A.; De Camilli, P., A Selective Activity-Dependent Requirement for Dynamin 1 in Synaptic Vesicle Endocytosis. *Science* **2007,** *316* (5824), 570-574.

9. Snead, W. T.; Zeno, W. F.; Kago, G.; Perkins, R. W.; Richter, J. B.; Zhao, C.; Lafer, E. M.; Stachowiak, J. C., BAR scaffolds drive membrane fission by crowding disordered domains. *Journal of Cell Biology* **2018,** *218* (2), 664-682.

10. Jensen, M. B.; Bhatia, V. K.; Jao, C. C.; Rasmussen, J. E.; Pedersen, S. L.; Jensen, K. J.; Langen, R.; Stamou, D., Membrane Curvature Sensing by Amphipathic

Helices: A SINGLE LIPOSOME STUDY USING α-SYNUCLEIN AND ANNEXIN B12*. *Journal of Biological Chemistry* **2011,** *286* (49), 42603-42614.

11. Calabresi, P.; Mechelli, A.; Natale, G.; Volpicelli-Daley, L.; Di Lazzaro, G.; Ghiglieri, V., Alpha-synuclein in Parkinson's disease and other synucleinopathies: from overt neurodegeneration back to early synaptic dysfunction. *Cell Death & Disease* **2023,** *14* (3), 176.

12. Zeno, W. F.; Thatte, A. S.; Wang, L.; Snead, W. T.; Lafer, E. M.; Stachowiak, J. C., Molecular Mechanisms of Membrane Curvature Sensing by a Disordered Protein. *J Am Chem Soc* **2019,** *141* (26), 10361-10371.

13. Bhatia, V. K.; Madsen, K. L.; Bolinger, P.-Y.; Kunding, A.; Hedegård, P.; Gether, U.; Stamou, D., Amphipathic motifs in BAR domains are essential for membrane curvature sensing. *The EMBO Journal* **2009,** *28* (21), 3303-3314.

14. Hatzakis, N. S.; Bhatia, V. K.; Larsen, J.; Madsen, K. L.; Bolinger, P.-Y.; Kunding, A. H.; Castillo, J.; Gether, U.; Hedegård, P.; Stamou, D., How curved membranes recruit amphipathic helices and protein anchoring motifs. *Nature Chemical Biology* **2009,** *5* (11), 835-841.

15. Madsen, K. L.; Bhatia, V. K.; Gether, U.; Stamou, D., BAR domains, amphipathic helices and membrane-anchored proteins use the same mechanism to sense membrane curvature. *FEBS Letters* **2010,** *584* (9), 1848-1855.

16. Zhao, W.; Hanson, L.; Lou, H.-Y.; Akamatsu, M.; Chowdary, P. D.; Santoro, F.; Marks, J. R.; Grassart, A.; Drubin, D. G.; Cui, Y.; Cui, B., Nanoscale manipulation of membrane curvature for probing endocytosis in live cells. *Nature Nanotechnology* **2017,** *12* (8), 750-756.

17. Lou, H.-Y.; Zhao, W.; Zeng, Y.; Cui, B., The Role of Membrane Curvature in Nanoscale Topography-Induced Intracellular Signaling. *Accounts of Chemical Research* **2018,** *51* (5), 1046-1053.

18. Ferhan, A. R.; Jackman, J. A.; Malekian, B.; Xiong, K.; Emilsson, G.; Park, S.; Dahlin, A. B.; Cho, N.-J., Nanoplasmonic Sensing Architectures for Decoding Membrane Curvature-Dependent Biomacromolecular Interactions. *Analytical Chemistry* **2018,** *90* (12), 7458-7466.

19. Hinman, S. S.; McKeating, K. S.; Cheng, Q., Surface Plasmon Resonance: Material and Interface Design for Universal Accessibility. *Analytical Chemistry* **2018,** *90* (1), 19-39.

20. Alanazi, N.; Almutairi, M.; Alodhayb, A. N., A Review of Quartz Crystal Microbalance for Chemical and Biological Sensing Applications. *Sensing and Imaging* **2023,** *24* (1), 10.

21. Hinman, S. S.; Ruiz, C. J.; Cao, Y.; Ma, M. C.; Tang, J.; Laurini, E.; Posocco, P.; Giorgio, S.; Pricl, S.; Peng, L.; Cheng, Q., Mix and Match: Coassembly of Amphiphilic Dendrimers and Phospholipids Creates Robust, Modular, and Controllable Interfaces. *ACS Applied Materials & Interfaces* **2017,** *9* (1), 1029-1035.

22. Schindelin, J.; Arganda-Carreras, I.; Frise, E.; Kaynig, V.; Longair, M.; Pietzsch, T.; Preibisch, S.; Rueden, C.; Saalfeld, S.; Schmid, B.; Tinevez, J.-Y.; White, D. J.; Hartenstein, V.; Eliceiri, K.; Tomancak, P.; Cardona, A., Fiji: an open-source platform for biological-image analysis. *Nature Methods* **2012,** *9* (7), 676-682.

23. Malinick, A. S.; Lambert, A. S.; Stuart, D. D.; Li, B.; Puente, E.; Cheng, Q., Detection of Multiple Sclerosis Biomarkers in Serum by Ganglioside Microarrays and Surface Plasmon Resonance Imaging. *ACS Sensors* **2020,** *5* (11), 3617-3626.

24. Mista, C.; Zalazar, M.; Peñalva, A.; Martina, M.; Reta, J. M., Open Source Quartz Crystal Microbalance with dissipation monitoring. *Journal of Physics: Conference Series* **2016,** *705* (1), 012008.

25. Phillips, K. S.; Wilkop, T.; Wu, J.-J.; Al-Kaysi, R. O.; Cheng, Q., Surface Plasmon Resonance Imaging Analysis of Protein-Receptor Binding in Supported Membrane Arrays on Gold Substrates with Calcinated Silicate Films. *J Am Chem Soc* **2006,** *128* (30), 9590-9591.

26. Adler, D. M. a. D. *RGL: A R-library for 3D visualization with OpenGL*, 2022.

27. Köβlinger, C.; Uttenthaler, E.; Drost, S.; Aberl, F.; Wolf, H.; Brink, G.; Stanglmaier, A.; Sackmann, E., Comparison of the QCM and the SPR method for surface studies and immunological applications. *Sensors and Actuators B: Chemical* **1995,** *24* (1), 107-112.

28. Wu, T.; Baumgart, T., BIN1 membrane curvature sensing and generation show autoinhibition regulated by downstream ligands and PI(4,5)P2. *Biochemistry* **2014,** *53* (46), 7297-309.

29. Niemelä, P. S.; Ollila, S.; Hyvönen, M. T.; Karttunen, M.; Vattulainen, I., Assessing the Nature of Lipid Raft Membranes. *PLOS Computational Biology* **2007,** *3* (2), e34.

30. Regan, D.; Williams, J.; Borri, P.; Langbein, W., Lipid Bilayer Thickness Measured by Quantitative DIC Reveals Phase Transitions and Effects of Substrate Hydrophilicity. *Langmuir* **2019,** *35* (43), 13805-13814.

31. Lewis, B. A.; Engelman, D. M., Lipid bilayer thickness varies linearly with acyl chain length in fluid phosphatidylcholine vesicles. *Journal of Molecular Biology* **1983,** *166* (2), 211-217.

32. Groza, R.; Ewers, H., Membrane deformation by the cholera toxin beta subunit requires more than one binding site. *Proceedings of the National Academy of Sciences* **2020,** *117* (30), 17467-17469.

33. Tae, H.; Yang, C.; Cho, N.-J., Artificial Cell Membrane Platforms by Solvent-Assisted Lipid Bilayer (SALB) Formation. *Accounts of Materials Research* **2022,** *3* (12), 1272-1284.

34. Keller, C. A.; Kasemo, B., Surface specific kinetics of lipid vesicle adsorption measured with a quartz crystal microbalance. *Biophys J* **1998,** *75* (3), 1397-1402.

Chapter 5: MALDI-MS Identification of Methicillin Resistant S. Aureus Strain and Machine Learning Classification of Bacterial Species

5.1 Introduction

Bacterial infections are one of the most common causes of human disease with recent reports attributing one in every eight deaths worldwide to bacterial infections[1]. Furthermore, *Staphylococcus aureus* (*S. aureus)* infection was found to the be the leading bacterial cause of death worldwide. Despite the presence of many effective antibiotic drugs these infections continue to impact communities across the globe due to the lack of access to antibiotics in many parts of the world[2, 3] and to the rise of antibiotic resistant bacterial strains[4]. With the emergence of resistant strains drug selection becomes increasingly important as improper prescription can at best be less effective or at worst lead to death and expansion of antibiotic resistance[5, 6]. This antimicrobial resistance is responsible for millions of deaths yearly[4] and is considered by the world health organization to be one of the biggest threats to global health[7]. One of these antibiotic resistant bacteria, methicillin resistant *Staphylococcus aureus* (MRSA), has seen a rise in many hospital populations[8] and an evolving resistance in recent decades[9, 10] two factors that have contributed to its role in many deaths. As such, methodologies to rapidly identify bacterial strains and classify resistance are key to appropriate treatment[1, 4, 11]. Unfortunately, current methodologies for bacteria identification can be time consuming, complex, and labor intensive, so new alternatives are necessary[12, 13]. Recently matrix assisted laser desorption ionization mass spectrometry (MALDI-MS) and polymerase chain reaction (PCR) have appeared as

effective methodologies for bacterial identification but require more research and advancement to improve accuracy and time to results[14].

Herein we demonstrate an aluminum microarray based MALDI-MS platform for rapid analysis of intact bacterial lipid profiles with proof-of-concept differentiation between susceptible and resistant of *S. aureus* bacterial strains. We employ the aluminum plasmonic microarrays for MALDI signal enhancement enabling robust signal for lipids and metabolites of these bacteria facilitating determination of distinct spectral differences between the two strains that can be utilized to classify resistance. Our analysis resulted in identification of peaks in the 2400 m/z range that are linked to the phenol-soluble modulin (PSM-mec) peptide[15] present in many antibiotic resistant *S. aureus* strains. This peptide has been shown to be a highly effective marker for resistant *S. aureus* strains in various other works[16]. Though our platform found a greater number and intensity of these peaks which we believe to be linked to the plasmonic enhanced ionization of the aluminum substrate[17, 18]. Also, machine learning algorithms were applied to tease out further spectral differences finding various lipid peaks specific to each strain. Then expanded to compare and differentiate these *S. aureus* strains from various other bacterial species analyzed in our lab. Demonstrating the ability to highly accurately differentiate between not only the *S. aureus* strains but also *Escherichia coli*, *Listeria monocytogenes*, *Salmonella typhimurium*, *Vibrio cholerae*, and a mixture of *E. coli* and *L. monocytogenes*. Thus, building the groundwork for a wide reaching MALDI-MS platform enabling lipidomic/metabolomic based bacterial identification.

5.2 Experimental Methods

Materials and Reagents.

Acetonitrile (ACN), super 2,5 - dihydroxybenzoic acid (sDHB), and lysogeny broth (LB) Broth (Miller) medium were purchased from Sigma-Aldrich. Plain BK-7 microscope slides as well as antibiotics methicillin, vancomycin, and oxacillin were acquired from Fisher Scientific (Hampton, NH). Ultrapure water (>18 MΩ cm-1) was acquired from a Barnstead E-Pure water purification system. Matrix solutions of sDHB to a final concentration of 10 mg/mL were prepared with a (2:1, v/v) mix of acetonitrile and a 1% TFA/water solution. Antibiotic stock solutions were prepared in ultrapure water accounting for manufacturer measured purity.

Fabrication of Aluminum MALDI μChips.

The aluminum microchip arrays were fabricated in the UCR Cleanroom facility following previously published procedures[19]. In short, the arrays were formulated via a photo-lithographic method. First, AZ5214E photoresist was spun-coated onto glass slides followed by a 1-minute bake on a hotplate at 110 °C. Then, the array was patterned onto the glass slide using a mask aligner and the chips were baked again before a UV flood curing step. After this the photoresist was developed using AZ400K developing solution. Next, 150 nm of Al was deposited on the arrays using an electron beam physical vapor deposition (EBPVD) system (Temescal, Berkeley, CA). Following this deposition, the photoresist was removed using acetone leaving open wells that were then coated in a further 15 nm of Al resulting in an array of 600 x 600 μm aluminum wells.

Bacterial Strain and Culture Conditions.

Bacteria isolates of methicillin susceptible *Staphylococcus aureus (*MSSA*)* ATCC 12600 and methicillin resistant *S. aureus* ATCC 43300 were obtained from the American Type Culture Collection (ATCC, Manassas, VA). First-generation bacterial strains were revived upon receipt following ATCC recommended growth conditions. Revived bacterial strains were grown overnight and aliquoted into vials with equal 250 μL quantities of bacterial culture and 40% (v/v) glycerol in water and frozen until further experimental use. For experimental purposes bacterial strains were grown overnight to early stationary phase in LB Broth (Miller) growth medium within a shaker at 37℃ and 220 rpms. The turbidity of bacterial suspensions was used to determine the cell density via an Agilent spectrophotometer (Cary 60 UV-Vis) based on the optical density at 600 nm as is well documented in the literature[20]. For MALDI-MS experiments bacteria were harvested by three-fold centrifugation at 8000 rpm for 10 min followed by washing with deionized water prior to suspension in water to selected concentrations and deposition on MALDI-MS substrates.

Antibiotic Treatment and Susceptibility Tests

Antibiotic susceptibility was measured using the broth microdilution method[21] as is recommended by the EUCAST[22]. First 100 μL of LB was added to all wells of a 96-well plate then 100 μL of the selected antibiotic solution with concentration 2x the desired highest concentration was added to the left most column and sequentially diluted across the plate providing a sequentially 2-fold diluted concentration range (0.0625 – 64 mg/L).

Finally, 5uL of bacteria (10^6 cells/mL) were pipetted into each of these wells. The two left most columns were utilized as negative and positive controls respectively by excluding them from receiving any antibiotics and the negative wells also did not have any bacteria added. Plates were placed into a shaker and bacteria were allowed to grow for 18 h at 37 °C prior to cell growth measurement via absorbance plate reader at 600 nm.

MALDI-TOF-MS Sample Preparation and Spectra Acquisition.

For each experiment 1uL of bacteria sample (~10^9 cells/mL) was deposited within wells of the aluminum microarray allowed to dry and then covered in 1uL of sDHB matrix solution. MALDI-MS experiments were then conducted on an AB-Sciex 5800 time-of-flight mass spectrometer with a 337nm nitrogen UV laser. Lipid/metabolite fingerprints of bacteria were acquired in both positive and negative ion mode with a laser power of 6000 a.u. Each spectrum consists of a compilation of 300 laser shots fired over a selected bacteria spot.

MALDI-MS Data Analysis and Machine Learning

MALDI-MS data was acquired in the TOF/TOF Series Explorer software version 4.1.0 (AB Sciex) and then visualized and processed using MMass[23] after conversion from t2d to mzxml file format. Raw spectra were also fed into a home-built R script for processing, peak selection and application in training and testing of machine learning models. These selected peak intensities were tabulated for each spectrum and utilized to train various machine learning models using the caret[24] package including linear discriminant analysis, neural networks, support vector machines, random forest, and k nearest neighbor models to identify the ideal model for bacterial species classification from the MS data.

5.3 Results and Discussion

Antibiotic Susceptibility of *S. aureus* Strains

We then focused on confirming and measuring the antibiotic susceptibility of the two *S. aureus* strains using broth microdilution method described in the methods section

EC_{50} Values	Susceptible Strain (12600)	Resistant Strain (43300)
Vancomycin	0.9735	0.9463
Methicillin	0.2573	3.3883
Oxacillin	0.0584	0.4695

Table 5.1. Calculated EC_{50} values of antibiotics against methicillin susceptible and resistant *S. aureus*.

with the resulting EC_{50} values shown in Table 5.1. From these absorbance values, we plotted dose response curves for each of the antibiotics against each strain as can be seen in Figure 5.1. These results showed a marked increase in resistance to methicillin and oxacillin as expected for the 43300 *S. aureus* strain and no change in susceptibility to vancomycin between the two strains. An over ten-fold increase in EC50 (Table 5.1) for methicillin was observed for the resistant strain while an eight-fold increase was realized for oxacillin, demonstrating the substantial impact on drug effectiveness caused by these strain mutations. Furthermore, with a cursory glance a minimum inhibitory concentration (MIC) of ~10 mg/L for methicillin and oxacillin placed the resistant strain well over the 4 mg/L cutoff used to denote antibiotic resistance[25]. Now that we had quantified the

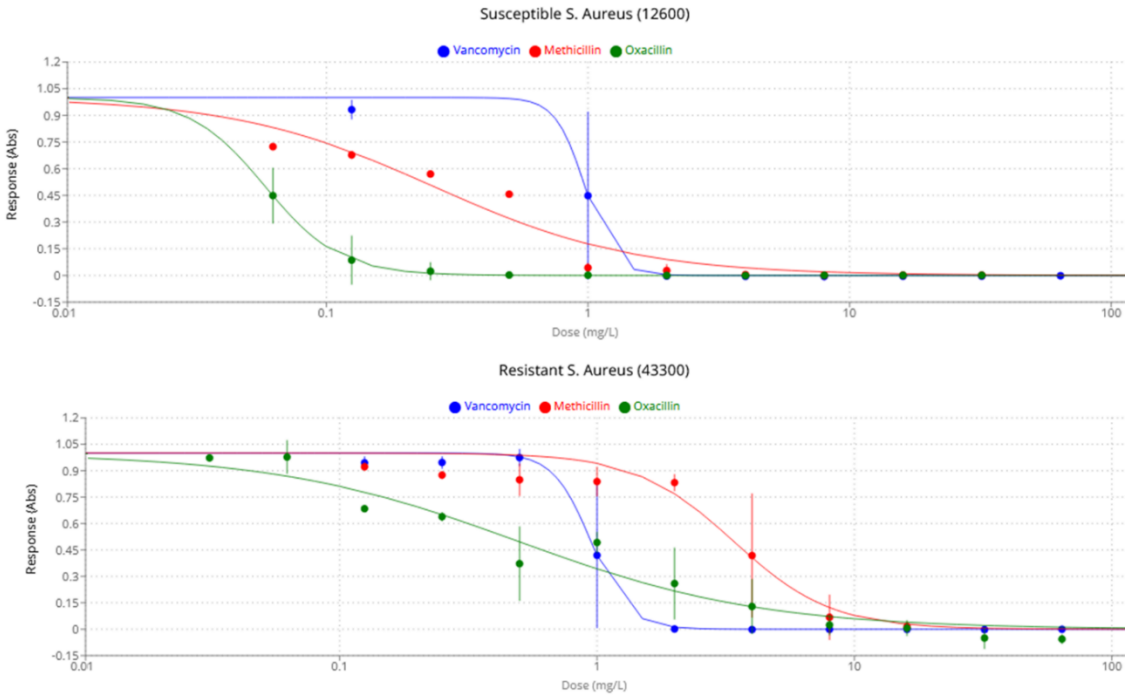

Figure 5.1. Dose response curves for vancomycin (blue), methicillin (red), and oxacillin (green) treatment against methicillin susceptible S. aureus (top) and resistant (bottom) strains.

antibiotic susceptibility differences between these *S. aureus* strains, we transitioned into analyzing how these differences translated into their lipid and metabolite profiles.

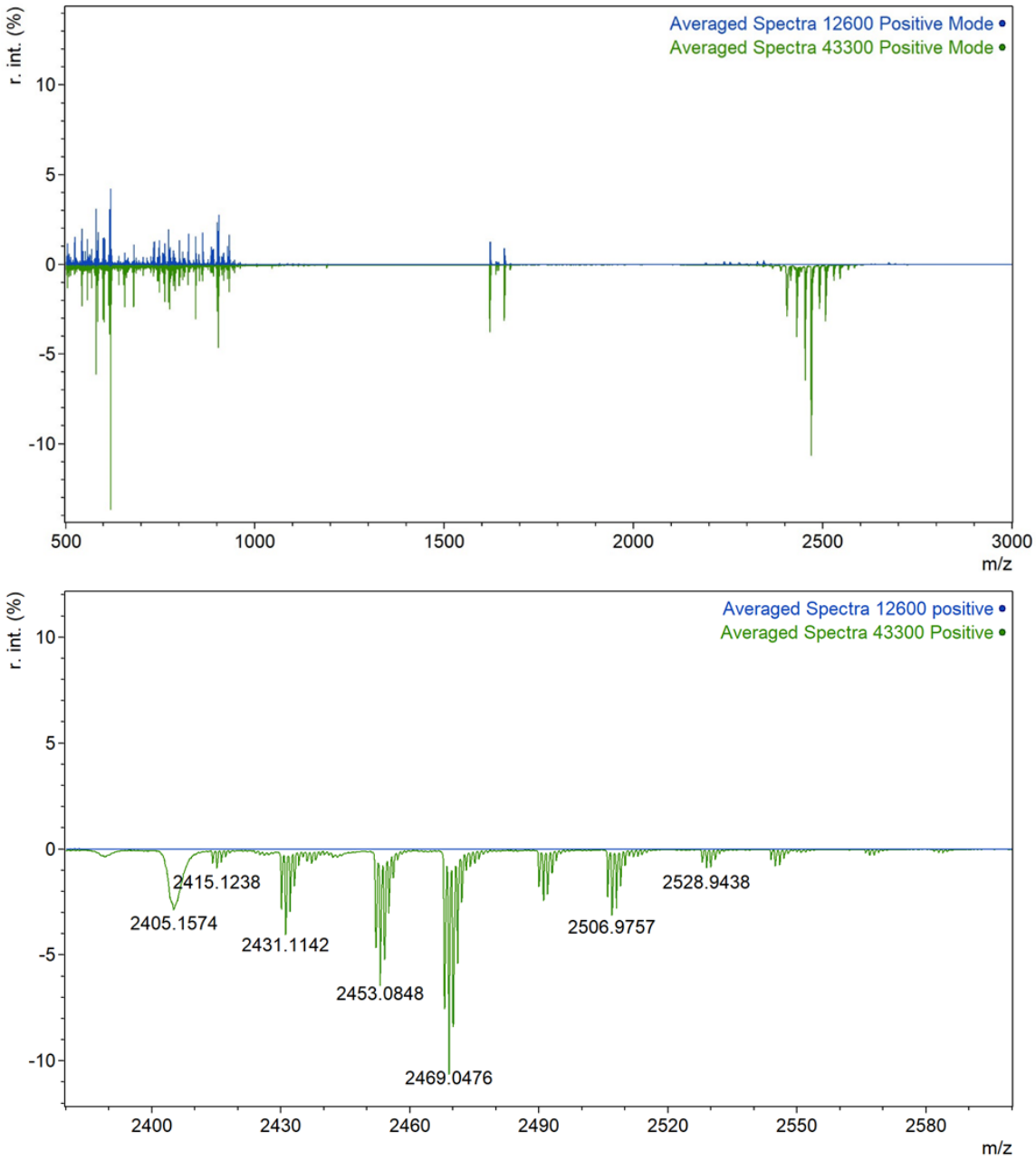

Figure 5.2. Comparison of averaged spectra collected from MSSA (blue) and MRSA (green) strains. With focus on the 2400-2600 m/z region (bottom) that shows distinct differences in the MALDI-MS profiles of the two strains.

Intact *S. aureus* bacteria were spotted on the array spots of fabricated aluminum microarrays coated in matrix and transferred to MALDI instrumentation for analysis of

lipids/metabolites. Ions were collected between 100 and 3000 m/z in both positive and negative ion mode though positive mode was selected for further studies due to improved resolution and a greater number of identifiable peaks. Then MALDI-MS spectra were compared between the two strains at ~10^9 cells/mL as our previous bacterial MALDI-MS studies that have found this as an ideal concentration for analysis[26]. When comparing spectra between the two strains at this cell count major peaks were identifiable in the 500-1000, 1600-1700, and 2200-2600 m/z regions (Figure 5.2). Upon inspection some clear differences were noticed, notably distinct peaks in the 2400-2600 m/z range were only observed in the resistant strain. This fit with literature reports finding a singular peak at 2415 m/z that was highly specific to MRSA resulting in highly confident identification[16, 27, 28]. This peak has been associated with an amphipathic alpha-helical peptide PSM-mec that is found in some resistant strains within the *Staphylococcus* cassette chromosome mec (SCC-mec) which codes for methicillin resistance[29, 30]. This peptide has a mass of 2386.834 Da based on its sequence (MDFTGVITSIIDLIKTCIQAFG) but the N-terminal methionine is formylated in cells resulting in the 2415 m/z peak seen in MALDI-MS analysis[15]. As such, it provides a peptide signature for these forms of MRSA which can be utilized to identify antibiotic resistance. We observed this peak as seen in Figure 5.2 however we also observed a larger number of other peaks in this region that were specific to the resistant strain that had not been reported in these works. One of these peaks, 2431 m/z, was also observed in work focused on peptide identification of MRSA strains where it was found to be present in SCCmec I and II strains[31]. This confirmed our results as the MRSA strain we analyzed in this work is SCCmec type II. Though other peaks notably 2453 and 2469 m/z

were observed at higher abundance than either of these previously established markers for MRSA. These are believed to also be related to psm-mec but will require a more in-depth study. One possibility is that they are sodiated and potassiated versions of the 2431 m/z [M+H+] peak as they fit the classic +22 and +38 of these adducts. Despite this the collected MS data demonstrates that our MALDI-MS platform is able to provide robust signal for these important peptide marker peaks via ionization of intact whole bacteria. We believe that the aluminum plasmonic array plays a role in enhancing the ionization of these molecules via a similar process as that identified in our previous work with gold microarrays[17]. However, profile differences in the lower m/z ranges were not as easily visually identifiable therefore more in-depth analysis was necessary.

Machine Learning Classification of *S. aureus* Strains

To piece through the more minute differences in the 600-2000 m/z lipid region we employed machine learning methods to help identify the most significant differences. To achieve this a home-built r script was written utilizing the maldiquant[32] package to process raw MALDI-MS spectrum, select, compile, and compare peak intensities across hundreds of spectra. First raw spectra obtained from the MALDI instrument software in t2d format were converted to mzxml form using a converter available at http://www.pepchem.org/download/converter.html. This data was then pulled into R and compiled into a spectra list with appended bacterial class information for later machine learning steps. Then each spectra's intensity was smoothed using the moving average method followed by baseline correction using the sensitive non-linear iterative peak-clipping algorithm. Spectral processing was completed with spectral alignments and

intensity normalization which was found to significantly improve machine learning algorithm results. Then peaks with signal to noise ratios above 10 were selected, binned, and filtered out if they did not appear in at least 30 percent of the spectra to limit impact of transient peaks. Peaks below 500 m/z were removed as they mostly represented matrix ions and therefore were found to provide little aid in effective separation due their addition convoluting the machine learning. The intensity values for the remaining peaks were compiled into an intensity matrix for each of the included spectra with their bacteria class. This information was then fed into chosen machine learning algorithms with a 70 percent split for training and the remaining 30 percent utilized as test cases. To limit over training and impact of individual spectra on algorithm results 3 time repeated 10-fold cross

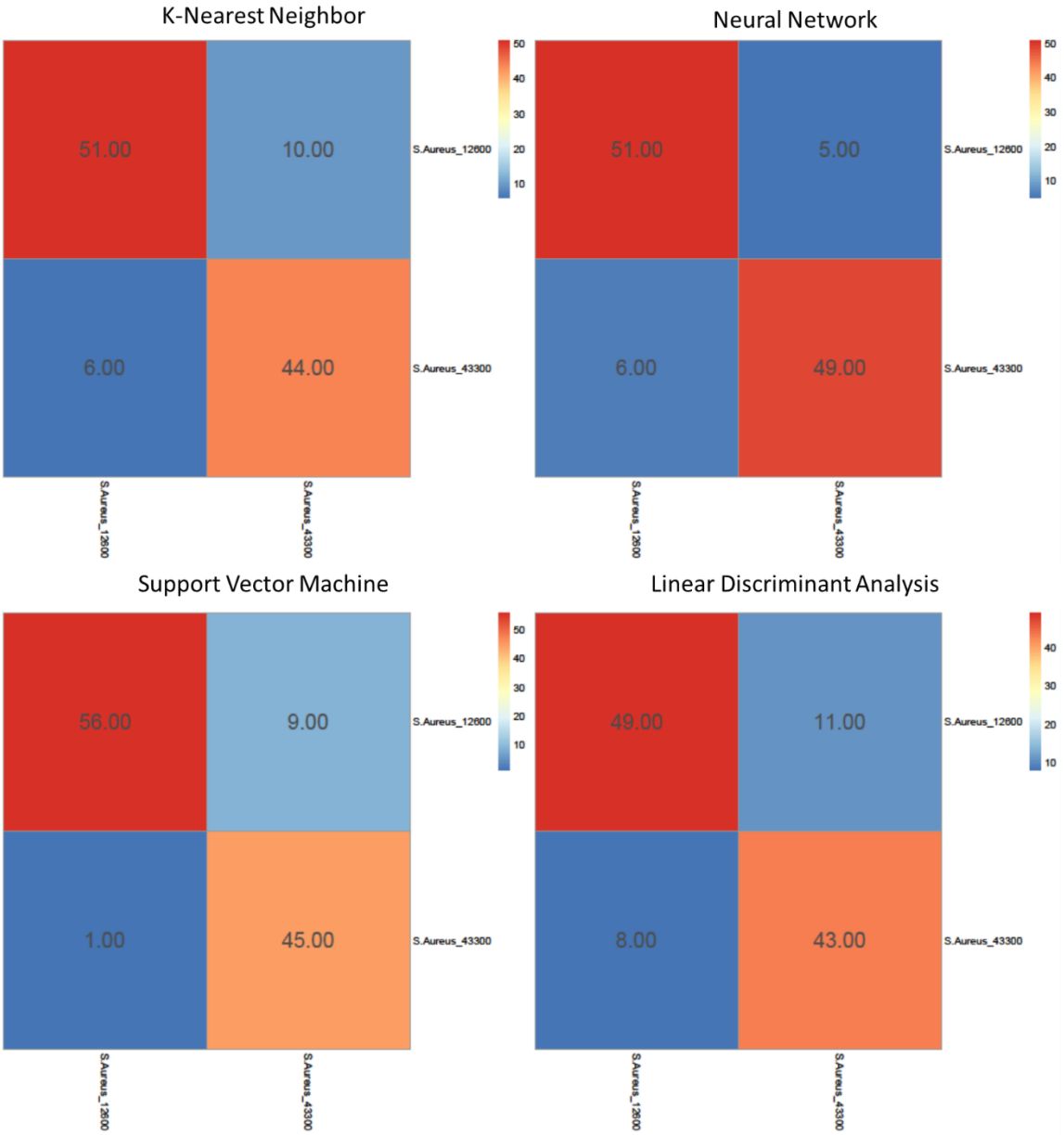

Figure 5.3. Classification results of 4 different machine learning models for S. aureus bacterial strain using MALDI-MS peak information from the 500-3000 m/z region.

validation was used. Classification results of individual spectra were then plotted as confusion matrices to visualize model accuracy as can be seen in Figure 5.3. As the accuracy of models can be variable based on the data selected for training and testing, especially when working with smaller datasets, we endeavored to investigate the variability

Model	Accuracy (500-3000 m/z)	Accuracy (500-2000 m/z)
Random Forest (rf)	89.37 ± 1.91 %	85.69 ± 2.30 %
Support Vector Machines (svmLinear2)	88.00 ± 2.83 %	87.64 ± 3.18 %
K-nearest neighbor (kknn)	86.05 ± 2.86 %	83.64 ± 2.82 %
Linear Discriminant Analysis (LDA)	82.59 ± 3.15 %	81.23 ± 3.67 %
Neural Network (nnet)	90.59 ± 2.38 %	86.09 ± 4.03 %

Table 5.2. Resulting accuracy and standard deviation of ML models when given *S. aureus* MALDI-MS data from peaks with the 500-3000 or 500-2000 m/z ranges indicating algorithm effectiveness at identifying S. aureus strain with and without peaks specific to PSM-mec.

of our models. As such, each model was trained 25 times, and the resulting accuracy was averaged to provide information about the expected accuracy and variability of model

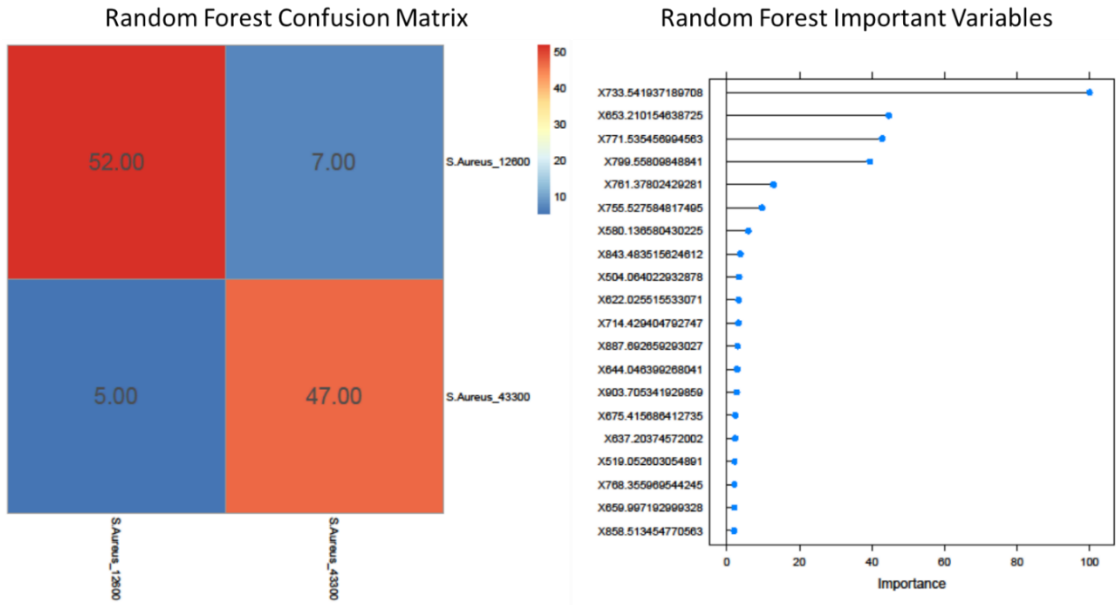

Figure 5.4. Results of random forest model training and testing using peaks from the 500-3000 m/z range shown in confusion matrix (left) demonstrating minimal misclassification. Also, indication of the most important variables (right) for classification showing peaks 2469 and 2431 m/z as top two factors in strain separation.

results (Table 5.2). This information helps identify the ML model that provides the most effective classification of the selected bacterial classes. For example, from these results we

can see that the neural network model provides the highest accuracy of 90.59 ± 2.38 % for differentiation between the two *S. aureus* strains with minimal variability. Finally, to provide a deeper insight into model classification the important variables of the random forest model were pulled out based on out-of-bag error providing a list of peaks most important for successful strain separation as can be seen in Figure 5.4. These model results were also completed for a truncated list of peaks excluding those peaks beyond 2000 m/z which were previously shown to be major indicators of MRSA. With the results shown in Table 5.2 displaying only a small decrease in accuracy for each of the tested ML

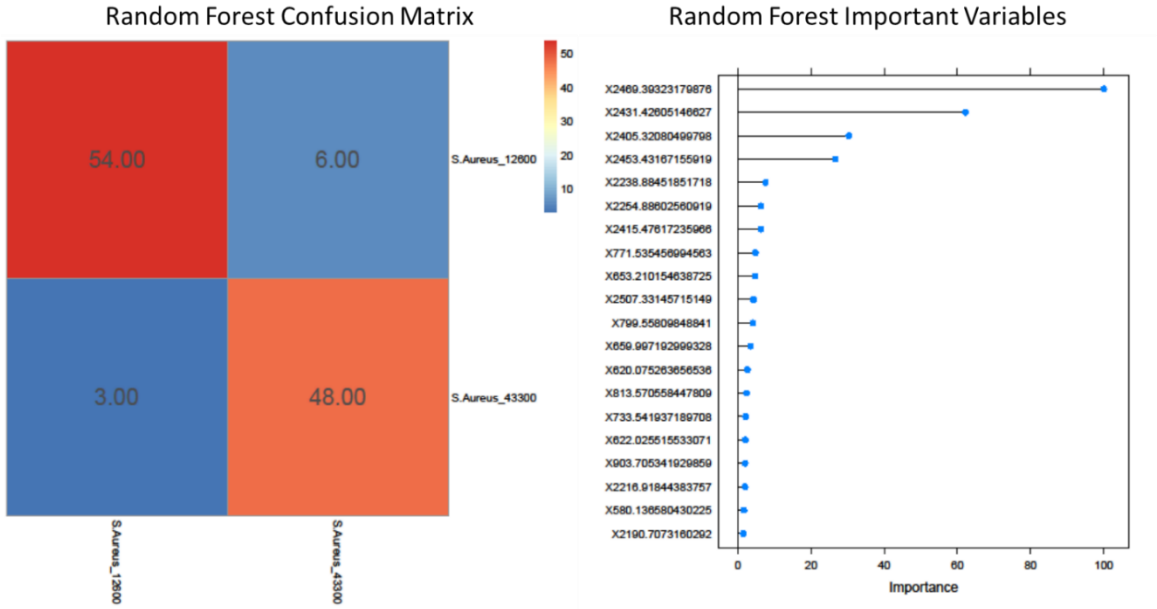

Figure 5.5. Results of random forest modeling on a truncated MALDI-MS peak dataset excluding peaks above 2000 m/z.

algorithms. This not only demonstrated that the *S. aureus* strains could still be separated without this but also provided the lipid peaks most crucial to this classification, Figure 5.5. Based on the random forest model peaks 733.5, 653.2, 771.5, and 799.5 m/z are found to be the most important for classification between the two *S. aureus* strains. Therefore, these peaks stand out as the targets for molecular identification in future work to understand the

lipid metabolism differences between the susceptible and resistant *S. aureus*. With these results we were able to accurately differentiate between a MRSA and susceptible *S. aureus* from a singular MALDI-MS spectrum even without the PSM-mec peaks showing substantial promise as a platform for bacterial identification. But of course, the consideration then arose of whether this lipid profile information was sufficient to enable bacterial identification from a larger set of possible species.

Expansion of Machine Learning Classification to Other Bacterial Species

To demonstrate the potential of applying this lipid profile data to separate a diverse range of bacteria we employed MALDI-MS lipidomics data collected across many different bacteria. This data was pulled into and processed using the same R script previously described with minor modifications to accommodate the larger dataset and

Model	Accuracy
Random Forest (rf)	89.97 ± 1.55 %
Support Vector Machines (svmLinear2)	86.73 ± 1.80 %
K-nearest neighbor (kknn)	81.61 ± 1.66 %
Linear Discriminant Analysis (LDA)	66.45 ± 4.10 %
Neural Network (nnet)	42.57 ± 3.77 %

Table 5.3. Average accuracy and standard deviation of the ML algorithms utilized for classification of bacterial species/strain, calculated from 25 repeated training and test cycles.

greater number of classes. These modifications included changing the minimum frequency for peak filtering to ensure that peaks specific to an individual bacteria were not lost and code alterations to accommodate the greater number of classes/data. The resulting models

were still able to accurately distinguish between this greater number of bacterial species in most cases as can be seen in Table 5.3. With these model accuracy results one surprising difference was the loss of neural network capability especially as it was the model that most accurately separated the *S. aureus* data. This indicated it was not suited to this classification task as the number of classes expanded. This could be in part due to the greater number of spectra from the S. aureus strains utilized in training limiting its ability to identify the other bacteria. However, the random forest model resulted in the most accurate classification between these 7 bacterial species/strains and a mixture of *E. coli* and *L. monocytogenes.* This nearly 90% accuracy with only minimal variability

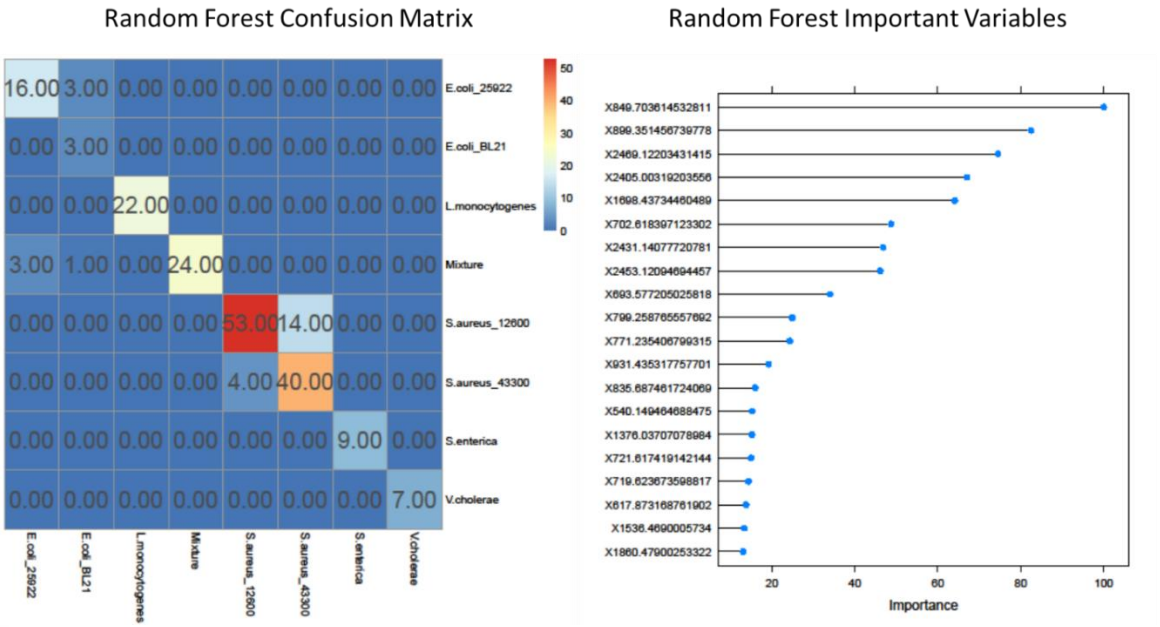

Figure 5.6. Confusion matrix and important variables obtained from random forest model training and testing on 8 different bacterial classes.

demonstrates a highly effective method for bacterial classification. We again employed the out-of-bag error from the random forest model to identify important peaks in this classification as seen in Figure 5.6. Though the greater number of bacterial species and thus peaks convoluted this a bit, the important peaks were found to match with those

previously found with the *S. aureus* ML classification. Notably the psm-mec 2469 m/z peak was the third most important peak for classification while lipid peaks 849.7 and 899.3 m/z were first and second respectively which match with machine learning results obtained

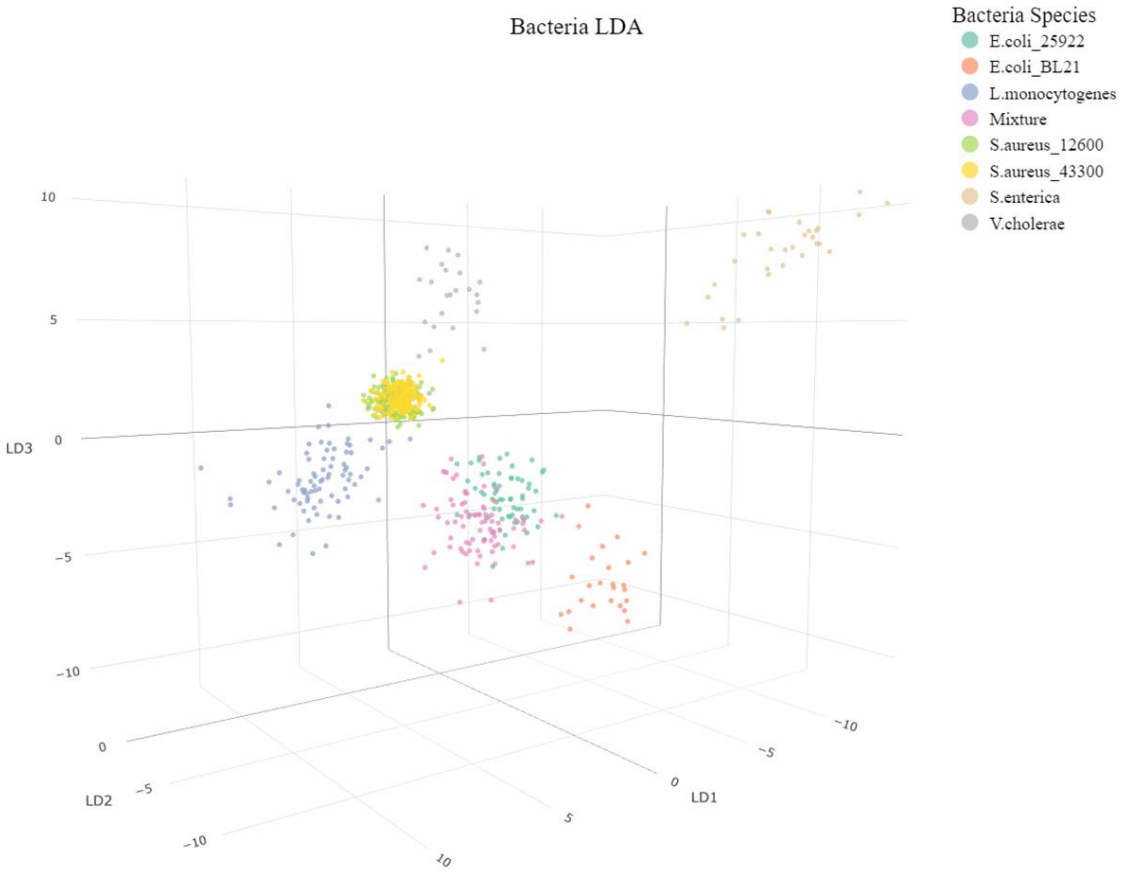

Figure 5.7. 3D plot of linear discriminant analysis separation of bacterial species.

from the six bacterial classes prior to addition of the *S. aureus* data. While the LDA accuracy was far from the most accurate its computation time was by far the fastest, which could be valuable when expanding to larger datasets or when time is limited. Furthermore, the linear discriminants utilized in LDA are conducive to plotting allowing for visualization of how the model is separating the bacterial classes. Therefore, we plotted the top three linear discriminant parameters in a 3-dimensional space (Figure 5.7). Interestingly, when

looking at the plot all species were separated except for the *S. aureus* strains but this is likely due to the limitation of only three linear discriminants while model classification takes into account many other linear discriminants.

5.4 Conclusion

We have demonstrated an aluminum plasmonic microarray platform for robust MALDI-MS spectra acquisition from intact MSSA and MRSA bacteria resulting in clear identification of peptides peaks specific to the MRSA strain. Machine learning algorithms were then employed to streamline the separation of these strains and exhibited the ability to accurately classify even without the inclusion of these MRSA specific peptide peaks. Furthermore, the important peaks for classification were pulled out and provide information about which peptide or lipid peaks should be investigated further. These algorithms were then expanded to explore the potential to enable identification of a larger range of bacterial species/strains from each other. This resulted in models that could accurately classify a bacterial sample from a list of 8 different possibilities with only the data from a singular MALDI-MS spectra. This platform can be easily applied to other bacterial species to broaden bacterial identification capabilities.

5.5 References

1. Collaborators, A. R., Global mortality associated with 33 bacterial pathogens in 2019: a systematic analysis for the Global Burden of Disease Study 2019. *The Lancet* **2022,** *400* (10369), 2221-2248.

2. Ren, M.; So, A. D.; Chandy, S. J.; Mpundu, M.; Peralta, A. Q.; Åkerfeldt, K.; Sjöblom, A. K.; Cars, O., Equitable Access to Antibiotics: A Core Element and Shared Global Responsibility for Pandemic Preparedness and Response. *The Journal of law, medicine & ethics : a journal of the American Society of Law, Medicine & Ethics* **2022,** *50* (S2), 34-39.

3. Outterson, K.; Orubu, E. S. F.; Rex, J.; Årdal, C.; Zaman, M. H., Patient Access in 14 High-Income Countries to New Antibacterials Approved by the US Food and Drug Administration, European Medicines Agency, Japanese Pharmaceuticals and Medical Devices Agency, or Health Canada, 2010–2020. *Clinical Infectious Diseases* **2021,** *74* (7), 1183-1190.

4. Collaborators, A. R., Global burden of bacterial antimicrobial resistance in 2019: a systematic analysis. *The Lancet* **2022,** *399* (10325), 629-655.

5. Samreen; Ahmad, I.; Malak, H. A.; Abulreesh, H. H., Environmental antimicrobial resistance and its drivers: a potential threat to public health. *Journal of Global Antimicrobial Resistance* **2021,** *27*, 101-111.

6. Ventola, C. L., The antibiotic resistance crisis: part 1: causes and threats. *P & T : a peer-reviewed journal for formulary management* **2015,** *40* (4), 277-83.

7. Organization, W. H., *Antimicrobial resistance: global report on surveillance*. World Health Organization: 2014.

8. Álvarez, A.; Fernández, L.; Gutiérrez, D.; Iglesias, B.; Rodríguez, A.; García, P., Methicillin-Resistant Staphylococcus aureus in Hospitals: Latest Trends and Treatments Based on Bacteriophages. *Journal of Clinical Microbiology* **2019,** *57* (12), 10.1128/jcm.01006-19.

9. Chen, C.-J.; Huang, Y.-C.; Shie, S.-S., Evolution of Multi-Resistance to Vancomycin, Daptomycin, and Linezolid in Methicillin-Resistant Staphylococcus aureus Causing Persistent Bacteremia. **2020,** *11*.

10. Vestergaard, M.; Frees, D.; Ingmer, H., Antibiotic Resistance and the MRSA Problem. **2019,** *7* (2), 10.1128/microbiolspec.gpp3-0057-2018.

11. Maugeri, G.; Lychko, I.; Sobral, R.; Roque, A. C. A., Identification and Antibiotic-Susceptibility Profiling of Infectious Bacterial Agents: A Review of Current and Future Trends. *Biotechnology Journal* **2019,** *14* (1), 1700750.

12. Dietvorst, J.; Vilaplana, L.; Uria, N.; Marco, M.-P.; Muñoz-Berbel, X., Current and near-future technologies for antibiotic susceptibility testing and resistant bacteria detection. *TrAC Trends in Analytical Chemistry* **2020,** *127*, 115891.

13. Franco-Duarte, R.; Černáková, L.; Kadam, S.; Kaushik, K. S.; Salehi, B.; Bevilacqua, A.; Corbo, M. R.; Antolak, H.; Dybka-Stępień, K.; Leszczewicz, M.; Relison Tintino, S.; Alexandrino de Souza, V. C.; Sharifi-Rad, J.; Coutinho, H. D. M.; Martins, N.; Rodrigues, C. F., Advances in Chemical and Biological Methods to Identify Microorganisms-From Past to Present. *Microorganisms* **2019,** *7* (5).

14. Giuliano, C.; Patel, C. R.; Kale-Pradhan, P. B., A Guide to Bacterial Culture Identification And Results Interpretation. *P & T : a peer-reviewed journal for formulary management* **2019,** *44* (4), 192-200.

15. Qin, L.; McCausland, J. W.; Cheung, G. Y.; Otto, M., PSM-Mec-A Virulence Determinant that Connects Transcriptional Regulation, Virulence, and Antibiotic Resistance in Staphylococci. *Front Microbiol* **2016,** *7*, 1293.

16. Rhoads, D. D.; Wang, H.; Karichu, J.; Richter, S. S., The presence of a single MALDI-TOF mass spectral peak predicts methicillin resistance in staphylococci. *Diagnostic Microbiology and Infectious Disease* **2016,** *86* (3), 257-261.

17. Shanta, P. V.; Li, B.; Stuart, D. D.; Cheng, Q., Lipidomic Profiling of Algae with Microarray MALDI-MS toward Ecotoxicological Monitoring of Herbicide Exposure. *Environmental Science & Technology* **2021,** *55* (15), 10558-10568.

18. Bondarenko, A.; Zhu, Y.; Qiao, L.; Cortés Salazar, F.; Pick, H.; Girault, H. H., Aluminium foil as a single-use substrate for MALDI-MS fingerprinting of different melanoma cell lines. *The Analyst* **2016,** *141* (11), 3403-10.

19. Lambert, A. S.; Valiulis, S. N.; Malinick, A. S.; Tanabe, I.; Cheng, Q., Plasmonic Biosensing with Aluminum Thin Films under the Kretschmann Configuration. *Analytical Chemistry* **2020,** *92* (13), 8654-8659.

20. Sultana, L.; Sanchis, A. G., Establishing the lower bacterial concentration threshold for different optical counting techniques. *Journal of Microbiological Methods* **2022,** *203*, 106620.

21. Kowalska-Krochmal, B.; Dudek-Wicher, R. The Minimum Inhibitory Concentration of Antibiotics: Methods, Interpretation, Clinical Relevance *Pathogens* [Online], 2021.

22. Determination of minimum inhibitory concentrations (MICs) of antibacterial agents by broth dilution. *Clinical Microbiology and Infection* **2003,** *9* (8), ix-xv.

23. Strohalm, M.; Kavan, D.; Novák, P.; Volný, M.; Havlíček, V., mMass 3: A Cross-Platform Software Environment for Precise Analysis of Mass Spectrometric Data. *Analytical Chemistry* **2010,** *82* (11), 4648-4651.

24. Kuhn, M., Building Predictive Models in R Using the caret Package. *Journal of Statistical Software* **2008,** *28* (5), 1 - 26.

25. J., S. A. a. K., *Methicillin-Resistant Staphylococcus aureus.* StatPearls Publishing: Treasure Island (FL), 2023.

26. Li, B. Sing-Cell Lipidomic Analysis and Cytotoxicity Studies of Microorganisms Enabled by Plasmonics-Enhanced MALDI-MS. UC Riverside, 2022.

27. Alksne, L.; Makarova, S.; Avsejenko, J.; Cibrovska, A.; Trofimova, J.; Valciņa, O., Determination of methicillin-resistant Staphylococcus aureus and Staphylococcus epidermidis by MALDI-TOF MS in clinical isolates from Latvia. *Clinical mass spectrometry (Del Mar, Calif.)* **2020,** *16*, 33-39.

28. Gao, W.; Li, B.; Ling, L.; Zhang, L.; Yu, S., MALDI-TOF MS method for differentiation of methicillin-sensitive and methicillin-resistant Staphylococcus aureus using (E)-Propyl α-cyano-4-Hydroxyl cinnamylate. *Talanta* **2022,** *244*, 123405.

29. Kaito, C.; Saito, Y.; Nagano, G.; Ikuo, M.; Omae, Y.; Hanada, Y.; Han, X.; Kuwahara-Arai, K.; Hishinuma, T.; Baba, T.; Ito, T.; Hiramatsu, K.; Sekimizu, K., Transcription and Translation Products of the Cytolysin Gene psm-mec on the Mobile Genetic Element SCCmec Regulate Staphylococcus aureus Virulence. *PLOS Pathogens* **2011,** *7* (2), e1001267.

30. Reichmann, N. T.; Pinho, M. G., Role of SCCmec type in resistance to the synergistic activity of oxacillin and cefoxitin in MRSA. *Scientific Reports* **2017,** *7* (1), 6154.

31. Lu, J.-J.; Tsai, F.-J.; Ho, C.-M.; Liu, Y.-C.; Chen, C.-J., Peptide Biomarker Discovery for Identification of Methicillin-Resistant and Vancomycin-Intermediate Staphylococcus aureus Strains by MALDI-TOF. *Analytical Chemistry* **2012,** *84* (13), 5685-5692.

32. Gibb, S.; Strimmer, K., MALDIquant: a versatile R package for the analysis of mass spectrometry data. *Bioinformatics* **2012,** *28* (17), 2270-2271.

Chapter 6: Surface Plasmon Resonance Gas Detection Enabled by Refractive Index Pressure Dependance

6.1 Introduction

In recent decades hydrogen has emerged as a potential sustainable energy source that can play an important role in reducing our reliance on fossil fuels.[1] It has been investigated for its applications in fuel cell based electric vehicles[2], energy storage[3], and power generation[4] as well as various other uses[5]. Though, for hydrogen to realize its full potential new infrastructure needs to be built to accommodate the storage, transport, usage, and monitoring of hydrogen which can become prohibitively expensive.[6] One consideration to alleviate these costs, that has attracted considerable attention, is the doping of hydrogen into our current natural gas pipelines to make use of the large-scale infrastructure already in place.[7] However, due to hydrogen's small size it is prone to leaking meaning that to achieve this without unwarranted danger to human life appropriate monitoring would need to be implemented.[8] As such, new sensing methodologies for hydrogen are necessary that can safely provide real time information about the gas mixture within a pipeline to identify leaks as they evolve before they become hazardous. Hydrogen sensors can also provide value in a variety of other areas of hydrogen usage such as hydrogen fueled turbines where robust sensors are needed to monitor the inputs and outputs of the energy production process. While there are currently various commercially available hydrogen sensors. These sensors commonly work through catalytic combustion or conductivity measurements which suffer from some limitations. Notably, the electrical components required for their usage increase the potential of accidental hydrogen ignition especially as the energy required for hydrogen ignition (0.02 mJ) is significantly lower than that for other gases.[9]

Also, many of these sensors have limited lifetimes, detection ranges, vulnerability to humidity, and limited stability.[10, 11] As such, optical hydrogen sensors have appeared as attractive alternatives as any electrical components can be separated from the sensing, but these sensors are still under explored. One methodology that shows substantial promise is surface plasmon resonance (SPR) spectroscopy a highly sensitive, real-time, and label free technique.[12] Recently SPR setups have been employed for sensing of nitrogen dioxide[13], methane[14], hydrogen sulfide[15], and hydrogen[16]. Demonstrating the feasibility of SPR based gas sensors and introducing them as a potential avenue to improve gas sensing methodologies. However, the vast majority of SPR applications are in the liquid phase[ref] with those in the gas phase generally focusing on singular gases. To truly enable gas based SPR sensing new methods or materials that impart gas selectivity are necessary, as without selectivity gas mixtures can severely convolute sensor signal.

Herein we report a real-time optical sensor for hydrogen gas detection based on SPR which has also has applicability to sensing of other gases and mixtures. Where small mass or refractive index changes can be monitored through changes in light reflection and absorption caused by changes in the dielectric adjacent to a thin plasmonic metal surface. In this work, we first explore the capability of SPR sensors to detect various percentages mixtures of gas phase hydrogen and examine the potential of MOF materials to provide selectivity to this SPR based gas phase detection. We then identify a unique relationship between pressure and SPR response that relates to differences in the polarizability of gases. We further demonstrate the potential to utilize these pressure effects to enable selective sensing of gases and gas mixtures without the need for a MOF for gas capture. Moreover,

machine learning algorithms were applied to demonstrate feasibility of differentiation even between gases (nitrogen, argon, and air) with highly similar refractive indices and polarizability. Overall demonstrating the potential for gas phase sensing using SPR spectroscopy methods and establishing a unique gas sensing platform based on combined SPR and pressure sensors providing the ability to monitor changes in gas mixture and pressure in real time. A methodology that can be highly effective in improving gas phase SPR analysis across the board.

6.2 Experimental Methods

Materials and Reagents.

Borosilicate glass microscope coverslips (18x18 mm) were purchased from Fisher Scientific (Pittsburgh, PA). Ultrapure water (>18 MΩ cm-1) was acquired from a Barnstead E-Pure water purification system. Regulators and small canisters of compressed hydrogen, nitrogen, methane, and hydrogen/nitrogen gas mixtures were purchased from Gasco (Oldsmar, FL). Compressed helium, nitrogen, carbon dioxide, argon, and air were obtained from Airgas (Radnor, PA). Metal organic framework crystals composed of zinc metal and imidazolate anions (ZIF-8) was acquired from Sigma-Aldrich (St. Louis, MO).

Fabrication of SPR Sensor Chips.

Surface plasmon resonance chips were fabricated with modifications from a previously published procedure[17] to accommodate coverslip glass instead of glass microscope slides. To begin, coverslips were cleaned in boiling piranha acid (3:1, H_2SO_4:H_2O_2) for 1 hour. Then piranha acid was poured off, and coverslips were thoroughly rinsed with ultrapure

water. Subsequently, coverslips were individually rinsed with water followed by ethanol before drying under nitrogen. Then 2 nm of chromium followed by 48 nm of gold was deposited upon the piranha cleaned coverslips via an electron beam physical vapor deposition (EBPVD) system (Temescal, Berkeley, CA) at the University of California, Riverside Center for Nanoscale Science and Engineering Nanofabrication Facility. Thin film gold chips were then directly utilized for SPR spectroscopy or further coated with materials to investigate their hydrogen binding capabilities.

SPR Analysis.

Gas phase sensing was achieved using a BI-2500 series (Biosensing Instrument, Tempe, AZ) equipped with a 670 nm laser light source. The instrument was fitted with a gas tight chamber above the sensor chip to enable gas flows to be introduced for spectroscopic measurement. For all experiments nitrogen was used as a carrier gas and a control to provide a consistent sensor baseline. Flow systems were set up to facilitate gas introduction into the sensing chamber and rapid transition between gases as well as outlet of gas into a fume hood.

Pressure Sensor Fabrication.

To augment SPR analysis a small pressure and temperature sensor was implemented in line with the gas flow immediately after the SPR sensor chip. Thus, enabling pressure and temperature data to be correlated with SPR spectroscopic shifts. The low-cost Arduino pressure sensor was assembled based on a design published by Goertzen et al.[18] The sensor housing was 3D printed using a Form 3 (Formlabs, Somerville, MA) stereolithography

printer using clear resin. The pressure sensor, resistors, capacitors, and solder paste were purchased from DigiKey Electronics (Thief River Falls, MN). The board (Adafruit Feather M0), pins, and a 3V lithium coin battery were bought from Adafruit (New York, NY). Additionally, a micro-USB cable and an SD card obtained from Amazon (Seattle, WA) were employed to upload code to the Arduino and for collection of pressure data. For data collection an Arduino library[ref], specific to the sensor (MS5803-01BA), was used to pull data from the pressure sensor and visualized using Arduino's serial monitor tool.

6.3 Results and Discussion

While SPR methodologies are capable of detecting small changes in refractive index within the dielectric close to the sensor surface, when working with gases these differences are significantly smaller than those commonly seen in liquid-based sensing.

Material	Refractive Index (n)	Extinction Coefficient (k)
BK7 Glass	1.5139	1.1715e-8
Chromium (Cr)	4.4409	4.6502
Gold (Au)	0.14360	3.8430
Hydrogen (H_2)	1.00013809	0
Nitrogen (N_2)	1.00029731	0
Methane (CH_4)	1.00044023	0

Table 6.1. Refractive index values for materials utilized in reflectivity curve modeling.

Therefore, to first test the theoretical feasibility of measuring differences between hydrogen and methane using SPR, characteristic reflective curves were simulated and compared to determine if refractive index differences would be detectable. This was achieved using WinSpall software based on layers input to match our experimental setup

with real (n) and imaginary (k) components of the material refractive index under 670 nm light (Table 6.1) obtained from experimental results compiled on refractiveindex.info.[19]

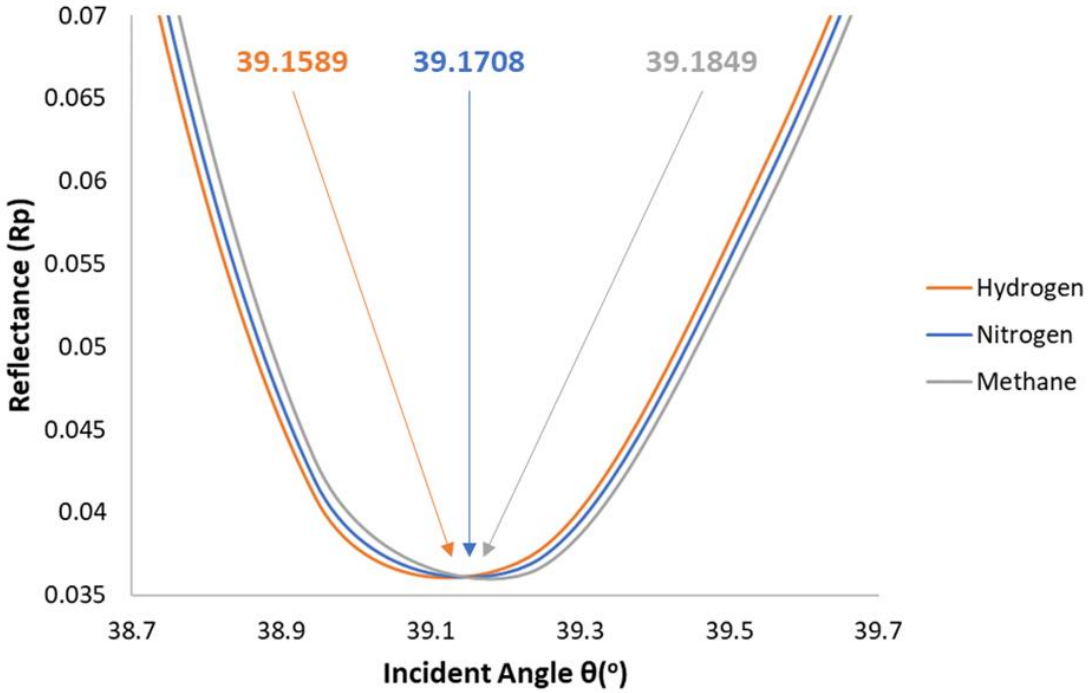

Figure 6.1. Modeled SPR reflectivity curves for hydrogen, nitrogen, and methane using parameters to match our experimental setup.

The simulation was formulated with layers composed of a BK-7 glass prism, 2 nm of chromium[20], 48 nm of gold[21], and 1 µm of the select gas[22-24]. The gases modeled here were hydrogen, methane, and nitrogen. As hydrogen was the gas we wanted to detect, methane is the major component in natural gas pipelines, and nitrogen would act as a carrier gas in much of our experimentation. These values were used to model reflectivity curves for each gas as can be seen in Figure 6.1. By comparing the minimum angle expected for each gas we also calculated expected angular shifts of the reflectivity minimum between gases. For example, the minimum angle shift between hydrogen and methane was found to be 0.026° which is well within the sensitivity capabilities of SPR instrumentation.[25] Furthermore,

nitrogen produced a very similar reflectivity curve to that of methane due to similarities in refractive index making it an ideal carrier gas for our studies in addition to being inert and readily available. So clearly the difference in refractive index between our gases of interest while small is likely enough to enable sensing but that still leaves the question of what limit of detection is possible and can gas selectivity be achieved.

Sensor Chip Fabrication and Characterization

Metal organic frameworks have been reported for their capabilities to selectively bind various gases from including hydrogen making them a potential source of sensor

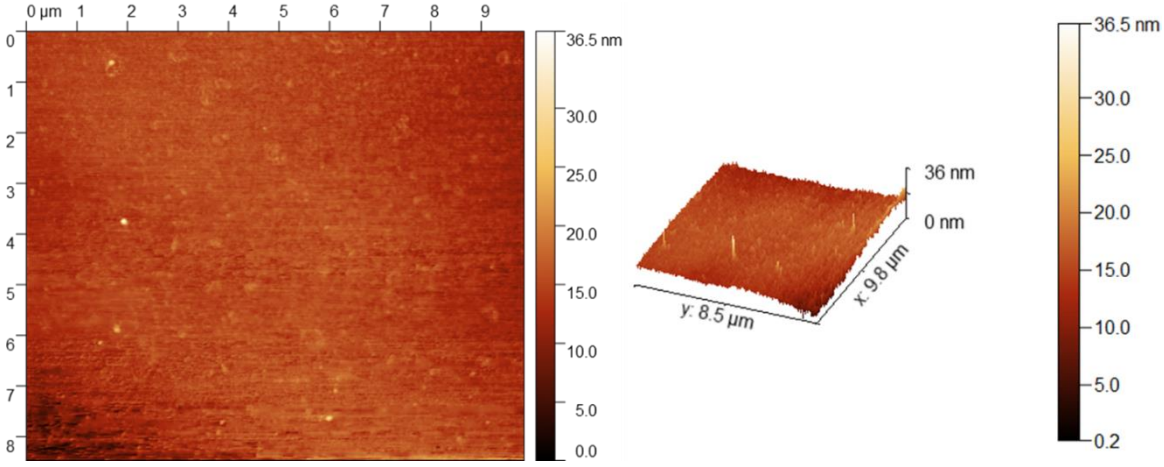

Figure 6.2. AFM images of thin film gold chips fabricated on glass coverslips demonstrating low surface roughness and high homogeneity essential to SPR sensing.

selectivity. However, metal organic frameworks on SPR chips have only recently been demonstrated and as the surface properties of SPR sensor chips are fundamental to their effectiveness in sensing applications careful fabrication and characterization is necessary. To this end, SPR chips were fabricated on coverslips as detailed above and characterized to ensure they maintained the surface characteristics necessary for effective sensing that has been identified for previously fabricated glass slide SPR chips.[12, 26] Using atomic force

microscopy the gold chips were found to have low surface roughness and a highly homogenous surface making them ideal for SPR sensing (Figure 6.2.). Furthermore, reflectivity curves obtained from these fabricated chips matched simulated curves quite well indicating applicability to gaseous systems. Then metal organic frameworks were formulated on the gold sensor surface through drop casting before characterization with optical microscopy and scanning electron microscopy (Figure 6.3). The first formulation of the metal organic framework formed into highly heterogenous clusters on the sensor surface with very high surface roughness which unfortunately limits MOF surface area

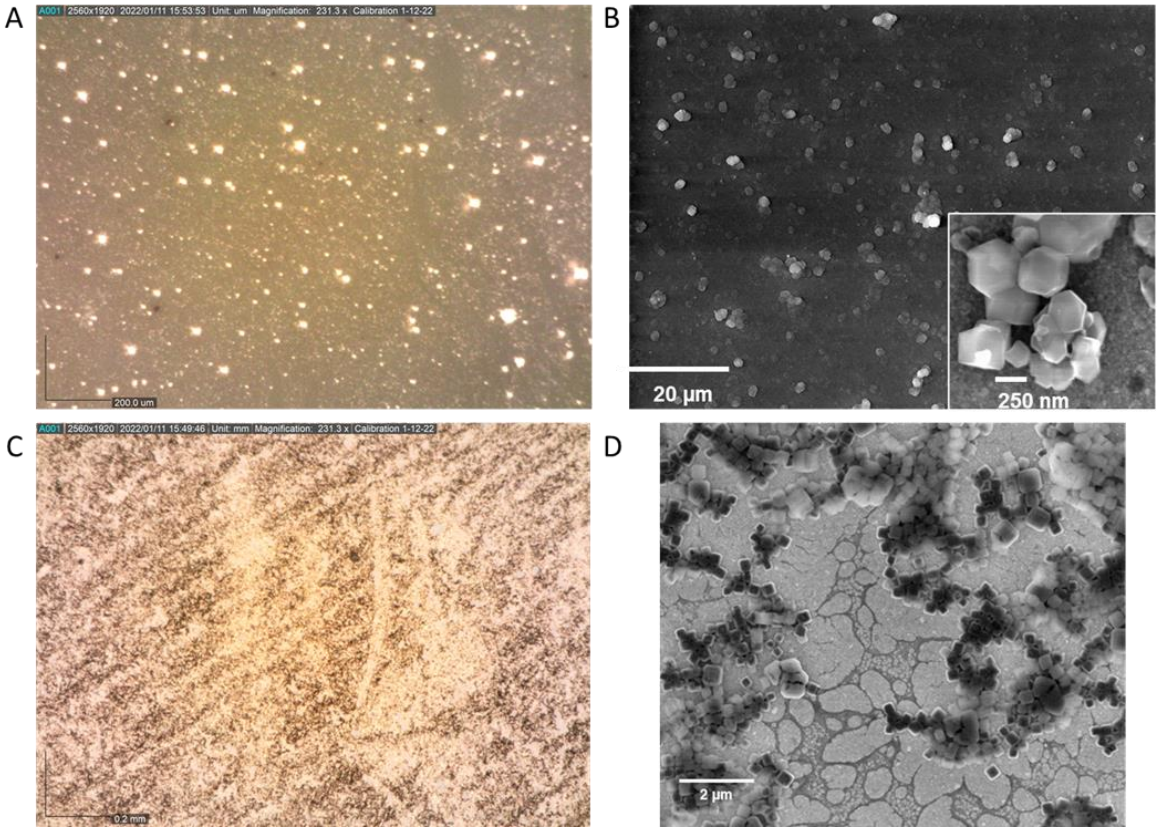

Figure 6.3. Optical microscopy (A and C) and SEM (B and D) images of MOF formulation before (A and B) and after (C and D) improved formulation procedures.

available within the penetration depth of SPR instrumentation. This high surface heterogeneity impacted the consistency and sensitivity of SPR sensing therefore new

methods for MOF surface formulation were tested finding significant improvement through reduction in MOF concentration and multiple deposition layers. Based on this

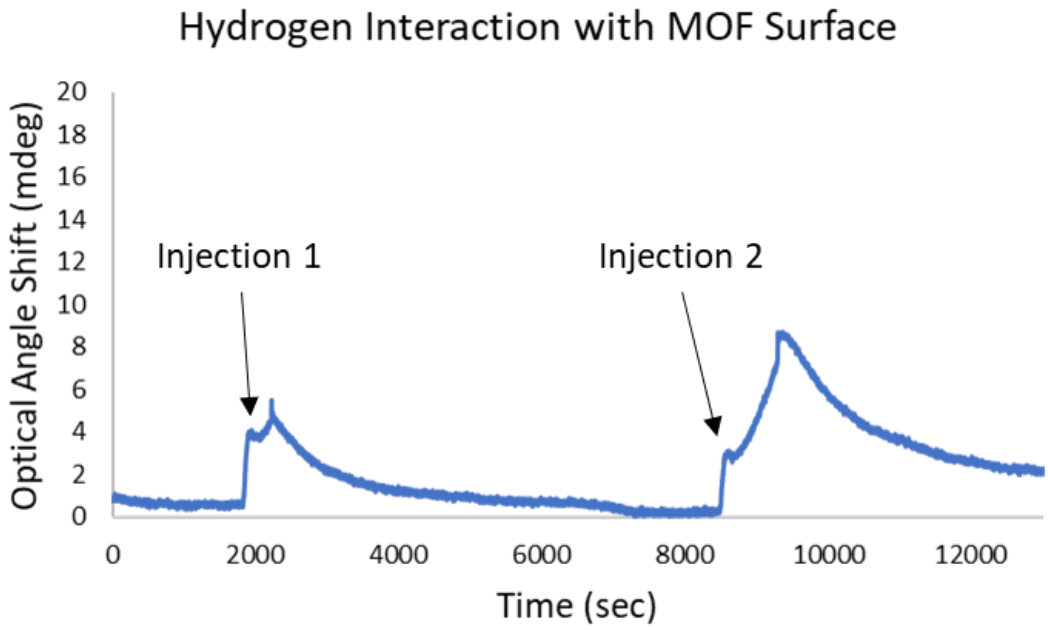

Figure 6.4. Binding of hydrogen to the MOF surface showing signal from hydrogen remaining for about an hour after hydrogen injection.

improved MOF surfaces were formulated (Figure 6.3 C and D) enabling SPR sensing to be achieved and some hydrogen selectivity was observed as can be seen in Figure 6.4. Despite this selectivity the binding of hydrogen within the MOF structure was found to remain for over an hour even after a nitrogen flush which severely limits the sensors feasibility for on off sensing applications. Some binding of methane was also observed which limits possibility of selectively sensing hydrogen. As such, we focused our efforts on finding alternative methods to enable hydrogen sensing with SPR instrumentation.

SPR Hydrogen Sensing

To begin testing of SPR based optical sensing of hydrogen we first flowed nitrogen through the sensor chamber to achieve an instrumental baseline and then periodically introduced various hydrogen/nitrogen mixtures. To account for any pressure effects an

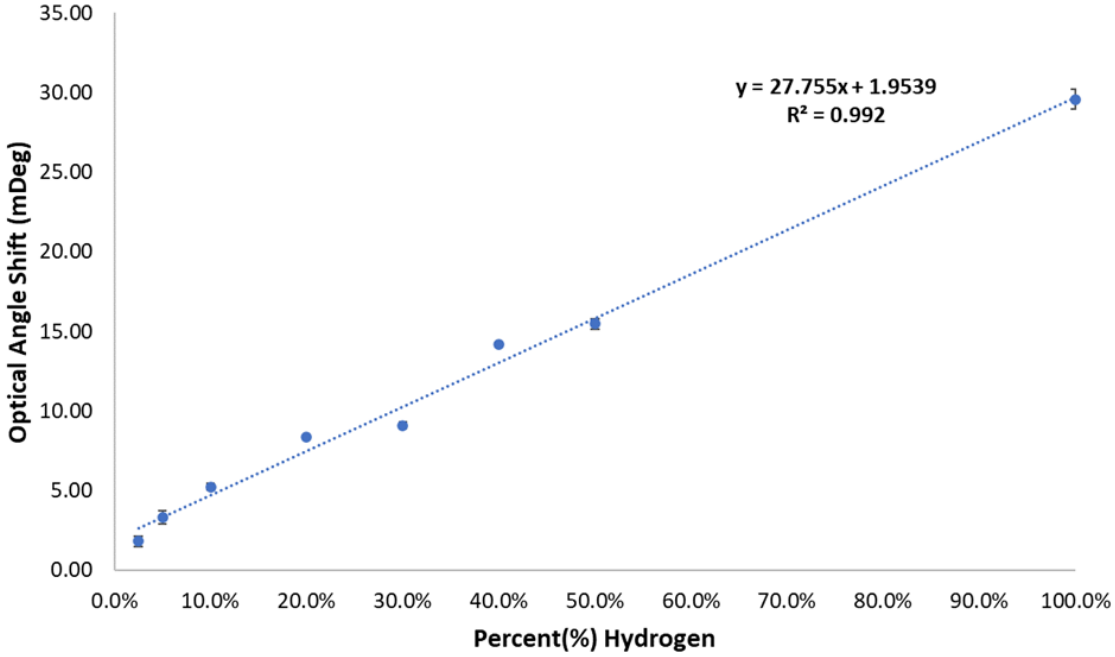

Figure 6.5. Calibration curve demonstrating detection of hydrogen from 2.5-100% hydrogen based on SPR sensor response.

injection of nitrogen was used as a control and subtracted from any hydrogen injection signal. A hydrogen concentration dependent signal relationship was quickly identified and used to formulate a calibration curve demonstrating hydrogen detection within nitrogen down to 2.5% (Figure 6.5). Furthermore, as detection was achieved in real time changes in hydrogen concentration could be identified within seconds and continually monitored. While other sensor methodologies can detect hydrogen at much lower concentrations our sensor was able to sense across a very large range from 2.5 to 100% hydrogen, something that is important in pipeline, turbine, or storage uses. Conventional sensors are commonly

focused on prevention and therefore tuned to detect concentrations before they reach ignition levels. However, this new SPR optical sensing methodology lends itself to use

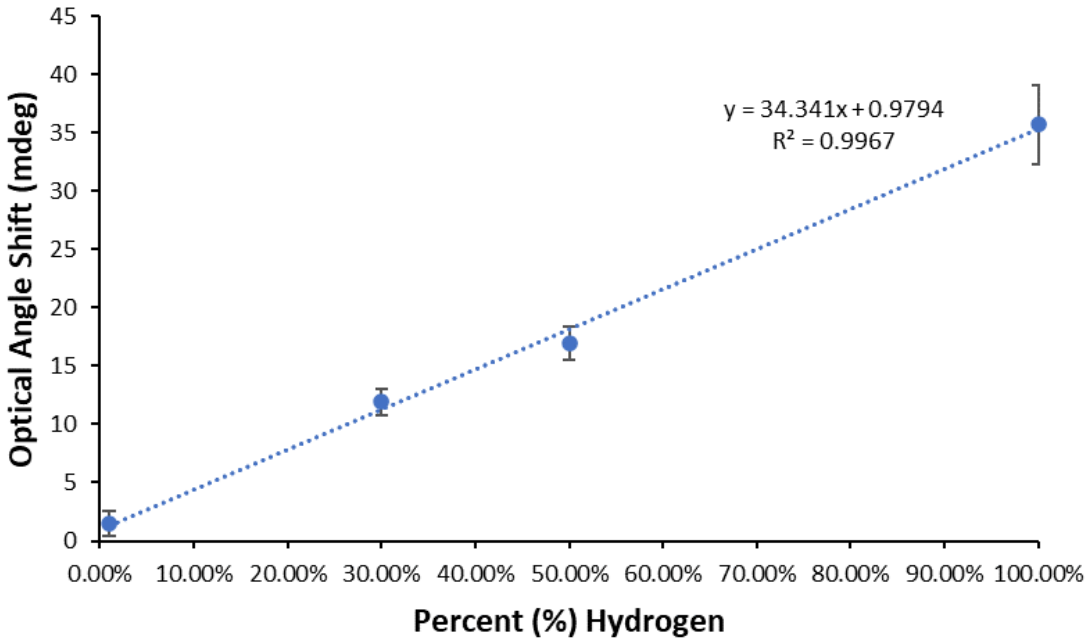

Figure 6.6. Calibration curve for hydrogen detection in a 20% methane/nitrogen mix indicating detection of lower hydrogen levels due to greater differences in refractive index between the gases.

cases where hydrogen levels would be consistently high and therefore monitoring would be key. As shown in our simulations the signal difference between hydrogen and methane was expected to be higher than that observed for hydrogen and nitrogen. Therefore, we also tested whether our sensor could distinguish hydrogen percentages with an added methane component. To achieve this our carrier gas was exchanged for a 20% methane blend and a similar hydrogen sensing analysis was performed. It quickly became apparent that a greater signal shift was detectable for hydrogen with the 20% methane carrier gas confirming simulation results. This also had the added benefit of enabling a lower hydrogen concentration to be detectable above noise providing identification of hydrogen down to 1% as can be seen in Figure 6.6. Thus, when working in a natural gas pipeline that is

composed of predominantly methane this sensor could be expected to be even more sensitive to hydrogen changes than what is reported here. All due to a much higher refractive index difference between the gases in question.

Using Pressure Effects to Identify Gases

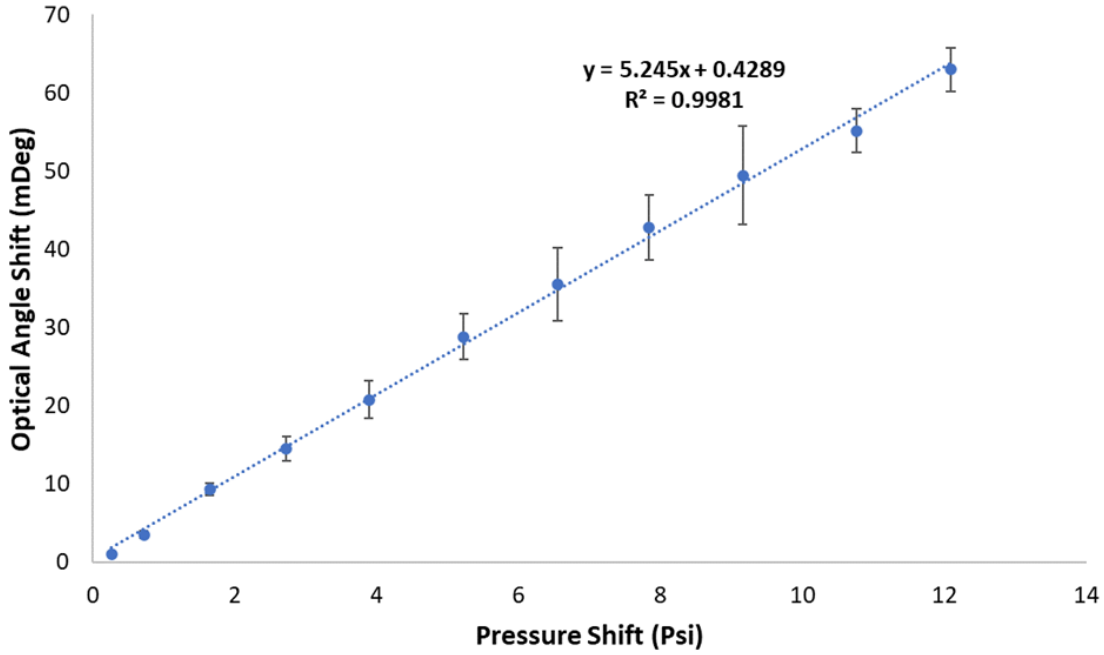

Figure 6.7. The impact of tank regulator output pressure on SPR minimum reflectivity angle shift.

While robust signal could be achieved for hydrogen gas using SPR spectroscopy the limitation of selectivity was clearly apparent and as the heterogeneity of MOF fabrications did not provide consistent selectivity new methodologies were needed. While in pipeline systems this sensor could provide robust monitoring when expanding to a more complex gas environment with changing variables, being able to attribute signal to a specific gas would be necessary. As previously mentioned during our optimization and testing, pressure was found to be an important factor in SPR signal that had to be controlled for which was easily achieved with a nitrogen injection as a control. However, then the

consideration of using its impact to our advantage came up potentially providing a unique avenue to provide selectivity to our gas phase SPR sensing system. Through some initial testing we found a significant impact of gas pressure on our sensor signal with a change in

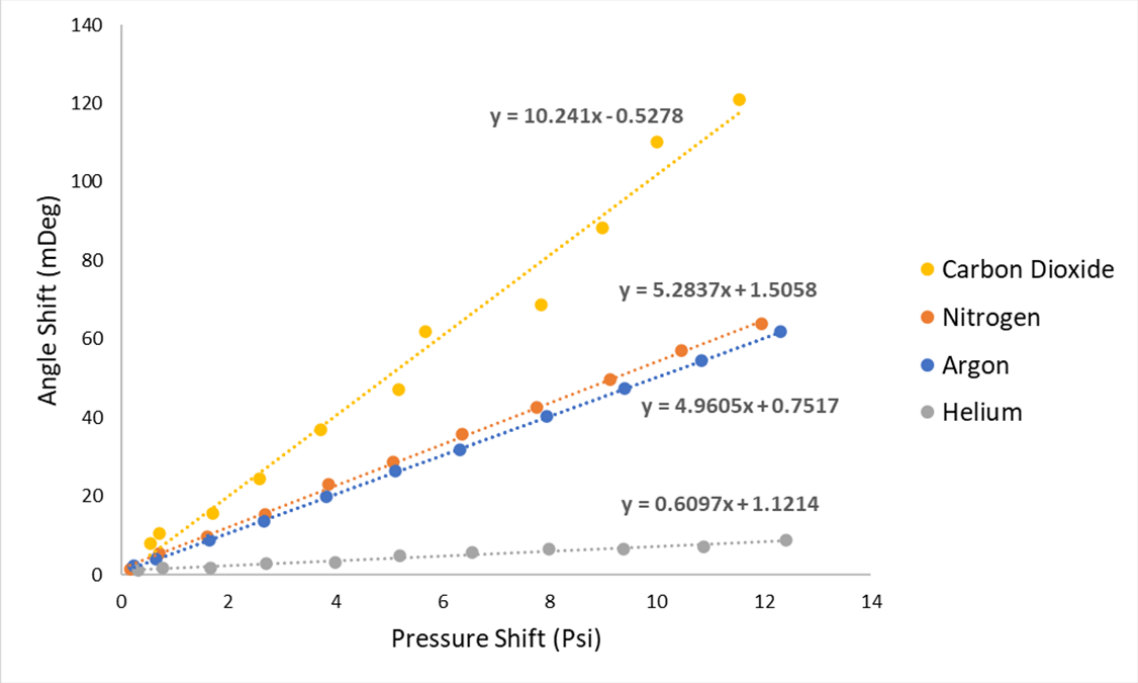

Figure 6.8. Gas specific changes in SPR angle with tank regulator pressure change. Demonstrating distinct slopes for four different gases carbon dioxide (yellow), nitrogen (orange), argon (blue), and helium (grey).

tank output pressure of 10 psi resulting in a 50 mdeg greater SPR angular shift as can be seen in Figure 6.7. Though the question became was there a gas specific relationship that could be exploited here. To this end, previous work by Sang and Jeon[27] that identified differences in refractive index with respect to pressure for various gases provided us an avenue to gas selectivity. They attribute these to differences in the polarizability of the gases as the refractive index of a gas is dependent on the molar refractivity R_n which is based on the molar mass M and density ρ of the gas as shown[28]:

$$R_n = \frac{M}{\rho}\frac{n^2-1}{n^2+2} \quad (6.1)$$

The polarizability a_e of the gas is also an aspect of the relationship as can be shown in its relation to the molar refractivity, modified from Pacák[28]:

$$a_e = \frac{3R_n}{4\pi N_A} \quad (6.2)$$

We tested this within our sensor setup and found that the data (Figure 6.8) matched well with the report of refractive index variability based on polarizability with SPR angular shift in place of refractive index as SPR shifts without binding events are attributable to bulk refractive index changes.

Therefore, we speculated that if we could incorporate a pressure sensor within our

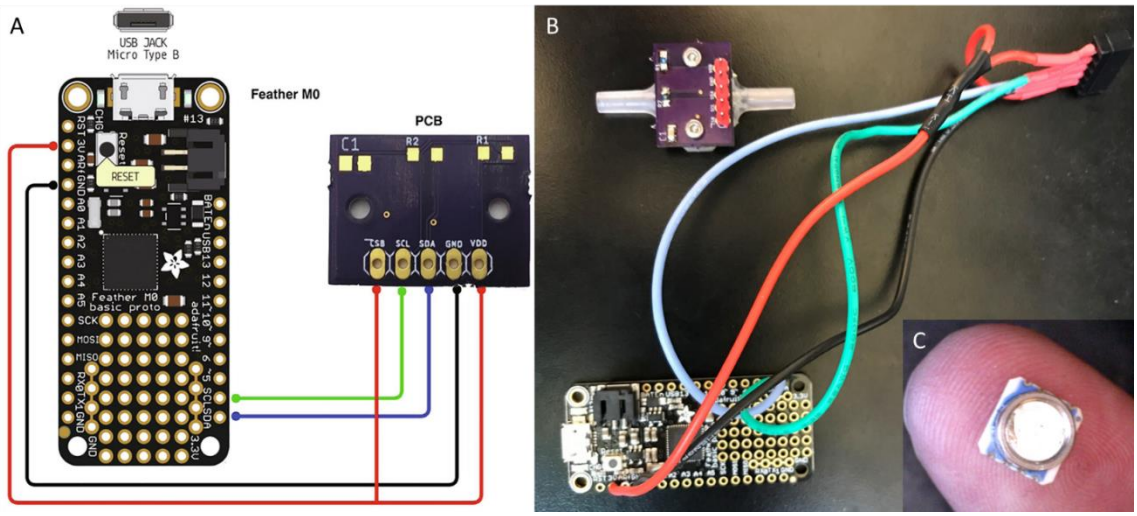

Figure 6.9. (A) Schematic of wiring for Arduino board reprinted from[18]. (B) Image of implemented board, sensor, and 3D printed flow channel making up the pressure sensor. (C) Image of pressure sensor component that is smaller than a fingertip.

SPR instrumentation then the combined data could potentially supply the gas selectivity we needed. To this end, we implemented a small inline pressure and temperature sensor, controlled by an Arduino, into the flow outlet of the SPR (Figure 6.9) as discussed in the methods section.[18] This furnished pressure data in real time that was then correlated with

SPR response. However, due to the remarkably sensitivity of SPR to refractive index changes we were able to identify differences at much lower pressure changes down to ~11 mBars. With a maximal pressure change of 177.92 mBar being measured due to the limitations of our tubing and sensor chamber. However, with increasing pressure changes the separation of gases was much more distinct indicating that this gas sensing system would be even more effective in higher pressure systems, like those in pipelines and gas

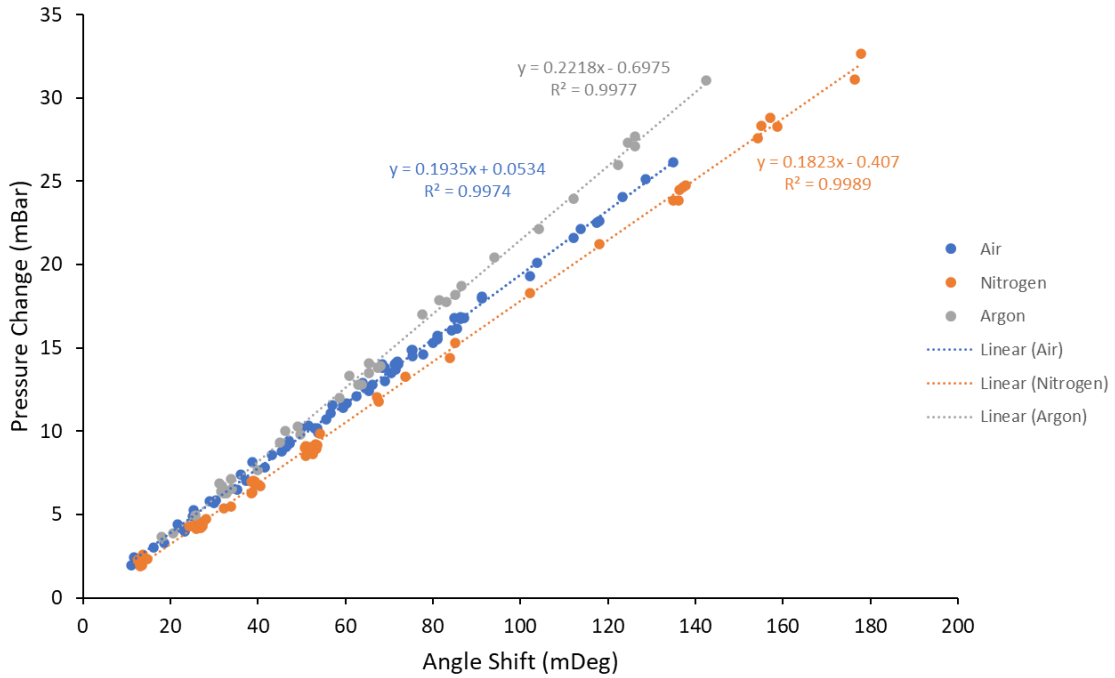

Figure 6.10. Combined SPR angular shift and pressure sensor shift for air, nitrogen, and argon demonstrating ability to separate these gases despite their similarities.

turbines. This not only provided the gas selectivity we were searching for to enable hydrogen sensing but also enabled selective sensing of essentially any gases with discernible differences in refractive index. As such, we investigated the limits of selectivity possible with the combined SPR and pressure sensor. To achieve this, we focused on three gases with similar refractive index (Nitrogen, Argon, and Air) to test the sensors ability to separate these highly similar gas systems. In particular, nitrogen makes up the majority of

air and therefore any detectable differences will only come from oxygen, carbon dioxide, and other trace gases. Which leads to a refractive index difference of only 0.00000784, a remarkably small difference to effectively distinguish. Furthermore, nitrogen and argon are both inert gases and have refractive indices of 1.00028110[23] and 1.00026546[29] respectively making them an ideal foundation for testing. As air is 78% nitrogen its refractive index of 1.00027610[30] is also very similar to that of nitrogen and argon resulting in it falling directly between them which should make separation of these three gases very difficult. Data was collected for each gas across a range of pressure changes and compared as shown in Figure 6.10. While separation was significantly less than that seen for other gases, they could still be easily visually isolated at higher pressure changes >80 mBar. However, at lower pressure these differences become muddled requiring other methods to improve and automate identification.

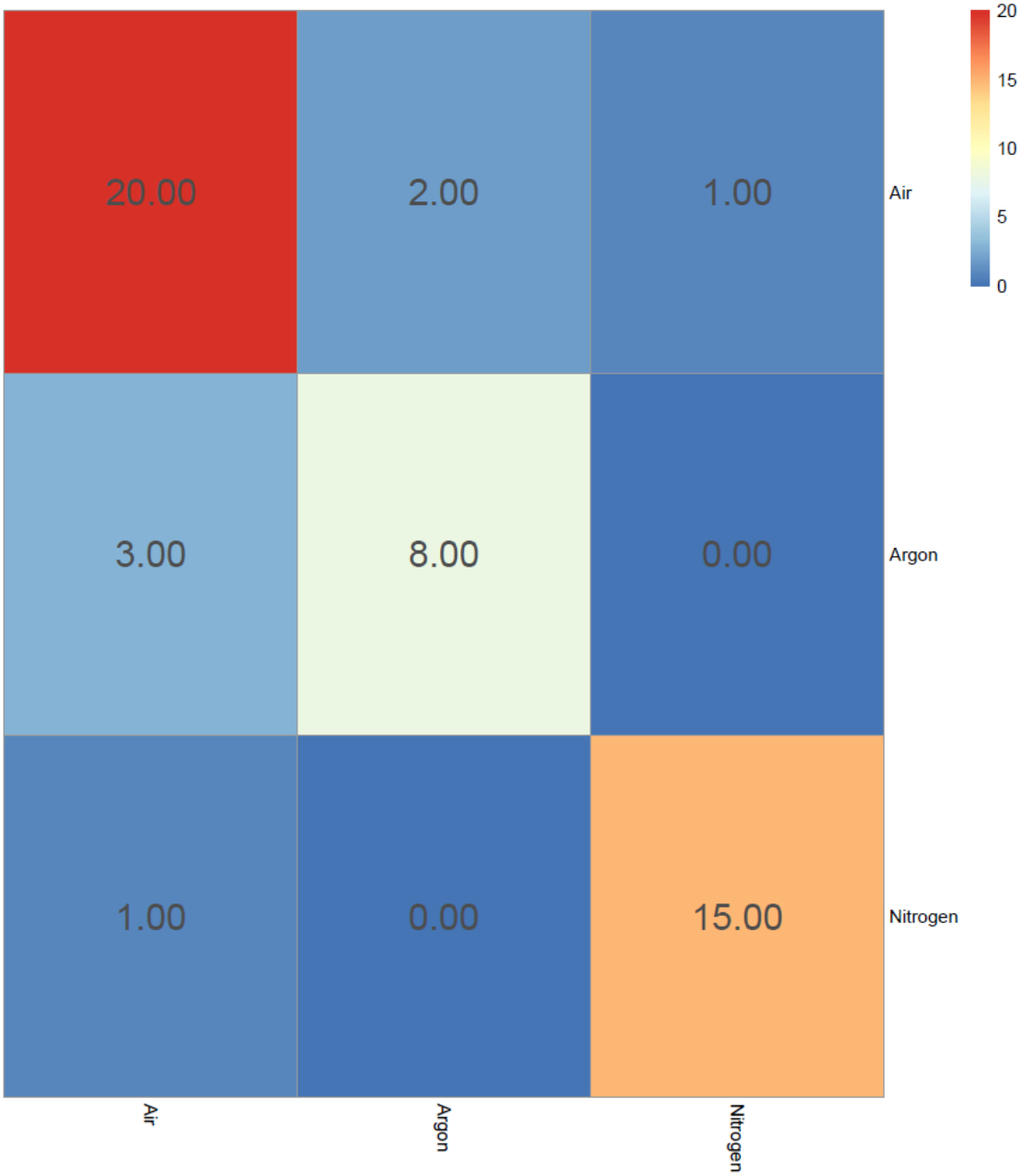

Figure 6.11. Confusion matrix heatmap of neural network classification results showing effective separation between air, argon, and nitrogen based on surface plasmon resonance and pressure data.

To this end, we implemented machine learning algorithms trained with a portion of the data from each gas not only to aid in identification but to build the foundation for further

machine learning applications to more complex gas systems. Neural network, random forest, support vector machine, linear discriminant analysis and k-nearest neighbor machine learning algorithms were all applied to identify the ideal method for gas classification. For each, data was split 70:30 for training and testing respectively and fed into selected algorithms from the caret[31] package in R. Also, repeated cross validation was employed to reduce model over training with 3 repeats of 10-fold cross validation. Results of model testing predictions were output as confusion matrices and plotted as heatmaps as seen in Figure 6.11. Further, prediction accuracy of each model was calculated from repeated training and testing cases of randomized data selection and averaged to account for variations and provide a computation of model deviation. It can be seen that each model resulted in minimal miss classification with miss classification events attributable to the lowest pressure data points.

This foundational machine learning comprises the first step in automating gas detection using this unique combination of SPR and pressure data. Thus, demonstrating the ability to accurately classify gas identity based on the SPR and pressure data that can be easily expanded to implement other gases and classify more complex gas mixtures. This gas classification can be identified by eye based on the line of best fit differences but within the field with increasingly large datasets machine learning model implementation will alleviate the time cost of manual separation and can be interfaced with expanding sensor networks to account for a greater number of parameters.

6.4 Conclusion

We have demonstrated the feasibility of utilizing SPR methodologies to develop an optical hydrogen gas sensor that can monitor hydrogen across a large range of 1 to 100% hydrogen. With the capability of detecting gas changes in real-time. Proving to be an effective sensor for hydrogen in applications especially where consistently high hydrogen levels are to be expected and continual monitoring is important. We also investigated the effect of pressure on SPR gas sensing and employed an inline pressure sensor in conjunction with SPR instrumentation to expand the capabilities of gas phase SPR sensing. Enabling gas selectivity to be achieved based on unique pressure and refractive index relationships for gases based on their polarizability. This is shown to enable differentiation of highly similar gasses air, nitrogen, and argon even at low pressures, with higher pressure changes resulting in significantly easier separation. This sensing methodology can be easily expanded to other gases and mixtures with the potential to impart selective gas sensing solely from SPR bulk angular shift and gas pressure measurements. This work also indicates the crucial role pressure plays in SPR gas sensing systems, something that should be considered in future gas sensing schemes as without appropriately controlling for it data could be highly variable.

6.5 References

1. Thomas, J. M.; Edwards, P. P.; Dobson, P. J.; Owen, G. P., Decarbonising energy: The developing international activity in hydrogen technologies and fuel cells. *Journal of Energy Chemistry* **2020,** *51*, 405-415.

2. Aminudin, M. A.; Kamarudin, S. K.; Lim, B. H.; Majilan, E. H.; Masdar, M. S.; Shaari, N., An overview: Current progress on hydrogen fuel cell vehicles. *International Journal of Hydrogen Energy* **2023,** *48* (11), 4371-4388.

3. Arsad, A. Z.; Hannan, M. A.; Al-Shetwi, A. Q.; Mansur, M.; Muttaqi, K. M.; Dong, Z. Y.; Blaabjerg, F., Hydrogen energy storage integrated hybrid renewable energy systems: A review analysis for future research directions. *International Journal of Hydrogen Energy* **2022,** *47* (39), 17285-17312.

4. Alhuyi Nazari, M.; Fahim Alavi, M.; Salem, M.; Assad, M. E. H., Utilization of hydrogen in gas turbines: a comprehensive review. *International Journal of Low-Carbon Technologies* **2022,** *17*, 513-519.

5. Okolie, J. A.; Patra, B. R.; Mukherjee, A.; Nanda, S.; Dalai, A. K.; Kozinski, J. A., Futuristic applications of hydrogen in energy, biorefining, aerospace, pharmaceuticals and metallurgy. *International Journal of Hydrogen Energy* **2021,** *46* (13), 8885-8905.

6. Kim, C.; Cho, S. H.; Cho, S. M.; Na, Y.; Kim, S.; Kim, D. K., Review of hydrogen infrastructure: The current status and roll-out strategy. *International Journal of Hydrogen Energy* **2023,** *48* (5), 1701-1716.

7. Kevin Topolski, E. P. R., Burcin Cakir Erdener,; Chris W. San Marchi, J. A. R., Lisa Fring,; Kevin Simmons, O. J. G. F.; Bri-Mathias Hodge, a. M. C. *Hydrogen Blending into Natural Gas Pipeline Infrastructure: Review of the State of Technology*; National Renewable Energy Laboratory: Golden, CO, 2022.

8. Li, H.; Cao, X.; Liu, Y.; Shao, Y.; Nan, Z.; Teng, L.; Peng, W.; Bian, J., Safety of hydrogen storage and transportation: An overview on mechanisms, techniques, and challenges. *Energy Reports* **2022,** *8*, 6258-6269.

9. Ryo, O.; Tetsuji, O., Spark ignition of hydrogen-air mixture. *Journal of Physics: Conference Series* **2008,** *142* (1), 012003.

10. Koo, W.-T.; Cho, H.-J.; Kim, D.-H.; Kim, Y. H.; Shin, H.; Penner, R. M.; Kim, I.-D., Chemiresistive Hydrogen Sensors: Fundamentals, Recent Advances, and Challenges. *ACS Nano* **2020,** *14* (11), 14284-14322.

11. Foorginezhad, S.; Mohseni-Dargah, M.; Falahati, Z.; Abbassi, R.; Razmjou, A.; Asadnia, M., Sensing advancement towards safety assessment of hydrogen fuel cell vehicles. *Journal of Power Sources* **2021,** *489*, 229450.

12. Hinman, S. S.; McKeating, K. S.; Cheng, Q., Surface Plasmon Resonance: Material and Interface Design for Universal Accessibility. *Analytical Chemistry* **2018,** *90* (1), 19-39.

13. Gaur, R.; Padhy, H. M.; Elayaperumal, M., Surface plasmon assisted toxic chemical NO2 gas sensor by Au / ZnO functional thin films. *J. Sens. Sens. Syst.* **2021,** *10* (2), 163-169.

14. Li, Y.; Chen, H.; Chen, Q.; Li, H.; Gao, Z., Surface plasmon resonance induced methane gas sensor in hollow core anti-resonant fiber. *Optical Fiber Technology* **2023,** *78*, 103293.

15. Chen, R.; Lan, G.; Wang, N.; Yan, W.; Yi, J.; Wei, W., Highly sensitive fiber-optic SPR sensor with surface coated TiO2/MWCNT composite film for hydrogen sulfide gas detection. *Journal of Physics D: Applied Physics* **2022,** *55* (10), 105108.

16. Deng, Y.; Li, M.; Cao, W.; Wang, M.; Hao, H.; Xia, W.; Su, F., Fiber optic coupled surface plasmon resonance sensor based Ag-TiO2 films for hydrogen detection. *Optical Fiber Technology* **2021,** *65*, 102616.

17. Abouhajar, F.; Chaudhuri, R.; Valiulis, S. N.; Stuart, D. D.; Malinick, A. S.; Xue, M.; Cheng, Q., Label-Free Analysis of Binding and Inhibition of SARS-Cov-19 Spike Proteins to ACE2 Receptor with ACE2-Derived Peptides by Surface Plasmon Resonance. *ACS Applied Bio Materials* **2023,** *6* (1), 182-190.

18. Goertzen, L.; Mehr, N.; Lopez, M.; Udell, C.; Selker, J. S., Low-cost and precise inline pressure sensor housing and DAQ for use in laboratory experiments. *HardwareX* **2020,** *8*, e00112.

19. Polyanskiy, M. N. Refractive index database. (accessed 2023-09-12).

20. Sytchkova, A.; Belosludtsev, A.; Volosevičienė, L.; Juškėnas, R.; Simniškis, R., Optical, structural and electrical properties of sputtered ultrathin chromium films. *Optical Materials* **2021,** *121*.

21. Olmon, R. L.; Slovick, B.; Johnson, T. W.; Shelton, D.; Oh, S.-H.; Boreman, G. D.; Raschke, M. B., Optical dielectric function of gold. *Physical Review B* **2012,** *86* (23), 235147.

22. Peck, E. R.; Huang, S., Refractivity and dispersion of hydrogen in the visible and near infrared. *J. Opt. Soc. Am.* **1977,** *67* (11), 1550-1554.

23. Peck, E. R.; Khanna, B. N., Dispersion of Nitrogen. *J. Opt. Soc. Am.* **1966,** *56* (8), 1059-1063.

24. Loria, S., Über die Dispersion des Lichtes in gasförmigen Kohlenwasserstoffen. *Annalen der Physik* **1909,** *334* (8), 605-622.

25. Nguyen, H. H.; Park, J.; Kang, S.; Kim, M. Surface Plasmon Resonance: A Versatile Technique for Biosensor Applications *Sensors* [Online], 2015, p. 10481-10510.

26. Liu, Y.; Ma, Y., One-Dimensional Plasmonic Sensors. **2020,** *8*.

27. Sang, B. H.; Jeon, T.-I., Pressure-dependent refractive indices of gases by THz time-domain spectroscopy. *Opt. Express* **2016,** *24* (25), 29040-29047.

28. Pacák, P., Molar refractivity and interactions in solutions I. Molar refractivity of some monovalent ions in aqueous and dimethyl sulfoxide solutions. *Chem. Pap.* **1988,** *43* (4), 289–500.

29. Peck, E. R.; Fisher, D. J., Dispersion of Argon. *J. Opt. Soc. Am.* **1964,** *54* (11), 1362-1364.

30. Ciddor, P. E., Refractive index of air: new equations for the visible and near infrared. *Appl. Opt.* **1996,** *35* (9), 1566-1573.

31. Kuhn, M., Building Predictive Models in R Using the caret Package. *Journal of Statistical Software* **2008,** *28* (5), 1 - 26.

Chapter 7: Conclusion and Future Perspectives

7.1 Summary of Dissertation Work

The work described in this Dissertation focused on the development of new methodologies to bypass current limitations of surface plasmonic resonance (SPR) sensors. With advancements made in the development, characterization, and application of biomimetic lipid membrane platforms, sensor capabilities, and data processing/analysis strategies.

Three biomimetic lipid platforms are described here, a tethered lipid membrane system, a highly antifouling lipid bilayer, and an easily tuned curved membrane platform. The tethered lipid system enabled analysis of drug delivery interactions with a fluid lipid membrane improving our understanding of these important interactions. The antifouling lipid system provided robust protection of sensor substrates from the complex matrix of human serum empowering sensor capabilities. While the curved membrane platform investigated the preferential binding of Alpha-synuclein to highly curved lipid surfaces.

New sensor capabilities were demonstrated in application of quartz crystal microbalance (QCM) to analyze curvature binding proteins, expansion of SPR gas phase sensing efficacy and for enhancement of matrix assisted laser desorption ionization mass spectrometry (MALDI-MS). The formulation of a substrate conducive to assembly of curved lipid surfaces was established as an effective sensor for Alpha-synuclein. SPR analysis of various gases was achieved based on a relationship between refractive index and gas pressure resulting in a robust gas sensor able to quickly distinguish between

gases at lower pressures. Plasmonic arrays were fabricated and utilized to analyze and distinguish between strains of *Staphylococcus aureus* that were susceptible or resistant to methicillin antibiotics, with the plasmonic arrays demonstrating robust lipid ionization.

Data processing strategies were developed to accommodate these platforms and sensors enabling differentiation of sensor targets. These novel strategies and code developed to facilitate data implementation into machine learning algorithms can also be easily applied to other sensor formulations empowering future SPR and MALDI-MS research.

7.2 Future Works

As the pursuit of knowledge is never over none of these chapters are complete, each work resulted in new questions and avenues for study. Here I will discuss the next steps in expanding the scope of each project as well as potential future utilizations of the developed sensors.

Biomimetic Tethered Lipid Bilayer

The PEG tethered lipid bilayer platform can be expanded in three main areas, through the application to sensing methodologies, implementation of other membrane components, and expansion of use in understanding drug delivery interactions. For the development of new sensors one protein systems appears as a clear next step, which is anaplastic lymphoma kinase (ALK) which is a membrane bound tyrosine kinase linked to cancer[1-3]. This can be accomplished by detergent based incorporation of transmembrane proteins into unilamellar vesicles[4-6] or formation of vesicles from native membranes[7-9] that can then be fused[10] with

our tethered system to provide a cushion between the solid sensor surface and the external portions of ALK. To properly mimic the cellular environment other cellular components will also need to be incorporated. Notably, cholesterol makes up a large portion of cellular bilayers[11] and plays and important role in membrane fluidity[12-14] and binding interactions[15] therefore its incorporation in the PEG tethered platform is a key next step. Charged lipid groups, also play roles in modifying membrane properties[16, 17] and have been shown to interact with proteins[18-20]. As such, these additions will not only benefit sensor studies like the ALK detailed above but also any biophysical studies of membrane systems through a more accurate representation of the cellular environment. Looking towards drug delivery and screening a biomimetic platform provides an easy first step to understand the important interactions occurring without the need for animal testing. This avenue also benefits from work improving the mimicry of the platform through incorporation of other important membrane components as they will interact with the delivery mechanism. So far, we have explored the interaction of dendrimer micelles with the lipid membrane which can be expanded to encompass other drugs and membrane components. However, other delivery mechanisms can also be investigated to gain a deeper understanding of how they deliver their payload. Notably, lipid vesicles[21, 22], nanomaterials[23, 24], and cell penetrating peptides[25] have seen extensive use as drug delivery vehicles and can be studied with this membrane system.

Antifouling Lipid Membrane

The exploration of the antifouling charged lipid membrane in this dissertation lays the foundation for understanding and expanding the capabilities of sensors, as it provides both

a biomimetic and antifouling substrate. As such the next steps for this project are two-fold, application into sensing systems and expansion of study into the properties involved in the antifouling process. Previous work has shown[26] that protein A works as a scaffold for antibody-based capture of proteins which can easily be applied to sense important protein biomarkers in human serum. Due to the antifouling capabilities of this membrane system, it provides a key link in reducing false positives in sensors. This can be enabled by work using trehalose to enable dehydration of lipid vesicles significantly improving shelf-life if used in a lateral flow assay or point of care sensor. Therefore, usage in this capacity as well as utilization in SPR imaging array setups can enable a broad array of sensors. However, the development of antifouling platforms is far from over as sensor needs change just as the biomarker targets change. As such, investigation of other charged lipids[27], buffer conditions[28, 29], changes in protein charge, and how different sensor substrates affect the nonspecific interactions at lipid surfaces is not only key to understanding the antifouling mechanism but to developing better sensors.

Curved Membrane

In chapter 4 a curved membrane platform was developed and applied to mimic curved cellular environments that various proteins preferentially bind to. First off due to the adaptability of this system other silica particles can easily be implemented in a greater variety of silica bead sizes ranging from 15 nm[30] to 2 microns[31] in size providing a more distinct image of the exact curvature that suits these curvature sensing proteins than can be achieved with the sizes explored in this work. A deeper understanding of the biophysical interactions at play can also be elucidated through the incorporation of other biological

components. Notably charged lipids such as 1,2-dioleoyl-sn-glycero-3-ethylphosphocholine (EPC+) and 1-palmitoyl-2-oleoyl-sn-glycero-3-phospho-(1'-rac-glycerol) (POPG-), as utilized in previous work, would produce significant shifts in the overall charge of these membranes which is an aspect of curvature binding proteins that has only recently been identified with preference for negatively charged surfaces[32, 33]. With that glycosphingolipids are also considered to play a role in these binding events both due to their part in generating curvature[34] and their binding interactions with curvature sensing proteins[35] and should therefore be included in the vesicle preparation process. Each of these additions also improves the biomimicry of the substrate which can be further improved through the incorporation of cholesterol[11, 13, 14] as previously mentioned. Furthermore, the membrane rigidity can be modified through a change in formulation by working with free floating or tethered vesicles as has been shown in some recent work providing insight into curvature sensing protein interactions on malleable surfaces as many of the proteins have roles in membrane reshaping.

Additionally future work should focus on other curved membrane systems beyond the alpha-synuclein used to demonstrate the platform's potential. Notably BIN1 should be studied as it has been shown to act as a recruitment site for various other proteins through conformational changes that make its auxiliary domains more accessible[36]. Included with these are the CLAP[37], Src homology 3 (SH3)[36, 38], and MYC-binding domains[39].

MALDI-MS

The lipidomics analysis and machine learning based identification of bacterial species demonstrated in chapter 5 can be expanded upon via three key avenues, application to other bacterial species, usage in lipid-based monitoring of toxicological impacts, or implementation in analysis of entirely new organismal classes.

First, the platform can be applied to investigate other bacterial species to grow the library and to demonstrate a greater effective number of bacterial species that can be accurately identified. This work on library development is key to the future application of this platform for use in clinical settings where hundreds of bacterial species and strains need to be distinguished to provide proper medical care. Three bacterial species that are prime candidates for the next step in this direction are *Acinetobacter* baumannii[40], *Pseudomonas aeruginosa*[41], and *Enterobacteriaceae*[42] which are currently the highest priority for the World Health Organization[43] and the United States Center for Disease Control and Prevention[44] due to their multidrug resistance and impact on hospitals. As detection of these priority bacterial species not only demonstrates platform feasibility in an area of need but can also facilitate research into drug resistance.

Secondly, the platform can be employed to investigate the impact of toxicants or drugs on these bacteria based on resulting changes in their lipid profiles which can then be linked to changes in lipid metabolism caused by the compound of interest. We have demonstrated this within algae in previous work[45] and recently investigated antibiotic impact on *E. coli*[46] using MALDI-MS. This can be applied to the *S. aureus* system to

investigate differences in response to antibiotics of susceptible and resistant strains providing insight into how MRSA is diminishing methicillin and oxacillin impacts at the metabolite level.

Finally, this platform is not specific to bacteria and can thus be expanded to other more complex organisms. One area of interest here is nematodes specifically *Caenorhabditis elegans* (*C. elegans*), which have been utilized as model organisms for decades due to the fact that they are one of the simplest organisms that poses a nervous system[47]. Future work utilizing the MALDI-MS platform can employ metabolomic analysis of *C. elegans* in concrete with the toxicological studies previously mentioned to interrogate the impact of toxic compounds on this system and draw parallels to human health.

Gas SPR

The utilization of SPR for detection of gases is still in its infancy and the work demonstrated in chapter 6 of this dissertation is the first step in a long process of continued sensor validation and application. In considering the next steps for this project two avenues appear, one connected to the original goal of sensing hydrogen in pipeline environments and another in exploration of the gas differentiation capabilities identified during the course of this work. In regards to the first, some pipelines are high very pressure systems up to 1400 pounds per square inch gauge (psig) therefore investigation of sensor capacity in both the lower 0.25–300 psig systems and these high pressure environments is of key importance to demonstrate sensor feasibility[48]. Further testing of sensor performance in

hydrogen and natural gas blends consistent with those expected in pipelines is also needed. Both goals are also facilitated by prototype development of small SPR sensors conducive to implementation within pipelines. In the second case the sensor has shown effectiveness at differentiating between multiple gases with apparent potential to extend to other gases as well. Therefore, the next steps here are to test other gases and particularly gas mixtures to ensure this methodology remains effective. With that further work investigating carbon dioxide (CO_2) is needed as the cooling effect caused by using CO_2 from a compressed gas tank increased variability.

7.3 References

1. Della Corte, C. M.; Viscardi, G.; Di Liello, R.; Fasano, M.; Martinelli, E.; Troiani, T.; Ciardiello, F.; Morgillo, F., Role and targeting of anaplastic lymphoma kinase in cancer. *Molecular cancer* **2018,** *17* (1), 30.

2. Du, X.; Shao, Y.; Qin, H. F.; Tai, Y. H.; Gao, H. J., ALK-rearrangement in non-small-cell lung cancer (NSCLC). *Thoracic cancer* **2018,** *9* (4), 423-430.

3. Hallberg, B.; Palmer, R. H., The role of the ALK receptor in cancer biology. *Annals of Oncology* **2016,** *27*, iii4-iii15.

4. Dezi, M.; Di Cicco, A.; Bassereau, P.; Lévy, D., Detergent-mediated incorporation of transmembrane proteins in giant unilamellar vesicles with controlled physiological contents. *Proceedings of the National Academy of Sciences of the United States of America* **2013,** *110* (18), 7276-81.

5. Richmond, D. L.; Schmid, E. M.; Martens, S.; Stachowiak, J. C.; Liska, N.; Fletcher, D. A., Forming giant vesicles with controlled membrane composition, asymmetry, and contents. *Proceedings of the National Academy of Sciences* **2011,** *108* (23), 9431-9436.

6. Pontani, L.-L.; van der Gucht, J.; Salbreux, G.; Heuvingh, J.; Joanny, J.-F.; Sykes, C., Reconstitution of an Actin Cortex Inside a Liposome. *Biophysical Journal* **2009,** *96* (1), 192-198.

7. Montes, L. R.; Alonso, A.; Goñi, F. M.; Bagatolli, L. A., Giant Unilamellar Vesicles Electroformed from Native Membranes and Organic Lipid Mixtures under Physiological Conditions. *Biophysical Journal* **2007,** *93* (10), 3548-3554.

8. Méléard, P.; Bagatolli, L. A.; Pott, T., Chapter 9 - Giant Unilamellar Vesicle Electroformation: From Lipid Mixtures to Native Membranes Under Physiological Conditions. In *Methods in Enzymology*, Academic Press: 2009; Vol. 465, pp 161-176.

9. Montes, L. R.; Ahyayauch, H.; Ibarguren, M.; Sot, J.; Alonso, A.; Bagatolli, L. A.; Goñi, F. M., Electroformation of Giant Unilamellar Vesicles from Native Membranes and Organic Lipid Mixtures for the Study of Lipid Domains under Physiological Ionic-Strength Conditions. In *Liposomes: Methods and Protocols, Volume 2: Biological Membrane Models*, Weissig, V., Ed. Humana Press: Totowa, NJ, 2010; pp 105-114.

10. Ma, M.; Bong, D., Controlled Fusion of Synthetic Lipid Membrane Vesicles. *Accounts of Chemical Research* **2013,** *46* (12), 2988-2997.

11. Subczynski, W. K.; Pasenkiewicz-Gierula, M.; Widomska, J.; Mainali, L.; Raguz, M., High Cholesterol/Low Cholesterol: Effects in Biological Membranes: A Review. *Cell biochemistry and biophysics* **2017,** *75* (3-4), 369-385.

12. Chapman, D., Phase transitions and fluidity characteristics of lipids and cell membranes. *Quarterly Reviews of Biophysics* **1975,** *8* (2), 185-235.

13. Ohvo-Rekilä, H.; Ramstedt, B.; Leppimäki, P.; Peter Slotte, J., Cholesterol interactions with phospholipids in membranes. *Progress in Lipid Research* **2002,** *41* (1), 66-97.

14. Zhang, Y.; Li, Q.; Dong, M.; Han, X., Effect of cholesterol on the fluidity of supported lipid bilayers. *Colloids and Surfaces B: Biointerfaces* **2020,** *196*, 111353.

15. Jaipuria, G.; Ukmar-Godec, T.; Zweckstetter, M., Challenges and approaches to understand cholesterol-binding impact on membrane protein function: an NMR view. *Cellular and molecular life sciences : CMLS* **2018,** *75* (12), 2137-2151.

16. Pöyry, S.; Vattulainen, I., Role of charged lipids in membrane structures — Insight given by simulations. *Biochimica et Biophysica Acta (BBA) - Biomembranes* **2016,** *1858* (10), 2322-2333.

17. Faizi, H. A.; Frey, S. L.; Steinkühler, J.; Dimova, R.; Vlahovska, P. M., Bending rigidity of charged lipid bilayer membranes. *Soft Matter* **2019,** *15* (29), 6006-6013.

18. Li, L.; Shi, X.; Guo, X.; Li, H.; Xu, C., Ionic protein-lipid interaction at the plasma membrane: what can the charge do? *Trends Biochem Sci* **2014,** *39* (3), 130-40.

19. Vorobyov, I.; Allen, T. W., On the role of anionic lipids in charged protein interactions with membranes. *Biochimica et Biophysica Acta (BBA) - Biomembranes* **2011,** *1808* (6), 1673-1683.

20. Muller, M. P.; Jiang, T.; Sun, C.; Lihan, M.; Pant, S.; Mahinthichaichan, P.; Trifan, A.; Tajkhorshid, E., Characterization of Lipid–Protein Interactions and Lipid-Mediated Modulation of Membrane Protein Function through Molecular Simulation. *Chemical Reviews* **2019,** *119* (9), 6086-6161.

21. van der Koog, L.; Gandek, T. B.; Nagelkerke, A., Liposomes and Extracellular Vesicles as Drug Delivery Systems: A Comparison of Composition, Pharmacokinetics, and Functionalization. **2022,** *11* (5), 2100639.

22. de Jong, O. G.; Kooijmans, S. A. A.; Murphy, D. E.; Jiang, L.; Evers, M. J. W.; Sluijter, J. P. G.; Vader, P.; Schiffelers, R. M., Drug Delivery with Extracellular Vesicles: From Imagination to Innovation. *Accounts of Chemical Research* **2019,** *52* (7), 1761-1770.

23. Singh, A. P.; Biswas, A.; Shukla, A.; Maiti, P., Targeted therapy in chronic diseases using nanomaterial-based drug delivery vehicles. *Signal Transduction and Targeted Therapy* **2019,** *4* (1), 33.

24. Amina, S. J.; Guo, B., A Review on the Synthesis and Functionalization of Gold Nanoparticles as a Drug Delivery Vehicle. *International Journal of Nanomedicine* **2020,** *15* (null), 9823-9857.

25. Park, S. E.; Sajid, M. I.; Parang, K.; Tiwari, R. K., Cyclic Cell-Penetrating Peptides as Efficient Intracellular Drug Delivery Tools. *Molecular Pharmaceutics* **2019,** *16* (9), 3727-3743.

26. McKeating, K. S.; Hinman, S. S.; Rais, N. A.; Zhou, Z.; Cheng, Q., Antifouling Lipid Membranes over Protein A for Orientation-Controlled Immunosensing in Undiluted Serum and Plasma. *ACS Sens* **2019,** *4* (7), 1774-1782.

27. Afanasenkau, D.; Offenhäusser, A., Positively Charged Supported Lipid Bilayers as a Biomimetic Platform for Neuronal Cell Culture. *Langmuir* **2012,** *28* (37), 13387-13394.

28. Peiró-Salvador, T.; Ces, O.; Templer, R. H.; Seddon, A. M., Buffers may adversely affect model lipid membranes: a cautionary tale. *Biochemistry* **2009,** *48* (47), 11149-51.

29. Bouvrais, H.; Duelund, L.; Ipsen, J. H., Buffers Affect the Bending Rigidity of Model Lipid Membranes. *Langmuir* **2014,** *30* (1), 13-16.

30. Ren, G.; Su, H.; Wang, S., The combined method to synthesis silica nanoparticle by Stöber process. *Journal of Sol-Gel Science and Technology* **2020,** *96* (1), 108-120.

31. Unger, K. K.; Kumar, D.; Grün, M.; Büchel, G.; Lüdtke, S.; Adam, T.; Schumacher, K.; Renker, S., Synthesis of spherical porous silicas in the micron and submicron size range: challenges and opportunities for miniaturized high-resolution chromatographic and electrokinetic separations. *Journal of Chromatography A* **2000,** *892* (1), 47-55.

32. Zeno, W. F.; Thatte, A. S.; Wang, L.; Snead, W. T.; Lafer, E. M.; Stachowiak, J. C., Molecular Mechanisms of Membrane Curvature Sensing by a Disordered Protein. *J Am Chem Soc* **2019,** *141* (26), 10361-10371.

33. Has, C.; Das, S. L., Recent developments in membrane curvature sensing and induction by proteins. *Biochimica et Biophysica Acta (BBA) - General Subjects* **2021,** *1865* (10), 129971.

34. Dasgupta, R.; Miettinen, M. S.; Fricke, N.; Lipowsky, R.; Dimova, R., The glycolipid GM1 reshapes asymmetric biomembranes and giant vesicles by curvature generation. **2018,** *115* (22), 5756-5761.

35. Martinez, Z.; Zhu, M.; Han, S.; Fink, A. L., GM1 Specifically Interacts with α-Synuclein and Inhibits Fibrillation. *Biochemistry* **2007,** *46* (7), 1868-1877.

36. Picas, L.; Viaud, J.; Schauer, K.; Vanni, S.; Hnia, K.; Fraisier, V.; Roux, A.; Bassereau, P.; Gaits-Iacovoni, F.; Payrastre, B.; Laporte, J.; Manneville, J.-B.; Goud, B., BIN1/M-Amphiphysin2 induces clustering of phosphoinositides to recruit its downstream partner dynamin. *Nature Communications* **2014,** *5* (1), 5647.

37. Ramjaun, A. R.; McPherson, P. S., Multiple Amphiphysin II Splice Variants Display Differential Clathrin Binding: Identification of Two Distinct Clathrin-Binding Sites. **1998,** *70* (6), 2369-2376.

38. Kojima, C.; Hashimoto, A.; Yabuta, I.; Hirose, M.; Hashimoto, S.; Kanaho, Y.; Sumimoto, H.; Ikegami, T.; Sabe, H., Regulation of Bin1 SH3 domain binding by phosphoinositides. *Embo j* **2004,** *23* (22), 4413-22.

39. Pineda-Lucena, A.; Ho, C. S.; Mao, D. Y.; Sheng, Y.; Laister, R. C.; Muhandiram, R.; Lu, Y.; Seet, B. T.; Katz, S.; Szyperski, T.; Penn, L. Z.; Arrowsmith, C. H., A structure-based model of the c-Myc/Bin1 protein interaction shows alternative splicing of Bin1 and c-Myc phosphorylation are key binding determinants. *J Mol Biol* **2005,** *351* (1), 182-94.

40. Howard, A.; O'Donoghue, M.; Feeney, A.; Sleator, R. D., Acinetobacter baumannii: an emerging opportunistic pathogen. *Virulence* **2012,** *3* (3), 243-50.

41. Wilson, M. G.; Pandey, S., Pseudomonas aeruginosa. In *StatPearls*, StatPearls Publishing Copyright © 2023, StatPearls Publishing LLC.: Treasure Island (FL) ineligible companies. Disclosure: Shivlal Pandey declares no relevant financial relationships with ineligible companies., 2023.

42. Janda, J. M.; Abbott, S. L., The Changing Face of the Family Enterobacteriaceae (Order: "Enterobacterales"): New Members, Taxonomic Issues, Geographic Expansion, and New Diseases and Disease Syndromes. **2021,** *34* (2), 10.1128/cmr.00174-20.

43. Asokan, G. V.; Ramadhan, T.; Ahmed, E.; Sanad, H., WHO Global Priority Pathogens List: A Bibliometric Analysis of Medline-PubMed for Knowledge Mobilization to Infection Prevention and Control Practices in Bahrain. *Oman medical journal* **2019,** *34* (3), 184-193.

44. Antibiotic resistance threats in the United States, 2019. **2019**.

45. Shanta, P. V.; Li, B.; Stuart, D. D.; Cheng, Q., Lipidomic Profiling of Algae with Microarray MALDI-MS toward Ecotoxicological Monitoring of Herbicide Exposure. *Environmental Science & Technology* **2021,** *55* (15), 10558-10568.

46. Li, B. Sing-Cell Lipidomic Analysis and Cytotoxicity Studies of Microorganisms Enabled by Plasmonics-Enhanced MALDI-MS. UC Riverside, ProQuest, 2022.

47. Kaletta, T.; Hengartner, M. O., Finding function in novel targets: C. elegans as a model organism. *Nature Reviews Drug Discovery* **2006,** *5* (5), 387-399.

48. Folga, S. M.; Decision; Sciences, I. *Natural gas pipeline technology overview*; United States, 2007; p Medium: ED.

Appendix

A.1 Example Code of Lipid Vesicle Modeling via Monte Carlo Methods

The code shown below is written in R and executed using RStudio to model lipid distribution within lipid vesicles. As well as calculate distance between lipids within these modeled vesicles and output resulting distribution results. Comments labeled as (##) denoting the purpose of a section of code and (#) for explanation of the purpose of individual lines of code.

```
## Required libraries
library("rgl")

## Sensor Parameters
SensorArea = 42.6

## Parameters of the lipid vesicles in question
Lipid1_Pct = 99
Lipid2_Pct = 1
Lipid1_Mass = 760.091
Lipid2_Mass = 1602.949
Vesicle_Diameter = 50
Vesicle_Radius = Vesicle_Diameter/2
Bilayer_Thickness = 5
Lipid_Area = .683
Lipid_Radius = sqrt(Lipid_Area/pi)

## Simplified calculation of vesicle number and mass based on sensor parameters
```

```
SensorAreaNM = SensorArea * 1e+12

VesicleArea = Vesicle_Radius ^ 2

NumVesicle = SensorAreaNM/VesicleArea

VesicleMass = (Num_Lipids1*Lipid1_Mass) + (Num_Lipids2*Lipid2_Mass)

TotalVesMass = VesicleMass * NumVesicle

Picogram = TotalVesMass / 6.022e+11

RU = Picogram / SensorArea

RU


## Calculates number of lipids in a vesicle and number of each lipid that makes up the vesicle

Num_Lipids = ceiling((4*pi*((Vesicle_Diameter/2)^2)+4*pi*(Vesicle_Radius-Bilayer_Thickness)^2)/Lipid_Area)

Outer_Lipids = ceiling(4*pi*((Vesicle_Diameter/2)^2)/Lipid_Area)

Num_Lipids1 = round(Outer_Lipids*(Lipid1_Pct/100))

Num_Lipids2 = round(Outer_Lipids*(Lipid2_Pct/100))


## Builds a base sphere for the lipid vesicle

spheres3d(0, 0, 0, radius=1, color="white")


## Randomly select locations for lipid 2

n <- Num_Lipids2

theta <- runif(n,0,2*pi)

u <- runif(n,-1,1)

x <- sqrt(1-u^2)*cos(theta)

y <- sqrt(1-u^2)*sin(theta)

z <- u


# Graphs a 3d representation of the lipids distributed on a sphere
```

```
spheres3d(x, y, z, col="red", radius=(Lipid_Radius/Vesicle_Radius))
rglwidget() #opens the 3d representation in R's viewer


iterations = round(50000/n) #reduces the number of iterations based on the number of lipids of this type in the vesicle
ChordList <- c() #initializes ChordList for the loops coming up


## Loop to iterate through thousands of vesicles and pull-out chord length of lipids nearest neighbors
for (i in 1:iterations){
  theta <- runif(n,0,2*pi)
  u <- runif(n,-1,1)
  x <- sqrt(1-u^2)*cos(theta)
  y <- sqrt(1-u^2)*sin(theta)
  z <- u
  NumValues <- length(x)
  for (i in 1:NumValues){
    x1 <- x[i]
    y1 <- y[i]
    z1 <- z[i]


    ChordLength <- c()


    for (i in 1:NumValues){
      x2 <- x[i]
      y2 <- y[i]
      z2 <- z[i]
      ChordLengthx <- sqrt((x2-x1)^2 + (y2-y1)^2 + (z2-z1)^2)
      ChordLength <- c(ChordLength, ChordLengthx)
```

```
    }

    ChordLength <- min(ChordLength[ChordLength>0])
    ChordList <- c(ChordList, ChordLength)
  }
}

ChordList <- unique(ChordList)
ChordList <- ChordList*Vesicle_Radius

ChordListLength <- length(ChordList)

## Convert these chord lengths into arc lengths
ArcList <- c()
for (i in 1:ChordListLength){
  ArcListx <- Vesicle_Radius*(2*(asin(ChordList[i]/Vesicle_Diameter)))
  ArcList <- c(ArcList, ArcListx)
}

## Output a histogram of the arc length data with given parameters
Title <- "1% GM1 Distribution in 100nm Vesicles"
hist(ArcList, main = Title, xlab = "Arc Distance (nm)", xlim = c(0,20), ylim = c(0, 3000), breaks = 50)
mean(ArcList)
max(ArcList)

## Plot all of the lipids within the selected vesicle, can be very intensive with larger vesicles
n <- Num_Lipids1
```

```
theta <- runif(n,0,2*pi)
u <- runif(n,-1,1)
x <- sqrt(1-u^2)*cos(theta)
y <- sqrt(1-u^2)*sin(theta)
z <- u
spheres3d(x, y, z, col="blue", (Lipid_Radius/Vesicle_Radius))
rglwidget()
```

A.2 Example Code of MALDI-MS Data Processing and Machine Learning for Bacteria Identification

Code provided below is written in R and executed in RStudio to pull in raw MALDI-MS spectra into R for data processing and compilation for implementation into machine learning algorithms to build models for bacterial identification. Code also includes automated figure output enabling quick analysis of model results. Comments labeled as (##) denoting the purpose of a section of code and (#) for explanation of the purpose of individual lines of code.

```
## List of packages
packages = c("dplyr", "rfUtilities", "caret", "R.utils", "pheatmap",
"MALDIquantForeign", "MLeval", "MASS", "MALDIquant", "caretEnsemble",
"corrplot", "readMzXmlData")
library(caret)
## Now load or install&load all
package.check <- lapply(
  packages,
  FUN = function(x) {
    if (!require(x, character.only = TRUE)) {
      install.packages(x, dependencies = TRUE)
      library(x, character.only = TRUE)
    }
  }
)
## Make sure your data is placed in the correct folder separated into folders by class
setwd("~/")
setwd("~/R/Spectra Analysis and ML/Place Data Here")
```

```
## Sets the number of folders to pull from, the number of classes, and then pulls out the folder names to be used as classes

foldernum = 8

folders <- list.files(full.names = T, include.dirs = T) #pulls out all of the folder names

classes <- sub("..", "", folders) #create class column to append to data


## Loop to go through all of the selected class folder and pull out spectral information

for (x in 1:foldernum){

  setwd("~/R/Spectra Analysis and ML/Place Data Here")

  setwd(folders[x]) #changes working directory to next folder

  directory <- list.files(pattern="*.mzxml", recursive = T) #pulls out spectra within selected folder

  s1 <- importMzXml(directory)

  outtest <- exists("s")

  if(outtest == FALSE){

  s <- s1 #combines all the pulled spectra together

  classifier <- as.character(c(rep(classes[x], length(s1)))) #creates classifier table

  }

  s <- c(s,s1)

  classifier1 <- as.character(c(rep(classes[x], length(s1)))) #creates classifer1 table as temporary store to append

  classifier <- as.character(c(classifier, classifier1)) #combines class names from each iteration

}

classifier <- as.factor(classifier) #converts classes to factors


## Process and align all the spectra

spectra <- smoothIntensity(s, method="MovingAverage", halfWindowSize=2)
```

```
rm(s)

gc()

spectra <- removeBaseline(spectra, method="SNIP", iterations=100)

spectra <- alignSpectra(spectra, halfWindowSize=20, SNR=4, tolerance=0.002,
warpingMethod="lowess")



## Detect peaks for all spectra and plot result for first spectra

peaks <- detectPeaks(spectra, method="MAD", halfWindowSize=20, SNR=10)



## Plots and example spectra to make sure it looks good

plot(spectra[[1]], xlim=c(100, 3000), ylim=c(0, 5000)) #peaks <- trim(peaks,
range=C(100, 1000))

points(peaks[[1]], col="red", pch=4)

spectra <- calibrateIntensity(spectra, method = "TIC") #normalize intensity



## Equalize similar peaks, remove inconsiastent peaks, combine into dataset of peak(m/z)
and intensity

peaks <- binPeaks(peaks, tolerance=0.0005)

peaks <- filterPeaks(peaks, minFrequency=0.30)

imatrix <- intensityMatrix(peaks, spectra)



## Sets the minimum and maximum mass to charge ratio of which peaks will be
considered for machine learning

minmass <- 500

maxmass <- 2000

cols <- as.integer(colnames(imatrix))

col_to_keep <- cols > minmass & cols < maxmass

imatrix <- imatrix[,col_to_keep]
```

```
## Add classification column to dataset
dataset <- data.frame(imatrix, classifier, stringsAsFactors = TRUE)
datasetsave <- dataset

## Split data into training(dataset) and testing(validation)
validation_index <- createDataPartition(dataset$classifier, p=0.70, list=FALSE)
validation <- dataset[-validation_index,]
dataset <- dataset[validation_index,]

## Train control
control <- trainControl(method="repeatedcv", number=10, repeats=3, savePredictions = "final", classProbs = TRUE, index = createFolds(dataset$classifier, 10), allowParallel = TRUE)

## Set metric for model success, Kappa can be good for low % of samples in 1 class
metric <- "Accuracy"

## Train models of chosen type's
algorithms <- c("rf", "nnet", "kknn", "lda", "svmLinear2") #input the algorithms you want to test
model_list <- caretList(classifier~., data=dataset, metric=metric, trControl=control, methodList=algorithms)

## Set output folders and prepare for ML analysis
setwd("~/")
setwd("~/R/S Aureus/All Bacteria/Results Output Here")
graphics.off()
```

```
## Output results of the training and compare success metrics

results <- resamples(model_list)

summary(results)

pdf("models comparisson.pdf", width = 7, height = 7, onefile = FALSE) #saves results as a pdf of given name with given size (in inches)

dotplot(results) #plot to be saved

dev.off() #completes the pdf save


## Loop to put together data as figures for each model and save them as PDFs

for (methodname in algorithms){

  ## Predict testing data with chosen model

  p <- predict(model_list[[methodname]], validation)

  cm <- confusionMatrix(p, validation$classifier)

  print(cm)


  ## Output heatmap of prediction results

  mat <- as.table(cm)

  pdf(paste(methodname, "heatmap.pdf"), width = 7, height = 7, onefile = F) #saves results as a pdf of given name with given size (in inches)

  map <- pheatmap(mat, cluster_rows = FALSE, cluster_cols = FALSE, display_numbers = TRUE, show_colnames = TRUE, show_rownames = TRUE, legend = TRUE, fontsize_number = 20)

  dev.off()


  ## Output correlation plot of prediction results

  co <- cor(mat)

  pdf(paste(methodname, "correlation plot.pdf"), width = 7, height = 7, onefile = FALSE) #saves results as a pdf of given name with given size (in inches)

  corrplot(co, method = "circle")

  dev.off()
```

```
}
## Output list of 20 most important variables for classification with chosen model
pdf("rf important variables.pdf", width = 7, height = 7, onefile = FALSE)
impvar <- varImp(model_list[["rf"]], scale = TRUE)
plot(impvar, top = 20)
dev.off()
setwd("~/")
graphics.off()

library(MASS)

## Trains an LDA model using the whole data set
lda_model <- lda(classifier ~ ., data = datasetsave)
lda_predict <- predict(lda_model)

## Plotting with plotly
library(plotly)

## Setting up lda data for plotly
lda_data <- cbind(datasetsave, lda_predict$x)
LD1 <- lda_data$LD1
LD2 <- lda_data$LD2
LD3 <- lda_data$LD3
class <- lda_data$classifier
lda_dat <- data.frame(LD1, LD2, LD3, class, stringsasfactors = TRUE)

## Setting up plot properties
t1 <- list(
```

```
  family = "Times New Roman",
  size = 24,
  color = "black"
)
t2 <- list(
  family = "Times New Roman",
  size = 18,
  color = "black")
axx <- list(title = "LD2")
axy <- list(title = "LD1")
axz <- list(title = "LD3")


## Plotly figure
fig <- plot_ly(lda_dat, x = LD2, y = LD1, z = LD3, type="scatter3d", mode="markers", color=classifier, size=3)%>%
  layout(title = list(text = "Bacteria LDA", font = t1, y = 0.95), scene = list(xaxis=axx,yaxis=axy,zaxis=axz), legend = list(title = list(text = "Bacteria Species"), font = t2))
fig
setwd("~/")


## Loop to train each model multiple times providing insight into model variability
for (i in 1:25){
  validation_index <- createDataPartition(datasetsave$classifier, p=0.70, list=FALSE)
  validation <- datasetsave[-validation_index,]
  dataset <- datasetsave[validation_index,]
  control <- trainControl(method="repeatedcv", number=10, repeats=3, savePredictions = "final", classProbs = TRUE, index = createFolds(dataset$classifier, 10), allowParallel = TRUE)
```

```
  model_list <- caretList(classifier~., data=dataset, metric=metric, trControl=control,
methodList=algorithms)


  for (methodname in algorithms){
    ## Predict testing data with chosen model
    p <- predict(model_list[[methodname]], validation)
    cm <- confusionMatrix(p, validation$classifier)


    ## Accuracy measurement
    acc1 <- cm[["overall"]][["Accuracy"]]
    acc <- c(acc,acc1)
    print(acc)
  }
  outtest <- exists("accuracydata")
  if(outtest == FALSE){
    accuracydata <- acc
  }
  if(outtest == TRUE){
    accuracydata <- data.frame(accuracydata, acc)
  }
  acc <- c()
  acc1 <- c()
}


## Output a CSV file containing all of the trained model accuracies
accuracydata <- t(accuracydata)
accuracydata <- data.frame(accuracy)
colnames(accuracy) <- (algorithms)
```

```
average <- c(mean(accuracy$rf), mean(accuracy$nnet), mean(accuracy$kknn),
mean(accuracy$lda2))

average <- t(data.frame(average))

colnames(average) <- (algorithms)

stdev <- c(sd(accuracy$rf), sd(accuracy$nnet), sd(accuracy$kknn), sd(accuracy$lda2))

stdev <- t(data.frame(stdev))

colnames(stdev) <- (algorithms)

AccuracyData <- rbind(accuracy, average, stdev)

setwd("~/R/Spectral Analysis/Results Output Here")

write.csv(accuracy, "AccuracyData.csv", row.names=TRUE)
```